N° d'ordre : 40296

Université de Lille 1

UMR CNRS 8207 Unité Matériaux et Transformations

THÈSE

pour obtenir le diplôme d'

HABILITATION A DIRIGER DES RECHERCHES

Discipline : Sciences Physiques

par

**Damien Jacob**

# Caractérisation microstructurale des matériaux : vers une diffraction électronique quantitative

Présentée devant la commission d'examen formée de :

| | |
|---|---|
| Monsieur Patrick Cordier | Examinateur / Directeur |
| Monsieur Martin Hytch | Rapporteur |
| Monsieur Hugues Leroux | Examinateur / Président |
| Madame Jany Thibault-Penisson | Examinatrice |
| Monsieur Pierre Stadelmann | Rapporteur |
| Monsieur Jian-Min Zuo | Rapporteur |

*Il faut créer ce que l'on cherche.*

René Magritte

# Sommaire :

Introduction 7

Première partie - Présentation des travaux

Chapitre 1 : Analyse des déformations par faisceau convergent. 13

1.1.1. Préambule : Contraintes et déformations dans les nanostructures semiconductrices. Mesures par MET. 13

1.1.2. Déformation d'un puis enterré dans une matrice. 14

1.1.3. Déformation en surface. 17

1.1.4. Conclusion : apports et limites des études. 18

Chapitre 2 : Maclage et abaissements de symétrie, études par précession électronique.

1.2.1. Précession électronique. 21

1.2.2. Maclage par pseudo-mériédrie réticulaire : cas de la coesite. 22

1.2.3. Maclage par mériédrie réticulaire : cas de quartz. 25

Chapitre 3 : Microstructures des échantillons cométaires de la mission Stardust. 31

Perspectives en cristallographie électronique. 37

Bibliographie. 43

Deuxième partie - Informations personnelles

2.1. Curriculum Vitae. 51

2.2. Production scientifique. 55

Troisième Partie - Articles 65

# Introduction

La microscopie électronique en transmission (MET) est un outil polyvalent et puissant pour les analyses microstructurales en sciences des matériaux. Sur la même zone d'observation, on peut imager la microstructure et ses défauts avec une résolution nanométrique, en faire une détermination structurale en diffraction, une analyse chimique - en micro-analyse X ou en perte d'énergie - et étudier les propriétés mécaniques électriques, optiques, magnétiques, post-mortem ou in-situ. Les développements technologiques récents concernant l'optique et les sources électroniques confortent sa position incontournable en sciences des matériaux et en physique du solide, particulièrement dans le domaine des nanosciences.

Chacune des possibilités offertes par la MET, par les conditions particulières d'observation qu'elles requièrent, la nature des échantillons et les interactions électrons-matière mises en jeu pour produire les effets analysés véhicule sa cohorte de « spécialistes », qui seront parfois difficilement capables de sortir de leur niches pour envisager les analyses par un autre bout de la lorgnette. Je suis peut-être un de ceux-là, tombé dans l'espace réciproque de la diffraction électronique et ses clichés à la symétrie envoûtante, comptant sur mes collègues et amis pour me ramener à la réalité de l'espace direct.

Ce mémoire décrit mon activité de recherche depuis une dizaine d'années au Laboratoire de Structure et Propriétés de l'Etat Solide (LSPES), devenu depuis janvier 2010 l'Unité Matériaux et Transformations (UMET). Cette activité porte essentiellement sur le développement de méthodes de *diffraction électronique quantitative* en MET pour la caractérisation microstructurale des matériaux. Par « quantitatif », nous entendons la mesure absolue ou relative des intensités diffractées et leur comparaison à des grandeurs simulées. Cette thématique, démarrée au sein du groupe « Semiconducteurs » de 1999 à 2006, se développe aujourd'hui dans l'équipe « Physique des Minéraux ».

Concernant les matériaux semiconducteurs, mes recherches ont porté sur la *mesure des déformations* dans les nanostructures épitaxiées. Dans ces systèmes, les champs de déformation jouent un rôle prépondérant sur les propriétés de maintien (mécanique) et sur les propriétés d'usage (opto-électroniques, transport). Il est donc important de les caractériser avec précision. Nous avons développé des méthodes de mesure originales basées sur l'analyse des intensités électroniques recueillies en *diffraction en faisceau convergent conventionnel et à grand angle* (CBED et LACBED).

Les développements actuels portent sur la caractérisation des phases cristallines et de leurs défauts structuraux dans les minéraux. Dans ces matériaux, de cristallochimie souvent complexe, l'analyse quantitative des intensités diffractées permet notamment de discerner des phases cristallographiquement proches ou de révéler les relations d'orientation existant entre des domaines voisins. Ceci est essentiel aux analyses microstructurales locales et à leur interprétation en vue de déterminer les conditions de pression, température et cinétique de transformation ayant prévalu à leur formation. Mon apport dans le domaine est essentiellement basé sur l'utilisation de la *précession électronique*.

Dans le domaine des minéraux, un autre type d'études a été menée parallèlement aux précédentes. Il s'agit de l'analyse des échantillons cométaires provenant de la mission américaine « *Stardust* ». Dans ce cas, on utilise toutes les techniques disponibles pour en révéler la nature et les mécanismes possibles de formation: micro-analyse X, imagerie conventionnelle et haute résolution, diffraction. Ma contribution a essentiellement porté sur l'analyse de la microstructure des pyroxènes présents dans ces échantillons, qui sont en général des traceurs fiables pour rendre compte du passé thermique et mécanique des minéraux.

Enfin, l'étude de ces échantillons met en évidence l'intérêt de disposer de techniques robustes pour appréhender à une échelle locale, micrométrique, leur histoire thermique. Ici encore, c'est l'analyse quantitative des intensités qui est en jeu. L'application aux électrons des méthodes utilisées en diffraction X pour les déterminations structurales serait une évolution naturelle de ces travaux, basée sur une véritable cristallographie électronique quantitative.

La première partie de ce mémoire concerne la présentation plus détaillée de ces travaux. Dans le premier chapitre, nous décrivons les résultats obtenus dans les domaines des semiconducteurs pour la mesure des déformations. Puis, nous présentons les travaux relatifs à l'utilisation de la précession électronique pour l'analyse du maclage issu d'abaissements de symétrie dans les minéraux. Enfin, nous décrivons les résultats obtenus sur les microstructures

des échantillons cométaires de la mission Stardust. La conclusion de cette partie porte sur les perspectives ouvertes par ces études concernant la cristallographie électronique. La description plus individuelle de mon parcours scientifique ainsi que la liste des publications, activités d'encadrement et d'animation scientifique associées à ma recherche sont exposées dans la deuxième partie. Les articles présentés sont reproduits dans la dernière partie de ce mémoire.

# Première partie : Présentation des travaux

# Chapitre I : Analyse des déformations par faisceau convergent.

*Collaborateurs* : Y. Androussi (UMET), F. Houdellier (CEMES), A. Lefebvre (LSPES), J. P. Morniroli (LMPGM), J. M. Zuo (University of Illinois).

## 1.1.1. Préambule : contraintes dans les nanostructures et mesures par MET.

Les nanostructures semiconductrices utilisées dans le domaine de la micro ou de l'opto-électronique sont généralement des systèmes contraints. Les contraintes sont produites de façon non-intentionnelle pendant les diverses étapes de la croissance des composants (dépôts en couches minces de matériaux aux propriétés mécaniques différentes) ou de façon directe par le désaccord paramétrique des couches épitaxiées sur le substrat. Quand elles sont présentes dans les zones actives des hétérostructures, les contraintes peuvent endommager les propriétés d'usage ou au contraire les optimiser, comme c'est le cas pour les propriétés de transport dans les composants à base de $Si_xGe_{1-x}$/Si. Il est donc important de les caractériser avec précision et ceci a constitué une thématique de recherche importante depuis les années 1980 jusqu'à aujourd'hui.

La MET, avec sa résolution spatiale nanométrique et sa grande sensibilité aux champs de déformation, est une technique bien adaptée pour aborder les mesures de déformations induites par les contraintes à une échelle très locale. Plusieurs méthodes existent, en mode imagerie ou en mode diffraction. En imagerie, c'est essentiellement la Microscopie Haute Résolution (MHR) qui est utilisée. Elle permet de mesurer les déplacements des colonnes atomiques dans les zones déformées par rapport à une zone de référence non déformée de l'échantillon. Le traitement peut se faire par mesures directes (« Peak Finding Method », Kret et al., 1998) ou par l'analyse des déphasages induits par les déformations (« Geometric Phase Analysis », Hÿtch et al., 1998). En mode diffraction, la technique la plus utilisée est celle du Faisceau Convergent (Convergent Beam Electron Diffraction, CBED). En CBED, la sonde électronique, de dimension nanométrique, est focalisée sur l'échantillon et le diagramme de diffraction obtenu est constitué de disques dans lesquels de nombreuses lignes sont visibles, les lignes de Bragg. Chaque ligne correspond à un plan réticulaire d'indices (hkl) en position de diffraction par rapport au faisceau incident. Pour les indices faibles, correspondant aux diffractions intenses interagissant fortement entre elles, ces lignes dites « dynamiques » sont

larges et présentent des profils d'intensité complexes. Pour les indices (hkl) élevés, correspondant aux réflexions de plus faible intensité et interagissant peu entre elles, ces lignes sont au contraire très fines et leur position à l'intérieur des disques très sensibles aux distances inter-reticulaires $d_{hkl}$ des plans atomiques diffractants. Les légères variations de ces distances induites par les déformations produisent des variations de position des lignes qui peuvent être analysées pour mesurer précisément les déformations.

Dans ces diverses méthodes, en modes imagerie et diffraction, l'échantillon est observé transversalement, c'est-à-dire avec la direction de croissance des nanostructures positionnée perpendiculairement à la direction du faisceau électronique incident. L'amincissement nécessaire des échantillons pour obtenir la transparence aux électrons crée dans ce cas des surfaces libres dans les zones contraintes qui modifient l'état de déformation des matériaux par rapport à leur état dans l'échantillon « massif » (Treacy et al., 1985). Ces phénomènes de relaxation de surface doivent être pris en compte pour passer de l'état de déformation dans la lame mince à celui existant dans l'échantillon massif. L'originalité de nos travaux consiste à se placer dans des conditions d'observation telles que ces phénomènes de relaxation puissent être en premier abord négligés. Pour ce faire l'échantillon est observé en « vue plane », c'est-à-dire avec le faisceau électronique parallèle à la direction de croissance des nanostructures. Dans ce cas, les surfaces libres créées par l'amincissement de l'échantillon sont situées loin des zones contraintes et modifient peu l'état de déformation de l'échantillon.

### 1.1.2. Déformation d'un puits enterré dans une matrice.

La technique initialement utilisée est celle du LACBED (Tanaka et al., 1980). L'avantage principal de ce mode d'observation est qu'il couple l'information de l'espace direct (celui de l'objet) à celle de l'espace réciproque (celui de la diffraction), ce qui est notamment très efficace pour l'analyse des défauts structuraux comme les dislocations (Cherns et Preston, 1986). De façon générale en microscopie électronique, le contraste d'un défaut est associé à son champ de déplacement $\vec{R}(x,y,z)$, qui produit un écart local aux conditions de diffraction. En mode image, on cherche à « allumer » le contraste du défaut en sélectionnant un vecteur de diffraction $\vec{g}$ sensible au champ de déplacement (tel que $\vec{g}.\vec{R} \neq 0$), ou au contraire à « l'éteindre » avec un vecteur de diffraction insensible (tel que $\vec{g}.\vec{R} = 0$). En diffraction en faisceau convergent, on visualise directement l'effet du champ de déplacement sur l'ensemble des diffractions excitées dans les conditions d'orientation de l'échantillon, c'est-à-dire sur les

lignes de Bragg. Pour l'analyse quantitative du champ responsable de ces modifications, on compare les résultats expérimentaux avec des simulations d'intensité incluant différents modèles de champs. Dans un premier temps, je me suis attaché à tester les potentialités de cette technique pour l'analyse du champ de déformation dans le cas d'une hétérostructure modèle (puits quantique) constituée d'une mince couche contrainte d'alliage ternaire III-V d'$In_xGa_{1-x}As$ enterrée dans une matrice de GaAs (Fig. 1.1). En m'inspirant des travaux de Hovespian (Hovespian et al., 1999), j'ai pu analyser l'effet de la déformation du puits sur les intensités diffractées, effet similaire à celui créé par une faute d'empilement quand l'échantillon est observé en vue plane. La déformation du puits introduisant un déplacement parallèlement à l'axe de croissance entre les couches de GaAs situées de part et d'autre du puits, la plupart des lignes de Bragg des réflexions cinématiques se trouvent dédoublées (Fig. 1.2). L'analyse quantitative de l'intensité de ces lignes permet, par comparaison avec des simulations, de remonter simplement à la teneur en indium du puits avec une bonne précision (Jacob et al., 2001). Les résultats ont montré un bon accord entre la composition mesurée et celle obtenue par diffraction des rayons X sur un système multi-couche élaboré dans les mêmes conditions. La méthode, couplée à une technique d'imagerie chimique en champ noir conventionnel, a également été appliquée avec succès à l'étude de la composition d'un alliage quaternaire $Ga_{1-x}In_xN_yAs_{1-y}$ enterré dans une matrice de GaAs (Jacob et al., 2003).

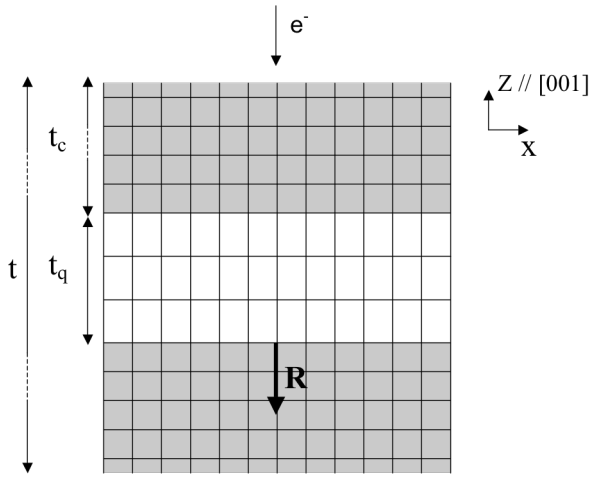


*Fig. 1.1 : Déformation quadratique d'une couche mince d'$In_xGa_{1-x}As$ d'épaisseur $t_q$ enterrée dans une matrice de GaAs d'épaisseur totale t. R est le déplacement induit par la déformation de la couche de part et d'autre de celle ci, $t_c$ est l'épaisseur du cap layer. Jacob et al., 2008a.*

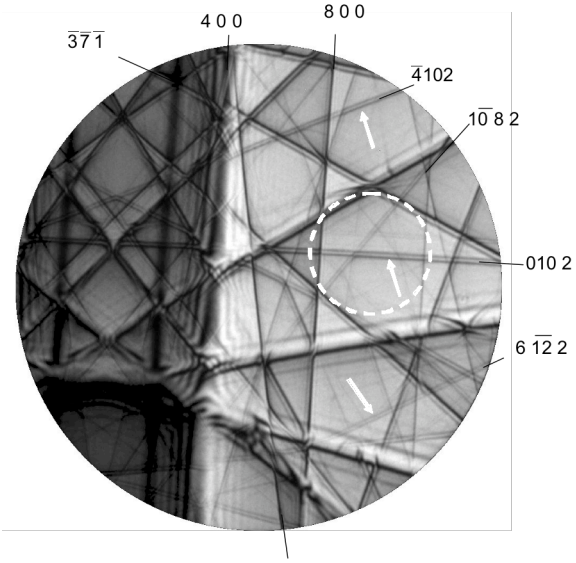


*Fig. 1.2 : Cliché LACBED obtenu en vue-plane sur l'échantillon schématisé Fig. 1.1. La plupart des lignes de Bragg cinématiques sont dédoublées. Axe de zone <015>. Jacob et al., 2008a.*

L'analyse a ensuite été reprise de façon plus quantitative en CBED filtré en énergie. Alors qu'avec le mode LACBED, une partie des électrons diffusés inélastiquement (et non pris en compte dans les simulations) est filtrée de façon mécanique par un diaphragme, en CBED, il est nécessaire d'utiliser un filtre en énergie pour procéder à des analyses quantitatives des intensités. Ceci a été possible à partir de l'installation au centre commun de microscopie de Lille en 2005 du nouveau microscope Tecnai G20 (FEI) équipé d'un filtre en énergie GIF (Gatan Imaging Filter). L'utilisation d'une sonde focalisée permet alors d'obtenir une résolution spatiale nanométrique, contrairement au LACBED qui est un mode défocalisé. Ainsi, il devient possible de détecter des hétérogénéités des champs de déformation associés à des variations de composition à une échelle très locale (quelques nanomètres). Pour l'analyse quantitative des résultats, il est alors nécessaire de prendre en compte les interactions dynamiques entre l'ensemble des faisceaux diffractés. C'est concernant ce point que la collaboration avec J. M. Zuo a été déterminante (Fig 1.3). *In fine*, la précision relative atteignable sur la mesure de la composition de l'alliage enterré est de 5% (Jacob et al., 2008a).

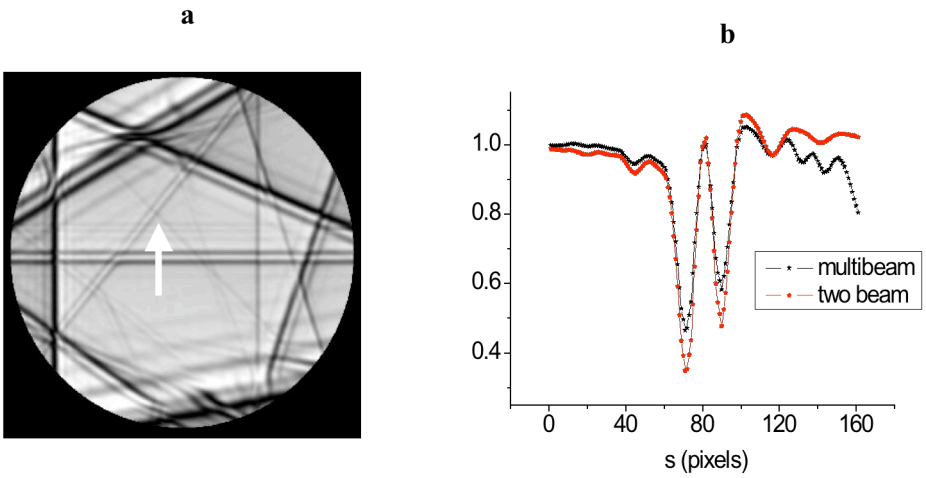


*Fig. 1.3 : (a) Cliché CBED simulé en multi-ondes. (b) Comparaison des profils d'intensité de la ligne 0 10 2 calculés en deux ondes et en muti-ondes. Composition en indium du puits : x = 0,12, épaisseur : $t_q$ =10 nm. Jacob et al., 2008a.*

## 1.1.3. Déformations en surface.

Nous avons également analysé la façon dont les intensités des réflexions dynamiques sont modifiées par la présence d'un champ de déformation localisé à la *surface* des échantillons.

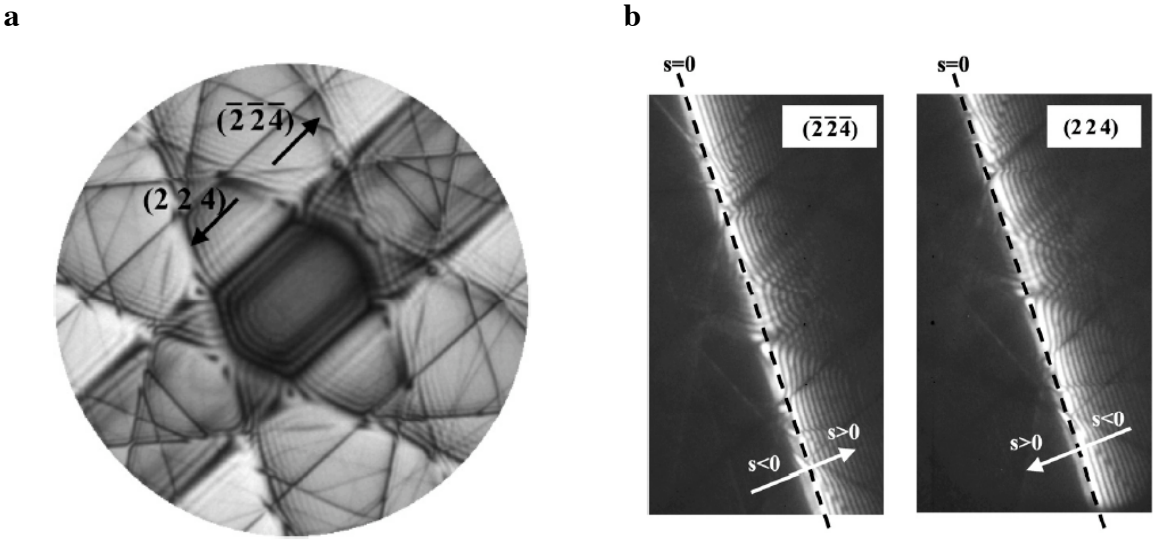


*Fig. 1.4 : (a) Cliché LACBED obtenu sur un échantillon de GaAs déformé en surface. (b) Champs noirs sur les lignes de Bragg repérées en a). Les lignes en champ noir sont asymétriques en intensité. Jacob and Lefebvre, 2003.*

Dans le domaine des semiconducteurs, cette situation se présente lors de l'analyse en vue

plane des couches épitaxiées sur un substrat massif. Une première étude réalisée en LACBED et s'inspirant des travaux de Vincent (Vincent et al., 1999) a montré que la présence de déformations à la surface des échantillons induisait une asymétrie forte et anormale des intensités des lignes de Bragg dynamiques (Jacob and Lefebvre, 2003. Fig. 1.4). Les résultats de simulation indiquent que cette asymétrie est liée à la position de la couche déformée par rapport à la surface de l'échantillon, à son épaisseur, ainsi qu'à son taux de déformation. Ces travaux ont été repris en CBED avec F. Houdellier (CEMES, Toulouse) dans une étude réalisée en couplant les simulations des intensités dynamiques avec des modélisations des champs de déformation par la méthode des éléments finis (Houdellier et al., 2008. Fig 1.5).

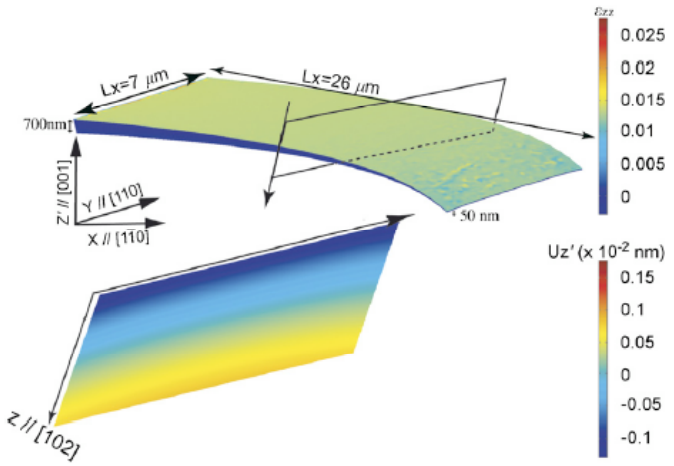


*Fig. 1.5 : Modélisation par la méthode des éléments finis d'une lame mince déformée par une couche contrainte située à la surface de l'échantillon. Houdellier et al., 2008.*

Les résultats ont montré que si les intensités diffractées étaient effectivement très sensibles aux champs de déformation hétérogènes, même très localisés à la surface de l'échantillon, leur analyse quantitative ne pouvait se faire qu'à condition de connaître très précisément la géométrie de l'échantillon aminci, ce qui est généralement hors de portée de l'expérimentateur. Les analyses ne restent donc la plupart des cas que semi-quantitatives.

### 1.1.4. Conclusion : apports et limites des études.

Ces études exploitent la grande sensibilité de la diffraction électronique aux champs de déformation présents dans les échantillons, même très localisés. En fonction de la nature du champ et de sa position dans l'échantillon, les effets se font principalement sentir sur les

lignes cinématiques ou sur les lignes dynamiques. L'originalité des études a consisté à s'affranchir partiellement des effets de relaxation de surface en observant les échantillons en vue plane. Quand les champs de déformation sont localisés loin des interfaces, comme dans le cas du puits enterré, les effets de relaxation sont inexistants et l'analyse peut être menée de façon quantitative. Cette situation est toutefois très limitée et dans la plupart des cas, la relaxation des contraintes en surface doit être prise en compte. Parallèlement à ces travaux, de nombreuses études ont été menées en CBED dans des échantillons observés en section transverse (faisceau électronique perpendiculaire à la direction de croissance). Les phénomènes de surface y sont nécessairement actifs, induisant une courbure des plans atomiques le long de la direction de propagation du faisceau d'électrons. Les lignes de Bragg paraissent alors le plus souvent avec un contraste multiple (Clement et al., 2004 ; Houdellier et al., 2006), ce qui rend l'analyse complexe. Le recours à la modélisation des champs de déformation est nécessaire et il faut pour ce faire maîtriser au mieux la géométrie de l'échantillon. C'est ainsi que l'utilisation de techniques de préparation sophistiquées comme l'amincissement par faisceau ionique focalisé dans un microscope à balayage (FIB, Focussed Ion Beam) est devenue courante pour ce type d'étude.

Notons enfin que parallèlement aux études réalisées en diffraction, de nombreuses avancées ont été faites dans le domaine de l'imagerie. On citera notamment la méthode d' « holographie en champ noir » (Hÿtch et al., 2008) dans laquelle des images d'interférence entre le faisceau transmis et un faisceau diffracté sont réalisées grâce à une sonde cohérente obtenue avec les sources à émission de champ (FEG). Cette technique permet d'extraire des cartographies des champs de déformation avec une très grande sensibilité, et ceci sur de larges plages de l'échantillon, ce qui constitue une avancée majeure par rapport à l'imagerie haute résolution couramment utilisée pour ce type d'études. Pour ce faire, l'utilisation d'un correcteur d'aberration de la lentille objectif du microscope, qui permet de maintenir la cohérence du faisceau électronique sur un grand domaine spatial, est un atout indéniable. Du côté de la diffraction, c'est certainement du côté de la correction des aberrations de la sonde électronique elle-même qu'on peut attendre des avancées significatives, en diminuant encore la taille de la sonde incidente sur l'échantillon. C'est le domaine en développement de la nanodiffraction électronique et de la nanocristallographie.

**Publications concernées par ces études** (les travaux précédés d'un astérisque sont reproduits à la fin de ce mémoire) :


1. *Houdellier, F., Jacob, D., Casanove, M.J., and Roucau, C. (2008) Effect of sample bending on diffracted intensities observed in CBED patterns of plan view strained samples. Ultramicroscopy, 108(4), 295-301.
2. Jacob, D., Androussi, Y., and Lefebvre, A. (2001) LACBED measurement of the chemical composition of a thin InxGa1-xAs layer buried in a GaAs matrix. Ultramicroscopy, 89(4), 299-303.
3. *Jacob, D., and Lefebvre, A. (2003) Interpretation of unexpected rocking curve asymmetry in LACBED patterns of semiconductors. Ultramicroscopy, 96(1), 1-9.
4. Jacob, D., Lefebvre, A., Chauveau, J.M., Trampert, A., and Tournié, E. (2003) LACBED analysis of the chemical composition of compound semiconductor strained layers. In I. Publishing, Ed. XIII$^{th}$ International Conference on Microscopy of Semiconducting Materials, 180, p. 221-224. Cullis, Cambridge, U.K.
5. *Jacob, D., Zuo, J.M., Lefebvre, A., and Cordier, Y. (2008a) Composition analysis of semiconductor quantum wells by energy filtered convergent-beam electron diffraction. Ultramicroscopy, 108(4), 358-366.
6. Morniroli, J.P., Albarede, P.H., and Jacob, D. (2005) TEM characterization of strained silicon. In E. Zschech, C. Whelan, and T. Mikolajick, Eds. Materials for Information Technology: Devices, Interconnects and Packaging, p. 99-108.

# Chapitre II : Maclage et abaissements de symétrie, études par précession électronique.

*Collaborateurs* : Patrick Cordier (UMET), Jean-Paul Morniroli (LMPGM).

## 1.2.1. Précession électronique

La diffraction électronique en précession (PED) développée en 1994 par Vincent et Midgley (Vincent and Midgley, 1994) connaît ces dernières années un nouvel essor, grâce notamment au développement de modules externes permettant son implantation sur tout type de MET. Avec ce mode « dynamique » de diffraction dans lequel le faisceau incident n'est pas fixe, mais balaye une surface conique convergeant sur l'échantillon, les clichés de points obtenus avec un faisceau parallèle ont retrouvé un intérêt certain pour les analyses structurales. Ces clichés sont utilisés dans les nombreuses situations où la diffraction en faisceau convergent n'est pas adaptée : volume diffractant insuffisant, échantillon sensible à l'irradiation électronique, zone observée trop mince, paramètres de maille trop grands… On est en pratique contraint de prendre les diffractions comme on le peut : au mieux, en « microdiffraction » avec une sonde de taille nanométrique très faiblement convergente et focalisée sur l'échantillon, au pire en « aire sélectionnée » avec un faisceau parallèle et un diaphragme de sélection le plus petit possible. Dans ce dernier cas, la taille minimale de la zone analysée est de quelques centaines de nanomètres. Sur ce type de clichés en aire sélectionnée, les intensités ne sont généralement pas exploitables pour les analyses quantitatives. D'une part, parce qu'elles sont moyennées sur une zone étendue spatialement et donc inhomogène en épaisseur et orientation. D'autre part, parce qu'elles sont modifiées par les interactions dynamiques entre faisceaux diffractés. On est donc généralement très loin de « l'approximation cinématique » valide avec les rayons X, dans laquelle les intensités sont proportionnelles au carré du facteur de structure des réflexions considérées. Seules les positions des taches de diffraction sont exploitables pour les mesures des distances inter-reticulaires, les indexations des réflexions et la détermination de l'orientation de l'échantillon. La précession remède partiellement à ce problème : le faisceau étant mobile, les réflexions ne sont pas excitées simultanément, ce qui réduit fortement les possibilités d'interactions entre faisceaux. Ainsi, un cliché de points acquis en précession sur un échantillon d'épaisseur

commune d'une centaine de nanomètres ressemble-t-il en premier examen à ce qu'on recueille sur un échantillon très mince, d'une dizaine de nanomètres : les intensités y paraissent pondérées par les facteurs de structure. C'est cette propriété majeure des clichés obtenus en précession que nous exploitons dans les études microstructurales présentées ici. Toutefois, plusieurs études (Own et al., 2006; Eggeman et al., 2010; White et al., 2010) révèlent le comportement complexe des intensités en fonction de l'épaisseur de l'échantillon. Les interactions dynamiques doivent être en général prises en compte pour analyser de façon fine les intensités, ce que nous avons également entrepris dans ces travaux. Enfin, notons que si les travaux présentés ici concernent les minéraux, les méthodes décrites sont généralisables à tout types de matériaux présentant des abaissements de symétrie (Morniroli et al. 2008, Ji et al. 2009).

### 1.2.2. Maclage par pseudo-mérihédrie réticulaire : cas de la coesite.

Une première étude porte sur l'étude du maclage par pseudo-mériedrie d'un échantillon naturel de coesite ($SiO_2$). Ce minéral est une phase haute pression de la silice (stable au delà de 3 GPa), monoclinique par ses symétries (groupe spatial *P*2/*c*) mais quasiment hexagonale par ses paramètres réticulaires : a = 0.71356, b = 1.23692, c = 0.71736 nm et β = 120.34° (Levien & Prewitt,1981) (Fig. 2.1).

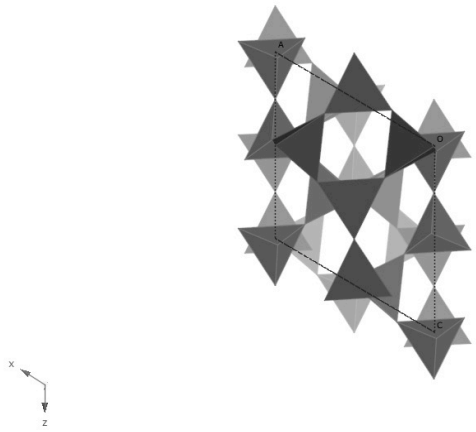


*Fig 2.1 : Projection suivant l'axe b de la coesite $SiO_2$. Les tetraèdres de $SiO_4$ partagent leurs sommets.*

Nous avons dans un premier temps caractérisé la macle en LACBED (Jacob et al., 2008b), technique bien adaptée pour l'analyse des défauts structuraux dans les échantillons sensibles à l'irradiation électronique (Cordier et al., 1995). La macle apparaît alors comme un miroir suivant le plan (021) (Fig 2.2) et le maclage s'associe à une rotation d'un angle proche de 90° autour de l'axe [100]. Cette rotation rend parallèle des directions non équivalentes de la structure monoclinique qui le seraient si la structure était parfaitement hexagonale : il s'agit d'une macle par pseudo-mériédrie réticulaire de la structure hexagonale. Ce type de macle avait déjà été proposé dans le cas d'échantillons synthétiques, mais jamais décrite de façon détaillée dans des échantillons naturels.

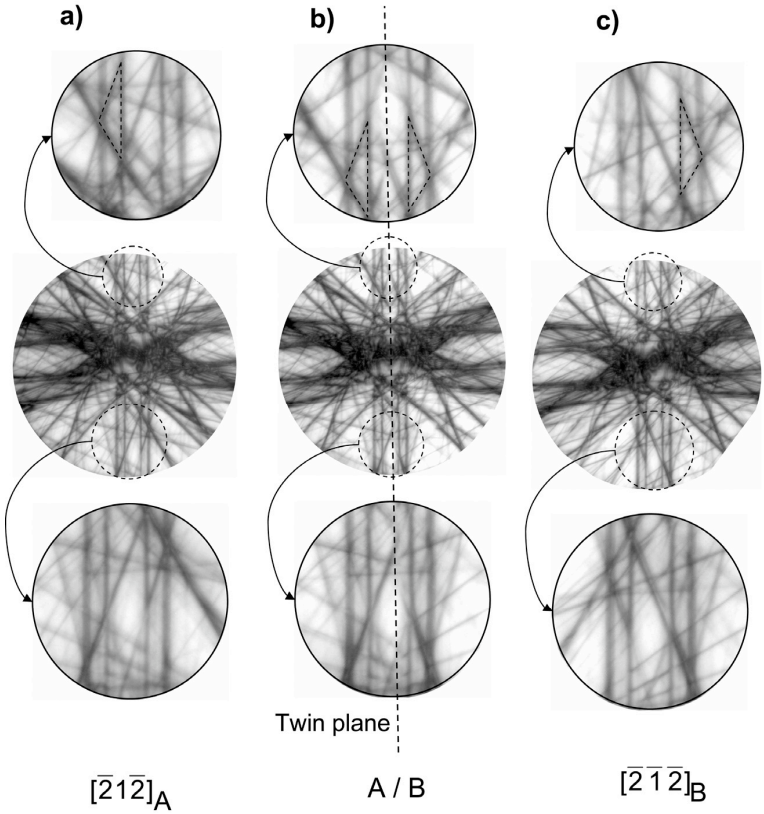


*Fig. 2.2 : Clichés LACBED en axe de zone recueillis de part et d'autre de la macle (a et c) et sur la macle (b). Sur le cliché (b) la trace du plan de macle est visible et la symétrie miroir induite par la macle est clairement mise en évidence (Jacob et al., 2008b).*

L'étude a ensuite été entreprise en précession électronique, avec des clichés de diffraction obtenus en aire sélectionnée (Jacob et al., 2009). Sans précession, les clichés enregistrés sur les différents variants de la macle sont indiscernables, la pseudo-symétrie de la structure ne permettant pas de séparer les réflexions des individus maclés (Fig 2.3). Par contre, les clichés

obtenus en précession se révèlent très facilement distinguables, non pas par la position de taches de diffraction mais par leur intensité (Fig. 2.4). La comparaison avec des simulations cinématiques permet alors d'indexer sans ambiguïté les orientations mises en parallèle dans les individus maclés et ainsi d'identifier la macle.

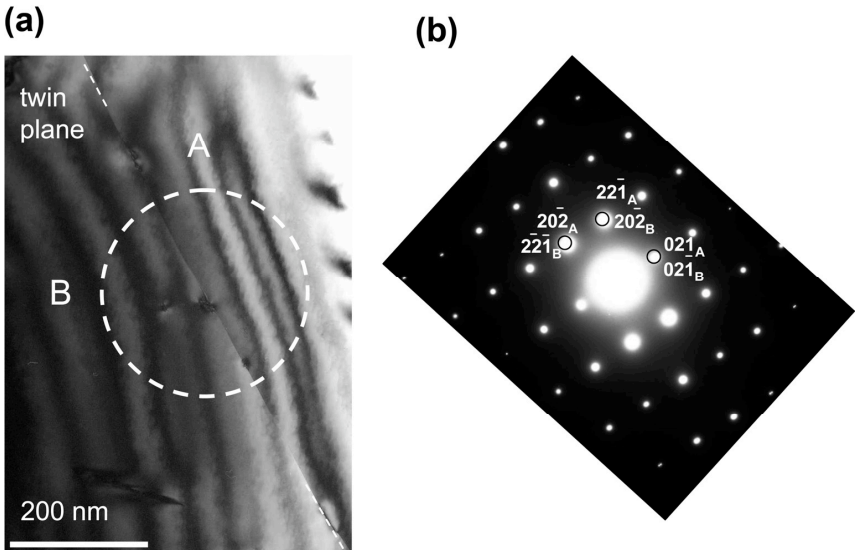


*Fig 2.3 : (a) Image en champ clair de la macle orientée parallèlement au faisceau électronique et (b) cliché de diffraction associé. Le cercle en pointillé correspond à la position du diaphragme de sélection d'aire incluant les deux variants A et B de la macle. Aucun dédoublement des taches n'est détecté sur le cliché de diffraction (Jacob et al. 2008b).*

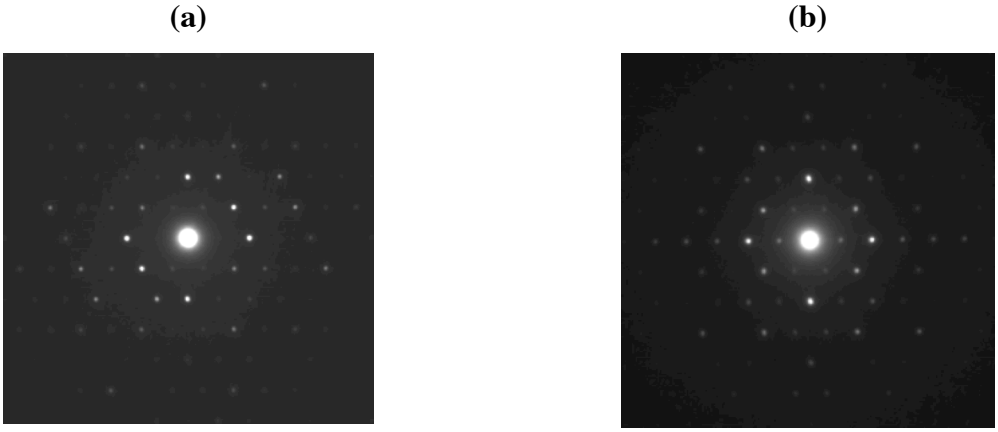


*Fig 2.4 : Clichés en précession (3°) obtenus en axe de zone $[\bar{1}10]$ (a) et $[\bar{1}0\bar{1}]$ (b) mis en parallèle sur les deux variants de la macle. La position des taches est la même, mais leurs intensités varient fortement.*

Notons ici que, même avec des clichés obtenus en aire sélectionnée sur une zone étendue de l'échantillon, la ressemblance entre les clichés expérimentaux et les clichés simulés dans l'approximation cinématique est forte, les effets dynamiques n'influant que légèrement l'allure globale des clichés. L'analyse est donc robuste et simple en comparaison de la

méthode LACBED. En effet, pour cette dernière, la comparaison des données expérimentales et simulées nécessite la prise en compte d'un grand nombre de clichés, ne différant les uns des autres que par de faibles variations des positions et intensités des lignes de Bragg. La comparaison est de plus affectée par les distorsions des lignes associées à la courbure de l'échantillon et à ses variations d'épaisseur sur la zone illuminée par le faisceau défocalisé.

1.2.3. Maclage par mérihédrie réticulaire : cas du quartz.

Dans le quartz, les macles formées lors de la transition de la phase haute température hexagonale vers la phase basse température trigonale ne perturbent pas le réseau cristallin: il s'agit d'une macle par mériédrie réticulaire (Frondel, 1945 ; Heaney and Veblen, 1991). Ce type de macle se produit dans les cristaux où le réseau est plus symétrique que le motif qui lui est associé. A haute température, la silice $SiO_2$ cristallise dans la phase β hexagonale du quartz, de groupe spatial $P6_222$ (droit) ou $P6_422$ (gauche). La structure se caractérise par une double spirale, autour de l'axe hélicoidal sénaire parallèle à [0001], de chaînes de tétraèdres de $SiO_4$ partageant leurs sommets (Fig 2.5). Les chaînes de chaque hélice sont reliées entre elles par un axe de rotation d'ordre 2 parallèle à l'axe hélicoïdal. Quand le quartz est refroidi en dessous de 573°C, les chaînes de tétraèdres se distordent (transformation displacive) et ne sont plus reliées entre elles par un axe d'ordre 2. Le quartz passe alors dans la structure trigonale α (axe de rotation d'ordre 3), de groupe spatial $P3_221$ (gauche) ou $P3_121$ (droit) respectivement (Fig. 2.5). Cet abaissement de symétrie produit des macles, dites du Dauphiné, qui séparent des variants $\alpha_1$ et $\alpha_2$ tournés l'un par rapport à l'autre de 180° autour de l'axe [0001] et qui reconstituent ainsi l'axe 2 perdu. Les plans diffractants de la structure hexagonale et des deux variants de la structure trigonale mis en relation de parallélisme par la macle ont des distances interréticulaires identiques, mais des intensités différentes. Sur des clichés de points acquis en aire sélectionnée conventionnelle le long d'une même direction dans les trois phases, ces différences d'intensité ne sont pas visibles, du fait des interactions dynamiques entre les faisceaux diffractés (Fig. 2.6). Ce n'est plus le cas en précession. Les clichés sont bien discernables et la caractérisation de la macle dans la phase α devient alors évidente à partir de projections stéréographiques conventionnelles.

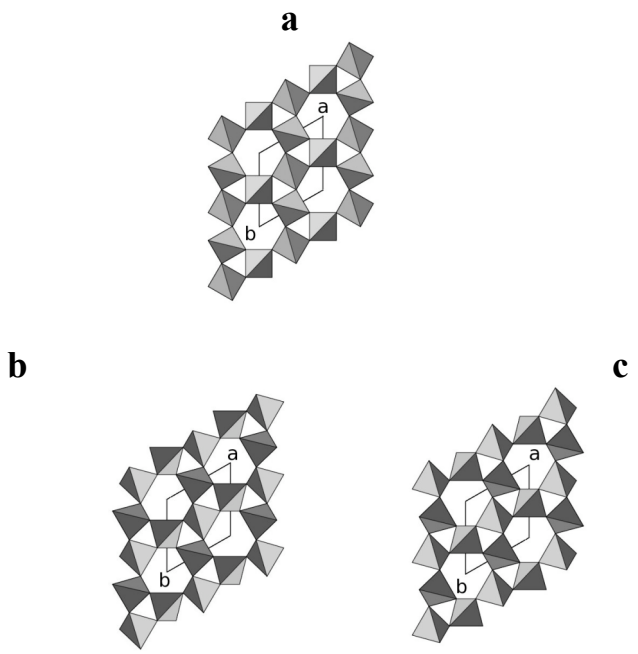


*Fig 2.5 : a) Quartz β haute température projeté suivant la direction c. b) et c) : Variants du quartz α basse température. Les deux variants sont reliés par une rotation de 180 °autour de l'axe c (d'après Heaney et al, 1991).*

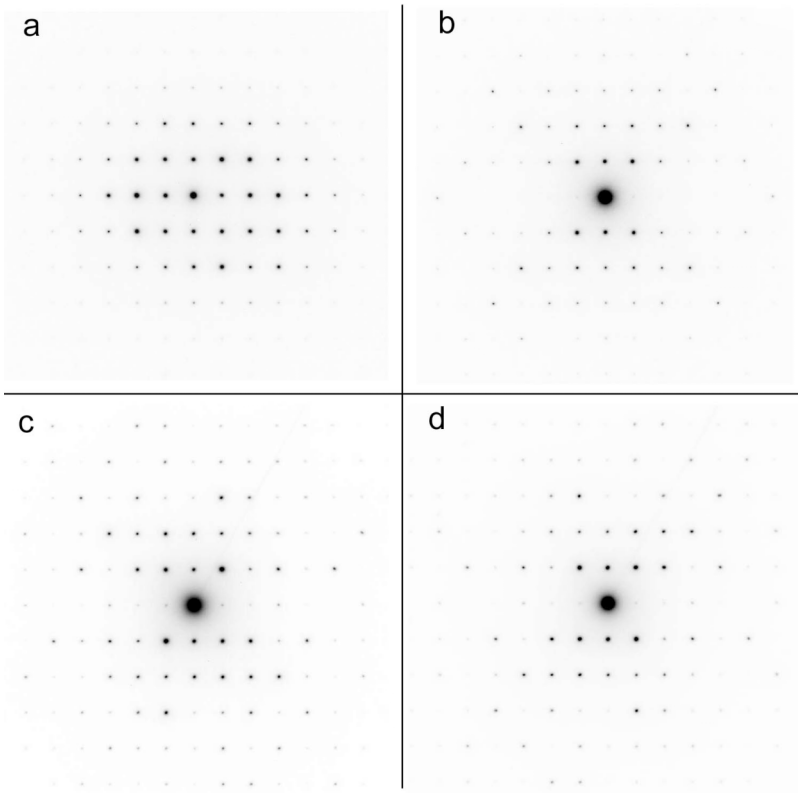


*Fig 2.6 : Diagrammes de diffraction en aire sélectionnée, axe de zone $< 11\bar{2}0 >$. a) sans précession ; b) avec précession, phase haute température β; c) et d) avec précession, phase basse température, variants $\alpha_1$ et $\alpha_2$ respectivement.*

Un autre aspect de l'étude concerne l'analyse de la symétrie des clichés de diffraction. Le quartz est un exemple intéressant car ce n'est ici qu'une légère distorsion du motif qui modifie la symétrie de la structure cristalline, sans modifier celle du réseau. Nous cherchons donc à savoir dans quelle mesure cet abaissement de symétrie se ressent sur les intensités relevées en précession sur des clichés en aire sélectionnée adaptés aux matériaux sensibles à l'irradiation. De façon générale, l'analyse des symétries doit se faire en faisceau convergent (CBED ou microdiffraction) pour révéler le groupe ponctuel, voire le groupe spatial, de la structure étudiée. On examine alors la « classe de diffraction » de l'axe de zone considéré (Buxton et al. 1976 ; Tanaka et al., 1983), en tenant compte des intensités et non pas seulement des positions des réflexions. Dans le cas du quartz, par exemple, la perte de l'axe 6 suivant l'axe c entre les structures β et α est bien visible sur les clichés obtenus en CBED (Fig. 2.7). Nous avons observé, et conforté par des simulations dynamiques, que sous certaines conditions d'épaisseur de l'échantillon, cet abaissement de symétrie était encore visible sur les clichés de points obtenus en précession (Fig. 2.8). On observe alors une symétrie plus haute que celle de la « classe de Laue » (projection centro-symmétrique du groupe ponctuel) (Morniroli et al., 2010), qui révélerait dans ce cas une symétrie d'ordre 6 et non 3 pour l'axe c de la phase α. Ceci peut être particulièrement utile pour la détermination des groupes spatiaux dans le cas des échantillons sensibles à l'irradiation électronique.

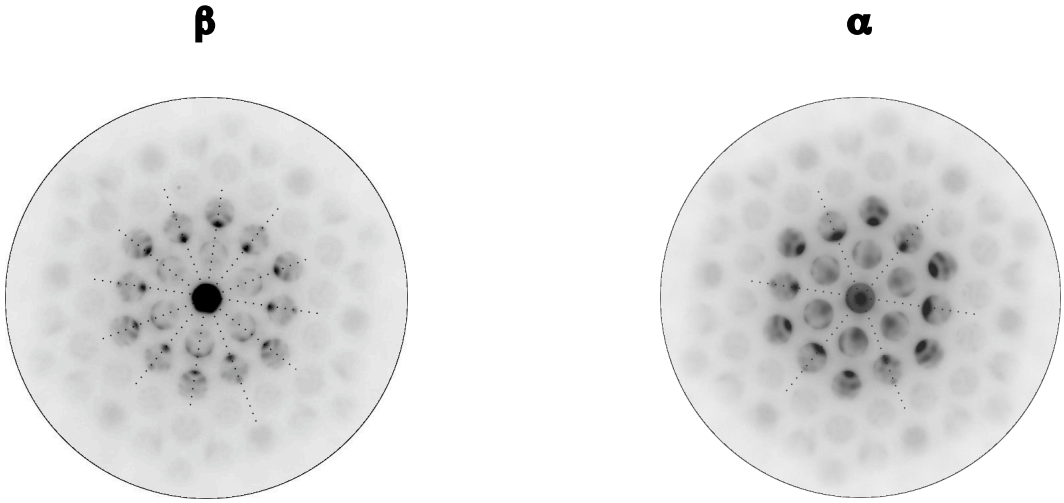


*Fig. 2.7 : Clichés CBED en axe de zone <0001> des phases β et α du quartz. La symétrie est d'ordre 6 dans β et d'ordre 3 α (Jacob and Cordier, 2010).*

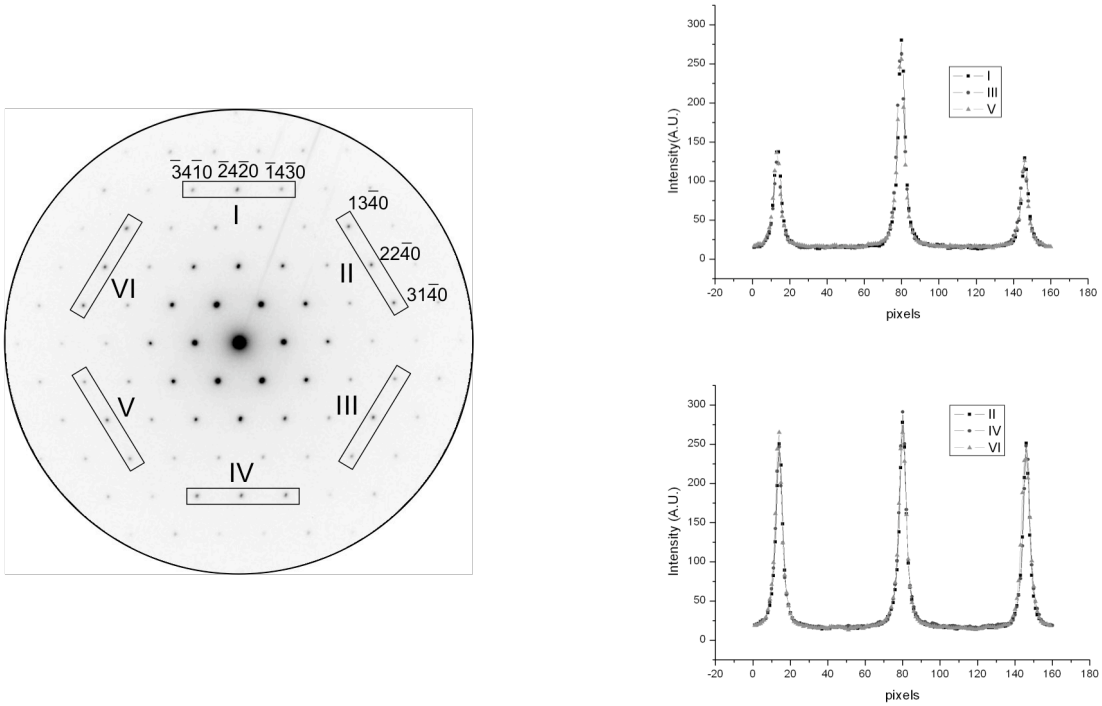


*Fig. 2.8 : Cliché en précesion (3°) le long de l'axe de zone <0001> de la phase α du quartz et intensité des réflexions repérées sur le cliché . La symétrie d'ordre 3 est visible sur les intensités. (Jacob and Cordier, 2010).*

**Publications concernées par ces études** (les travaux précédés d'un astérisque sont reproduits à la fin de ce mémoire) :

1. *Jacob, D., Cordier, P., Morniroli, J.P., and Schertl, H.-P. (2008) Large-angle convergent-beam electron diffraction (LACBED) characterization of (021) twinning in natural coesite. Eur. J. Mineral., 20(1), 119-124.
2. *Jacob, D., Cordier, P., Morniroli, J.P., and Schertl, H.P. (2009) Application of precession electron diffraction to the characterization of (021) twinning in pseudo-hexagonal coesite. American Mineralogist 94(5-6), 684-692.
3. Ji, G., Morniroli, J.P., Auchterlonie, G.J., Drennan, J., and Jacob, D. (2009) An efficient approach to characterize pseudo-merohedral twins by precession electron diffraction: Application to the LaGaO3 perovskite. Ultramicroscopy, 109(10), 1282-1294.
4. *Jacob, D. and Cordier P. (2010) A precession electron diffraction study of α, β phases and Dauphiné twin in quartz. Ultramicroscopy, accepted manuscript.

# Chapitre III: Microstructures des échantillons cométaires de la mission Stardust.

*Collaborateurs* : P. Cordier (UMET), H. Leroux (UMET), M. Roskosz (UMET), J. Stodolna (Thèse, UMET).

En janvier 2006, la sonde de la mission américaine Stardust ramène sur Terre des poussières récoltées dans la coma de la comète 81P/Wild 2 (Brownlee et al. 2006, Zolensky et al. 2006). C'est le deuxième retour d'échantillons extra-terrestres d'origine connue après les missions lunaires Apollo. Grâce à Hugues Leroux, responsable de la thématique « Astrominéralogie » de l'équipe, nous avons eu la chance de faire partie des équipes impliquées dans les observations préliminaires des échantillons. La MET, qui, par les dimensions des échantillons observables, arrive généralement en fin de chaîne de caractérisation, est ici l'outil de choix pour les analyses microstructurales de ces poussières micrométriques. Les techniques utilisées sont la microanalyse X pour réaliser des cartographies de composition, l'imagerie conventionnelle et haute résolution pour l'analyse des défauts et la diffraction en aire sélectionnée pour les études structurales. Notons que l'utilisation en « routine » de la précession électronique, donnant des clichés de diffraction en axe de zone symétriques et équilibrés en intensité même si l'échantillon n'est pas parfaitement orienté, est ici d'un intérêt indéniable. Elle facilite en effet grandement la détermination des phases dans ces échantillons constitués de petits cristallites imbriqués et laissant peu de marge de manœuvre pour la recherche des orientations caractéristiques.

Il s'agit donc, à partir de l'observation des microstructures, de renseigner sur les chemins thermiques ayant pu être subis par les particules et ayant abouti à leur formation. Notre contribution a essentiellement porté sur les particules « terminales », retrouvées à l'extrémité des traces de décélération (« tracks ») laissées dans l'aérogel utilisé pour récolter les poussières (Fig. 3.1). Ces particules sont constituées d'assemblages de grains cristallins de quelques centaines de nanomètres. Les phases majoritaires sont des silicates, pyroxènes ($(Mg,Fe,Ca)_2Si_2O_6$) et olivine ($(Fe,Mg)SiO_4$), s'étalant sur un large domaine de compositions. Les pyroxènes, dont la microstructure est un bon indicateur des événements thermiques et mécaniques expérimentés par le cristal, ont particulièrement retenu notre attention (Leroux et

al. 2008a ; Jacob et al., 2009). Les microstructures sont variables d'une particule à l'autre en fonction des compositions majoritaires et des assemblages.

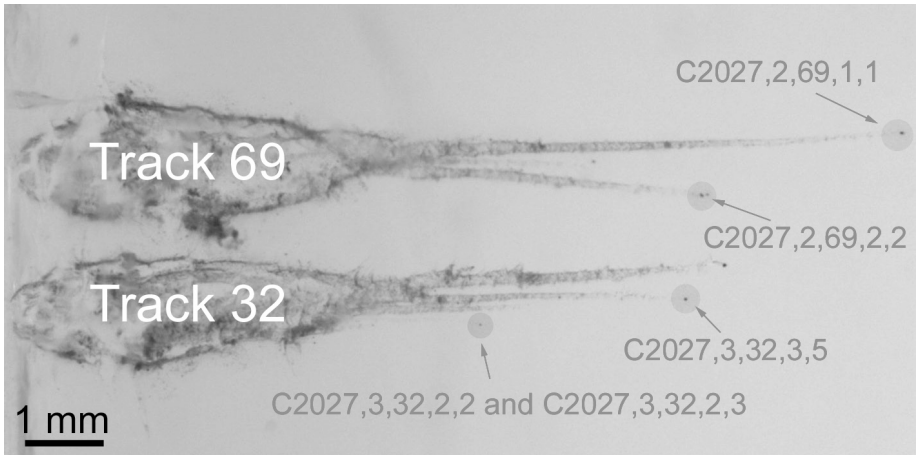


*Fig. 3.1 : Micrographie optique des tracks 32 et 69. Les particules terminales étudiées sont encerclées. Crédits Nasa J.S.C.*

Dans une des particules étudiées, un grain riche en Ca (diopside) présentant une exsolution lamellaire de phase pauvre en Ca (pigeonite), révèle une origine ignée (Fig. 3.2), c'est-à-dire par refroidissement depuis un liquide à haute température. La vitesse de refroidissement peut être estimée à partir de la largeur des lamelles exsolvées. Elle est cohérente avec celles des « chondres » retrouvés dans les météorites chondritiques, témoins de processus de fusion et refroidissement rapides des poussières silicatées dans le nuage proto-stellaire. Dans une autre des particules, on observe majoritairement des pyroxènes riches en Fe (pigeonite, de structure monoclinique), présentant de nombreuses macles polysynthétiques (Fig 3.3). Toutefois, dans la majorité des échantillons, les pyroxènes sont riches en Mg (enstatite), et présentent alors des alternances de domaines monocliniques (clino-enstatite) et orthorhombiques (ortho-enstatite) le long des plans (100) communs aux deux structures (Fig. 3.4).

Pour la particule riche en pigeonite, une formation par refroidissement depuis une phase solide haute température (protopyroxène, ortho-rhombique) est probable, tandis que pour les particules riches en enstatite, la microstructure peut être obtenue par refroidissement depuis une phase haute température ou par déformation d'une phase mère ortho-enstatite. Quoi qu'il en soit, la diversité des compositions et des microstructures observées indique des origines variées pour les divers grains formant les poussières récoltées. Ces résultats corroborent la théorie d'un mélange radial, grand brassage au sein du disque proto-planétaire de particules

formées à des distances plus ou moins proches du soleil, avant l'accrétion dans les astéroïdes et les planètes formant aujourd'hui le système solaire.

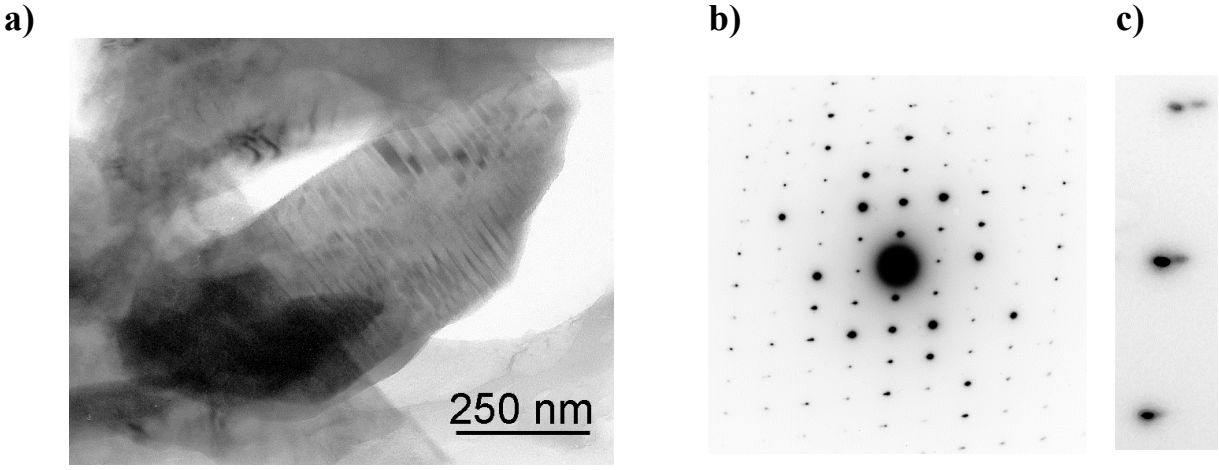


*Fig. 3.2 : a) Image en fond clair d'un grain de pyroxène riche en Ca présentant des lamelles d'exsolution (échantillon C2027,2,69,2,2). b) Diagramme de diffraction correspondant, axe de zone [1$\bar{1}$0]. Les taches de diffraction le long de la direction [110]* sont dédoublées, ainsi que le montre clairement l'agrandissement reproduit en c). (Leroux et al., 2008a)*

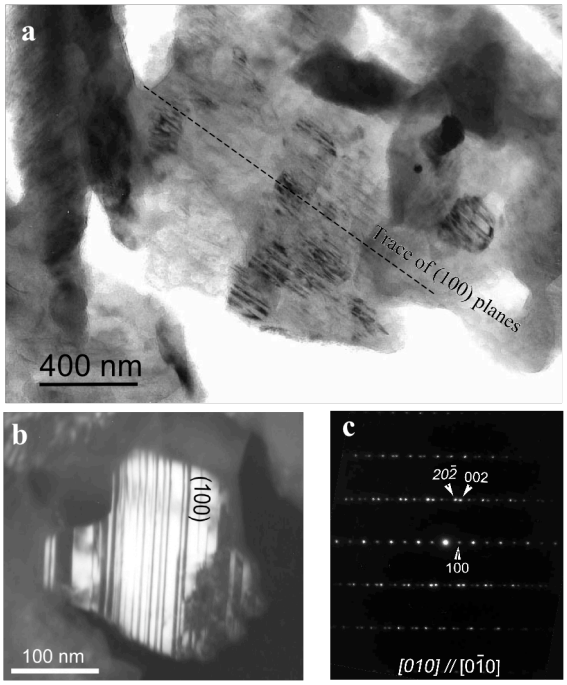


*Fig 3.3 : Echantillon C2027,2,69,1,1. a) Vue générale. Les grains de pyroxènes montrent une structure striée associée à du maclage suivant les plans (100). b) Image en champ sombre d'un grain orienté avec les plans (100) debout révélant le contraste associé aux domaines maclés. c) Diagramme de diffraction associé à b), correspondant à la superposition des axes de zone [010] et [0$\bar{1}$0] mis en parallèle par le maclage. (Jacob et al. 2009)*

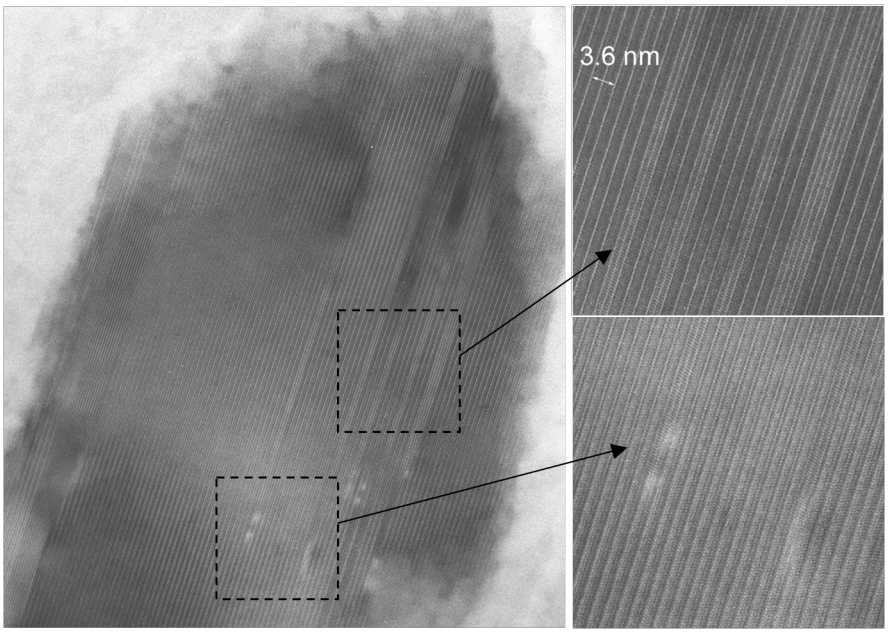


*Fig 3.4 : Echantillon C2027,2,69,2,2. Image haute résolution d'un grain d'enstatite. Les franges à 1,8 nm correspondent à l'ortho-pyroxène, celles à 0,9 nm au clino-pyroxène. Un contraste de déformation résiduel associé aux dislocations partielles est observé à la fin des domaines de clino-enstatite. (Jacob et al. 2009).*

Un autre enjeu dans l'analyse des échantillons consiste à reconnaître dans les microstructures observées, ce qui a été préservé dans son état original, de ce qui a été affecté par la récolte, cette dernière ayant consisté en une décélération quasi-instantanée dans un aerogel de très faible densité depuis une vitesse relative de 6,1 $kms^{-1}$. Au cours du choc, les particules, constituées d'agrégats faiblement cohésifs, se sont dispersées le long des traces de décélération. Les plus petits grains ou les plus fragiles ont fondu sous l'effet de la brusque élévation de température associée à la décélération et se sont mélangés à l'aérogel pour donner un verre de composition mixte. L'analyse des profils de composition dans ces parties vitreuses permet de remonter à la température atteinte pendant le choc et à la vitesse de refroidissement (Roskosz et al., 2008). La modification de la chimie et de l'état redox des grains thermiquement affectés par la récolte a également été mise en évidence (Leroux et al., 2008b ; Leroux et al., 2009, Stodolna et al., 2009). Concernant les particules terminales, nous avons observé des dislocations en configuration de glissement dans l'ensemble des échantillons analysés (Fig. 3.5). Alors que des études théoriques suggèrent que l'intensité moyenne du choc associé à la capture était insuffisante pour déformer plastiquement les grains récoltés (Trigo-Rodriguez et al., 2008), les observations réalisées sur des échantillons provenant de tirs expérimentaux (Stodolna et al., 2010 ) montrent au contraire qu'un tel choc peut produire le déplacement des dislocations. Dans ces conditions, il est difficile de conclure sur l'origine des dislocations dans les échantillons Stardust.

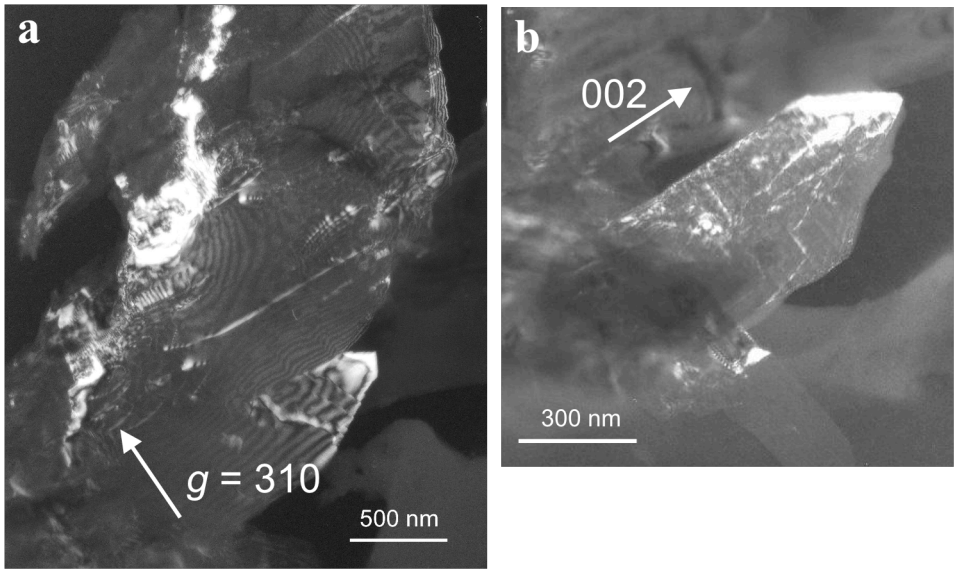


*Fig 3.5 : Echantillon C2027,2,69,2,2. Images en champ faible des dislocations présentes dans un grain d'orthoenstatite (a) et dans le grain exsolvé (b). (Jacob et al. 2009).*

**Publications concernées par ces études** (les travaux précédés d'un astérisque sont reproduits à la fin de ce mémoire) :


1. Brownle D. et al. (2006) Comet 81P/Wild 2 Under a Microscope. Science, 314(5806), 1711-1716.
2. *Jacob, D., Stodolna, J., Leroux, H., Langenhorst, F., and Houdellier, F. (2009) Pyroxenes microstructure in comet 81P/Wild 2 terminal Stardust particles. Meteoritics & Planetary Science, 44(10), 1475-1488.
3. *Leroux, H., Jacob, D., Stodolna, J., Nakamura-Messenger, K., and Zolensky, M. (2008a) Igneous Ca-rich pyroxene in comet 81P/Wild 2. American Mineralogist, 93, 1933-1936.
4. Leroux, H., and Rietmeijer, F.J.M.M.A.V., A. J. Brearley, D. Jacob, F. Langenhorst, J. C. Bridges, T. J. Zega, R. M. Stroud, P. Cordier, R. P. Harvey, M. Lee, M. Gounelle, M. E Zolensky. (2008) TEM study of thermally modified Wild 2 dust particles by interactions with the aerogel matrix during the Stardust capture process. Meteoritics & Planetary Science, 43(1/2), 97–120.
5. *Leroux, H., Roskosz, M., and Jacob, D. (2009) Oxidation state of iron and extensive redistribution of sulfur in thermally modified Stardust particles. Geochimica et Cosmochimica Acta, 73(3), 767-777.
6. Stodolna, J., Jacob, D., and Leroux, H. (2009) A TEM study of four particles extracted from the Stardust track 80. Meteoritics & Planetary Science, 44(10), 1511-1518.
7. *Zolensky, M.E. et al. (2006) Mineralogy and Petrology of Comet 81P/Wild 2 Nucleus Samples. Science, 314(5806), 1735-1739.

# Perspectives en cristallographie électronique.

## Introduction

L'évolution actuelle de la microscopie électronique est orientée vers le développement d'approches de plus en plus quantitatives. Le microscope devient un véritable instrument de métrologie, permettant des mesures à une échelle subnanométrique, et n'est plus uniquement un outil de description qualitative des microstructures. Ceci concerne par exemple :

- les propriétés physiques (électriques, magnétiques) mesurées en holographie,
- les propriétés mécaniques (champs de déformation) mesurées en HREM ou Dark-field holography,
- les propriétés optiques mesurées en perte d'énergie des électrons (EELS),
- les cartographies chimiques réalisées en STEM-HAADF (High-Angular Dark Field) ou en EELS.

Cette évolution est en grande partie liée aux progrès récents dans le domaine de l'optique électronique, avec la mise au point de correcteurs d'aberrations (lentille objectif, sonde), de monochromateurs, de filtres en énergie (dans la colonne ou post-colonne) et de détecteurs (cameras CCD), qui équipent aujourd'hui les microscopes modernes. Ces progrès permettent de travailler avec des résolutions spatiales et spectrales ultimes tout en augmentant considérablement le rapport signal sur bruit des grandeurs analysées et rendent ainsi possible la quantification de données jusqu'alors noyées dans le bruit de fond.

La diffraction électronique n'est pas en marge de cette évolution. La technique du faisceau convergent, dont les premières applications ont concerné l'examen qualitatif des symétries et la détermination des groupes ponctuels (Buxton et al, 1976 ; Tanaka et al. 1983), a été très tôt

utilisée pour les mesures quantitatives, avec les travaux pionniers de Spence et Zuo (Spence et Zuo, 1992). Dans ses applications les plus poussées, elle permet de mesurer les facteurs de structure des réflexions, les densités de charge dans les liaisons et les coefficients de Debye-Waller relatifs à l'agitation thermique. Outre les progrès récents associés à la précession électronique que je décrirai par la suite, les évolutions actuelles sont liées à l'utilisation de sondes nanométriques, cohérentes et parallèles, permettant de reconstruire par inversion de Fourier l'image d'un objet diffractant de dimension nanométrique avec une résolution atomique (Zuo et al, Science 2003).

Ma pratique de la microscopie a toujours été tournée vers ses aspects quantitatifs. Pendant ma thèse, il s'agissait de mesurer des champs de déformation en mode imagerie à deux ondes pour caractériser des phénomènes de relaxation de surface dans des hétérostructures contraintes. Ensuite, ces mesures de champs de déformation ont été réalisées en faisceau convergent (LACBED, CBED). Enfin, c'est l'analyse quantitative des intensités recueillies en précession qui est utilisée actuellement pour les analyses microstructurales. Le laboratoire est depuis longtemps impliqué dans les études microstructurales en diffraction, avec l'influence majeure des travaux de Jean-Paul Morniroli. En phase avec l'évolution générale de la microscopie, il me semble aujourd'hui pertinent de poursuivre dans la voie du développement de méthodes d'analyses quantitatives en diffraction électronique. La précession offre dans ce cadre des perspectives très intéressantes concernant les déterminations structurales que je veux développer ici.

**Résolutions structurales : apport de la précession électronique**

La détermination de la structure cristallographique des cristaux est un enjeu fondamental en physico-chimie du solide et en sciences des matériaux pour la compréhension des propriétés physiques et fonctionnelles des matériaux et de l'interaction avec leur environnement. La diffraction des rayons X est une technique bien établie et largement utilisée pour réaliser cette détermination *ab inito* sur des monocristaux. Elle est cependant limitée par sa résolution spatiale. C'est sur la diffraction des électrons qu'il faut compter aujourd'hui pour aborder les analyses structurales à l'échelle sub-micrométrique.

Concernant les rayons X, le problème majeur de la « perte de phase » des facteurs de structure lors de l'enregistrement des intensités des faisceaux diffractés ($I_{exp}$ proportionnelle à $|F_{hkl}|^2$) a été résolu via l'utilisation des « méthodes directes ». Ces méthodes font usage *a priori*

d'informations très générales (atomicité, densité de charge dans la maille élémentaire, positivité de la densité de charge du cristal) pour contraindre les valeurs des phases des réflexions mesurées et les relations entre elles. A partir de valeurs arbitraires imposées aux phases de quelques réflexions constituant une base, et en les répercutant sur l'ensemble des réflexions par des règles d'additivité et de cohérence issues des contraintes initiales, les codes des méthodes directes convergent rapidement vers un petit ensemble de solutions. Cet ensemble possibilités contient la solution correspondant au cristal analysé à condition que les intensités recueillies soient de qualité suffisante, c'est à dire que leurs valeurs ne soient pas trop éloignées du carré des facteurs de structure. Cette « approximation cinématique » est généralement réalisée avec les rayons X et les solutions possibles peuvent être alors affinées en comparant les intensités mesurées avec les intensités calculées sur ces modèles. Le modèle retenu est celui pour lequel le facteur de corrélation entre les intensités mesurées et calculées en faisant varier légèrement les positions atomiques est le plus faible.

L'application directe de ces méthodes à la diffraction des électrons se heurte à la nature même des interactions électrons-matière. Ces dernières sont fortes et les diffractions sont multiples, dynamiques, avec des échanges continus d'intensité entre les différents faisceaux diffractés et le faisceau transmis au cours de la traversée du cristal. De fait, les intensités recueillies ne reproduisent généralement pas le pouvoir de diffusion des réflexions relatif à leur facteur de structure. L'application des méthodes directes pour la résolution des structures à partir de données de diffraction électronique ne peut être menée avec succès que dans des cas particuliers concernant notamment des échantillons très minces (5-10 nm), ou quand la diffusion est dominée par un seul type d'atome (Marks and Sinkler, 2003).

Dans ce contexte, la précession électronique proposée en 1994 par Vincent and Midgley (Vincent and Midgley, 1994), offre de réelles possibilités d'évolution. Outre l'augmentation considérable du nombre de réflexions présentes sur un cliché obtenu en axe de zone, l'avantage principal de la méthode vient du fait que, les réflexions n'étant plus excitées en même temps mais de manière séquentielle au cours de la rotation du faisceau incident autour de l'axe de zone considéré, les interactions dynamiques sont très largement réduites. On retrouve alors un comportement quasi-cinématique qui rend *a priori* possible l'application des méthodes directes utilisées avec les rayons X, après avoir appliqué aux intensités mesurées des facteurs de correction géométrique issus des études sur la diffraction de poudre (Blackman, 1939). Les études ont été menées avec succès sur plusieurs structures (Boulahya et al, 2007 (oxydes); Dorset et al, 2007 ; Dorset, 2010 (zeolites); Gemmi et al, 2007 (minéraux) ; Kverneland et al. 2006 (alliages d'aluminium) ; Own et al, 2005 (oxydes

métalliques et minéraux) ; Weirich et al, 2006 (oxydes métalliques)). Son application routinière paraît cependant encore prématurée pour la détermination *ab initio* des structures, chaque étude faisant appel à des traitements particuliers des réflexions recueillies expérimentalement (facteurs de correction géométriques, prise en compte ou non des effets dynamiques en deux-ondes, suppression des réflexions trop dynamiques) en fonction du cristal analysé. Les structures les plus critiques sont celles présentant de grands paramètres de maille et celles dont le motif contient à la fois des éléments lourds et des éléments légers. Un bel exemple de résolution *ab initio* d'une telle structure ($Pb_{13}Mn_9O_{25}$) à partir de données de diffraction électronique en précession été publié très récemment dans Ultramicroscopy (Hadermann et al, 2010). Il semble cependant que pour une application systématique, les effets dynamiques doivent être globalement pris en compte (Sinkler and Marks, 2010).

**Perspectives**

Par rapport aux problèmes évoqués plus haut concernant la détermination *ab initio* des structures par diffraction électronique, une première approche pourrait, plutôt que d'essayer de s'affranchir des interactions dynamiques, tenter de les exploiter pour mesurer des paramètres structuraux dans le cas de structures connues, tout en bénéficiant de l'apport de la précession. Cette approche est dans la continuité des études concernant les structures présentant des abaissements de symétrie (coesite, quartz) décrites précédemment. Je pense ici plus particulièrement aux phénomènes de mise en ordre. Dans les cas des structures simples, comme les alliages intermétalliques ($Fe_xAl_{1-x}$, par exemple), le passage de la phase désordonnée (cubique centrée) à la phase ordonnée (cubique simple) se manifeste par l'apparition de réflexions dites de surstructure dont l'intensité, dans l'approximation cinématique, est proportionnelle au carré du taux de mise en ordre des éléments sur les sites spécifiques. En diffraction des rayons X, la mesure du rapport des intensités de ces réflexions avec celles des réflexions fondamentales permet une mesure directe du taux de mise en ordre. Réaliser ces mesures en diffraction des électrons pour étudier des grains de dimension submicrométrique est empêché par les effets dynamiques, qui se manifestent notamment par une grande sensibilité des intensités à l'épaisseur des échantillons (oscillations) et à leur orientation exacte. Avec la précession, ces intensités, si elles restent dynamiques dans le sens où elles sont sensibles à celle des réflexions avoisinantes, ne montrent plus les oscillations typiques des effets dynamiques. Les rapports des intensités présentent alors des évolutions simples en fonction de l'épaisseur. Ils peuvent être comparés avec une bonne précision à ceux

issus de simulations dynamiques pour en déduire le taux de mise en ordre, connaissant l'épaisseur de l'échantillon mesurée en CBED. Les premières études réalisées avec Gang Ji (UMET, équipe métallurgie physique et génie des matériaux) sur des alliages $Fe_xAl_{1-x}$ sont prometteuses et révèlent dans le cas d'un alliage totalement ordonné la possibilité de comparer les mesures expérimentales des rapports d'intensités avec des valeurs calculées par simulations dynamique (JEMS, P. Stadelmann, 2004). Ce type d'approche devrait pouvoir s'appliquer dans des cas plus complexes concernant la mise en ordre des cations $Fe^{2+}$ et $Mg^{2+}$ dans les silicates (pyroxènes et olivines). Un exemple concerne les pyroxènes d'origine ignée présents dans les météorites. Il s'agirait alors de déterminer à terme des paramètres importants concernant la formation de ces pyroxènes tels les vitesses de refroidissement et les températures de fermeture des processus de diffusion, qui renseigneront de façon déterminante sur le passé thermique des échantillons analysés (Zema et al, 1997). Cette problématique s'étend en fait à un large champ, concernant l'étude des météorites aussi bien que des échantillons terrestres.

A plus long terme, je souhaite m'engager dans la résolution des structures à l'échelle submicrométrique. L'intérêt de disposer d'une méthode de résolution à cette échelle, inaccessible en rayon X, est évident dans de nombreux domaines des sciences des matériaux, tournés vers la synthèse de nanocristaux et la compréhension de leurs propriétés physico-chimiques. En minéralogie, l'étude récente des échantillons cométaires de la mission Stardust, constitués de grains de dimensions (sub)micrométriques de composition et structure variées, révèle l'apport majeur des analyses structurales en MET pour la compréhension des conditions de formation de ces grains.

Pour l'implantation des méthodes de résolution structurale au laboratoire, des collaborations sont envisagées avec des spécialistes de diffraction des rayons X (P. Roussel, UCCS, UMR CNRS 8181). Nous recevrons en 2011 L. Palatinus (Institute of Physics, Prague), spécialiste mondialement reconnu dans le domaine du développement des méthodes directes pour la détermination des structures (Palatinus and Chapuis, 2007). Il se consacre actuellement à l'application de ces méthodes aux données de diffraction électronique en précession. Il s'agira à terme d'être capable de prendre totalement en compte les interactions dynamiques pour la comparaison des intensités expérimentales et simulées.

# Bibliographie

Brownlee, D., Tsou, P., Aleon, J., Alexander, C.M.O.D., Araki, T., Bajt, S., Baratta, G.A., Bastien, R., Bland, P., Bleuet, P., Borg, J., Bradley, J.P., Brearley, A., Brenker, F., Brennan, S., Bridges, J.C., Browning, N.D., Brucato, J.R., Bullock, E., Burchell, M.J., Busemann, H., Butterworth, A., Chaussidon, M., Cheuvront, A., Chi, M., Cintala, M.J., Clark, B.C., Clemett, S.J., Cody, G., Colangeli, L., Cooper, G., Cordier, P., Daghlian, C., Dai, Z., D'Hendecourt, L., Djouadi, Z., Dominguez, G., Duxbury, T., Dworkin, J.P., Ebel, D.S., Economou, T.E., Fakra, S., Fairey, S.A.J., Fallon, S., Ferrini, G., Ferroir, T., Fleckenstein, H., Floss, C., Flynn, G., Franchi, I.A., Fries, M., Gainsforth, Z., Gallien, J.P., Genge, M., Gilles, M.K., Gillet, P., Gilmour, J., Glavin, D.P., Gounelle, M., Grady, M.M., Graham, G.A., Grant, P.G., Green, S.F., Grossemy, F., Grossman, L., Grossman, J.N., Guan, Y., Hagiya, K., Harvey, R., Heck, P., Herzog, G.F., Hoppe, P., Horz, F., Huth, J., Hutcheon, I.D., Ignatyev, K., Ishii, H., Ito, M., Jacob, D., Jacobsen, C., Jacobsen, S., Jones, S., Joswiak, D., Jurewicz, A., Kearsley, A.T., Keller, L.P., Khodja, H., Kilcoyne, A.L.D., Kissel, J., Krot, A., Langenhorst, F., Lanzirotti, A., Le, L., Leshin, L.A., Leitner, J., Lemelle, L., Leroux, H., Liu, M.-C., Luening, K., Lyon, I., et al. (2006) Comet 81P/Wild 2 Under a Microscope. Science, 314(5806), 1711-1716.

Blackman, M. (1939) On the intensities of electron diffraction rings. Proc. Roy. Soc., 173, 68-82.

Boulahya, K., Ruiz-Gonz·lez, L., Parras, M., Gonz·lez-Calbet, J.M., Nickolsky, M.S., and Nicolopoulos, S. (2007) Ab initio determination of heavy oxide perovskite related structures from precession electron diffraction data. Ultramicroscopy, 107(6-7), 445-452.

Buxton, B.F., Eades, J.A., Steeds, J.W., and Rackham, G.M. (1976) Symmetry of electron-difraction zone axis patterns. Philosophical Transactions of the Royal Society of London Series a-Mathematical Physical and Engineering Sciences, 281(1301), 171-&.

Cherns, D., and Preston, A.R. (1986) Convergent-beam diffraction of crystal defects. Proceedings Eleventh International Congress on Electron Microscopy, 1, p. 721, Kyoto.

Clement, L., Pantel, R., Kwakman, L.F.T., and Rouviere, J.L. (2004) Strain measurements by convergent-beam electron diffraction: The importance of stress relaxation in lamella preparations. Applied Physics Letters, 85(4), 651-653.

Cordier, P., Morniroli, J.P., and Cherns, D. (1995) Characterization of crystal defects in quartz by large-angle convergent-beam electron diffraction. Philos. Mag., 72(5), 1421-1430.

Dai, Z.R., and Bradley, J.P. (2001) Iron-nickel sulfides in anhydrous interplanetary dust particles. Geochimica et Cosmochimica Acta, 65(20), 3601-3612.

Dorset, D.L., Gilmore, C.J., Jorda, J.L., and Nicolopoulos, S. (2007) Direct electron crystallographic determination of zeolite zonal structures. Ultramicroscopy, 107(6-7), 462-473.

Dorset, D.L. (2010) Direct methods and refinement in electron and X-ray crystallography - diketopiperazine revisited. Zeitschrift Fur Kristallographie, 225(2-3), 86-93.

Eggeman, A.S., White, T.A., and Midgley, P.A. Is precession electron diffraction kinematical? Part II: A practical method to determine the optimum precession angle. Ultramicroscopy, In Press, Corrected Proof.

Frondel, C. (1945) Secondary Dauphiné twinning in quartz. American Mineralogist, 30(5-6), 447-460.

Gemmi, M., and Nicolopoulos, S. (2007) Structure solution with three-dimensional sets of precessed electron diffraction intensities. Ultramicroscopy, 107(6-7), 483-494.

Hadermann, J., Abakumov, A.M., Tsirlin, A.A., Filonenko, V.P., Gonnissen, J., Tan, H., Verbeeck, J., Gemmi, M., Antipov, E.V., and Rosner, H. (2010) Direct space structure solution from precession electron diffraction data: Resolving heavy and light scatterers in Pb13Mn9O25. Ultramicroscopy, In Press, Corrected Proof.

Heaney, P.J., and Veblen, D.R. (1991) Observations of the alpha-beta-phase transition in quartz - A review of imaging and diffraction studies and some new results. American Mineralogist, 76(5-6), 1018-1032.

Houdellier, F., Roucau, C., Clément, L., Rouvière, J.L., and Casanove, M.J. (2006) Quantitative analysis of HOLZ line splitting in CBED patterns of epitaxially strained layers. Ultramicroscopy, 106(10), 951-959.

Hovespian, A., Cherns, D., and Jaeger, W. (1999) Analysis of ultrathin Ge layers in Si by large angle convergent beam electron diffraction. Philosophical Magazine a-Physics of Condensed Matter Structure Defects and Mechanical Properties, 79(6), 1395-1410.

Houdellier, F., Jacob, D., Casanove, M.J., and Roucau, C. (2008) Effect of sample bending on diffracted intensities observed in CBED patterns of plan view strained samples. Ultramicroscopy, 108(4), 295-301.

Hÿtch, M.J., Snoeck, E., and Kilaas, R. (1998) Quantitative measurement of displacement and strain fields from HREM micrographs. Ultramicroscopy, 74(3), 131-146.

Hÿtch, M., Houdellier, F., Hue, F., and Snoeck, E. (2008) Nanoscale holographic interferometry for strain measurements in electronic devices. Nature, 453(7198), 1086-1089.

Jacob, D., Androussi, Y., and Lefebvre, A. (2001) LACBED measurement of the chemical composition of a thin InxGa1-xAs layer buried in a GaAs matrix. Ultramicroscopy, 89(4), 299-303.

Jacob, D., and Lefebvre, A. (2003) Interpretation of unexpected rocking curve asymmetry in LACBED patterns of semiconductors. Ultramicroscopy, 96(1), 1-9.

Jacob, D., Lefebvre, A., Chauveau, J.M., Trampert, A., and Tournié, E. (2003) LACBED analysis of the chemical composition of compound semiconductor strained layers. In I. Publishing, Ed. XIIIth International Conference on Microscopy of Semiconducting Materials, 180, p. 221-224. Cullis, Cambridge, U.K.

Jacob, D., Zuo, J.M., Lefebvre, A., and Cordier, Y. (2008a) Composition analysis of semiconductor quantum wells by energy filtered convergent-beam electron diffraction. Ultramicroscopy, 108(4), 358-366.

Jacob, D., Cordier, P., Morniroli, J.P., and Schertl, H.-P. (2008b) Large-angle convergent-beam electron diffraction (LACBED) characterization of (021) twinning in natural coesite. Eur. J. Mineral., 20(1), 119-124.

Jacob, D., Cordier, P., Morniroli, J.P., and Schertl, H.P. (2009) Application of precession electron diffraction to the characterization of (021) twinning in pseudo-hexagonal coesite. American Mineralogist 94(5-6), 684-692.

Jacob, D., Stodolna, J., Leroux, H., Langenhorst, F., and Houdellier, F. (2009) Pyroxenes microstructure in comet 81P/Wild 2 terminal Stardust particles. Meteoritics & Planetary Science, 44(10), 1475-1488.

Jacob, D. and Cordier P. (2010) A precession electron diffraction study of α, β phases and Dauphiné twin in quartz. Ultramicroscopy, accepted manuscript.

Ji, G., Morniroli, J.P., Auchterlonie, G.J., Drennan, J., and Jacob, D. (2009) An efficient approach to characterize pseudo-merohedral twins by precession electron diffraction: Application to the LaGaO3 perovskite. Ultramicroscopy, 109(10), 1282-1294.

Kret, S., Delamarre, C., Laval, J.Y., and Dubon, A. (1998) Atomic-scale mapping of local lattice distortions in highly strained coherent islands of InxGa1-xAs/GaAs by high-resolution electron microscopy and image processing. Philosophical Magazine Letters, 77(5), 249-256.

Kverneland, A., Hansen, V., Vincent, R., Gjönnes, K., and Gjönnes, J. (2006) Structure analysis of embedded nano-sized particles by precession electron diffraction. [eta]'-precipitate in an Al-Zn-Mg alloy as example. Ultramicroscopy, 106(6), 492-502.

Leroux, H., Jacob, D., Stodolna, J., Nakamura-Messenger, K., and Zolensky, M. (2008a) Igneous Ca-rich pyroxene in comet 81P/Wild 2. American Mineralogist, 93, 1933-1936.

Leroux, H., and Rietmeijer, F.J.M.M.A.V., A. J. Brearley, D. Jacob, F. Langenhorst, J. C. Bridges, T. J. Zega, R. M. Stroud, P. Cordier, R. P. Harvey, M. Lee, M. Gounelle, M. E Zolensky. (2008b) TEM study of thermally modified Wild 2 dust particles by interactions

with the aerogel matrix during the Stardust capture process. Meteoritics & Planetary Science, 43(1/2), 97–120.

Leroux, H., Roskosz, M., and Jacob, D. (2009) Oxidation state of iron and extensive redistribution of sulfur in thermally modified Stardust particles. Geochimica et Cosmochimica Acta, 73(3), 767-777.

Levien, L., and Prewitt, C.T. (1981) High-Pressure Crystal-Structure and Compressibility of Coesite. American Mineralogist, 66(3-4), 324-333.

Marks, L.D., and Sinkler, W. (2003) Sufficient conditions for direct methods with swift electrons. Microscopy and Microanalysis, 9(5), 399-410.

Morniroli, J.P., Albarede, P.H., and Jacob, D. (2005) TEM characterization of strained silicon. In E. Zschech, C. Whelan, and T. Mikolajick, Eds. Materials for Information Technology: Devices, Interconnects and Packaging, p. 99-108.

Morniroli, J.P., Auchterlonie G. J., Drennan J., Zou J. (2008) Contribution of electron precession to the study of perovskites displaying small symmetry departures from the ideal cubic $ABO_3$ perovskite: applications to the $LaGaO_3$ and LSGM perovskites. Journal of Microscopy, 232(1), 7-26.

Morniroli, J.-P., Stadelmann, P., Ji, G., and Nicolopoulos, S. (2010) The symmetry of precession electron diffraction patterns. Journal of Microscopy, 237(3), 511-515.

Own, C.S. (2005) System design and verification of the precesssion electron diffraction technique, Ph. D. Thesis, Northwestern University.

Own, C.S., Marks, L.D., and Sinkler, W. (2006) Precession electron diffraction 1: multislice simulation. Acta Crystallographica Section A, 62(6), 434-443.

Palatinus L., Chapuis G. (2007): SUPERFLIP - a computer program for the solution of crystal structures by charge flipping in arbitrary dimensions. J. Appl. Cryst., 40, 786-790

Roskosz, M., Leroux, H., and Watson, H.C. (2008) Thermal history, partial preservation and sampling bias recorded by Stardust cometary grains during their capture. Earth and Planetary Science Letters, 273(1-2), 195-202.

Sinkler, W., and Marks, L.D. (2010) Characteristics of precession electron diffraction intensities from dynamical simulations. Zeitschrift Fur Kristallographie, 225(2-3), 47-55.

Spence, J.C.H and Zuo, J. M. (1992) Electron microdiffraction. Plenum Press, New York.

Stadelmann, P., JEMS, Electron Microscopy Software, java version, CIME-EPFL, CH 1015 Lausanne, 2004.

Stodolna, J., Jacob, D., and Leroux, H. (2009) A TEM study of four particles extracted from the Stardust track 80. Meteoritics & Planetary Science, 44(10), 1511-1518.

Stodolna, J., Jacob, D., Burchell, M.J., and Leroux, H. (2010) Collect-induced Microstructure Modifications in Stardust Samples: Some Experimental Evidences. Lunar and Planetary Institute Science Conference Abstracts, 41, p. 1659.

Tanaka, M., Ueno, K., and Harada, Y. (1980) Large-angle convergent beam electron-diffraction. J. Electron Microsc., 29(3), 277-277.

Tanaka, M., Saito, R., and Sekii, H. (1983) Point-Group determination by convergent-beam electron diffraction. Acta Crystallographica Section A, 39(MAY), 357-368.

Treacy, M.M.J., Gibson, J.M., and Howie, A. (1985) On Elastic Relaxation and Long Wavelength Microstructures in Spinodally Decomposed Inxga1-Xasyp1-Y Epitaxial Layers. Philosophical Magazine a-Physics of Condensed Matter Structure Defects and Mechanical Properties, 51(3), 389-417.

Vincent, R., and Midgley, P.A. (1994) Double conical beam-rocking system for measurement of integrated electron diffraction intensities. Ultramicroscopy, 53(3), 271-282.

Vincent, R., Walsh, T.D., and Pozzi, M. (1999) Iterative phase retrieval from kinematic rocking curves in CBED patterns. Ultramicroscopy, 76(3), 125-137.

Weirich, T.E., Portillo, J., Cox, G., Hibst, H., and Nicolopoulos, S. (2006) Ab initio determination of the framework structure of the heavy-metal oxide CsxNb2.54W2.46O14 from 100†kV precession electron diffraction data. Ultramicroscopy, 106(3), 164-175.

White, T.A., Eggeman, A.S., and Midgley, P.A. Is precession electron diffraction kinematical? Part I:: "Phase-scrambling" multislice simulations. Ultramicroscopy, In Press, Corrected Proof.

Zema, M., Domeneghetti, M.C., Molin, G.M., and Tazzoli, V. (1997) Cooling rates of diogenites: A study of Fe2+-Mg ordering in orthopyroxene by single-crystal x-ray diffraction. Meteoritics & Planetary Science, 32(6), 855-862.

Zolensky, M.E., Zega, T.J., Yano, H., Wirick, S., Westphal, A.J., Weisberg, M.K., Weber, I., Warren, J.L., Velbel, M.A., Tsuchiyama, A., Tsou, P., Toppani, A., Tomioka, N., Tomeoka, K., Teslich, N., Taheri, M., Susini, J., Stroud, R., Stephan, T., Stadermann, F.J., Snead, C.J., Simon, S.B., Simionovici, A., See, T.H., Robert, F., Rietmeijer, F.J.M., Rao, W., Perronnet, M.C., Papanastassiou, D.A., Okudaira, K., Ohsumi, K., Ohnishi, I., Nakamura-Messenger, K., Nakamura, T., Mostefaoui, S., Mikouchi, T., Meibom, A., Matrajt, G., Marcus, M.A., Leroux, H., Lemelle, L., Le, L., Lanzirotti, A., Langenhorst, F., Krot, A.N., Keller, L.P., Kearsley, A.T., Joswiak, D., Jacob, D., Ishii, H., Harvey, R., Hagiya, K., Grossman, L., Grossman, J.N., Graham, G.A., Gounelle, M., Gillet, P., Genge, M.J., Flynn, G., Ferroir, T., Fallon, S., Ebel, D.S., Dai, Z.R., Cordier, P., Clark, B., Chi, M., Butterworth, A.L., Brownlee, D.E., Bridges, J.C., Brennan, S., Brearley, A., Bradley, J.P., Bleuet, P., Bland, P.A., and Bastien, R. (2006) Mineralogy and Petrology of Comet 81P/Wild 2 Nucleus Samples. Science, 314(5806), 1735-1739.

Zuo, J.M., Vartanyants, I., Gao, M., Zhang, R., and Nagahara, L.A. (2003) Atomic Resolution Imaging of a Carbon Nanotube from Diffraction Intensities. Science, 300(5624), 1419-1421.

# Deuxième partie : informations personnelles

# 2.1 Curriculum Vitae

**Jacob Damien**

Né le 17 juillet 1971 à Lille,

Marié, deux enfants.

**Situation actuelle**

Maître de Conférences, classe normale (5° échelon), 28° section du CNU, depuis le 1er novembre 1999.

UMET – UMR CNRS 8207

Université de Lille I,

59 655 Villeneuve d'Ascq Cedex

**Parcours professionnel**

1999 -

Maître de Conférences, Université de Lille 1.

1998 - 1999

Contrat Post-doctoral, Laboratoire EME, Université de Barcelone.

Financement : réseau européen TMR « UV-coatings ».

1995 – 1998

Thèse de doctorat en sciences des Matériaux. Laboratoire Structure et Propriétés de l'Etat Solide, UMR CNRS 8008, Université de Lille 1

Directeur de thèse : A. Lefebvre

1994 – 1995

Scientifique du contingent, ONERA Châtillon

Responsable : M. Naka

**Parcours académique**

1995-1998 :

Thèse de doctorat en sciences des Matériaux. Laboratoire Structure et Propriétés de l'Etat Solide, UMR CNRS 8008, Université de Lille 1

Directeur de thèse : A. Lefebvre

Mention très honorable avec les félicitations du jury.

1993-1994 :

DEA en Sciences des Matériaux, Université de Lille I.

Mention bien. Major de promotion.

1991-1993 :

Licence et Maîtrise de Physique, Université de Lille I.

Mention bien.

**Encadrement doctoral**

- Master M2-Recherche Sciences des Matériaux :

  B. Kedjar en 2003/2004 (50%),

  A. Adjarzadeh Oskouei en 2005/2006 (100 %)

  J. Stodolna en 2006/2007 (50 %)

- Doctorat en Science des matériaux :

  J. Stodolna depuis septembre 2007 à 50 %. Soutenance prévue : sept. 2010

  Sujet : Etude par MET des échantillons cométaires de la mission *Stardust*.

  J. Stodolna est auteur d'un article et co-auteur de deux articles dans des revues de rang A.

- Examinateur du travail de thèse de F. Houdellier. « Contribution au développement du CBED et de l'holographie HREM pour l'analyse des déformations de couches épitaxiées », septembre 2006.

**Enseignement et diffusion des connaissances**

- Enseignements dispensés à l'université: service complet (192 HTD)

  - Physique générale en licence de physique L1, L2 et L3 (cours, TDs et TPs) : Mécanique du point, mécanique des fluides, physique pour les sciences de la Terre, informatique et calcul formel, thermodynamique.

- Intervenant "Physique Itinérante" dans les lycées et collèges.

- Chargé de cours dans plusieurs écoles thématiques portant sur la microscopie électronique en transmission et ses applications (niveau doctoral et post doctoral)

**Organisation d'écoles et congrès**

- Membre du comité d'organisation et chargé de cours pour les écoles suivantes :

  - Ecole Européenne du CNRS/SFmu (Soc. Française des Microscopies) « School on Electron Precession » en juillet 2009, Bouvines, France. http://umet.univ-lille1.fr/Animation/precession2009.php

  - Ecole Européenne du CNRS « Quantitative Electron Microscopy » en 2005 et en 2009, Saint-Aygulf, France. http://www.qem2009.org/

  - Ecole CNRS-Formation « Diffraction électronique appliquée à la caractérisation microstructurale des matériaux » dirigée par J. P. Morniroli, de 2003 à 2008.

  - Ecole Européenne CNRS/ SFmu « School on LACBED» en juin 2002, dirigée par J. P. Morniroli, Bouvines, France.

- Membre du comité d'organisation des congrès et journées scientifiques suivants:

  - Journée Thématique « Microscopie Electronique en Transmission » de la Société Française de Minéralogie et Cristallographie (SFMC), 15 janvier 2009, Univ. Lille 1.

  - Journée du Plateau Technique Microscopie de la Fédération Chevreul « Microscopies Electroniques », 17 janvier 2008, Univ. Lille 1.

  - 36$^{\text{èmes}}$ Journées du GUMP (Groupement des Utilisateurs de Microscopes Philips), 2005, Lille.

  - Congrès de la Soc. Française des Microscopies (SFmu), JMM 2002, Lille, Juin 2002.

**Fonctions d'intérêt collectif**

- Membre du comité de programme du réseau CNRS de microscopie électronique METSA. http://www.metsa.cnrs.fr/

- Reviewer pour les revues Ultramicroscopy (Elsevier), Micron (Elsevier) et Philosophical Magazine (Francis and Taylor).

- Membre élu du conseil de laboratoire (2002-2010), du conseil d'administration de l'UFR de physique (depuis 2003) et de la commission de spécialistes 28 - 30 - 37èmes sections (2004 à 2008).

# 2.2 Production scientifique

**Publications internationales de rang A non liées à la thèse : 18, dont 8 en 1er auteur**

1. D. Jacob and P. Cordier. A precession electron diffraction study of α, β phases and Dauphiné twin in quartz. In press, Ultramicroscopy (2010).
2. D. Jacob, P. Cordier, J. P. Morniroli and H. P. Schertl. Application of precession electron diffraction to the characterization of (021) twinning in the pseudo-hexagonal coesite. American Mineralogist 94, 684–692 (2009).
3. G. Ji, J.P. Morniroli, G.J. Auchterlonie, J. Drennan, D. Jacob. An efficient approach to characterize pseudo-merohedral twins by precession electron diffraction : Application to the $LaGaO_3$ perovskite. Ultramicroscopy 109, 1282-1294 (2009).
4. D. Jacob, J. Stodolna, H. Leroux, F. Langenhorst and F. Houdellier. Pyroxenes microstructure in comet 81P/wild2 terminal Stardust particles. Meteoritics & Planetary Science, 44(10), 1475-1488 (2009).
5. J. Stodolna, D. Jacob, and H. Leroux. A TEM study of four particles extracted from the Stardust track 80. Meteoritics & Planetary Science, 44(10), 1511-1518 (2009)
6. H. Leroux, M. Roskosz, D. Jacob. Oxidation state of iron and extensive redistribution of sulfur in thermally modified Stardust particles. Geochimica et Cosmochimica Acta 73, 767–777 (2009).
7. H. Leroux, D. Jacob, J. Stodolna, K. Nakamura-Messenger and M. E. Zolensky. Igneous Ca-rich pyroxene in comet 81P/Wild 2. American Mineralogist 93, 1933–1936 (2008).
8. H. Leroux, F. J.M. Rietmeijer, M. A. Velbel, A. J. Brearley, D. Jacob, F. Langenhorst, J. C. Bridges, T. J. Zega, R. M. Stroud, P. Cordier, R. P. Harvey, M. Lee, M. Gounelle, M. E Zolensky. TEM study of thermally modified Wild 2 dust particles by

interactions with the aerogel matrix during the Stardust capture process. Meteoritics & Planetary Science 43(1/2), 97–120 (2008).

9. D. Jacob, P. Cordier, J. P. Morniroli, H. P. Schertl. Large-angle convergent-beam electron diffraction (LACBED) characterization of (021) twinning in natural coesite. European Journal of Mineralogy 20 (1), 119-124 (2008).
10. H. Idrissi, P. Cordier, D. Jacob and N. Walte. Dislocations and plasticity of experimentally deformed coesite. European Journal of Mineralogy 20, 665-671 (2008).
11. D. Jacob, J. M. Zuo, A. Lefebvre, Y. Cordier. Composition analysis of semiconductor quantum wells by energy filtered convergent beam electron diffraction. Ultramicroscopy 108, 358 (2008).
12. F. Houdellier, D. Jacob, M. J. Casanove, C. Roucau. Effect of sample bending on diffracted intensities observed in CBED patterns of plan view samples. Ultramicroscopy 108, 295 (2008).
13. D. Brownlee, et al. Comet 81P/Wild 2 Under a Microscope. Science 314, 1711-1716 (2006).
14. M. E. Zolensky, et al. Mineralogy and Petrology of Comet 81P/Wild 2 Nucleus Samples. Science 314, 1735-1739 (2006).
15. A. Lefebvre, D. Jacob and Y. Androussi. Periodic antiphase boundary spinel-based structures in aluminates, gallates, aluminium oxynitrides and transition aluminas. Philosophical Magazine 85 (20), 2211-2225 (2005).
16. Jacob, D. and Lefebvre, A. Interpretation of unexpected rocking curve asymmetry in LACBED patterns of semiconductors. Ultramicroscopy 96, 1-9 (2003).
17. Jacob, D. and Lefebvre, A. Characterisation of implanted surface layers in ion-thinned semiconductors by Transmission Electron Microscopy. Material Science and Engineering B 101, 133-136 (2003).
18. Jacob, D., Androussi, Y. and Lefebvre, A. LACBED measurement of the chemical composition of a thin $In_xGa_{1-x}As$ layer buried in a GaAs matrix. Ultramicroscopy 89, 299-303 (2001).

**Publications internationales de rang A liées à la thèse : 2 en 1er auteur**

1. Jacob, D., Androussi, Y., Benabbas, T., Francois, P., Ferre, D., Lefebvre, A., Gendry, M., and Robach, Y. Elastic misfit stress relaxation in $In_{0.25}Ga_{0.75}As$ layers grown under tension on InP (001). Journal of Crystal Growth, 179(3-4), 331-338 (1997).

2. Jacob, D., Androussi, Y., Benabbas, T., Francois, P., and Lefebvre, A. Surface relaxation of strained semiconductor heterostructures revealed by finite-element calculations and transmission electron microscopy. Phil. Mag., 78(4), 879-891 (1998).

**Publications internationale de rang A liées au séjour post-doctoral : 2 dont 1 en 1er auteur**

1. Jacob, D., Peiro, F., Quesnel, E. & Ristau, D. Microstructure and composition of $MgF_2$ optical coatings grown on Si substrate by PVD and IBS processes. Thin Solid Films 360, 133-138 (2000).
2. Quesnel, E., Dumas, L., Jacob, D. & Peiro, F. Optical and microstructural properties of $MgF_2$ UV coatings grown by ion beam sputtering process. J. of Vac. Sc. & Tech. A -Vacuum Surfaces and Films 18, 2869-2876 (2000).

**Chapitres de livre : 1**

1. TEM Characterization of Strained Silicon. J.P. Morniroli, P.H. Albarède, D. Jacob. Materials for Information Technology, Devices, Interconnects and Packaging. Series: Engineering Materials and Processes.
   Zschech, Ehrenfried; Whelan, Caroline; Mikolajick, Thomas (Eds.). Springer, 2005.

**Proceedings à comité de lecture : 3 dont 1 en premier auteur**

1. Androussi, Y., Benabbas, T., Jacob, D. & Lefebvre, A. A TEM study of compositionnal inhomgeneity in semiconductor quantum dots, in Microscopy of Semiconducting Materials 2003 95-98 (2003).
2. Jacob, D., Lefebvre, A., Chauveau, J. M., Trampert, A. & Tournié, E. LACBED analysis of the chemical composition of compound semiconductor strained layers, in Microscopy of Semiconducting Materials 2003 221-224 (2003).
3. D. Ristau, W. A., S. Bosch, A. Duparré, E. Massetti, D. Jacob, G. Kiriakidis, F. Peiro, E. Quesnel and A. Tikhonravov. UV-Optical and Microstructural Properties of MgF2-Coatings Deposited by IBS and PVD Processes. International Symposium on Optical Systems Design and Production, Berlin, 26-29 May 1999. Proc. SPIE Vol.3738, 436-445 (1999).

**Communications invitées: 7**

1. D. Jacob, Strain measurements by CBED, International Workshop on « Current Topics in TEM: Plasmonics and Strain Mapping ». Ringberg Castle, Tegernsee Lake, Germany. July 22-25, 2009.
2. D. Jacob, J.P. Morniroli, Les alignements en diffraction électronique, 43èmes journées du GUMP, 8-10 avril 2009, Eindhoven, Netherlands.
3. D. Jacob, Quantitative electron diffraction applied to strain measurements and defect characterization, Workshop on Electron Diffraction, Trondheim, Norway, May 29-30, 2008.
4. D. Jacob, Diffraction Electronique en Faisceau Convergent Quantitative, 36èmes journées du GUMP (Groupement des Utilisateurs de Microscopes Philips), Lille, 16-17 novembre 2005.
5. D. Jacob, Y. Androussi, T. Benabbas, A. Lefebvre, Détermination par MET des champs de déformation et des compositions chimiques dans les nanostructures d'alliages de semiconducteurs III-V. MIMEA, VIIIème Colloque de la Société Française des Microscopies (SF$\mu$). Toulon (France), 23-26 juin 2003.
6. D. Jacob, A. Lefebvre, J. M. Chauveau, A. Trampert, E. Tournié. Analyse par LACBED de la composition chimique de couches minces dans les composés semi-conducteurs. Réunion du GdR "Relax". Poitiers (France), février 2003.
7. D. Jacob, J. P. Morniroli. Technique LACBED (Large Angle Convergent Beam Electron Diffraction), 26èmes journées du GUMP (Groupement des Utilisateurs de Microscopes Philips), Metz, 9-10 novembre 2000.

**Communications orales non invitées: 8 dont 5 en orateur**

1. Stodolna J., Jacob D. and Leroux H. Mineralogy of Stardust Track 80 : Evidences for Aqueous Alteration and Igneous Process, Lunar and Planetary Institute Science, Houston, Texas, USA, 2010.
2. Stodolna J., Jacob D. and Leroux H., Etude par MET Analytique d'échantillons cométaires de la mission Stardust, 11ème Colloque de la Société Française des Microscopies, Paris, 2009.
3. D. Jacob, Etude par diffraction électronique du maclage dans la coesite, Journée Thématique de la SFMC, 15 janvier 2009, Université de Lille 1.

4. D. Jacob, J. Stodolna and H. Leroux, Pyroxene microstructure in Stardust terminal particles, Timber Cove II, Stardust Science 2, Timber Cove Inn, California, October 26-29, 2008.
5. H. Leroux, F. J. M. Rietmeijer, D. Jacob and M. Roskosz, Evidence for hot chemistry under reduced conditions in the thermally modified stardust samples. 39th Lunar and Planetary Science Conference, March 10-14 2008, Houston, Texas,USA.
6. D. Jacob and A. Lefebvre, Electron diffraction studies of strain fields in semiconductors epilayers, XII International Conference on Electron Microscopy of Solids, Kazimierz Dolny, 05-09 June 2005, Poland
7. D. Jacob, Y. Androussi, T. Benabbas, A. Lefebvre, Etude par Microscopie Electronique en Transmission de la relaxation élastique des contraintes dans les nanostructures de semiconducteurs épitaxiés. Réunion du GDR "relax". Paris, mars 2002.
8. D. Jacob, Y. Androussi, A. Lefebvre et J.P. Morniroli, Mesures de composition chimique dans les nanostructures semiconductrices : étude par microscopie électronique en transmission, IVème Colloque de la Société Française des Microscopies (SFμ). Toulouse, 6-8 septembre 2000.

**Communications par affiche : 30 dont 14 en premier auteur**

1. Stodolna J., Jacob D., Burchell M. J. and Leroux H., Collect-induced Microstructure Modifications in Stardust Samples : Some Experimental Evidences, Lunar and Planetary Institute Science 41th, Houston, Texas, USA, 2010.
2. J. Stodolna, D. Jacob, H. Leroux, Mineralogy and Petrology of Stardust particles encased in the aerogel of track 80, METSOC Nancy, 2009.
3. D. Jacob, P. Cordier, J. P. Morniroli, Transition α/β et macle du Dauphiné dans le quartz : une étude par diffraction électronique en précession, 11ème Colloque de la Société Française des Microscopies. Paris, 22-26 juin 2009.
4. J. Stodolna, D. Jacob, H. Leroux, Mineralogy and Petrology of Stardust particles extracted from the walls of track 80, 40th Lunar and Planetary Science Conference, Houston, Texas, USA, 2009.
5. J. Stodolna, D. Jacob, H. Leroux, ATEM study of four thermally modified Stardust particles from track 80, 40th Lunar and Planetary Science Conference, Houston, Texas, USA, 2009.

6. H. Leroux, D. Jacob and P. Cordier, Fine-Grained Material trapped in stardust track walls. 40th Lunar and Planetary Science Conference, Houston, Texas, USA, 2009.
7. J.P. Morniroli, G. Ji, D. Jacob, G. Auchterlonie, Contribution of electron precession to the study of crystals displaying small symmetry departures. European Microscopy Congress, Aachen, Germany, 2008.
8. D. Jacob, J. Stodolna, H. Leroux, TEM study of Comet Wild 2 pyroxene particles collected during the stardust mission. European Microscopy Congress, Aachen, Germany, 2008.
9. D. Jacob, P. Cordier, J.P. Morniroli, H.P. Schertl, Precession Electron Diffraction for the characterization of twinning in pseudo-symmetrical crystals: case of coesite. European Microscopy Congress 2008, Aachen, Germany. September, 2008.
10. Stodolna J., Jacob D. and Leroux H, ATEM study of four thermally modifed Stardust particles from track 80, Timber Cove 2 Stardust Workshop, 2008.
11. D. Jacob, J. Stodolna, H. Leroux, TEM Investigation of Pyroxenes Microstructure in Comet 81P/Wild 2 Terminal Particles, 39th Lunar and Planetary Science Conference, Houston, Texas, USA, 2008.
12. D. Jacob , P. Cordier , J. P. Morniroli, H. P. Schertl, Apport de la diffraction électronique en précession pour la caractérisation microstructurale des défauts : cas du maclage dans la coesite, Xeme colloque de la société française des microscopies (SFμ), Grenoble, 2007.
13. D. Jacob, F. Houdellier, A. Lefebvre, CBED Measurement of Strain in Semiconductor Buried Layers Observed in Plan-View, 16th International Microscopy Congress, Sapporo JAPAN, 2006.
14. F. Houdellier, D. Jacob, M. J. Casanove, C. Roucau, A. Lefebvre, CBED Measurement of Strain in Semiconductor Epilayers as Observed in Plan-View: the Importance of Sample Preparation Techniques, 16th International Microscopy Congress, Sapporo JAPAN, 2006.
15. D. Jacob, B. Kedjar, A. Lefebvre and X. Wallart, TEM determination of the composition of strained epitaxial semiconductors surface layers using LACBED, XIIIth European Microscopy Congress, University of Antwerp, 2004.
16. Y. Androussi, D. Jacob, T. Benabbas, A. Lefebvre, V. Yam and D. Bouchier, A TEM study of the shape and chemical composition of SiGe/Si quantum dots, XIIIth European Microscopy Congress, University of Antwerp, 2004.

17. D. Jacob, A. Lefebvre, J. M. Chauveau, A. Trampert, E. Tournié, LACBED analysis of the chemical composition of compound semiconductor strained layers, XIII$^{th}$ International Conference on Microscopy of Semiconducting Materials, Cambridge (U.K.), 31 March-3 April 2003.
18. Y. Androussi, T. Benabbas, D. Jacob and A. Lefebvre, A TEM study of compositional inhomogeneity in semiconductor quantum dots, XIII$^{th}$ International Conference on Microscopy of Semiconducting Materials, Cambridge (U.K.), 31 March-3 April 2003.
19. D. Jacob and A. Lefebvre, Interpretation of the asymmetry of the LACBED patterns obtained in semiconductor materials : the effect of ion-milling, Joint Microscopy Meeting 2002, Lille, 24-28 juin 2002.
20. Y. Androussi, T. Benabbas, D. Jacob, A. Lefebvre, Transmission electron microscopy analysis of the elastic strain relaxation in semiconductors epitaxial nanostructures, Joint Microscopy Meeting 2002, Lille, 24-28 juin 2002.
21. J. P. Morniroli, D. Jacob, C. Jäger, W. Jäger Polarity determination of III-V, AB semiconductors from kossel patterns, Joint Microscopy Meeting 2002, Lille, 24-28 juin 2002.
22. J. P. Morniroli, D. Jacob, C. Jäger, W. Jäger, CBED characterization of the polarity of III-V semiconductors, XX$^{th}$ European Crystallographic Meeting, ECM 20, Krakow, August 25-31 2001.
23. D. Jacob, Y. Androussi, A. Lefebvre and J. P. Morniroli, Determination of the composition of a semiconductor quantum well by LACBED, Electron Crystallography Euro-Summer school, Barcelona (Spain), July 23-27 2001.
24. D. Jacob, Y. Androussi, A. Lefebvre et J. P. Morniroli, Analyse par LACBED de la composition chimique d'un puits d'InxGa1-xAs enterré dans une matrice de GaAs, VII$^{èmes}$ Journées de la matière condensée. Poitiers, 29 août-1er septembre 2000.
25. J. P. Morniroli, B. Decamps, D. Jacob, Analyse par LACBED de bulles d'hélium dans des alliages Pd90Pt10 tritiés, IVème Colloque de la Société Française des Microscopies (SFμ). Toulouse, 6-8 septembre 2000.
26. D. Jacob, F. Peiro, S. Bosch and E. Quesnel, Composition and microstructure of $MgF_2$ optical coatings grown by Ion Beam Sputtering on Si (111) substrate. VI$^{ème}$ Réunion Nationale de Matériaux. San Sebastian (Espagne), 22-24 juin 1999.
27. Y. Androussi, D. Jacob, T. Benabbas, A. Lefebvre et M. Gendry, Détermination par microscopie électronique en transmission des hétérogénéités de contrainte associées

aux structures nanométriques épitaxiées: cas des semiconducteurs, Réunion du GDR "relax". Toulouse, mars 1998.

28. D. Jacob, Y. Androussi, T. Benabbas, P. François, A. Lefebvre et Y. Druelle, Relaxation en surface d'un puits contraint: caractérisation par Microscopie Electronique en Transmission et calculs par Eléments finis, II$^{ème}$ Colloque de la Société Française des Microscopies. Nancy, 30 juin-4 juillet 1997.
29. D. Jacob, Y. Androussi, T. Benabbas, P. François, D. Ferré, A. Lefebvre, M. Gendry, Y. Robach. Caractérisation par Microscopie à Effet Tunnel (STM), Microscopie à Force Atomique (AFM) et Microscopie Electronique à Transmission (MET) des morphologies de couches d'In0,25Ga0,75As contraintes en tension sur InP (001). VI$^{èmes}$ Journées Nationales de Microélectronique et Optoéléctronique III-V. Chantilly, janvier 1997.
30. Y. Androussi, D. Jacob, A. Lefebvre, C. Delamarre, L.P Wang, J.Y. Laval, A. Dubon. B. Courboules et J. Massie, Effet du mode de croissance (2D ou 3D) sur la relaxation des hétérostructures InxGa1-xAs / GaAs, Ecole thématique sur les effets des gradients de contrainte dans les semiconducteurs. PIRMAT, Marseille, septembre 1994.

**Séminaires de laboratoire : 5**

1. Mesure par diffraction électronique des champs de déformation dans les couches minces épitaxiées, Laboratoire de Métallurgie Physique, Poitiers, 11 janvier 2007.
2. La Diffraction Electronique en Faisceau Convergent et ses Applications, CIME, Ecole Polytechnique Fédérale de Lausanne, Suisse, 13 mars 2006.
3. Mesure des champs de déformation dans les nanostructures semiconductrices : Apport de la diffraction électronique quantitative, CNRS-CRHEA, Valbonne, Septembre 2005.
4. Déformation et interdiffusion dans les nanostructures semiconductrices : Apport de la Microscopie Electronique en Transmission, Séminaire « Microscopie Electronique en Transmission » de l'ESPCI, Paris, 31 mars 2004.
5. Measurement of the composition of III-V ternary semiconductor alloy nanostructures as studied by transmission electron microscopy. GFE , RWTH, Aachen, Germany. Septembre 2001.

# Troisième partie : articles

# Analyse des déformations par faisceau convergent

Available online at www.sciencedirect.com
ScienceDirect
Ultramicroscopy 108 (2008) 358–366
ultramicroscopy
www.elsevier.com/locate/ultramic

# Composition analysis of semiconductor quantum wells by energy filtered convergent-beam electron diffraction

D. Jacob[a,*], J.M. Zuo[b], A. Lefebvre[a], Y. Cordier[c,1]

[a]Laboratoire de Structure et Propriétés de l'Etat Solide (UMR CNRS 8008), Université des Sciences et Technologies de Lille, Bâtiment C6, 59655 Villeneuve d'Ascq cedex, France
[b]Department of Materials Science and Engineering, F. Seitz Materials Research Laboratory, University of Illinois at Urbana-Champaign, IL 61801, USA
[c]IEMN–CNRS, UMR 8520, Avenue Poincaré, P.O. Box 69, 60069 Villeneuve d'Ascq, France

Received 17 November 2006; received in revised form 28 May 2007; accepted 5 June 2007

**Abstract**

We show how energy-filtered convergent-beam electron diffraction (EFCBED) patterns can be used to determine the chemical composition of buried semiconductor strained quantum wells. Our method is based on a quantitative analysis of the intensities of high-order Bragg lines in the transmitted disc of EFCBED patterns taken from plan-view samples. This analysis makes it possible to determine the displacement vector **R** introduced between the top and bottom parts of the matrix by the deformation of the quantum well and consequently to determine its composition. This is illustrated in the case of an $In_xGa_{1-x}As$ quantum well buried in a GaAs matrix. A detailed analysis of the effect of experimental parameters on Bragg lines intensity is performed. In particular, the importance of the choice of the diffraction vector is pointed out. The relative uncertainty on the measurement of the indium content $x$ is found to be lower than 5% and a possible occurrence of slight compositional fluctuations in the (0 0 1) growth plane is pointed out.
© 2007 Elsevier B.V. All rights reserved.

*PACS:* 68.55.Nq; 6114.Lj; 61.82.Fk; 68.55.−a

*Keywords:* Transmission electron microscopy; Convergent-beam electron diffraction; Semiconductor quantum wells; Composition analysis

## 1. Introduction

Progress in semiconductor nanostructures for device applications requires chemical composition analysis at nanometre or subnanometre (atomic) scale. The high spatial resolution of transmission electron microscopy (TEM) is particularly suited to such investigations. Analytical TEM techniques for composition analysis include energy dispersive spectroscopy (EDS) and electron energy loss spectroscopy (EELS) (see for instance Ref. [1]). High-resolution TEM methods are based on strain analysis [2–4] or on the chemical sensitivity of the 0 0 2 reflections used for fringe imaging in the case of the sphalerite structure of III–V semiconductors [5]. Dark field 0 0 2 imaging has also been used in conventional mode [5–7]. In this case, much effort has been devoted to the careful study of the various parameters influencing the 0 0 2 intensity since the pioneer work of Bithell and Stobbs [8], especially the effects of charge redistribution in crystals, strain and static atomic displacements [9–11]. All these methods are based on the observation of cross-sectional samples and possible thin foil stress relaxation effects have to be taken into account. This drawback can be avoided with plan-view samples in the case of thin strained quantum wells (QWs) and the analysis of large-angle convergent-beam electron diffraction (LACBED) patterns makes it possible to accurately determine the QW composition [12,13]. The present work is aimed at showing that diffraction analysis can be further improved using curve fitting and energy-filtered

*Corresponding author. Tel.: +33 3 20 43 65 94; fax: +33 3 20 43 65 91.
*E-mail address:* damien.jacob@univ-lille1.fr (D. Jacob).
[1]Present address: CRHEA–CNRS, rue B. Gregory, Parc de Sophia Antipolis, 06560 Valbonne, France.

0304-3991/$ - see front matter © 2007 Elsevier B.V. All rights reserved.
doi:10.1016/j.ultramic.2007.06.001

convergent-beam electron diffraction (EFCBED) patterns. $In_xGa_{1-x}As$ QW buried in a GaAs matrix is used as an example. Two types of calculations are performed to match experimental intensities with computed ones. The first type uses the two-beam approximation and solves the Howie–Whelan dynamical equations. The second one uses the scattering matrix calculated using the Bloch wave approach and includes multi-beam effects. A special program has been developed to apply this formalism to an imperfect strained crystal.

## 2. Experiment

The specimens were grown by conventional solid source molecular beam epitaxy on a (0 0 1) semi-insulating GaAs substrate. A nominally 10-nm-thick $In_{0.12}Ga_{0.88}As$ single QW was grown, sandwiched between a 500-nm-thick GaAs buffer layer and a 100-nm-thick GaAs cap layer. The GaAs and $In_{0.12}Ga_{0.88}As$ layers were grown at the substrate temperature of 510 °C. The QW thickness is too small to carry out precise indium content measurements using X-ray diffraction. A GaAs/$In_{0.12}Ga_{0.88}As$/GaAs superlattice was then grown, as a calibration sample, in the same conditions as the single QW. Double X-ray diffraction experiments performed on this sample gave $x = 0.120 \pm 0.005$. This value was then used as the nominal indium content of the single QW.

Specimens for TEM observations were mechanically thinned to transparency from the buffer side using a South Bay Technology tripod polisher. EFCBED patterns were acquired with a 10–20 nm probe size on a FEI Tecnai 20-G2 microscope with the $LaB_6$ filament operated at 200 kV, equipped with a Gatan Imaging Filter 2000 and a Gatan slow-scan CCD camera. The energy window used for the zero loss imaging was 10 eV. For quantitative intensity analysis, EFCBED patterns have been deconvoluted using the Richardson–Lucy algorithm and the modulation transfer function of the CCD camera obtained by the noise method [14]. Deconvolution was found to have a small effect on the absolute intensity values of EFCBED patterns.

## 3. Composition analysis of quantum wells

### 3.1. Principle of the method

The tetragonal strain of a thin $In_xGa_{1-x}As$ QW sandwiched between the GaAs substrate and cap layer is shown in Fig. 1. The corresponding displacement vector **R** between the upper GaAs cap layer (taken as a reference) and the lower GaAs buffer layer is $\mathbf{R} = [0, 0, -R_z]$ with

$$R_z = \varepsilon_0 t_q \frac{1+\nu}{1-\nu}, \quad (1)$$

where $\varepsilon_0$ is the lattice mismatch: $\varepsilon_0 = (a_{In_xGa_{1-x}As} - a_{GaAs})/a_{GaAs} = 0.07166x$ ($a_{In_xGa_{1-x}As}$ is calculated using the Vegard's law with $a_{GaAs} = 0.56532$ nm and $a_{InAs} =$ 0.60583 nm), $\nu$ is the Poisson coefficient of the QW (also calculated with the Vegard's law using $\nu_{GaAs} = 0.31$ and $\nu_{InAs} = 0.35$), and $t_q$ is the QW thickness (10 nm). Considering the small value of $t_q$ with respect to the total sample thickness, the strained layer is expected to act as a stacking fault, producing the well-known splitting of the kinematical Bragg lines [15]. The resulting doublets are due to the phase shift $\alpha = 2\pi\mathbf{g}\cdot\mathbf{R}$ of the electron waves from the two matrix parts (buffer and cap layers) of the GaAs crystal. This effect can be clearly seen for instance in the LACBED pattern taken from the plan-view QW sample around the $[0\,\bar{1}\,5]$ zone axis, inclined at 11° from [0 0 1] (Fig. 2). Doublets are observed for the Bragg lines for which $\mathbf{g}\cdot\mathbf{R} \neq 0$ (modulo 1). A few selected doublets are indicated with arrows in Fig. 2.

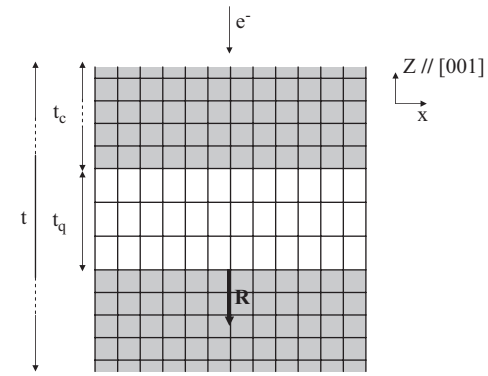


Fig. 1. Tetragonal deformation of a thin $In_xGa_{1-x}As$ layer buried in a GaAs matrix and the resulting displacement vector **R**. $t$, $t_q$ and $t_c$, respectively, are the thickness of the sample, of the strained layer and of the cap layer.

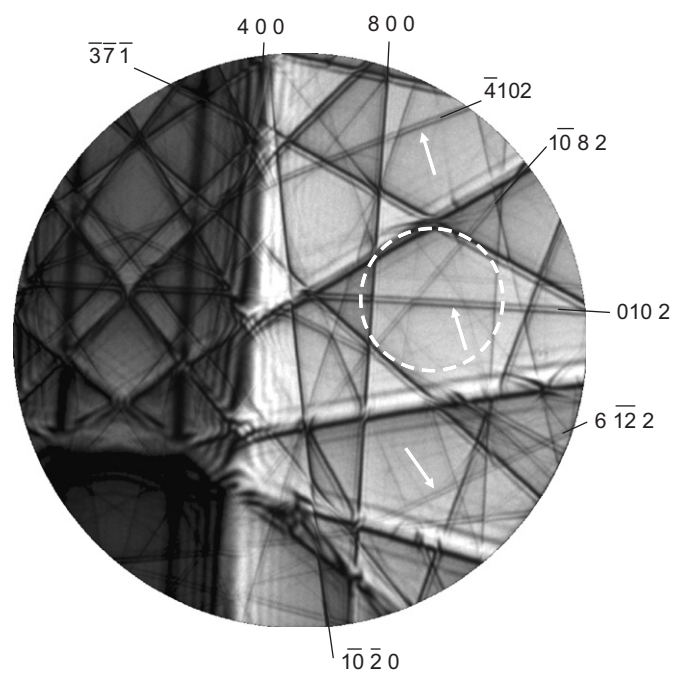


Fig. 2. $[0\,\bar{1}\,5]$ zone axis LACBED pattern taken on the plan-view sample schematized in Fig. 1. A few split Bragg lines are marked with arrows.

The composition determination is based on the measurement of $R_z$ by a quantitative comparison of the intensities of the experimental doublets with those of calculated ones for various value of $R_z$. The value of $R_z$ deduced from this comparison is then related to $\varepsilon_0$ using Eq. (1) and then to the composition $x$ of the QW.

Fig. 3a is an EFCBED pattern taken from the encircled area in Fig. 2. The intensity profile of the $\mathbf{g} = 0\,10\,2$ doublet shown in Fig. 3b is taken with increasing deviation parameter ($s$ values) along the arrow drawn in Fig. 3a. The experimental contrast ratio of the doublet can be quantified by $K = (I_m - I_0)/(I_M - I_0)$, where $I_m$ and $I_M$ are the intensities of the weak and strong lines and $I_0$ is the mean value of the background intensities as measured on both sides of the doublet for large $s$ values. $I_m$ and $I_M$ are measured by integrating the intensities of the corresponding lines with respect to $I_0$. It should be noted that secondary lines can also appear in the background. The adjustment of the experimental background with the calculated one will be discussed in Section 3.3.

### 3.2. Intensity calculations

In order to fully understand the effect of the various experimental parameters on the intensity of Bragg line doublets, we first perform a two-beam analysis of diffracted intensities. This analysis is made using simulations based on the integration of the Howie and Whelan equations in the column approximation [17] and performed on the QW model displayed in Fig. 1. The effects of multibeam diffraction are then considered for a further quantification of intensities.

#### 3.2.1. Two-beam calculations

Several parameters are involved in the calculation of the intensity profiles, namely the displacement vector $R_z$, the thickness of the QW ($t_q$), of the cap layer ($t_c$) and of the whole thin sample ($t$). In addition to these experimental parameters, the two-beam extinction distance $\xi_g$ and the anomalous absorption parameter $A_g$ ($A_g = \xi_g/\xi'_g$, where $\xi'_g$ is the absorption distance) must be calculated. We discuss hereafter the influence of these parameters on the intensity profile of Bragg lines.

The absorption parameter $A_g$ is not accurately known in the case of GaAs and $In_xGa_{1-x}As$. The commonly assumed value of 0.10 is used here because calculations made with $A_g = 0.05$ or 0.15 show no significant difference with those performed with $A_g = 0.10$.

The two-beam extinction distances $\xi_g$ for GaAs and $In_xGa_{1-x}As$ alloys can be calculated using atomic scattering factors with good accuracy for medium- and high-order reflections. Calculations show that intensity profiles are insensitive to the effect of the extinction distance of the $In_xGa_{1-x}As$ QW. This is due to the small QW thickness with respect to that of the whole sample. Calculations can then be performed with the same $\xi_g$ value for GaAs and $In_xGa_{1-x}As$.

Fig. 4 shows the intensity profiles calculated as a function of $\mathbf{g}\cdot\mathbf{R}$ in the case of a 10-nm-thick QW approximately located in the middle of the thin foil ($t_c = 100$ nm and $t = 200$ nm). The single deficient Bragg line observed in the rocking curve at $s = 0$ in the case $\mathbf{g}\cdot\mathbf{R} = 0$, splits into a doublet of lines as soon as $\mathbf{g}\cdot\mathbf{R}$ deviates from 0. The highest precision in the measurement of the contrast ratio $K$ is obtained when the intensities of both lines are strong—giving high $K$ values—and the diffraction vector $\mathbf{g}$ must then be chosen so that

$$\sim\tfrac{1}{3} \leqslant \mathbf{g}\cdot\mathbf{R} \leqslant \sim\tfrac{2}{3} \text{(modulo 1)}. \quad (2)$$

An optimal range of sample thicknesses can be chosen for the analysis. Experimental thicknesses higher than ~100 nm are generally selected in order to avoid thin foil artefacts, but choosing a too thick sample can lead to complex intensity profiles that cannot be readily analysed using the simple contrast ratio method proposed in Section 3.1. To illustrate this, Fig. 5 shows intensity profiles calculated as a function of $t/\xi_g$: the doublet

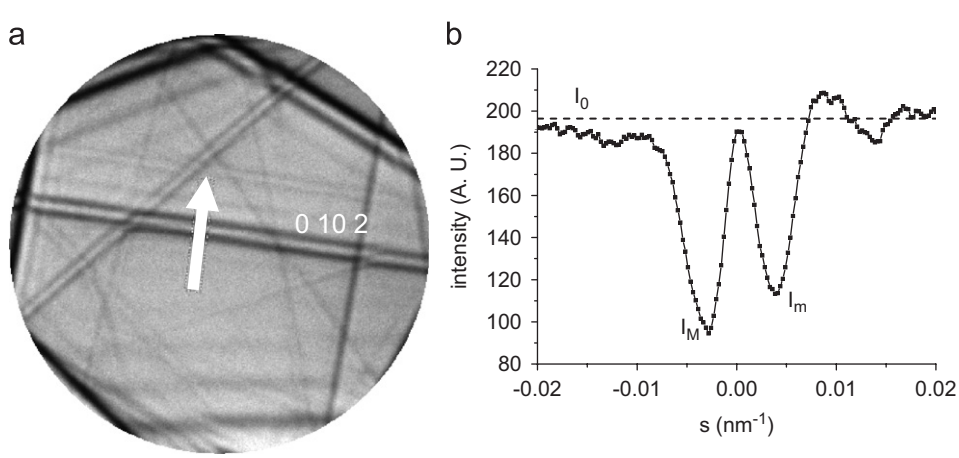


Fig. 3. (a) EFCBED pattern taken on the encircled area in Fig. 2. (b) Intensity profile of the $\mathbf{g} = 0\,10\,2$ Bragg line doublet taken along the arrow drawn in (a).

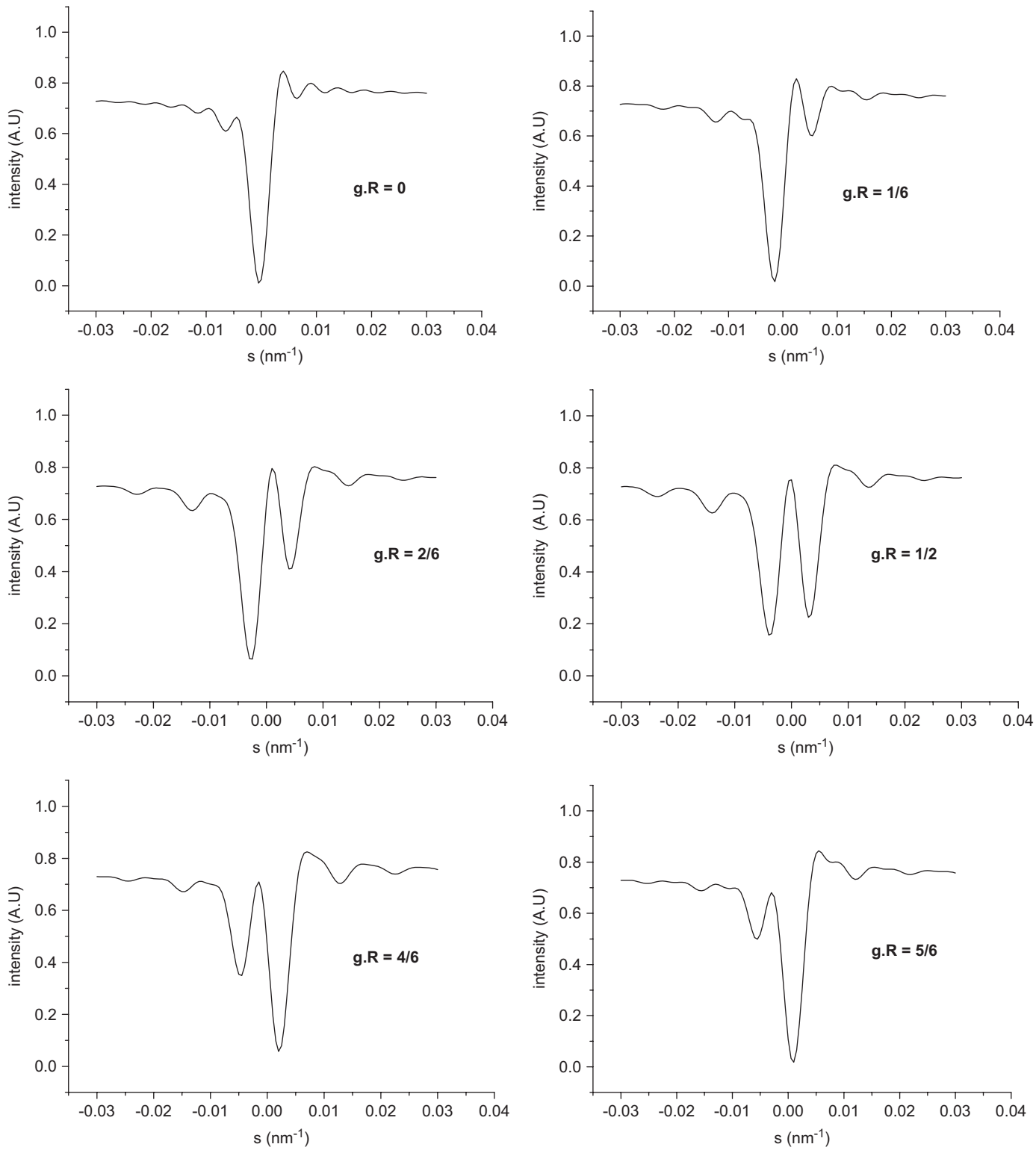


Fig. 4. Two-beam intensity profiles calculated as a function of $\mathbf{g}\cdot\mathbf{R}$ ($A_g = 0.1$, $\xi_g = 500\,\text{nm}$, $t = 200\,\text{nm}$, $t_c = 100\,\text{nm}$, $t_q = 10\,\text{nm}$).

contrast analysis is applicable only for values of

$$\frac{t}{\xi_g} \leqslant \sim 0.7. \tag{3}$$

Finally, Fig. 6 shows various intensity profiles as a function of the position of the QW in the whole sample, given by the ratio $t_c/t$. The doublet contrast analysis is appropriate only for

$$\sim 0.3 \leqslant \frac{t_c}{t} \leqslant \sim 0.5. \tag{4}$$

For a given cap layer thickness $t_c$, the thin foil local thickness must then be chosen to fulfil both conditions (3) and (4).

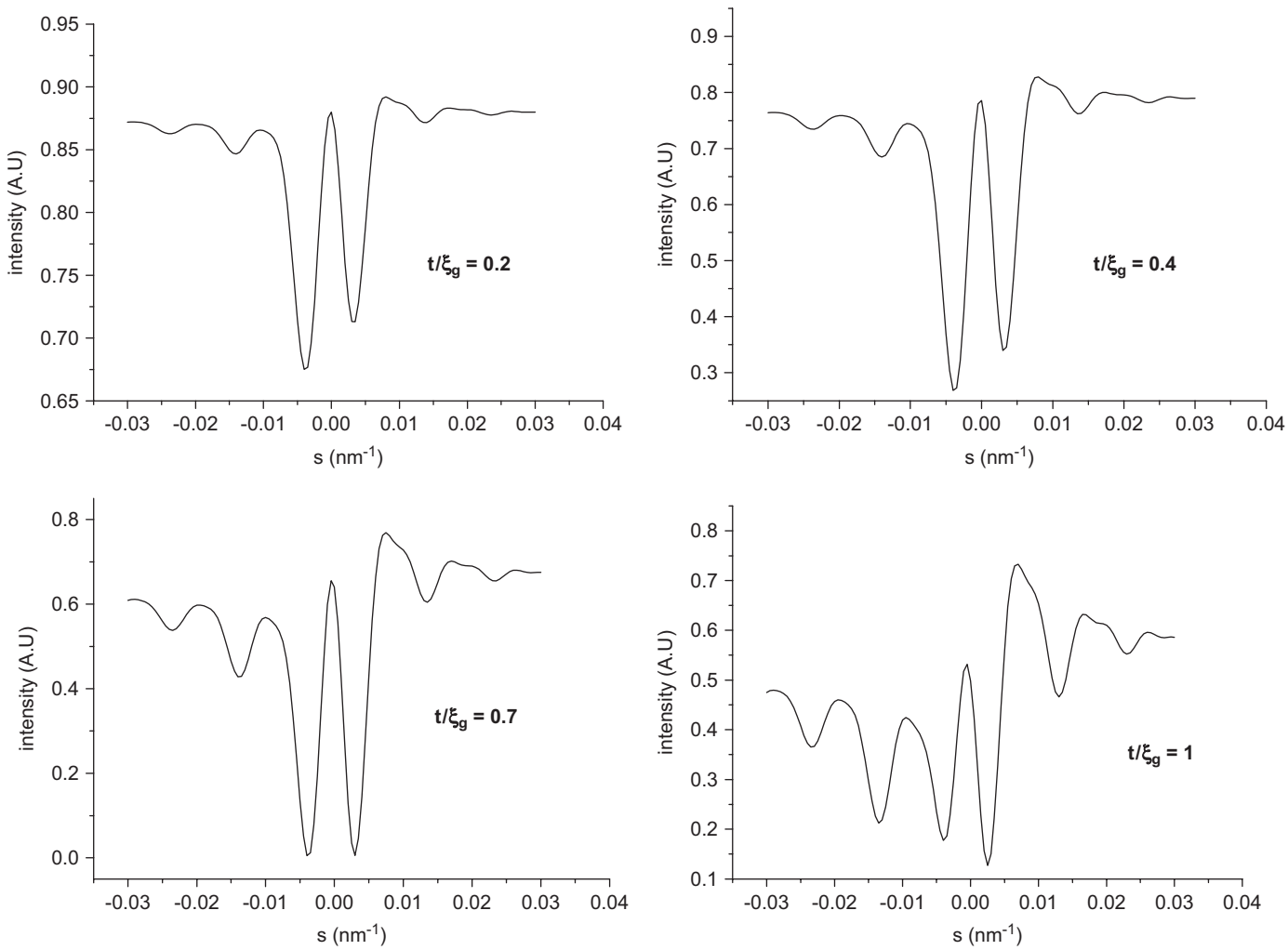


Fig. 5. Two-beam intensity profiles calculated as a function of $t/\xi_g$ ($A_g = 0.1$, $t = 200$ nm, $t_c = 100$ nm, $t_q = 10$ nm).

### 3.2.2. Multi-beam calculations

To treat multi-beam effects, we use the scattering matrix method of Sturkey [16] for imperfect crystals [17]. Briefly, the imperfect strained QW is divided into $N$ thin slices of equal thickness and each slice is displaced from the substrate by a vector proportional to its distance from the $In_xGa_{1-x}As$/substrate interface. This kind of treatment has already been successfully applied to multilayer systems by Rossouw et al. [18]. The exit wave function $\Psi$ is related to the incident wave $\Psi_0$ through

$$\Psi = P_n P_{n-1} \cdots P_1 \Psi_0,$$

where $P_n$ stands for the scattering matrix of the $n$th slice of the imperfect crystal and $P$ can be calculated using the Bloch wave method [19] using

$$P = QC\Upsilon C^{-1}Q^{-1}.$$

Here $C$ is the Bloch wave eigenvector matrix and both $Q$ and $\Upsilon$ are diagonal matrices

$$Q = \{\exp(2\pi i\vec{g}\cdot\vec{R}(z))\} \quad \text{and} \quad \Upsilon = \{\exp(2\pi i\gamma^i\Delta z)\},$$

where $\Delta z$ is the slice thickness and $\gamma^i$ is the eigenvalue of Bloch wave $i$.

Fig. 7a shows the multi-beam CBED pattern calculated with 37 beams and corresponding to the experimental pattern in Fig. 3. In this calculation, the $In_{0.12}Ga_{0.88}As$ layer is divided in $N = 10$ slices of equal thickness and each slice is displaced from the substrate by $R_z^n = \varepsilon_0 t_s^n(1+\nu)/(1-\nu)$, with $t_s^n = n(t_q/N)$ and $n$ varying from 1 to $N$. In each slice, the displacement introduces a phase shift $\alpha = \exp(2i\pi g_z R_z^n)$ for all the Fourier components $U_g$ of the crystal potential. The $In_{0.12}Ga_{0.88}As$ layer is sandwiched between perfect 100-nm-thick GaAs crystals. The intensity profiles of the 0 10 2 Bragg line deduced from the multi-beam calculated pattern and from a two-beam calculation are compared in Fig. 7b. For small values of the deviation parameter, i.e., far from intersections with other Bragg lines, the qualitative aspects of the profiles are very similar and the multi-beam interactions only affect the intensity levels. It should be noted that in all cases, multi-beam contrast values have been found to be lower than those of two-beam ones by a few percents. In the following

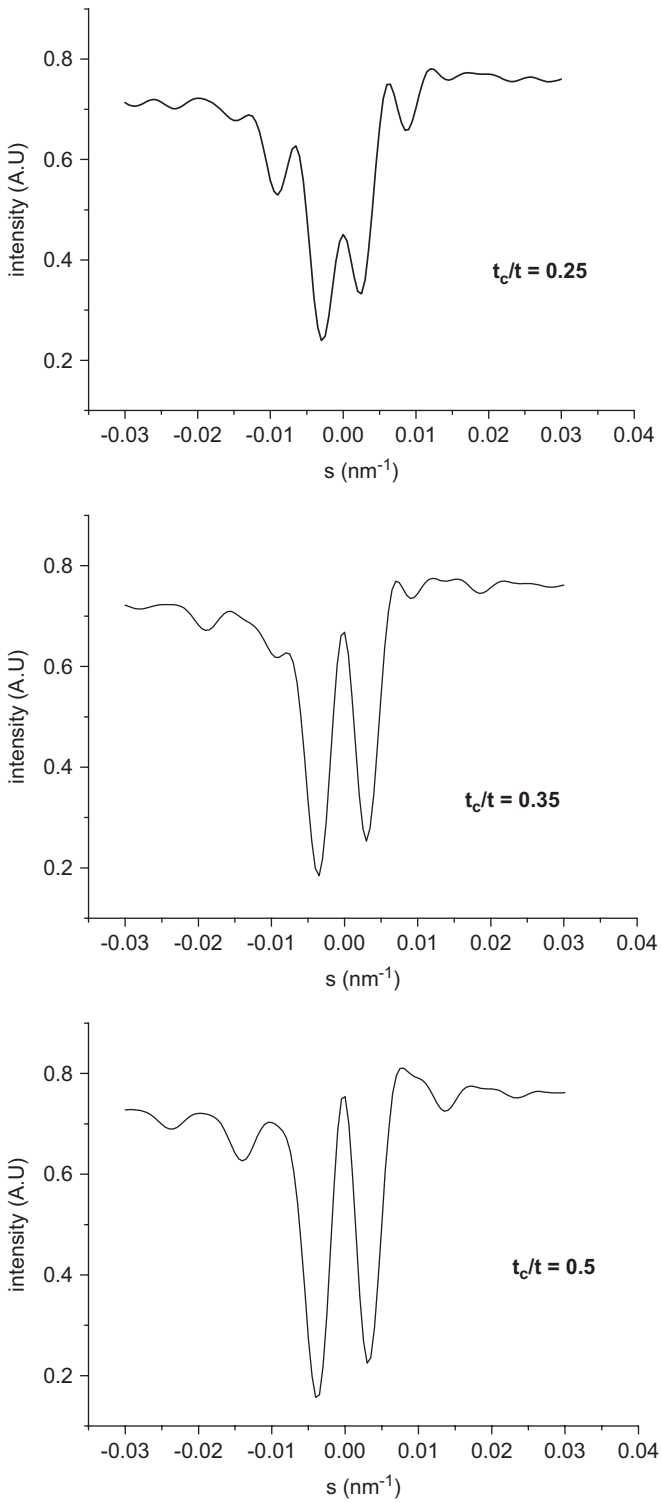


Fig. 6. Intensity profiles calculated as a function of $t_c/t$ ($A_g = 0.1$, $\xi_g = 500$ nm, $t = 200$ nm, $t_q = 10$ nm).

quantitative analysis, multi-beam calculations are systematically used.

### 3.3. Results

The EFCBED patterns were taken from areas with a local thickness $t \sim 200$ nm, leading to $t_c/t > \sim 0.3$, which is fully consistent with condition (4). The thickness was measured with the Kelly et al. procedure [20] using a two-beam CBED pattern taken with $\mathbf{g} = 400$ or 040, diffraction vectors for which $\mathbf{g} \cdot \mathbf{R} = 0$. The corresponding uncertainty is $\pm 5$ nm and calculations have shown that such an uncertainty was sufficiently low so as not to affect the comparison between experimental and computed intensity profiles because Bragg line doublets are insensitive to $\pm 10$ nm thickness variations. It should be noted that EFCBED patterns for doublet intensity analysis are always taken first: the local thickness measurement is then performed as close as possible to the contamination spot resulting from the previous pattern record.

Applying Eq. (1) with the nominal values of $t_q = 10$ nm and $x = 0.120$, $\mathbf{g} \cdot \mathbf{R}$ is calculated to be equal to $-0.290l$ for every diffraction vector $\mathbf{g} = h\,k\,l$. Condition (2) ($\sim 1/3 < \mathbf{g} \cdot \mathbf{R} < \sim 2/3$) can then be fulfilled for $l = 2$ (modulo 4). Only the reflections with $l = 2$ are experimentally obtainable because satisfying the Bragg conditions of other reflections requires a too high tilt of the sample from the initial [0 0 1] orientation. The comparison of experimental intensity profiles with calculated ones was then carried out for $\mathbf{g}_1 = 0\,10\,2$, $\mathbf{g}_2 = 4\,10\,2$ and $\mathbf{g}_3 = \bar{6}\,8\,2$, close to the $[0\,\bar{1}\,5]$ zone axis and for which condition (3) is fulfilled ($\xi_{g_1} = \xi_{g_3} = 520$ nm, $\xi_{g_2} = 640$ nm). These reflections are indicated on the experimental LACBED pattern reproduced in Fig. 8.

The steps involved for comparing experimental and computed intensity profiles are then illustrated in the case of $\mathbf{g}_1 = 0\,10\,2$ (Fig. 3). The first step consists in measuring $I_0^{\exp}$ as the mean value of the background intensities measured on both sides of the Bragg line doublet. Integrating the intensities $I_m$ and $I_M$ of the doublet makes it possible to determine the contrast $K^{\exp} = (I_m^{\exp} - I_0^{\exp})/(I_M^{\exp} - I_0^{\exp})$ for every EFCBED pattern ($K^{\exp} = 0.76$ in the case of Fig. 3). The experimental uncertainty on this contrast value is due to slight intensity variations along the Bragg line doublet in the CBED pattern and it is estimated to be $\pm 0.01$. The second step consists in calculating $K^{\text{calc}} = (I_m^{\text{calc}} - I_0^{\text{calc}})/(I_M^{\text{calc}} - I_0^{\text{calc}})$ as a function of $x$ for the experimentally measured thickness ($t = 215$ nm in the case of Fig. 3). The curve of $K$ as a function of $x$ for $t = 215$ nm and $\mathbf{g}_1 = 0\,10\,2$ is reproduced in Fig. 9. As an example, comparing $K^{\text{calc}}(x)$ with $K^{\exp} = 0.76$ leads to $x = 0.090$ or 0.123. Calculating $\mathbf{g.R}$ gives $-0.430$ for $x = 0.090$ and $-0.584$ for $x = 0.123$, respectively. Examining Fig. 4 shows that the intensity minimum $I_m$ is observed at $s > 0$ for $0 < \mathbf{g.R} < 1/2$ (modulo 1) whereas it is observed at $s < 0$ for $1/2 < \mathbf{g.R} < 1$ (modulo 1). $I_m$ is observed at $s > 0$ in the case of the experimental profile shown in Fig. 3b: the correct value for $x$ is then 0.123 (rather than 0.090). Finally, experimental and calculated intensity profiles are compared for $x = 0.123$ (Fig. 10); the good match obtained between experimental and calculated secondary lines observed in the background is a further proof of the accuracy of the method. The experimental uncertainty of the contrast ratio $K$ is $\pm 0.01$, which in turn leads to a composition uncertainty $\Delta x = \pm 0.002$.

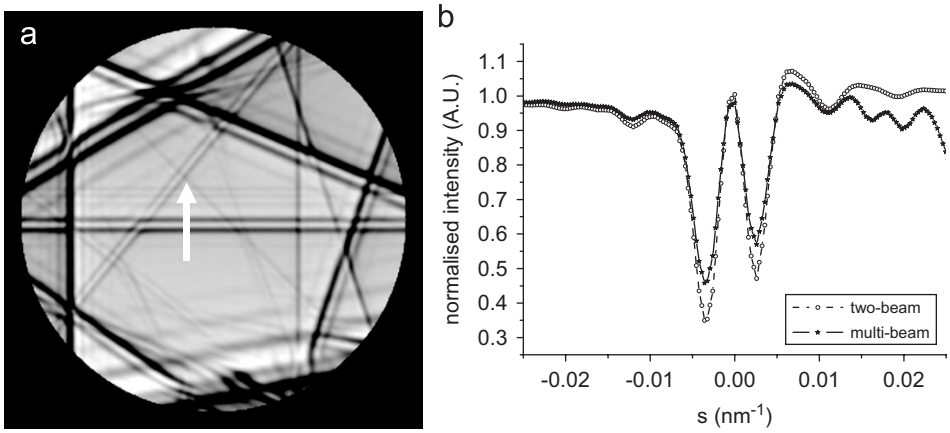


Fig. 7. (a) Calculated multi-beam CBED pattern for the same orientation of the sample as in Fig. 3 with $t_q = 10$ nm and $x = 0.12$. (b) Intensity profile of the $\mathbf{g} = 0\,10\,2$ Bragg doublet taken along the arrow indicated in (a) and compared with that obtained with a two-beam calculation.

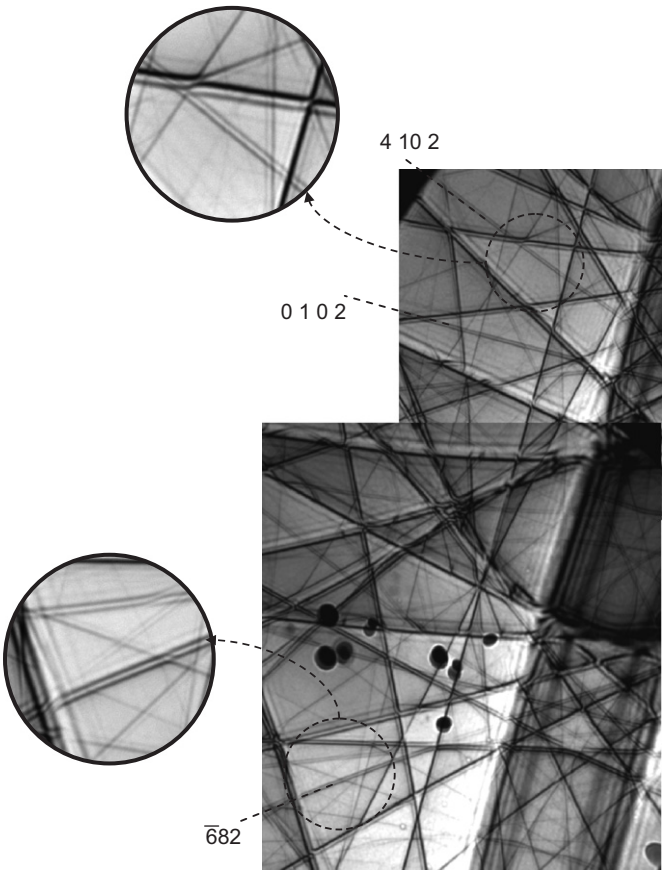


Fig. 8. LACBED pattern taken close to the $[0\,\bar{1}\,5]$ zone axis. Examples of EFCBED patterns taken for composition measurement with $\mathbf{g_2} = 4\,10\,2$ and $\mathbf{g_3} = \bar{6}\,8\,2$ are reproduced in the insets. Black spots are due to contamination resulting from EFCBED patterns acquisition.

The above analysis procedure has been applied for the three reflections $\mathbf{g}_1$, $\mathbf{g}_2$ and $\mathbf{g}_3$, and for various locations of the electron microprobe in areas with $t = 205 \pm 10$ nm. The results are reported in Table 1. The corresponding indium compositions have been found to be spread out between 0.117 and 0.128, giving a composition variation $\Delta x_m = \pm 0.005$.

## 4. Discussion and conclusion

A quantitative composition measurement procedure is reported here for buried QW structures. It is based on an analysis of line splitting in EFCBED patterns. Our results show that the uncertainty in the composition measurement $\Delta x = \pm 0.002$ obtained using different diffraction vectors and different beam locations is significantly smaller than the variation of $x$ measured in the sample ($\Delta x_m = \pm 0.005$). The composition variation measured from different locations must then be attributed to inhomogeneities inherent to the studied sample. As our method is based on the measurement of the displacement $R$, proportional to the product of the QW composition and thickness ($xt_q$), the inhomogeneities can be due to variations in $t_q$, to composition fluctuations in the growth plane or to both. Supposing that there are no composition fluctuations, the measured dispersion $\Delta x_m = \pm 0.005$ would be the result of local variations of $\pm 0.5$ nm for $t_q$ (approximately two GaAs monolayers). Such variations in the QW thickness were not detected by TEM cross-sectional observations. Thus, a significant part of the $\Delta x_m$ dispersion comes from composition fluctuations in the (0 0 1) growth plane. This fluctuation is on a ~100 nm length scale. It should be noted that this result could not be obtained using LACBED, as in our previous work [13], for the following reasons. First, the comparison of experimental and calculated LACBED intensity profiles is not as accurate as in the case of CBED experiments because the match between experimental and calculated secondary lines in the background is not as good as in the case of CBED experiments. Secondly, due to the defocus used to obtain LACBED patterns, the probed area size is generally larger than 50–100 nm, comparable with the ~100 nm scale of composition fluctuations.

As far as the sensitivity of the method is concerned, the two-beam analysis reported here shows that the highest accuracy in the measurement of the $K$ contrast is obtained for $\mathbf{g} \cdot \mathbf{R}$ chosen within the range [1/3–2/3] (condition (2)). In the case of a 10-nm-thick $In_xGa_{1-x}As$ QW and using a $\mathbf{g}$

vector with $l = \pm 2$ as in the present study, only the $x$ values within the range [0.05–0.15] can be properly determined. Higher index $\mathbf{g}$ vectors can be used for measuring lower (or higher) indium contents. For instance, a 10-nm-thick QW with $x \sim 0.03$ could still be analysed with $\mathbf{g} = 4\,8\,4$ or $\mathbf{g} = 10\,6\,4$ lying close to the [0 1 2] zone axis, giving $\mathbf{g} \cdot \mathbf{R} \sim 0.3$. For lower indium contents, high order reflections should be used. The practical limitation in this case is the Bragg line intensity that is generally too low for a proper analysis.

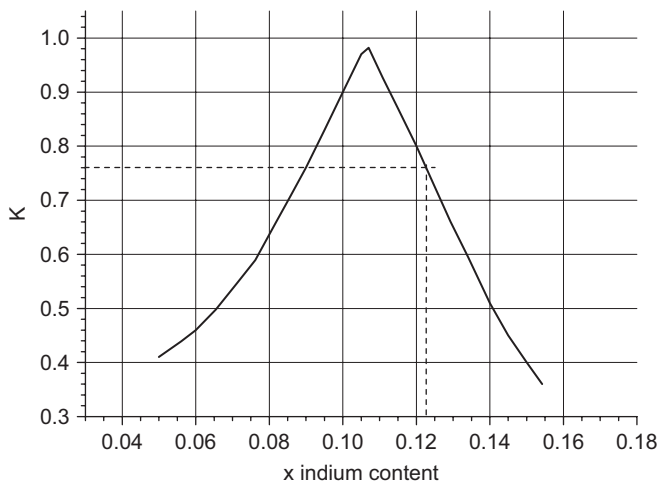


Fig. 9. Calculated doublet contrast for the 0 10 2 Bragg line as a function of the QW indium content ($t = 215$ nm, $t_c = 100$ nm, $t_q = 10$ nm).

The main advantage of the method described here is the use of plan-view samples for which surface relaxation phenomena can be fully neglected. However, as it is based on measuring the displacement induced by the QW along the $z$ growth direction, possible composition gradients along $z$ [21,22] cannot be directly determined. This can be remedied by using the whole CBED pattern matching technique along several orientations instead of single Bragg line doublets. This should be explored in future studies to reveal 3-D composition gradients.

## Acknowledgement

This work has been partly supported by the French Région Nord-Pas de Calais.

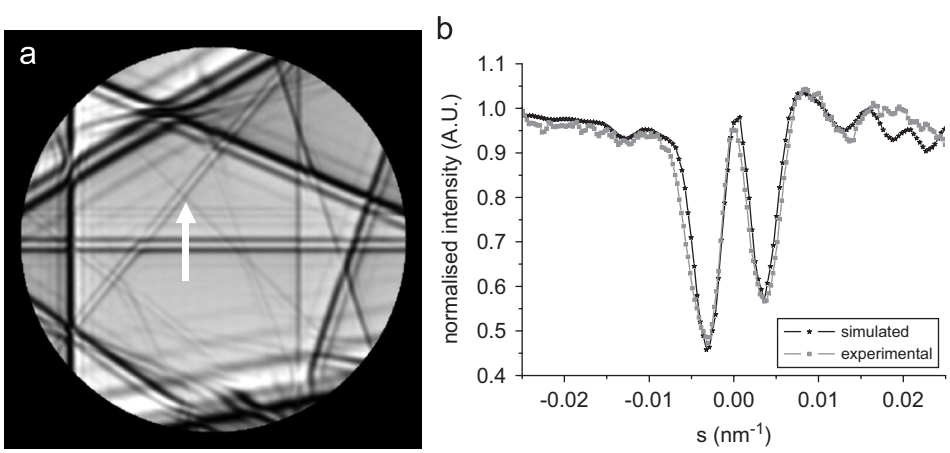


Fig. 10. (a) Calculated multi-beam CBED pattern for the same orientation of the sample as in Fig. 3 ($x = 0.123$). (b) Comparison of the experimental profile in Fig. 3b with the calculated profile of the 0 10 2 Bragg doublet taken along the arrow indicated in (a).

Table 1
QW composition measurement results obtained for various diffraction vectors and probe locations with $t = 205 \pm 10$ nm

| | Doublet contrast, $K$ | QW indium composition, $x$ | Mean value and dispersion |
|---|---|---|---|
| $\mathbf{g}_1 = 0\,10\,2$, $\xi_g = 520$ nm | 0.80 | 0.120 | $0.122 \pm 0.005$ |
| | 0.80 | 0.120 | |
| | 0.76 | 0.123 | |
| | 0.76 | 0.123 | |
| | 0.70 | 0.127 | |
| | 0.67 | 0.128 | |
| | 0.84 | 0.117 | |
| | 0.71 | 0.126 | |
| $\mathbf{g}_2 = 4\,10\;2$, $\xi_g = 640$ nm | 0.77 | 0.118 | |
| | 0.67 | 0.125 | |
| $\mathbf{g}_3 = \bar{6}\,8\,2$, $\xi_g = 520$ nm | 0.78 | 0.122 | |

## References


[1] J. Verbeeck, S. Van-Aert, Ultramicroscopy 101 (2004) 207.
[2] R. Bierwolf, M. Hohenstein, F. Phillipp, O. Brandt, G.E. Crook, K. Ploog, Ultramicroscopy 49 (1993) 273.
[3] A. Rosenauer, S. Kaiser, T. Reisinger, J. Zweck, W. Gebhardt, D. Gerthsen, Optik 102 (1996) 63.
[4] S. Kret, C. Delamarre, J.Y. Laval, A. Dubon, Philos. Mag. Lett. 77 (1998) 249.
[5] A. Rosenauer, Transmission Electron Microscopy of Semiconductor Nanostructures–An Analysis of Composition and Strain, Springer, Heidelberg, 2003.
[6] J. Cagnon, P.A. Buffat, P.A. Stadelmann, K. Leifer, Inst. Phys. Conf. Ser. 180 (2003) 203.
[7] G. Patriarche, L. Largeau, J.C. Harmand, D. Gollub, Appl. Phys. Lett. 84 (2004) 203.
[8] E.G. Bithell, W.M. Stobbs, Philos. Mag. 60 (1989) 39.
[9] F. Glas, Philos. Mag. 84 (2004) 2055.
[10] A. Rosenauer, M. Schowalter, F. Glas, D. Lamoen, Phys. Rev. B 72 (2005) 085326.
[11] K. Volz, O. Rubel, T. Torunski, D. Baranovskii, W. Stolz, Appl. Phys. Lett. 88 (2006) 081910.
[12] A. Hovsepian, D. Cherns, W. Jaeger, Philos. Mag. A 79 (1999) 1395.
[13] D. Jacob, Y. Androussi, A. Lefebvre, Ultramicroscopy 89 (2001) 299.
[14] J.M. Zuo, Microsc. Res. Tech. 49 (2000) 245.
[15] M. Tanaka, M. Terauchi, K. Tsuda, Convergent Beam Electron Diffraction, vol. III, JEOL Ltd., Tokyo, 1994, pp. 162–165.
[16] L. Sturkey, Acta Cryst. 10 (1957) 858.
[17] P.B. Hirsch, A. Howie, R.B. Nicholson, R.B. Pashley, M.J. Whelan, in: Electron Microscopy of Thin Crystals, E. Robert (Ed.), Krieger, New York, 1977.
[18] C.J. Rossouw, M. AL-Khafaji, D. Cherns, J.W. Steeds, R. Touaitia, Ultramicroscopy 35 (1991) 229.
[19] J.C.H. Spence, J.M. Zuo, Electron Microdiffraction, Plenum Press, New York, 1992.
[20] P.M. Kelly, A. Jostsons, R.G. Blake, J.G. Napier, Phys. Stat. Sol. A 31 (1975) 771.
[21] J. Nagle, J.P. Landesman, M. Larive, C. Mottet, P. Bois, J. Crystal Growth 127 (1993) 550.
[22] K. Tillmann, W. Jäger, J. Electron. Microsc. 49 (2000) 245.

Available online at www.sciencedirect.com
SCIENCE DIRECT®
ELSEVIER
Ultramicroscopy 96 (2003) 1–9
ultramicroscopy
www.elsevier.com/locate/ultramic

# Interpretation of unexpected rocking curve asymmetry in LACBED patterns of semiconductors

D. Jacob*, A. Lefebvre

*Laboratoire de Structure et Propriétés de l'Etat Solide (UMR CNRS 8008), Université des Sciences et Technologies de Lille, Bâtiment C6, 59655 Villeneuve d'Ascq cedex, France*

Received 12 February 2002; received in revised form 9 September 2002

**Abstract**

Transmission electron microscopy rocking curves diffracted from inclined planes in argon ion-thinned Si and III–V semiconductors display a significant asymmetry around the Bragg condition. Kinematical and dynamical calculations of the rocking curves show that such an asymmetry can be attributed to the dilation of coherent crystalline surface layers implanted with argon atoms. The surface layers are characterized with two parameters, their width $h$ and the strain component $\varepsilon_z$ normal to the thin foil plane. The dark-field rocking curve asymmetry is shown, for sufficiently high values of $h$ ($> \sim 2$ nm), to strongly depend on $\varepsilon_z$ which is directly related to the density of implanted argon atoms in the surface layers. Calculations also show that a significant rocking curve asymmetry is only observed for intermediate values of $\varepsilon_z$ of about a few percents.
© 2002 Elsevier Science B.V. All rights reserved.

*PACS:* 61.14.Lj; 61.82.Fk; 68.55-a

*Keywords:* Transmission electron microscopy; Large-angle convergent beam electron diffraction; Ion milling; Semiconductors

## 1. Introduction

Ion milling as a method for preparing specimens for transmission electron microscopy (TEM) is a powerful technique for the investigation of a wide range of materials (for a review see, e.g. Ref. [1]). In the case of elemental semiconductors, Ge and Si develop amorphous surface layers when ion-bombarded with argon [2]. It is also the case for compound semiconductors, but great differences are found in the response of various compound semiconductors to ion irradiation [3–6]. The occurrence of amorphous surface layers is a crucial limiting factor in the quantitative interpretation of high-resolution electron microscopy images and it is thus essential to ensure that the specimen is undamaged if intensities are to be interpreted correctly [7].

Very recently, an additional damaged layer type was evidenced in ion-milled silicon specimens, i.e. argon atoms implanted in the *crystalline* layers beneath the amorphous layers [8]. Such a damaged

*Corresponding author. Tel.: 33-3-20-43-65-94; fax: 33-3-20-43-65-91.
*E-mail address:* damien.jacob@univ-lillel.fr (D. Jacob).

0304-3991/03/$ - see front matter © 2002 Elsevier Science B.V. All rights reserved.
PII: S0304-3991(02)00342-X

layer is responsible for the observation of asymmetric dark-field rocking curves and thus modifies the intensity of most of the diffracted beams. Such an asymmetry had been mentioned in silicon and diamond well before [9], and the authors had concluded that it could not be attributed only to symmetry breaking related to the non-symmetry Laue case and that it should be essentially due to "some non-ideal aspect of the specimen such as being bent or wedged or having rough surfaces".

This paper is aimed at showing that the observation of a large asymmetry in dark-field rocking curves is not restricted to ion-milled elemental semiconductors and that it can also be observed in ion-thinned III–V semiconductors. A qualitative interpretation is proposed, based on the dilation of the surface layers resulting from implanted argon atoms as proposed by Vincent et al. [8].

## 2. Experimental details

TEM specimens were prepared from (0 0 1) Si or III–V semiconductor wafers by mechanical polishing to a thickness of 50 $\mu$m. They were then thinned to transparency by argon ion milling of both surfaces in the Gatan Duomill. The variable parameters were accelerating voltage, beam inclination to the surface and temperature of the specimen. A few other samples were also thinned to transparency either mechanically using a South Bay Technology tripod polisher or by chemical polishing (e.g. in a mixture of 30% HF and 70% $HNO_3$ in the case of GaAs).

Large-angle convergent beam electron diffraction (LACBED) patterns were taken with a Philips CM30 microscope (operated at 300 kV) and directly captured with a cooled slow-scan charge-coupled device Gatan camera. The [0 0 1] direction was chosen to be perpendicular to the thin foil plane.

The simulated diffracted intensities were calculated either in the kinematical approximation or in dynamical two-beam conditions.

## 3. Results

### 3.1. TEM observations

LACBED patterns were taken rather than conventional CBED patterns for two reasons. The first reason is that, contrary to CBED patterns, LACBED patterns are efficiently energy filtered and subsequently give more precise information on intensities. The second reason lies in the fact that LACBED patterns give bidimensional information (in the whole plane of the transparent sample), whereas information obtained from CBED patterns only concerns the microprobe area.

Fig. 1 shows a $g=(2\,2\,4)$ dark-field Bragg line and its opposite $-g$, in the case of a GaAs crystal ion-thinned with 4.5 keV argon ions incident at 13° to the surface and at room temperature. These dark-field Bragg lines were obtained from the $[0\,\bar{2}\,1]$ zone axis pattern in Fig. 2. The large asymmetry displayed around the Bragg condition in Fig. 1. is characteristic of all the GaAs samples thinned in the aforementioned conditions and for $\{h\,k\,l\}$ Bragg lines with $l\neq 0$, which is not consistent with the results of dynamical theory applied to perfect crystals, for which all the $\{h\,k\,l\}$ dark-field Bragg lines should be symmetrical [10]. Besides, it should be noted that the highest intensities are observed for $s<0$ in the case of $g=(2\,2\,4)$, for $s>0$ in the case of $-g$ and that the symmetry property $I_g(s)=I_{-g}(-s)$ is relevant for all $\{h\,k\,l\}$ Bragg lines with $l\neq 0$. Fig. 3 shows a $\{2\,2\,4\}$ dark-field Bragg line as obtained from mechanically thinned GaAs samples: no asymmetry can be observed in this case (as well as for all $\{h\,k\,l\}$ Bragg lines with $l\neq 0$). The same result was obtained with all the chemically thinned samples we have observed. The asymmetry of the dark-field rocking curves can therefore be attributed to the superficial defects induced by argon ion milling.

### 3.2. Kinematical calculations

Kinematical calculations are carried out assuming that the asymmetry of $\{h\,k\,l\}$ ($l\neq 0$) rocking curves is due to the dilation of surface layers

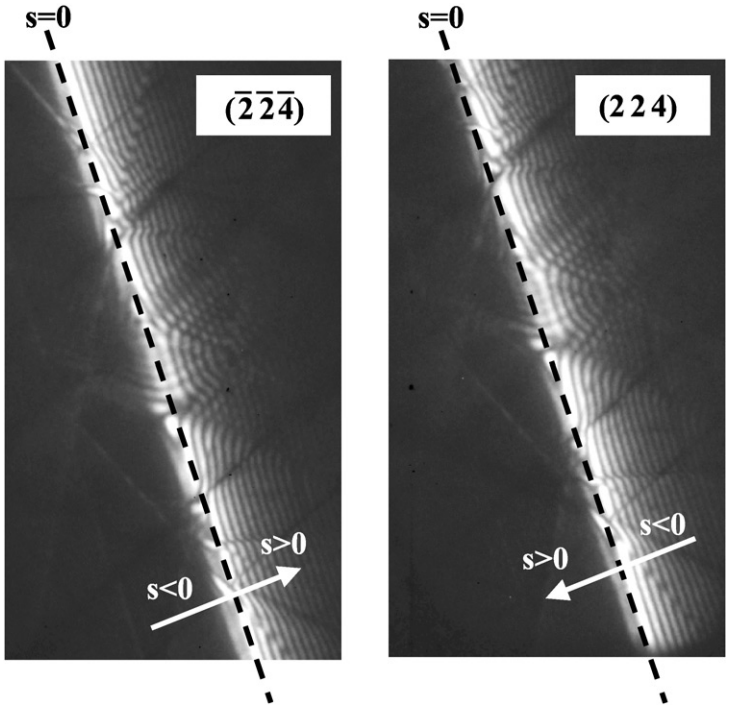


Fig. 1. (2 2 4) and $(\bar{2}\,\bar{2}\,\bar{4})$ dark-field Bragg lines obtained from those arrowed in Fig. 2.

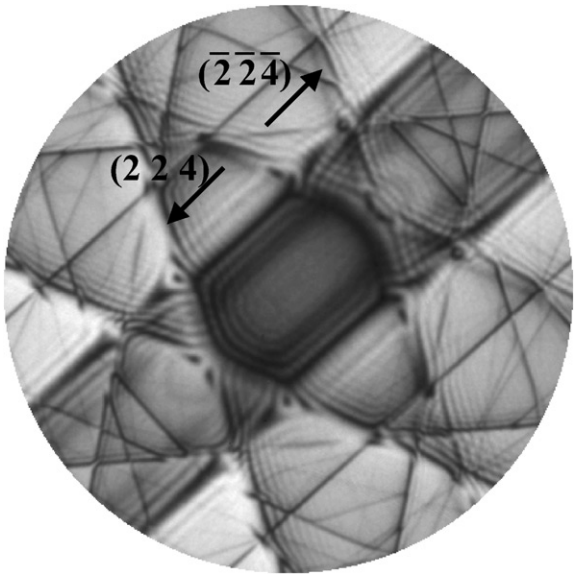


Fig. 2. $[0\,\bar{2}\,1]$ zone axis LACBED pattern for a GaAs argon ion-thinned crystal in the conditions mentioned in the text.

induced by the implantation of Ar atoms [8]. The calculations are performed in the case of a perfect cubic crystal (thickness $2t$ and crystalline parameter $a_p$) sandwiched between two implanted layers I and II (thickness $h$; Fig. 4). It is further assumed that the density of implanted Ar atoms is uniform and the same in both layers (which have then the same bulk crystalline parameter $a_d$) and that the perfect crystal and the implanted layers have the same Poisson's ratio $\nu$. Strain in layers is thus identical to the strain component $\varepsilon_z = (1+\nu)(a_d - a_p)/[(1-\nu)a_p]$, which explains why the dark-field rocking curve asymmetry is not observed for $hk0$ Bragg lines.

The phase angles introduced between the perfect crystal and layers I and II, respectively, are $\alpha_I = 2\pi g_z u_{zI}$ and $\alpha_{II} = 2\pi g_z u_{zII}$, where $u_{zI} = \varepsilon_z(t+z)$ and $u_{zII} = \varepsilon_z(-t+z)$ are the component displacements in layers I and II, and $g_z$ is the projection of the diffracting vector $\mathbf{g}$ onto the $Oz$ axis. The diffracted amplitude of the $\mathbf{g}$ reflection at the exit

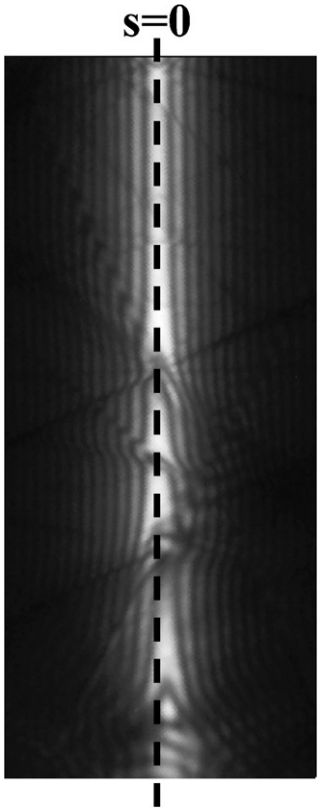


Fig. 3. A (2 2 4) dark-field Bragg line obtained from a mechanically polished GaAs crystal.

of the thin foil is calculated as

$$\phi_g = \int_{-t-h}^{-t} \exp[-i\alpha_I - 2\pi i s z]\,dz + \int_{-t}^{+t} \exp(-2\pi i s z)\,dz + \int_{+t}^{+t+h} \exp[-i\alpha_{II} - 2\pi i s z]\,dz.$$

This leads to the equation

$$I_g = |\phi_g|^2 = \frac{(s\,sin\,B + \varepsilon_z g_z \sin A)^2}{\pi^2 s^2 (\varepsilon_z g_z + s)^2} \quad (1)$$

with $A = 2\pi s t$ and $B = 2\pi[\varepsilon_z g_z h + s(t+h)]$.

First, it should be noted that this equation is consistent with the symmetry property $I_g(s) = I_{-g}(-s)$ mentioned above.

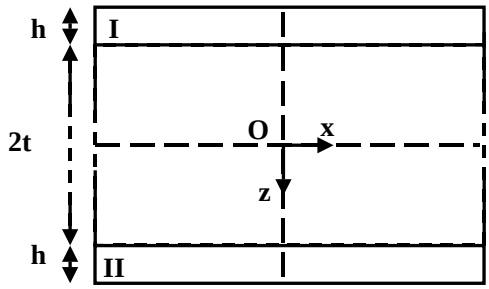


Fig. 4. Schematic cross section of a sample argon ion thinned on both surfaces: perfect crystal in the central part (thickness $2t$); I and II are the implanted layers (thickness $h$). $Oz$ is parallel to the [0 0 1] direction.

Let us consider then the diffracted intensity of a perfect crystal with crystal thickness $2t$:

$$I_{gp} = \frac{\sin^2(2\pi s t)}{\pi^2 s^2}.$$

$I_{gp}$ can be regarded as the product of the oscillating part $\sin^2(2\pi s t)$ and of the rapidly decreasing part $1/\pi^2 s^2$ centred around $s=0$, which leads to a symmetrical rocking curve. Regarding $I_g$ in the same way, the oscillating part $(s \sin B + \varepsilon_z g_z \sin A)^2/s^2$ is dependent on both $h$ and $\varepsilon_z$ in a complicated way. But as its relative weight is low comparatively to that of the rapidly decreasing term $[\pi(\varepsilon_z g_z + s)]^{-2}$, the behaviour of $I_g$ as a function of $s$ is mainly due to this rapidly decreasing term which is not centred around $s=0$ and which is thus responsible for the asymmetry of $I_g$ around the Bragg condition (Fig. 5, for instance with $\varepsilon_z g_z > 0$). Three cases have to be considered in this figure, depending on the relative values of $s$ and $\varepsilon_z g_z$. In the first case ($\varepsilon_z g_z \ll |s|$, Fig. 5a), the rapidly decreasing term contribution is roughly centred around $s=0$ and the resulting diffracted intensity is approximately symmetrical around the Bragg condition. In the second case ($\varepsilon_z g_z \sim |s|$, Fig. 5b), the relative positions of the oscillating part contribution and of the rapidly decreasing term contribution lead to a large asymmetry around the Bragg condition. Finally, in the third case ($\varepsilon_z g_z \gg |s|$, Fig. 5c), the rapidly decreasing term is centred far from $s=0$, its contribution is almost constant and it corresponds to an approximate symmetry around the Bragg condition. Comparing now the orders of magnitude of $s$

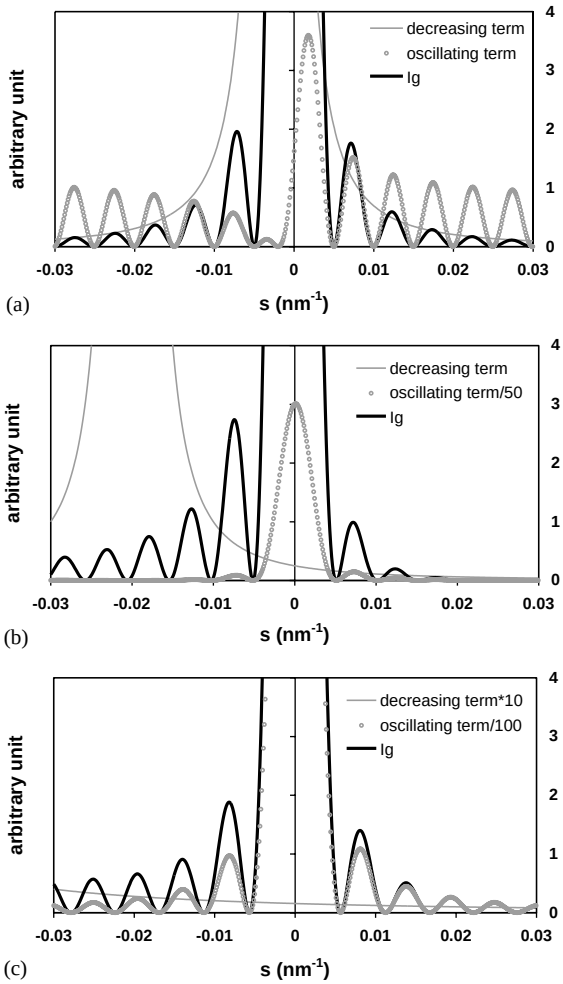


Fig. 5. Kinematical diffracted intensity $I_g$ for the damaged crystal as in Fig. 4, in the case $\varepsilon_z g_z > 0$: (a) $\varepsilon_z g_z \ll |s|$; (b) $\varepsilon_z g_z \sim |s|$; and (c) $\varepsilon_z g_z \gg |s|$.

and $\varepsilon_z g_z$ yields the values of $\varepsilon_z$ that are liable to result in asymmetric dark-field rocking curves: $s \sim 10^{-2}\,\mathrm{nm}^{-1}$ and $g_z \sim 1\,\mathrm{nm}^{-1}$ leads to $\varepsilon_z \sim 1\%$.

The quasi-symmetry of dark-field rocking curves for $\varepsilon_z g_z \ll |s|$ and for $\varepsilon_z g_z \gg |s|$, can be directly demonstrated from the analysis of Eq. (1) (see Appendix A).

Finally, the kinematical calculation of rocking curves in the case of samples ion thinned on a single surface layer is given in Appendix B. It refers to the important class of materials exhibiting epitaxial nanostructures such as quantum wells, wires or islands. This calculation leads to similar results as those in the previous case (samples ion thinned on both faces).

### 3.3. Dynamical two-beam calculations

Let us recall first the main features of dynamical dark-field rocking curves computed on the two-beam theory in the case of perfect crystals [10]. Fig. 6a shows a typical aspect of such rocking curves. They are symmetrical around the Bragg position, a lot of intensity maxima are observed and the absolute maximum of intensity is generally not observed for $s=0$. Fig. 6b shows a rocking curve characteristic of all the rocking curves calculated for ion-thinned GaAs samples. The asymmetry can be characterized by two asymmetry coefficients $\zeta_{g1} = I_{g1+}/I_{g1-}$ and $\zeta_{g2} = I_{g2+}/I_{g2-}$ where $I_{gi+}$ and $I_{gi-}$,respectively, are the $i$th intensity maxima of the rocking curve for $s>0$ and $s<0$.

Calculations of rocking curves as functions of $t$, $h$ and $\varepsilon_z$ show that every rocking curve asymmetry can be approximated by a single coefficient

$$\zeta_g = \frac{(\zeta_{g1} + \zeta_{g2})}{2}$$

and that $\zeta_g$ is approximately independent on the total thickness $2(t+h)$ of the sample (for instance in the case of $\varepsilon_z = 1\%$ in Fig. 7). Fig. 8 shows the variations of $\zeta_g$ as a function of $\varepsilon_z$ for various values of $h$ and for a total thickness of the sample of 200 nm. The analysis of these results is somewhat more complicated than in the case of kinematical calculations because the variations of $\zeta_g$ as a function of $\varepsilon_z$ are now strongly dependent on $h$. For instance no asymmetry ($\zeta_g \sim 1$) is observed for $h = 1$ nm, whatever the value of $\varepsilon_z$, and the main features of the kinematical analysis are found only for higher values of $h$: an asymmetry is observed for intermediate values of $\varepsilon_z$($\varepsilon_z > \sim$a few percents) and this asymmetry tends to disappear for higher values of $\varepsilon_z$. Besides, Fig. 8 also shows the high sensitivity of $\zeta_g$ to $\varepsilon_z$ as soon as $\varepsilon_z$ is different from zero.

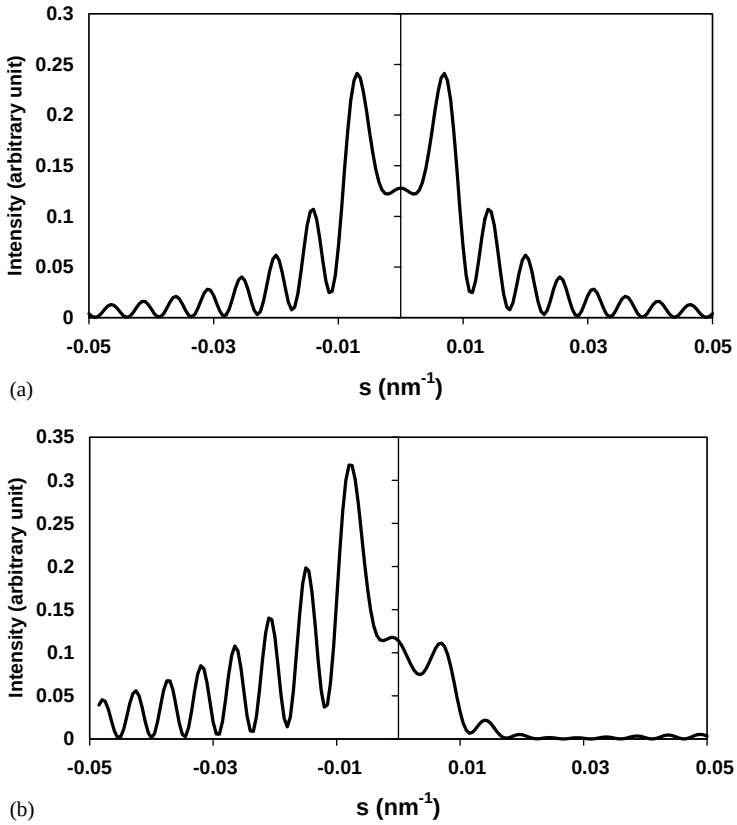


Fig. 6. (a) A typical dynamical two-beam rocking curve of a perfect crystal ($t = 200$ nm, extinction distance $\xi_g = 100$ nm, anomalous absorption $A_g = 1/10$). (b) A typical dynamical two-beam rocking curve characteristic of ion-thinned GaAs samples (same parameters as in (a) and $h = 10$ nm, $\varepsilon_z = 0.02$).

## 4. Discussion and conclusion

A simple kinematical interpretation of dark-field rocking curve asymmetry in LACBED patterns of semiconductors is presented. It accounts for the two main features of these patterns: the property $I_g(s) = I_{-g}(-s)$ and the fact that rocking curve asymmetry is observed only for $\{h\,k\,l\}$ reflections with $l \neq 0$ are readily related to the $\varepsilon_z$ dilation of coherent crystalline surface layers implanted with argon atoms.

The dynamical analysis makes it possible to assess the variations of this asymmetry as a function of the width $h$ of the surface layers and of their $\varepsilon_z$ dilation. The main result is that the rocking curve asymmetry is very sensitive to the variations of $\varepsilon_z$ as soon as $\varepsilon_z$ is different from zero and does not exceed $\sim 10\%$. Only a *qualitative* characterization of ion-milled GaAs samples was performed because the mechanisms of the incorporation of Ar atoms in III–V semiconductors are not well known and full characterizations of ion-milled semiconductors are seldom found in the literature because argon implantation is just an "artefact" for electron microscopists. Nevertheless, our results show that a *quantitative* dynamical analysis of the asymmetry of dark-field rocking curves could be interestingly performed in the case of epitaxial coherently-strained layers so as to study the deformation state and the chemical composition of such layers: although information is averaged in the $z$–direction parallel to the

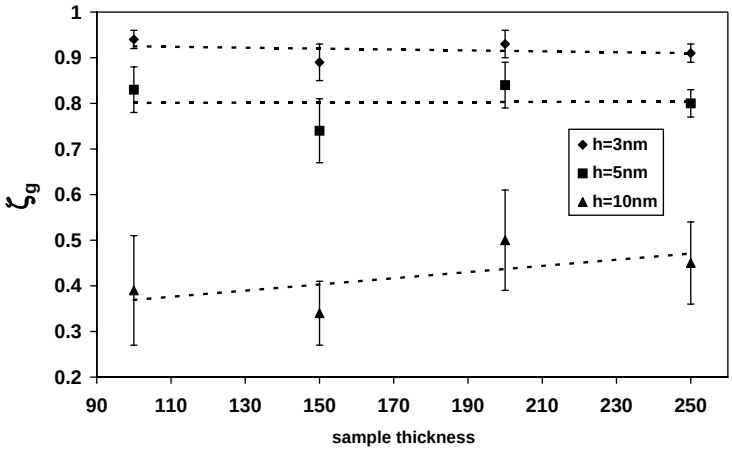


Fig. 7. Variations of the asymmetry coefficient $\zeta_g$ as a function of the sample thickness $2(t+h)$ for various values of $h$.

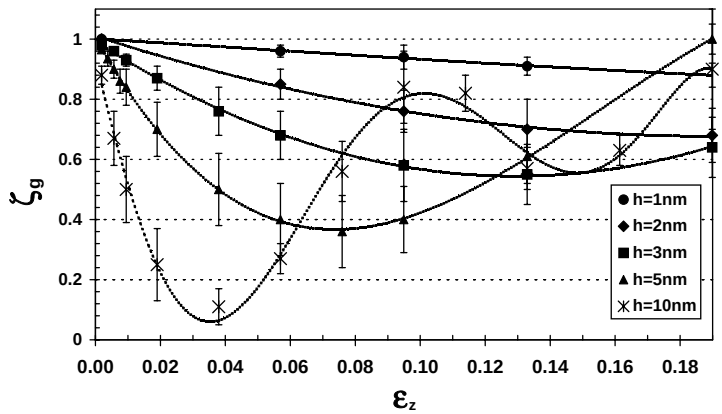


Fig. 8. Variations of $\zeta_g$ as a function of $\xi_z$ for various values of $h$.

electron beam, possible fluctuations in the (0 0 1) plane could be readily detected. This is what is currently being done in the case of III–V epilayers. Besides, such a quantitative analysis would also be of interest in the case of *intentionally* implanted surfaces in order to study the density of implanted defects and the width of the corresponding damaged surface layers.

Finally, it should be noticed that this approach for the study of *surface* defect layers or epilayers requires the study of the fine structure of dynamical (high intensity) reflections. It is complementary to another approach recently proposed for the study of *embedded* quantum wells [11] and based on the study of the splitting of kinematical (low intensity) reflections.

## Acknowledgements

We are indebted to Dr. J. Ayache and Mrs. S. Colin (CSNSM-CNRS, Orsay, France) for valuable help in the mechanical thinning of GaAs samples.

Many thanks are due to Dr. D. Cherns (H.H. Wills Physics Laboratory, Bristol, UK) for drawing our attention to Refs. [8,9].

This work was partly supported by the French Région Nord-Pas de Calais and by the European fund FEDER (Fonds Européen de Développement Régional).

## Appendix A. Rapid analysis of kinematical diffracted intensity for a crystal ion thinned on both surfaces

$$I_g = |\phi_g|^2 = \frac{(s\sin B + \varepsilon_z g_z \sin A)^2}{\pi^2 s^2 (\varepsilon_z g_z + s)^2}.$$

*A.1. First case:* $\varepsilon_z g_z \ll |s|$

$B = 2\pi[\varepsilon_z g_z h + s(t+h)]$ can be approximated to $2\pi s(t+h) \sim 2\pi st = A(h \ll t)$. $I_g$ is then roughly equal to

$$I_g \sim \frac{\sin^2(2\pi st)}{\pi^2 s^2}$$

and $I_g(s) \sim I_g(-s)$.

*A.2. Second case:* $\varepsilon_z g_z \gg |s|$

$$B = 2\pi[\varepsilon_z g_z h + s(t+h)] \sim 2\pi[\varepsilon_z g_z h + st]$$

$$= 2\pi\varepsilon_z g_z h + A(h \ll t)$$

$\phi_g$ can then be written as

$$\phi_g = \frac{(s\sin B + \varepsilon_z g_z \sin A)}{\pi s(\varepsilon_z g_z + s)}$$

$$\sim \frac{1}{\pi s \varepsilon_z g_z}[s\sin(2\pi\varepsilon_z g_z + A) + \varepsilon z g_z \sin A]$$

$$= \frac{1}{\pi s \varepsilon_z g_z}\{[\varepsilon_z g_z + s\cos(2\pi\varepsilon_z g_z h)] \times \sin A + s\sin(2\pi\varepsilon_z g_z h)\cos A\}$$

$$\sim \frac{1}{\pi s \varepsilon_z g_z}[\varepsilon_z g_z \sin A + s\sin(2\pi\varepsilon_z g_z h)\cos A]$$

and $\phi_g(s) \sim \phi_g(-s)$.

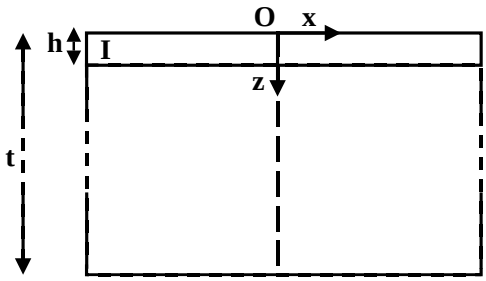


Fig. 9. Schematic cross section of a sample argon ion thinned on the upper surface: the perfect crystal has a thickness $t-h$; the implanted layer has a thickness $h$. $Oz$ is parallel to the [0 0 1] direction.

## Appendix B. Kinematical diffracted intensity for a crystal ion thinned on one surface

The calculations are performed in the case of a perfect cubic crystal (thickness $t$) and of an implanted upper layer $I$ (thickness $h$; Fig. 9).

The diffracted amplitude of the **g** reflection at the exit of the thin foil is calculated as

$$\phi_g = \int_0^h \exp[-i\alpha - 2\pi i s z]\,dz + \int_h^t \exp(-2\pi i s z)\,dz$$

with $\alpha = 2\pi g_z u_z = -2\pi\varepsilon_z(h-z)g_z$. The integration leads to

$$\phi_g = \frac{\exp(2\pi i\varepsilon_z h g_z)}{2\pi i(g_z\varepsilon_z + s)}[1 - \exp(-2\pi i\varepsilon_z h g_z - 2\pi i s h)] + \frac{[\exp(-2\pi i s h) - \exp(-2\pi i s t)]}{2\pi i s}$$

and

$$I_g = \frac{1}{2\pi^2 s^2 (g_z\varepsilon_z + s)^2}[s^2 + g_z^2\varepsilon z^2 + s g_z\varepsilon_z - g_z\varepsilon_z(g_z\varepsilon_z + s) \times \cos 2\pi s(t-h) - s(s + g_z\varepsilon_z)\cos 2\pi(st + g_z\varepsilon z h) + s g_z\varepsilon_z \cos 2\pi h(g_z\varepsilon_z + s)].$$

## References

[1] D.J. Barber, Ultramicroscopy 52 (1993) 125.
[2] Y. Kido, H. Nakano, Surf. Sci. 239 (1990) 254.
[3] A.G. Cullis, N.G. Chew, C.R. Whitehouse, D.C. Jacobson, J.M. Poate, S.J. Pearton, Appl. Phys. Lett. 55 (1989) 211.
[4] A. Barna, B. Pécz, M. Menyhard, Micron 30 (1999) 267.

[5] M.W. Bench, I.M. Robertson, M.A. Kirk, Nucl. Instrum. Methods. B 59/60 (1991) 372.
[6] A.G. Cullis, N.G. Chew, J.L. Hutchinson, in: MRS Symposium Proceedings, Vol. 62, Pittsburg, 1986, p. 83.
[7] J.P. Chevalier, M.J. Hÿtch, Ultramicroscopy 52 (1994) 253.
[8] R. Vincent, T.D. Walsh, M. Pozzi, Ultramicroscopy 76 (1999) 125.
[9] D.M. Bird, J.C. Walmsley, R. Vincent, EMAG 83, Institute of Physics. Conference. Series. No 68, 1983, p. 41.
[10] P.B. Hirsch, A. Howie, R.B. Nicholson, D.W. Pashley, M.J. Whelan, Electron Microscopy of Thin Crystals Krieger, Malabar, FL, 1977.
[11] D. Jacob, Y. Androussi, A. Lefebvre, Ultramicroscopy 89 (2001) 299.

Available online at www.sciencedirect.com
ScienceDirect
Ultramicroscopy 108 (2008) 295–301
ultramicroscopy
www.elsevier.com/locate/ultramic

# Effect of sample bending on diffracted intensities observed in CBED patterns of plan view strained samples

F. Houdellier[a,*], D. Jacob[b], M.J. Casanove[a], C. Roucau[a]

[a]CEMES/CNRS, 29 rue jeanne Marvig, 31055 Toulouse, France
[b]LSPES, UMR CNRS 8008, Université des Sciences et Technologies de Lille, Bâtiment C6, 59655 Villeneuve d'Ascq cedex, France

Received 23 October 2006; received in revised form 26 February 2007; accepted 10 April 2007

**Abstract**

Convergent beam electron diffraction is used to study the effect of the sample bending on diffracted intensities as observed in transmission electron microscopy (TEM). Studied samples are made of thin strained semiconductor $Ga_{1-x}In_xAs$ epitaxial layers grown on a GaAs substrate and observed in plan view. Strong variations of the diffracted intensities are observed depending on the thinning process used for TEM foil preparation. For chemically thinned samples, strong bending of the substrate occurs, inducing modifications of both kinematical and dynamical Bragg lines. For mechanically thinned samples, bending of the substrate is negligible. Kinematical lines are unaffected whereas dynamical lines have slightly asymmetric intensities. We analyse these effects using finite element modelling to calculate the sample strain coupled with dynamical multibeam simulations for calculating the diffracted intensities. Our results correctly reproduce the qualitative features of experimental patterns, clearly demonstrating that inhomogeneous displacement fields along the electron beam within the substrate are responsible for the observed intensity modifications.
© 2007 Elsevier B.V. All rights reserved.

*PACS:* 68.55.Nq; 6114.Lj; 61.82.Fk; 68.55.−a

*Keywords:* Convergent beam electron diffraction; Semiconductors; Elastic stress relaxation; Dynamical simulations

## 1. Introduction

The nanoscale measurement of strain fields in semiconductor mismatched epilayers is of high technological and fundamental interest for the understanding of mechanical and optical properties of semiconductor devices. Convergent beam electron diffraction (CBED) performed in a transmission electron microscope (TEM) has nanometer spatial resolution and high sensitivity to strain and is thus well adapted to this kind of study. Nevertheless, it is well known that the preparation of thin foils for TEM observations modifies strain fields through the introduction of free surfaces which induces elastic stress relaxation phenomena [1–10]. Generally, these modifications have to be taken into account in order to interpret the resulting diffracted intensities observed in TEM foils. This considerably complicates the strain analysis, particularly for cross-sectional observations [9,10]. A possible alternative consists in observing the samples in plan view [11–14]. For buried layers, free surfaces are then created sufficiently far away from the strained areas and their influence can be considered as negligible. Strain in the layer can then be precisely measured using high-order Bragg line intensities [13,14]. In the case of epilayers, it has been previously shown [15] that strain fields can induce a significant asymmetry in dynamical rocking curves allowing the determination of the chemical composition of the layer. It is however important to know how surface relaxation influences this asymmetry.

In this work, we study the influence of the bending of the sample associated with stress relaxation phenomena for various thinning processes, and the subsequent modifications of the diffracted intensities in the case of a thin

*Corresponding author.
*E-mail address:* florent@cemes.fr (F. Houdellier).

0304-3991/$ - see front matter © 2007 Elsevier B.V. All rights reserved.
doi:10.1016/j.ultramic.2007.04.003

$In_xGa_{1-x}As$ layer grown on a (0 0 1) GaAs substrate. Two kinds of TEM foils are prepared: chemically and mechanically thinned samples to electron transparency. In the first case, elastic stress relaxation occurs through the bending of cleaved lamellas, inducing modifications of kinematical as well as dynamical diffracted intensities as observed in CBED patterns. In the second case, the sample remains flat without cleavage. Kinematical intensities are then unaffected whereas dynamical intensities show the previously reported asymmetry. Then, as in [10], finite element modelling (FEM) is used to determine the displacement field along the electron beam for the various samples geometries, and the results are combined with dynamical simulations based on a time-dependant perturbation theory to calculate the associated CBED patterns. Simulations performed using this approach show good qualitative agreement with experimental patterns. Our results also indicate that the determination of the initial strain state of the layer, based on a quantitative analysis of diffracted intensities, could only be achievable thanks to a precise knowledge of the actual shape of the sample.

## 2. Experimental details

A nominally 10 nm thick $Ga_{0.8}In_{0.2}As$ layer was grown by molecular beam epitaxy (MBE) on a GaAs (0 0 1) substrate. Due to the lattice misfit the layer undergoes a compressive in-plane biaxial strain, $\varepsilon = -1.4\%$. Two methods are used to obtain TEM foils by thinning the substrate side of the samples: chemical thinning using a Br–methanol solution (sample A), and mechanical thinning using a Tripod polisher (sample B). CBED experiments are performed using the SACTEM-Toulouse, a TECNAI F20 (FEI) operated at a nominal high-voltage of 200 kV. CBED patterns are recorded on a 2k × 2k slow scan CCD camera attached to a post-column Gatan TRIDIEM Imaging Filter. A 10 eV wide energy slit centred on the zero-loss peak is inserted in order to suppress the contribution of inelastic scattered electrons in the CBED patterns. The finite element program COMSOL multiphysics is used to calculate the displacements fields in the TEM samples with various geometries. The misfit strain between the layer and the substrate is introduced through a thermal strain tensor component [16]. The elastic constants used in the calculations are taken from [17]. The calculated displacements are then introduced in a software package developed in-house to simulate the corresponding CBED patterns. The method used is based on a time-perturbation approach first developed by Portier and Gratias [18] and applied to CBED simulations by Houdellier et al. [10].

## 3. TEM results

### 3.1. Bright-field observations

In order to determine the shape of the samples, conventional bright-field observations were performed for both specimens (see Fig. 1). In sample A, cleavage occurs along ⟨1 1 0⟩ directions in thinner areas of the sample. The resulting isolated lamellas are significantly bent, as indicated by the occurrence of numerous bend contours. Scanning electron microscopy observations also confirmed the strong bending of cleaved lamellas. On the contrary, sample B is made of a flat wedge without cleavage and in that case, thickness fringes without bend contours are observed close to the edge of the sample. CBED thickness measurements in various places of the samples (from the edge to thick areas) enable the estimation of the edge angle $\alpha$ for both samples: for sample A, $\alpha < 5^\circ$, whereas for sample B, $\alpha \sim 20^\circ$.

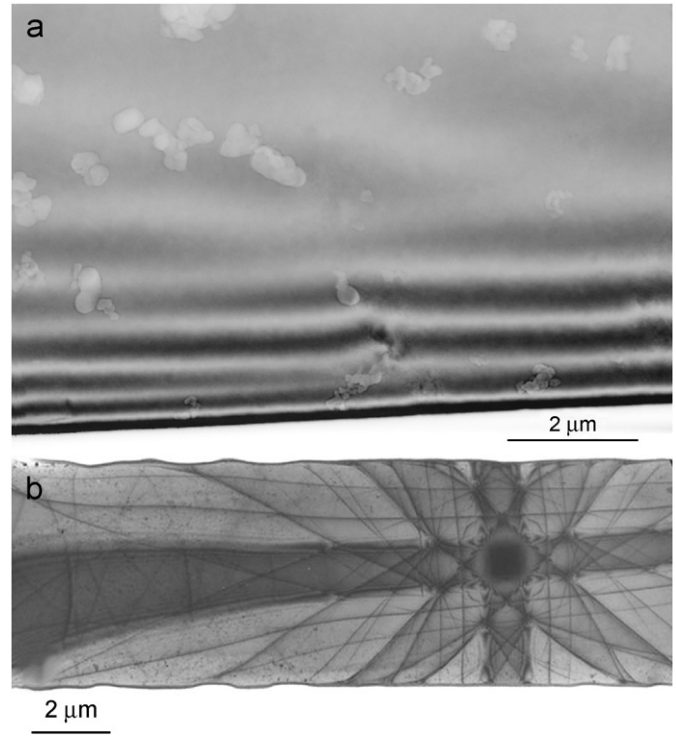


Fig. 1. (a) Bright field (BF) image of the mechanically thinned sample. (b) BF image of the chemically thinned sample (cleaved lamella).

### 3.2. CBED observations

Fig. 2(a) shows the [1 0 2] zone axis LACBED pattern (inclined to 26° from the [0 0 1] initial orientation) observed on the chemically thinned sample (sample A). The pattern is obtained in the middle of a cleaved lamella for a thickness $t \sim 300$ nm. As can be noticed on this pattern, most of the deficiency kinematical Bragg lines are strongly perturbed and are split into multiple parallel fringes. An example of intensity profile is shown for the perturbed $(\bar{8}\,0\,4)$ Bragg line in Fig. 3(a), showing a doublet intensity instead of a single sharp line. The perturbation of kinematical lines is also very sensitive to the orientation of the sample. Fig. 2(c) is a LACBED pattern taken on sample A oriented close to the [1 0 5] zone axis (inclined to 11° from [0 0 1]). Perturbation of the kinematical Bragg lines is weaker than for the previous orientation of the sample. Finally, we also record very

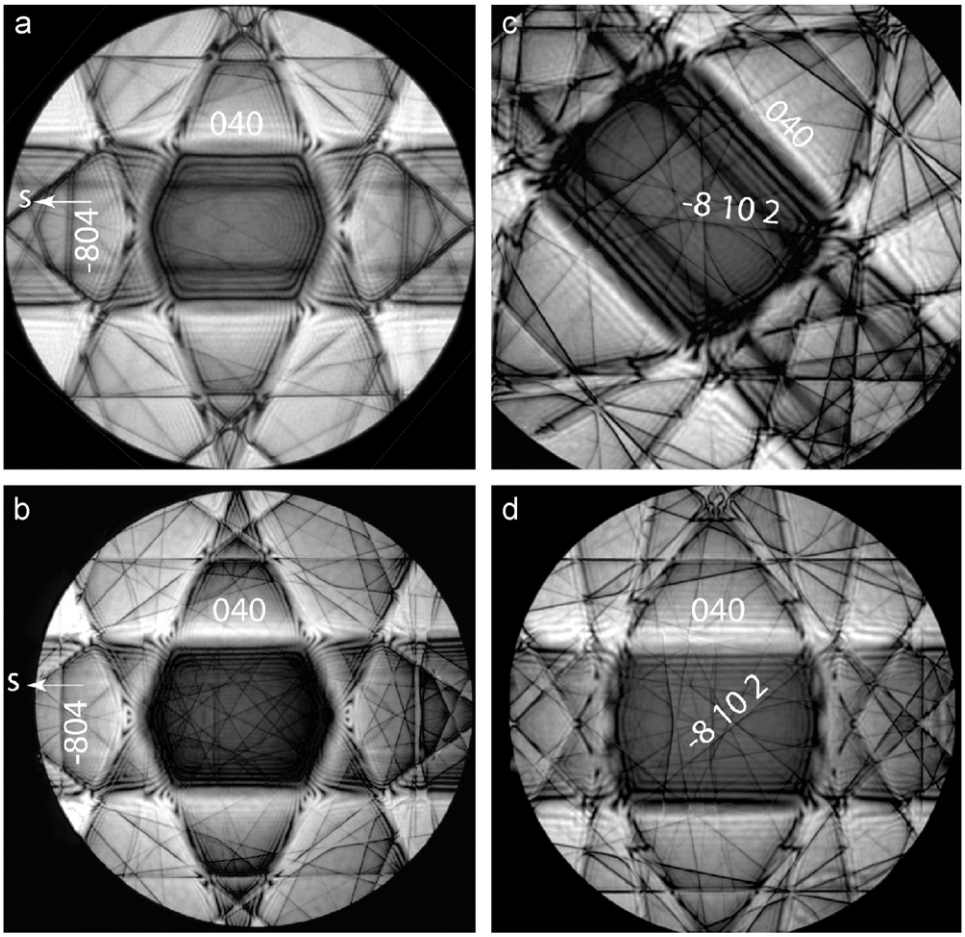


Fig. 2. [1 0 2] and [1 0 5] zone axis LACBED patterns taken on sample A (respectively, a and c) and B (respectively, b and d). The arrows indicate the sense of the increasing deviation parameters.

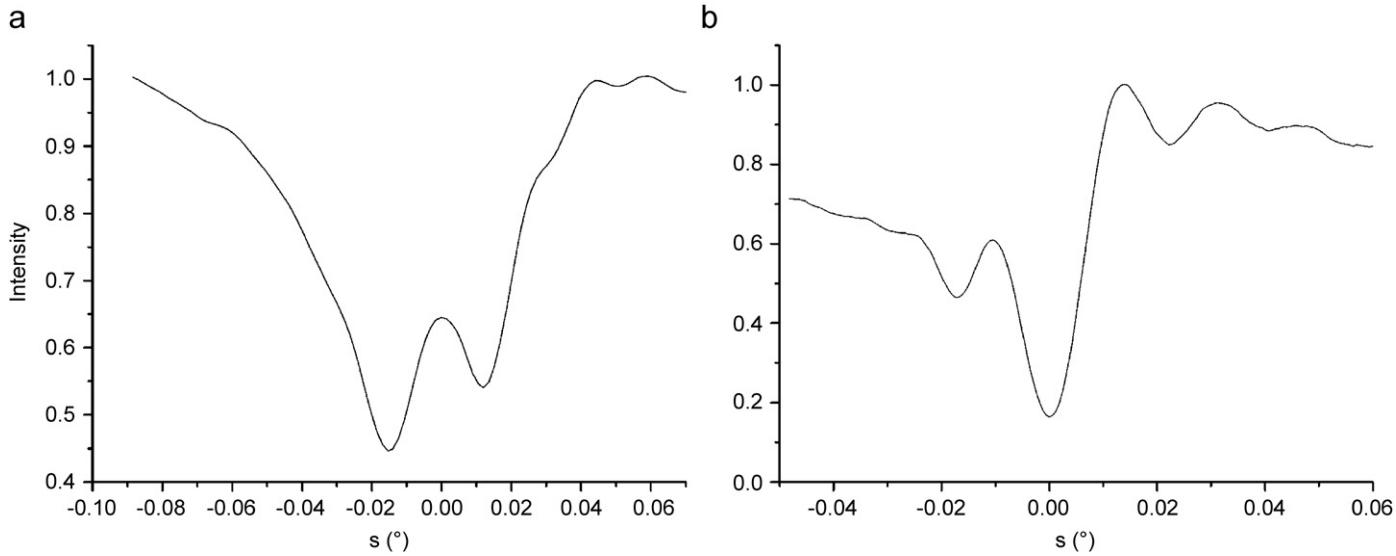


Fig. 3. Bragg ($\bar{8}$ 0 4) line intensity profiles taken along the arrows drawn in Figs. 2(a) and (b). (a): sample A, (b): sample B.

perturbed profiles for dynamical Bragg lines, appearing much broader that for a perfect crystal.

Figs. 2(b) and (d) present [1 0 2] and [1 0 5] zone axis LACBED patterns observed on the mechanically thinned sample (sample B, thickness $t \sim 300$ nm), respectively. Contrary to sample A, kinematical Bragg lines are unperturbed, exhibiting a single minimum intensity for $s = 0$ (see for instance profile of the ($\bar{8}$ 0 4) line in Fig. 3(b).

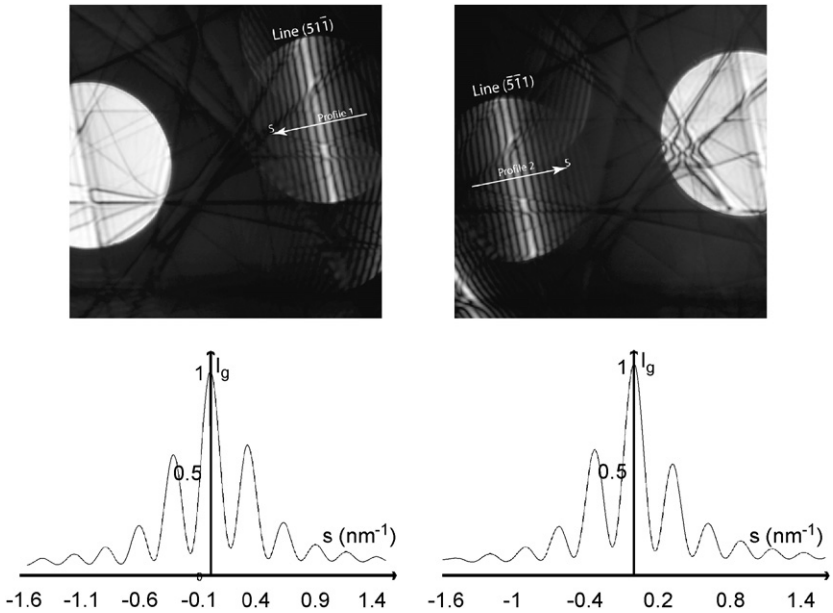


Fig. 4. CBED patterns taken close to the [1 0 5] orientation of the sample showing the (5 1 $\bar{1}$) and ($\bar{5}$ $\bar{1}$ 1) dynamical excess Bragg lines in sample B. Intensity profiles of the Bragg lines along the arrows are also given.

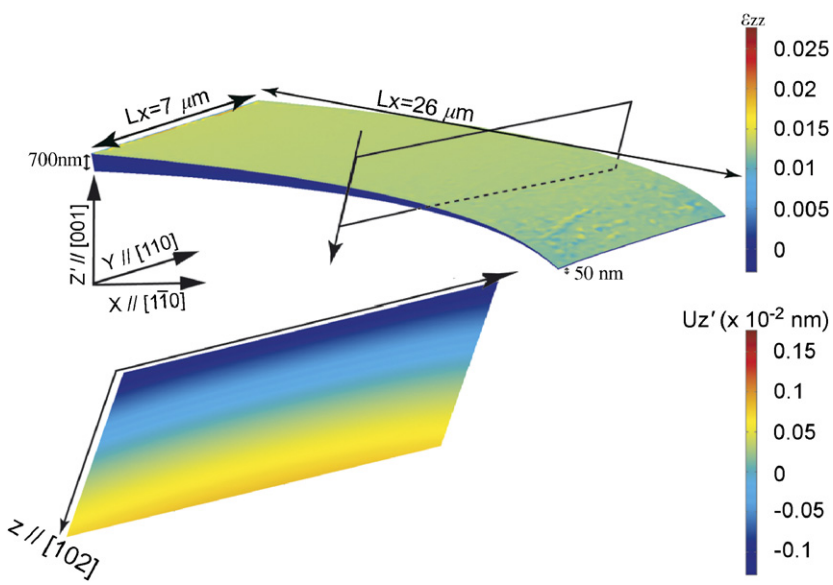


Fig. 5. FEM strain and displacement results obtained on the cleaved lamella model. The 2D map is given for the displacement field along the [1 0 2] zone axis direction.

We also note that contrary to the previous case (sample A) dynamical lines are just slightly asymmetric with respect to the excitation value $s = 0$. The sense of this asymmetry with respect to increasing $s$ values changes with that of the $g$ vector, as reported in Fig. 4 for the ($\bar{5}$ $\bar{1}$ 1) and (5 1 $\bar{1}$) Bragg lines taken from the [1 0 5] sample orientation.

## 4. Structural models and strain calculations

In order to qualitatively interpret our TEM results, we performed strain calculations using FEM for various thin foil shapes deduced from bright-field images. Two 3D models are used (Figs. 5 and 6): the first one—corresponding to the chemically thinned sample (sample A)—consists of an isolated wedge-shaped lamella with an edge angle of $\alpha = 2.5^\circ$ and lateral dimensions ($L_x$, $L_y$) equal to 26 and 7 μm, respectively. In order to simulate the connection of the cleaved lamella to the rest of the sample in thick areas, boundary conditions prevent the displacement of the face perpendicular to $X$ for $t = 700$ nm. The others faces are free to move. The second model—corresponding to the mechanically thinned sample (sample B)—consists of an infinite wedge in the $Y$ direction with an edge angle of $\alpha = 20^\circ$. Boundary conditions are the same as before except

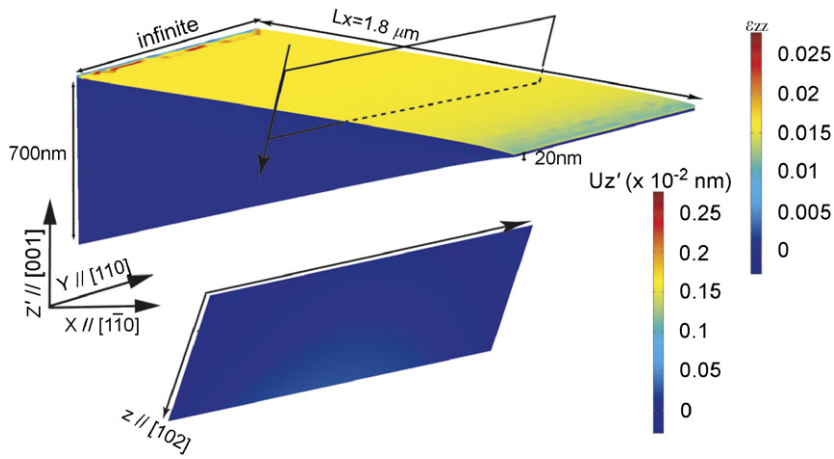


Fig. 6. FEM strain and displacement results obtained on the mechanically thinned model. The 2D map is given for the displacement field along the [1 0 2] zone axis direction.

for faces perpendicular to $Y$ for which displacements are blocked in order to simulate an infinite sample. In the $X$ direction $L_x = 1.8\,\mu$m. Strain and displacements resulting from the two models are shown in Figs. 5 and 6. For the cleaved lamella (sample A), strong bending of the sample associated with stress relaxation is clearly seen (Fig. 5). The resulting heterogeneous displacement field in a plane parallel to the [1 0 2] axis is also shown in this figure, for sample thickness $t\sim300$ nm. For the model corresponding to sample B (Fig. 6), the resulting bending is negligible and the displacement field along the [1 0 2] direction is mainly homogeneous, except at the surface of the sample corresponding to the strained layer. These results are in clear agreement with experimental observations relative to the bending of the two samples. Calculations made for various shapes of the models ($L_x$, $L_Y$, and $\alpha$) show that the edge angle $\alpha$ is the major parameter influencing relaxation phenomena, indicating that the strong bending differences for the two studied models are mostly due to the significant difference in $\alpha$ for the two models.

## 5. Dynamical simulations of the CBED patterns

Fig. 7(a) shows the simulated [1 0 2] zone axis LACBED pattern obtained for the model of the cleaved lamella using the displacement fields displayed in Fig. 5. As can be observed, the simulated CBED pattern correctly reproduces the main features of the experimental patterns for sample A, i.e. the strong perturbation of most of the kinematical lines. The simulated intensity profile of the ($\bar{8}$ 0 4) line (Fig. 7(b)) confirms the good agreement between theory and experiment. This clearly indicates that the heterogeneous strain field along the electron beam direction from the bending of the sample is responsible for the modification of kinematical Bragg line observed experimentally. Fig. 7(c) is the simulated [1 0 2] pattern obtained using the displacement fields calculated for the mechanically thinned sample. No perturbation of the kinematical Bragg lines occurs (see Fig. 7(d)) and the pattern is quite similar to that of a perfect crystal. Nevertheless, dynamical Bragg lines show asymmetric intensity profiles, as reported in Fig. 8 for $g = (\bar{5}\ \bar{1}\ 1)$ and $g = (5\,1\ \bar{1})$. The inversion of the asymmetry with respect to increasing $s$ values for both vectors should be noted. These features are in good agreement with those observed experimentally on sample B (Fig. 4), corresponding to the mechanically thinned sample.

## 6. Discussion

The good agreement between simulated and experimental CBED patterns allows us to reach the following conclusions. Strain heterogeneities in the sample from elastic stress relaxation induce strong modifications of kinematical and dynamical Bragg lines intensities. In plan-view samples of strained epitaxial layers, these heterogeneities are more or less pronounced, depending on the thinning process used for sample preparation: chemical thinning induces the formation of strongly bent cleaved lamellas, resulting in a strongly heterogeneous strain field, whereas mechanical thinning prevents this relaxation and the substrate is nearly unstrained. In the former case, CBED patterns are strongly perturbed for kinematical as well as for dynamical Bragg lines, whereas in the latter case, kinematical lines are unaffected and dynamical lines exhibit asymmetric intensities. It should be noted that the kinematical Bragg line perturbations observed in the case of the bent samples are similar to that observed in strained areas of cross-sectional samples of epitaxial layers [10].

An important question remains: can the initial strain state of the bulk sample—directly related to the composition of the $Ga_{1-x}In_xAs$ epilayer in the present case—be deduced from the quantitative comparison between experimental and simulated intensities? An approach is to use the asymmetry of dynamical rocking curves obtained in the case of fully mechanically thinned samples to determine the actual composition of the layer. In Fig. 9 are presented simulated ($\bar{5}\ \bar{1}\ 1$) Bragg lines obtained with the mechani-

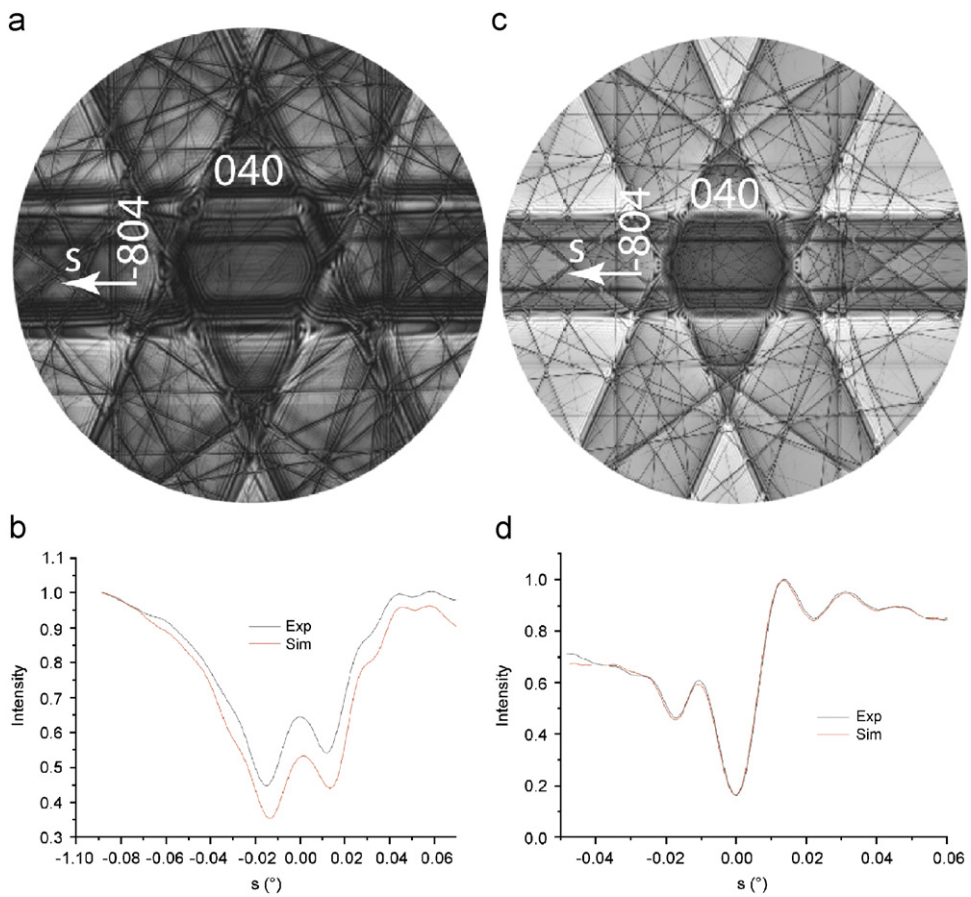


Fig. 7. (a) and (c) Multibeam dynamical simulations of [1 0 2] zone axis LACBED patterns obtained using the displacement fields displayed in Figs. 5 and 6, respectively. In (b) and (d), the simulated intensity profiles of the ($\bar{8}$ 0 4) lines are displayed and compared with the experimental profiles of Fig. 3.

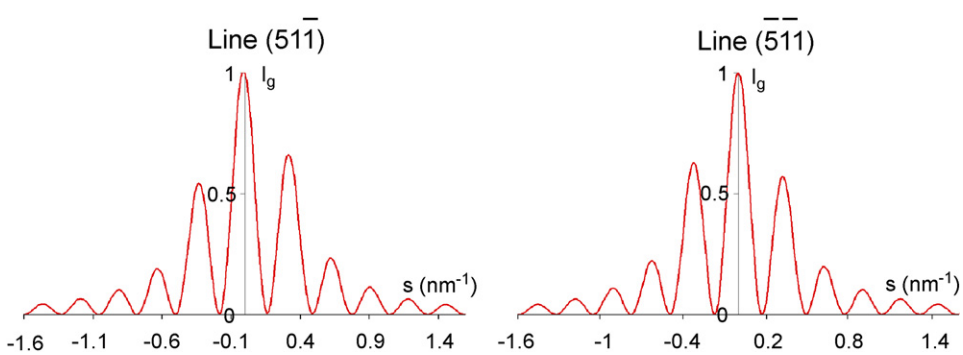


Fig. 8. Simulated dynamical (5 1 $\bar{1}$) and ($\bar{5}$ $\bar{1}$ 1) Bragg lines obtained using displacement fields displayed in Fig. 6.

cally thinned model for various $x$ values of the indium content of the layer. As can be concluded from this figure, the sensitivity of the rocking curve asymmetry to the composition of the layer is very poor. Furthermore, calculations show that introducing small variations of the edge angle $\alpha$ in the FEM models induces effects on the rocking curves that are of the same magnitude as those associated with compositional variations. Thus, quantitative analysis of the asymmetric dynamical Bragg lines is only possible if the shape of the sample is known accurately, which is not the case for tripod prepared samples. A second approach is to use the perturbation of the kinematical rocking curves occurring in bent samples, such as those obtained by chemical thinning. Simulations performed for various sample shapes and strain values revealed that the intensity of these high-index Bragg lines are very sensitive to the actual strain state along the electron propagation direction, and thus to the actual shape of the sample, including local thickness and orientation. However, complete agreement between experimental and simulated CBED patterns in their entirety, like those reported in Figs. 2(a) and 7(a), was not possible in

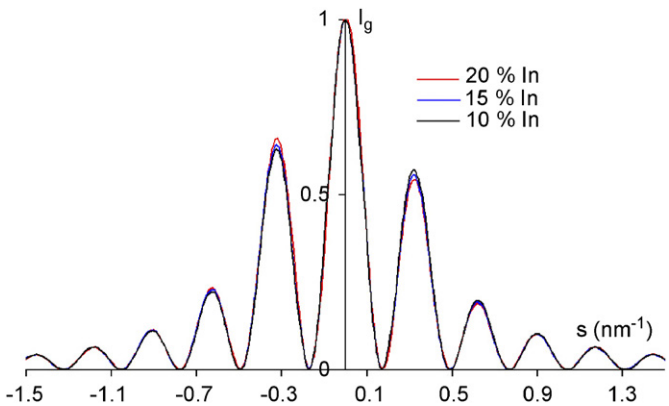


Fig. 9. Simulated dynamical ($\bar{5}\,\bar{1}\,1$) Bragg lines obtained with the model of Fig. 6 and various $x$ indium content of the layer.

this case due to the lack of information about the exact shape of the sample. Only a few lines are properly reproduced (Fig. 7(b)). In conclusion, if the diffracted intensities recorded in CBED patterns are to be used for the strain determination of plan-view samples, a more controlled preparation technique is required. Focus Ion Beam preparation (FIB) is a promising technique for this purpose and further developments in this direction are now in progress.

## 7. Conclusion

In this paper, we demonstrate the effect of elastic stress relaxation on Bragg lines intensities observed in convergent beam electron diffraction (CBED) patterns in the case of plan-view samples of strained epitaxial layers. Finite element modelling of the samples are coupled with dynamical calculations of CBED patterns, performed by a time-dependent perturbation approach, to interpret experimental data. We demonstrate the major influence of the sample preparation technique on relaxation phenomena resulting from bending of the structure. When sample bending occurs, as in chemically thinned samples, strongly inhomogeneous displacement fields along the electron propagation direction induce significant modifications of the diffracted intensities. When bending is reduced, only dynamical intensities are affected by the strain in the sample, which then appear asymmetric. This is the case for tripod prepared samples. As far as the quantitative analysis of the intensities are concerned, in order to determine the actual strain state of the sample, our results show that due to the very high sensitivity of diffraction to experimental parameters such as the actual shape of the sample, local thickness and orientation, a very precise knowledge of the sample configuration is required. Thus, the use of more sophisticated sample preparation techniques, such as focus ion beam milling, is planned as a perspective to the present study.

## Acknowledgements

The CNRS funded network GdR Relax is gratefully acknowledged for financial support. The authors gratefully thank M.J. Hÿtch for rereading the manuscript.

## References

[1] F.D. Auret, C.A.B. Ball, H.C. Snyman, Thin Solid Films 61 (1979) 289.
[2] M.M.J. Treacy, J.M. Gibson, J. Vac. Sci. Technol. B 4 (1986) 1458.
[3] D.D. Perovic, G.C. Weatherly, D.C. Houghton, Phil. Mag. A 64 (1991) 1.
[4] C.T. Chou, S.C. Anderson, D.J.H. Cockayne, A.Z. Sizorski, M.R. Vaughan, Ultramicroscopy 55 (1994) 334.
[5] X.F. Duan, D. Cherns, J.W. Steeds, Phil. Mag. A 70 (1994) 1091.
[6] X.F. Duan, Appl. Phys. Lett. 66 (1995) 2247.
[7] D. Jacob, Y. Androussi, T. Benabbas, P. Francois, A. Lefebvre, Phil. Mag. A 78 (1998) 879.
[8] L. Clément, R. Pantel, L.K. Wakman, J.L. Rouvière, Appl. Phys. Lett. 85(4) (2004) 651.
[9] A. Chuvilin, U. Kaiser, Q. de Robillard, H.J. Engelmann, J. Electron Microsc. 54 (2005) 515.
[10] F. Houdellier, C. Roucau, L. Clément, J.L. Rouvière, M.J. Casanove, Ultramicroscopy 106 (2006) 951.
[11] D. Cherns, R. Touaitia, A.R. Preston, C.J. Rossouw, D.C. Houghton, Phil. Mag. A 64 (1991) 597.
[12] A. Hovsepian, D. Cherns, W. Jaeger, Phil. Mag. A 79 (1999) 1395.
[13] D. Jacob, Y. Androussi, A. Lefebvre, Ultramicroscopy 89 (2001) 299.
[14] D. Jacob, J.M. Zuo, A. Lefebvre, Y. Cordier, Ultramicroscopy, submitted.
[15] D. Jacob, A. Lefebvre, Ultramicroscopy 96 (2003) 1.
[16] S. Christiansen, M. Albrecht, H. Strunk, Appl. Phys. Lett. 64 (1994) 3614.
[17] M. Choy, W. Cook, R. Hearnon, H. Jaffe, J. Jerphagnon, S.K. Kurtz, S.T. Liu, D.F. Nelson, Elastic, Piezoelectric and Related Constants of Crystals III/11, Springer, Berlin, 1979.
[18] D. Gratias, R. Portier, Acta Crystallogr. A 39 (1983) 576.

# Maclage et abaissements de symétrie, études par précession électronique.

Eur. J. Mineral.
Fast Track DOI: 10.1127/0935-1221/2008/0020-1786

Fast Track Article

# Large-angle convergent-beam electron diffraction (LACBED) characterization of (021) twinning in natural coesite

Damien JACOB[1,*], Patrick CORDIER[1], Jean-Paul MORNIROLI[2] and Hans-Peter SCHERTL[3]

[1] Laboratoire de Structure et Propriétés de l'Etat Solide - UMR CNRS 8008, Université des Sciences et Technologies de Lille – Bât. C6, 59655 Villeneuve d'Ascq Cedex, France
*Corresponding author, e-mail: damien.jacob@univ-lille1.fr
[2] Laboratoire de Métallurgie Physique et Génie des Matériaux, UMR CNRS 8517, Ecole Nationale Supérieure de Chimie de Lille, Université des Sciences et Technologies de Lille – Bât. C6, 59655 Villeneuve d'Ascq Cedex, France
[3] Institut für Geologie, Mineralogie und Geophysik, Ruhr-Universität Bochum, 44780 Bochum, Germany

**Abstract:** Large-angle convergent-beam electron diffraction (LACBED) is used to characterize a (021) twinning in metamorphic coesite from Parigi, Dora-Maira Massif, Western Alps. The orientation relationships between the adjacent parts of the twin are characterized in detail and the twin is described as a mirror along (021). This microscopic description is fully consistent with original descriptions of twinning in synthetic coesite. Due to the quasi-hexagonal dimensions of coesite (belonging to the monoclinic space group $C12/c1$ with $a \sim c$ and $\beta \sim 120°$) such a result could not have been obtained using conventional electron diffraction experiments.

**Key-words:** coesite, twin, TEM, LACBED.

## 1. Introduction

Coesite is a high-pressure polymorph of silica stable in the pressure range 2.5–9 GPa, which corresponds to a minimum depth in Earth of *ca.* 90 km. It has been synthesized for the first time by Loring Coes (1953). The first occurrence of natural coesite was reported in Meteor Crater, Arizona (Chao *et al.*, 1960), giving strong evidence for shock metamorphism by a meteorite impact. Since then, coesite has been identified in several impact craters as well as in large scale TNT and nuclear explosion craters (see references in Stöffler & Langenhorst, 1994). Coesite has also been found later in xenoliths from kimberlites (Smyth & Hatton, 1977) and in garnets of a pyrope-quartzite from the Dora-Maira massif (Chopin, 1984).

Twinning in coesite has already been studied by several authors. Ramsdell (1955) has described (100) and (021) twinning in synthetic coesite, as derived from X-ray investigations. Optical studies in synthetic samples revealed (021) twinning (Sclar *et al.*, 1962) but also $(\bar{1}21)$ and $(\bar{2}33)$ twinning (Naka *et al.*, 1975). More recently, (021) and $(\bar{1}01)$ twinning were detected by universal stage measurements in natural coesite from Dora-Maira (Schertl *et al.*, 2005). Finally, (100) microtwinning has been characterized by Bourret *et al.* (1986) using high resolution electron microscopy. Nevertheless, detailed description of (021) twinning is still missing. Thus, the goal of this study is to give an extensive characterization based on transmission electron microscopy (TEM). Twinning of coesite is an important petrographical feature which might help to identify coesite in UHP-metamorphic rocks and thus to discover possible new UHP-metamorphic terranes.

Coesite exhibits a monoclinic symmetry with space group $C12/c1$. Cell parameters are $a = 0.71356$, $b = 1.23692$ and $c = 0.71736$ nm, $\beta = 120.34°$ (Levien & Prewitt, 1981). While monoclinic in symmetry, the crystal is pseudo-hexagonal. For this reason, conventional selected-area electron diffraction (SAED) can easily lead to misindexing. We propose here to apply the large-angle convergent-beam electron diffraction (LACBED), which has already proved to be a very efficient method in the characterization of crystals defects, including twins (Tanaka *et al.*, 1994; Cordier *et al.*, 1995; Morniroli, 2004).

## 2. Experimental procedures

The twinned coesite investigated in this study comes from a fine-grained pyrope quartzite rock collected at Parigi, Dora-Maira Massif, Western Alps – the "classical" locality where Chopin (1984) discovered for the first time coesite within a metamorphic rock. Coesite grains were selected based on optical examination of 30 μm thick sections of the sample. Specimens were then drilled out and glued to a 3 mm-diameter copper TEM grid and ion-milled to electron transparency at 5 kV with an incident beam angle of 15°. Finally, the samples were coated with a thin carbon layer to promote electron conduction.

DOI: 10.1127/0935-1221/2008/0020-1786

0935-1221/08/0020-1786 $ 2.70
© 2008 E. Schweizerbart'sche Verlagsbuchhandlung, D-70176 Stuttgart

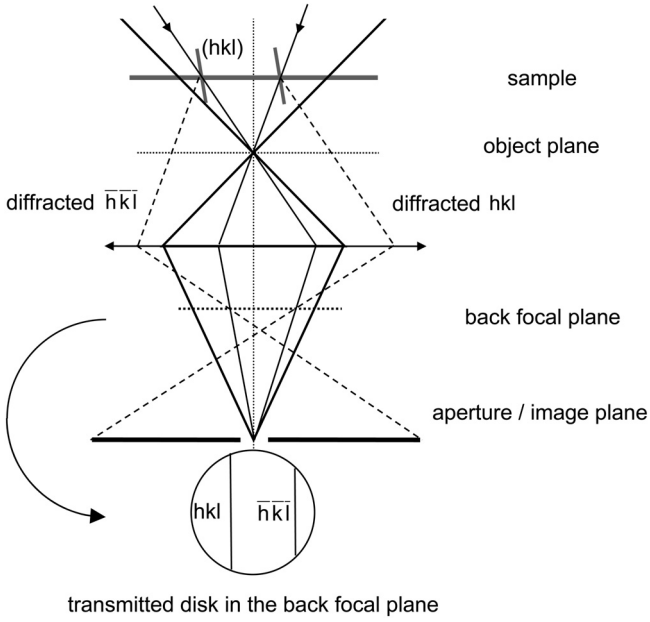


Fig. 1. Description of the LACBED configuration.

TEM observations were carried out on a Philips CM30 microscope operated at 300 kV. Images and conventional SAED patterns were acquired using the microprobe mode. For LACBED patterns acquisition, the nanoprobe mode was used with a probe size of about 20 nm and a beam convergence semi-angle of about 3°. In the LACBED configuration, the specimen is not located in the object plane, i.e. at the focussed beam crossover, as in the conventional CBED mode and a selected-area aperture (10 $\mu$m in diameter) is introduced in the image plane to select either the transmitted beam or a diffracted beam (see Fig. 1). For the present study, this technique has the following advantages: (1) the convergence angle is not limited by the need to avoid overlapping of diffracted beams, which allows the observation of a high number of Bragg lines in the large transmitted disk; (2) the quality of the patterns is very good thanks to the aperture that acts as a natural momentum filter removing almost all diffuse scattering; (3) a shadow image of the extended illuminated region is superimposed to the diffraction pattern; and (4) the method is low dose, which is very convenient for the study of material sensitive to electron irradiation damage such as coesite.

## 3. TEM observations

Figure 2 shows an optical micrograph of the coesite grain investigated in this study. It forms an inclusion within pyrope and is surrounded by a rim of retrograde palisade-textured quartz. Twinning is clearly visible in the coesite grain. A TEM foil has been extracted from the twinned area, at the location shown by an arrow on the micrograph. Figure 3a is a TEM bright-field image of this twin. The right- and left-hand sides of the twin are labelled A and B respectively. Figure 3b shows the SAED pattern taken on the twin in this orientation, with the aperture including

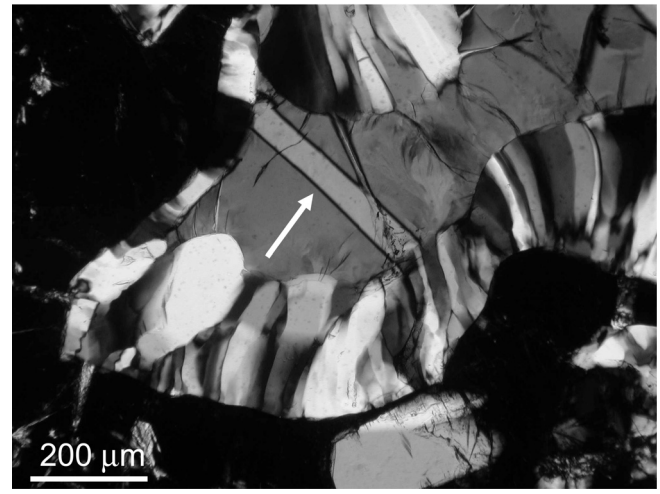


Fig. 2. Optical micrograph of a coesite grain surrounded by a rim of retrograded quartz. The arrow locates the area where the TEM foil has been extracted.

A and B areas. No multiple or split spots are observed on the pattern, indicating that all the twin reflections from A and B areas nearly coincide. Due to the pseudo-hexagonal symmetry of coesite the indexation of this SAED pattern is very ambiguous. As a matter of fact, indexation of this pattern based on the lengths and angles between reflections gives rise to four possible zone axes: $[\bar{2}1\bar{2}]$, [212], $[0\bar{1}2]$ and [012]. To remove this ambiguity, LACBED experiments were performed (Fig. 4). Indeed, LACBED patterns contain a very large number of Bragg lines and have been unambiguously indexed using kinematical simulations calculated with the software "Electron Diffraction" from J.P. Morniroli. Results gave the following orientations for A and B:

$$[\bar{2}1\bar{2}]_A \,//\, [\bar{2}\bar{1}\bar{2}]_B. \quad (1)$$

For this specific orientation, the twin plane is parallel to the optical axis of the microscope so that it can be directly identified from trace analysis (Morniroli & Gaillot, 2000). Since this trace is parallel to the $021_A$ and $02\bar{1}_B$ Bragg lines, the twin plane is:

$$(021)_A \,//\, (02\bar{1})_B. \quad (2)$$

We also note a mirror symmetry appearing on the LACBED pattern along the twin plane (Fig. 4b). This mirror is not present on either the A or B variants (Fig. 4a and c).

For the full characterization of the twin, the three following sets of quasi-parallel directions in A and B were obtained by tilting the specimen along two specific diffraction lines ($002_A$ and $220_A$; $020_B$ and $22\bar{2}_B$), as shown in Fig. 5a and b:

$$[010]_A \,//\, [\bar{1}0\bar{2}]_B, \quad (3)$$

$$[\bar{1}10]_A \,//\, [\bar{1}0\bar{1}]_B, \quad (4)$$

$$[\bar{1}1\bar{1}]_A \,//\, [\bar{3}\bar{1}\bar{4}]_B. \quad (5)$$

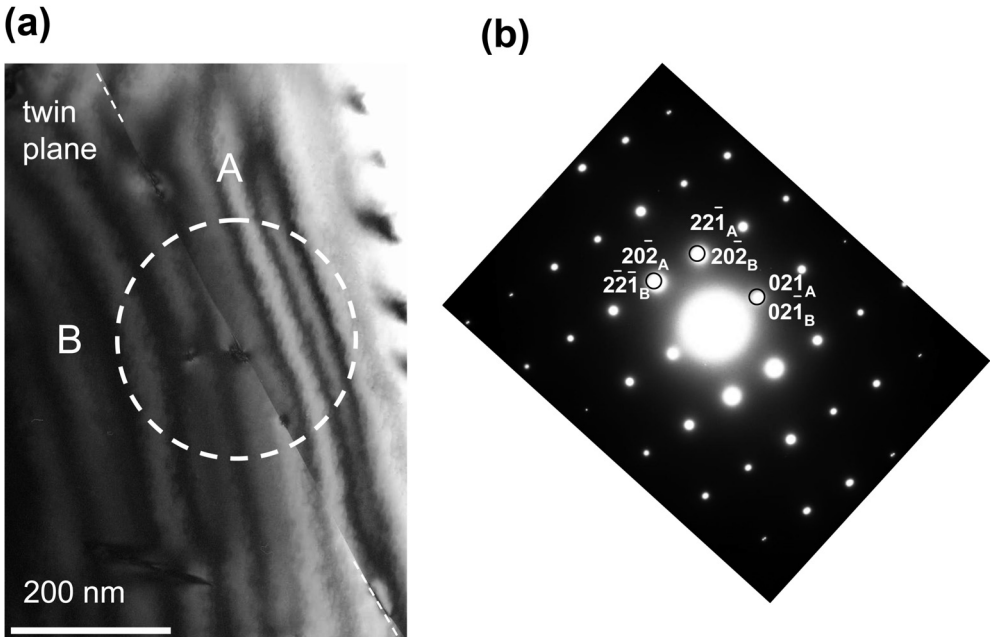


Fig. 3. (a) TEM bright-field of the twin parallel to the electron beam and (b), the associated zone axis SAED pattern. The dashed circle corresponds to the aperture position, including A and B areas. A and B are oriented along the $[\bar{2}1\bar{2}]_A$ and $[\bar{2}\bar{1}\bar{2}]_B$ zone axes respectively. No multiple spots are observed on the pattern. Indexation is based on the LACBED patterns reproduced in Fig. 4.

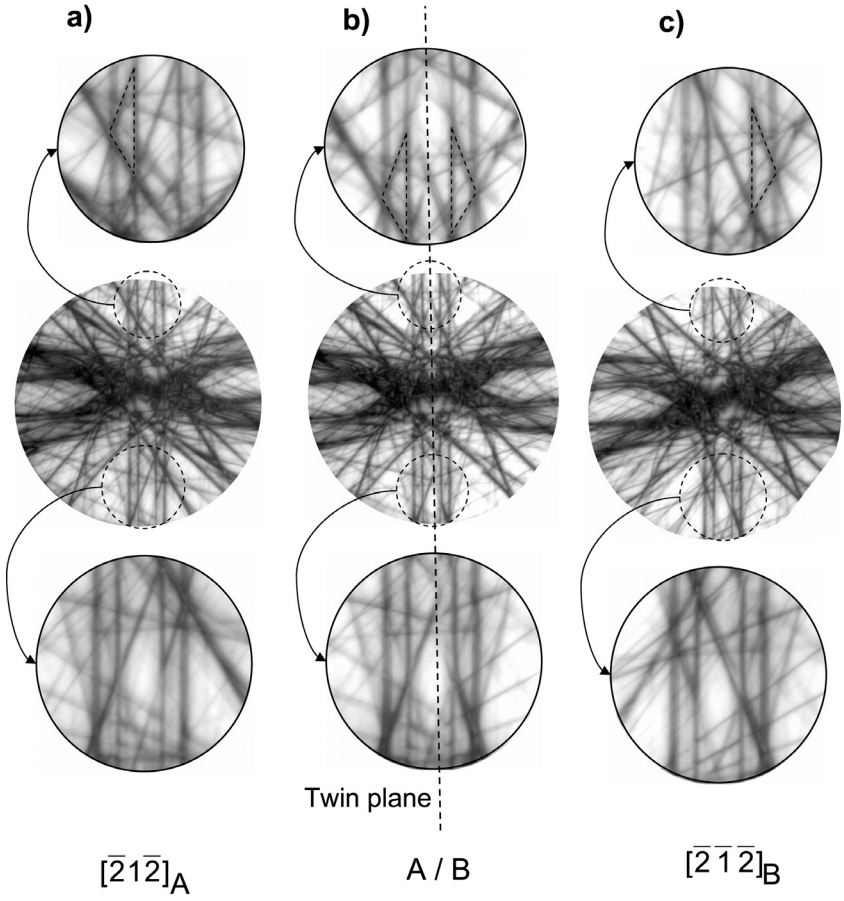


Fig. 4. LACBED patterns taken in the same orientation as in Fig. 3 on the variant A (a), on the twin area (b) and on the variant B (c). In (b), the trace of the twin plane is visible and parallel to $(021)_A$ and $(02\bar{1})_B$ Bragg lines. The mirror symmetry induced by the twin is clearly seen in the enlarged areas of the patterns in (b) and not present in patterns from either the A or B variants.

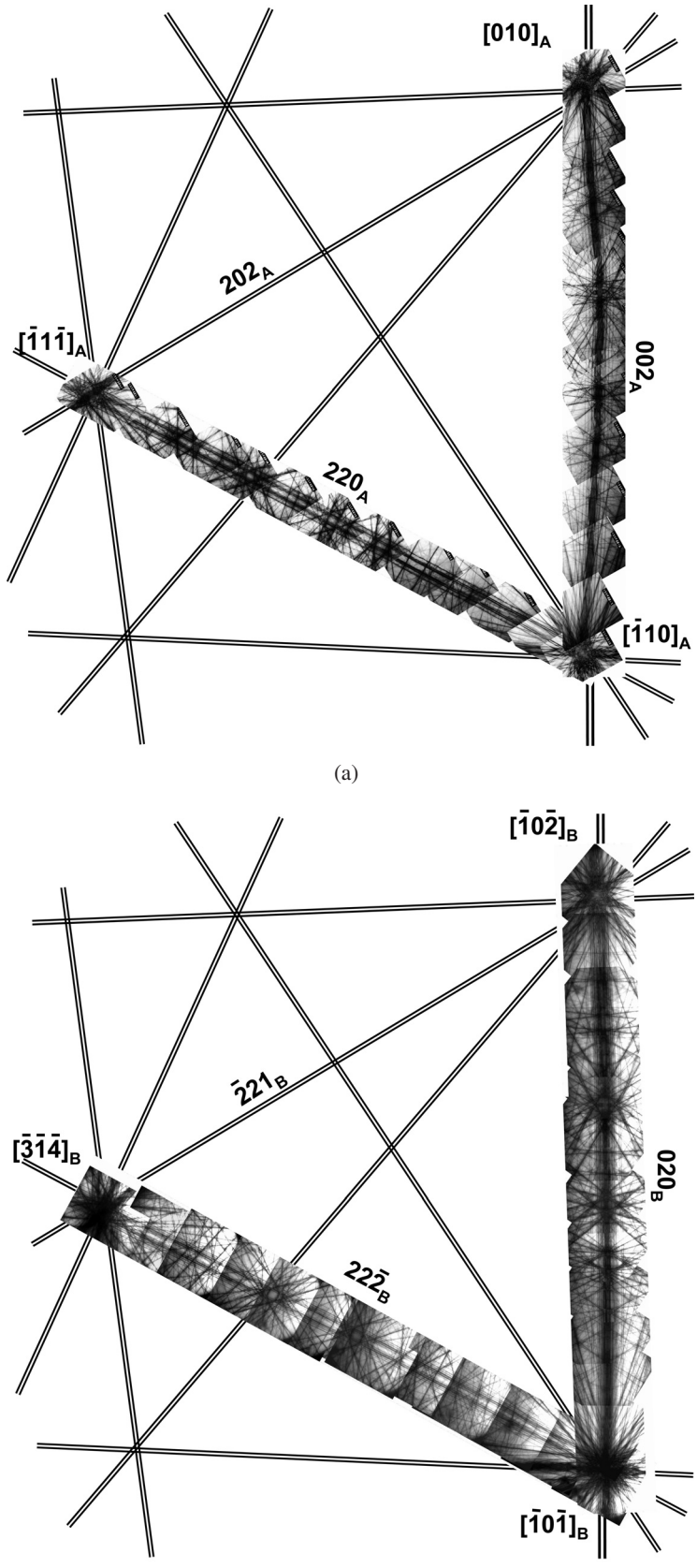


Fig. 5. LACBED characterization of the absolute orientation of the variants A (a) and B (b) based on the indexation of three non coplanar zone axes.

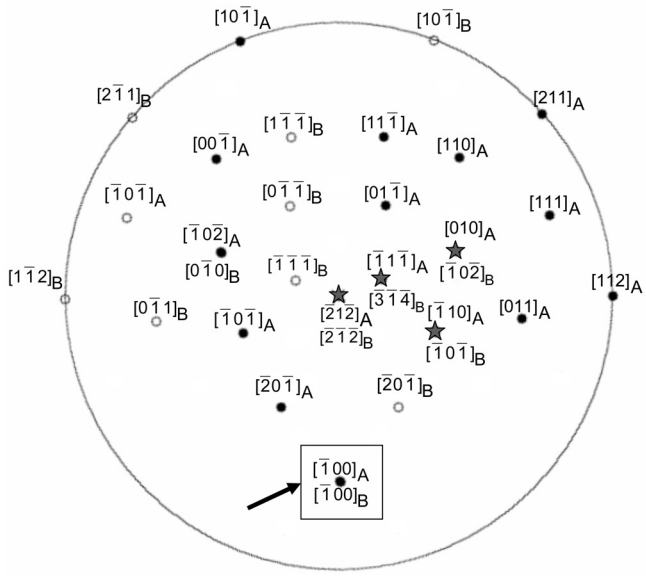


Fig. 6. Superimposed stereographic projections in the $[\bar{2}1\bar{2}]_A$ and $[\bar{2}\bar{1}\bar{2}]_B$ orientations.

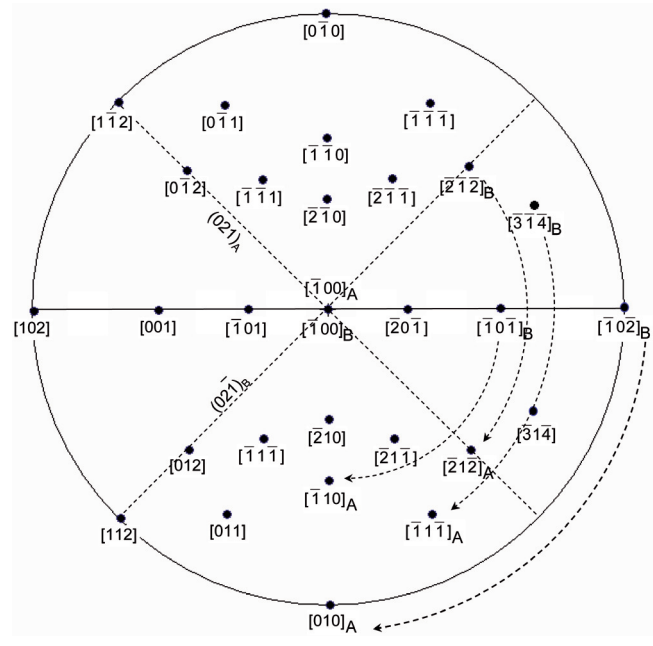


Fig. 7. $[\bar{1}00]$ stereographic projection showing the rotation between A and B. Traces of the $(021)_A$ and $(02\bar{1})_B$ are also drawn on the stereogram.

Note that for the area A, the [010] zone axis corresponds to the twofold rotation axis of the $C12/c1$ space group and it is thus unambiguously determined, and then are the $[\bar{1}10]_A$ and $[\bar{1}1\bar{1}]_A$ orientations.

## 4. Twin law determination

Stereographic projections are used to characterize the twin law. The superimposed stereographic projections of direction poles along the $[\bar{2}1\bar{2}]_A$ and $[\bar{2}\bar{1}\bar{2}]_B$ axes (relation 1) are reproduced in Fig. 6. The projections have been rotated along the common central pole so as to put into quasi-coincidence the directions described by relations 3, 4 and 5. Note that the poles superposition is not perfect, since the angles between respectively $[\bar{2}1\bar{2}]$ and the three directions in variant A, and $[\bar{2}\bar{1}\bar{2}]$ and the three directions in variant B, are not exactly the same. Nevertheless, the stereogram shows that $[\bar{1}00]$ is common to both variants and is thus an invariant for the twinning. On the projection draw along this axis (Fig. 7), the rotation bringing $[\bar{1}0\bar{2}]_B$ on $[010]_A$(relation 3), $[\bar{1}0\bar{1}]_B$ on $[\bar{1}10]_A$(relation 4) and $[\bar{3}\bar{1}\bar{4}]_B$ on $[\bar{1}1\bar{1}]_A$ (relation 5) – also brings the contact planes $(02\bar{1})_B$ on $(021)_A$ in coincidence, such creating a mirror for twinning. The exact value of the rotation angle is then that of the angle between the $(02\bar{1})$ and (021) planes in the perfect crystal, which is equal to 89.94°.

In Fig. 8a and 8b are drawn the projections of the direct lattices of the structure seen along the $[\bar{1}00]$ direction for the A and B variants. The lattice B has been rotated of −89.94° with respect to the lattice A in order to align the $(021)_A$ and $(02\bar{1})_B$ planes. The lattice nodes are disposed on a pseudo bi-dimensional square lattice (the misfit between the square edges is only 0.11%). The diagonal planes (021) and $(02\bar{1})$, which are at 45.03° with respect to $b$ and at 44.97° with respect to $c{\cdot}\cos(\beta - \pi/2)$, are nearly some mirror planes for the lattice. Figure 8c is a schematic description of the twin arrangement, where the (021) and $(02\bar{1})$ planes have been put into coincidence. An exact mirror is then created between A and B lattice nodes. Due to the slight departure from hexagonal symmetry, nodes from A and B do not belong any more to a common lattice and the twin is pseudo-merohedral.

## 5. Conclusion

In the present study, the TEM-LACBED method has been successfully used for the accurate characterization of the twin law of a natural coesite sample from metamorphic origin. The twin law is found to be (021). Using conventional electron diffraction techniques, no extra or split spots are observed on the patterns, since the twin reflections are nearly superimposed. Furthermore, due to the hexagonal pseudo-symmetry of coesite, indexation of conventional electron diffraction patterns is often ambiguous, so that the twin law cannot be directly obtained. This drawback is clearly avoided using LACBED. In the configuration introduced here, a large number of hkl Bragg lines can be observed which enables the determination of absolute orientations. The twin is thus described as a mirror along (021). This description is fully consistent with the observations by Ramsdell (1955) and Sclar *et al.* (1962) based respectively on X-ray and optical observations of crystal surfaces, which however were obtained on synthetic material.

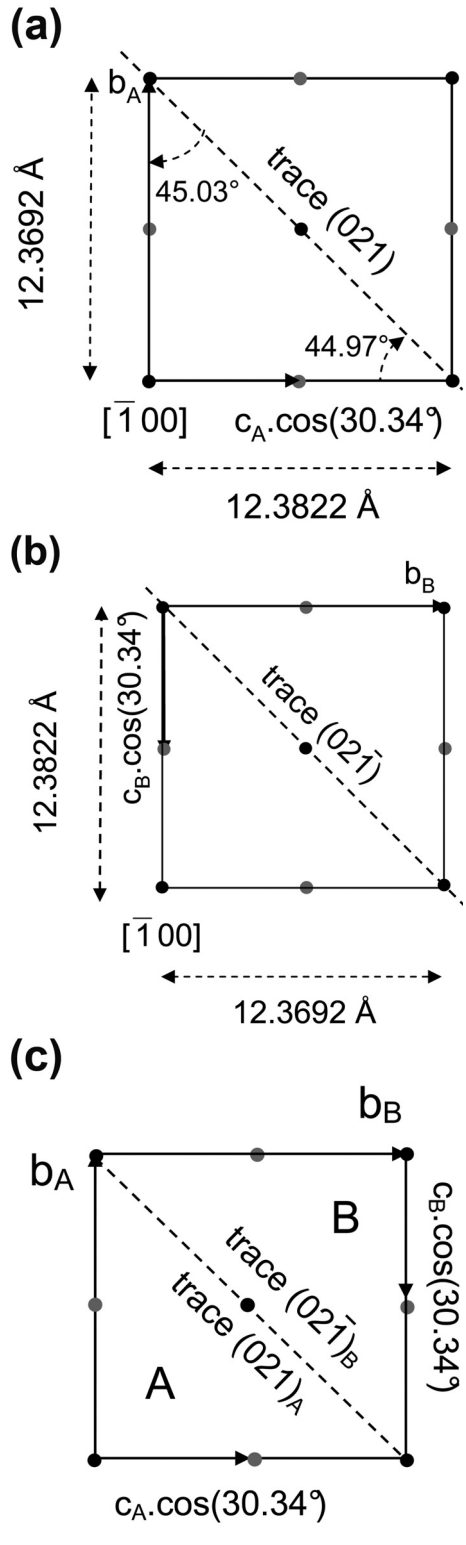


Fig. 8. (a) and (b) Projections of the direct lattices of the structure seen along the [$\bar{1}$00] direction for respectively the A and B variants. The lattice nodes in black are at height 0 and lattice nodes in grey are at height 1/2. The lattice B is rotated of –89.94° with respect to A. (c) Twin arrangement corresponding to the creation of an exact mirror between A and B.

In essence, we recommend the approach of LACBED, which is a very important and useful technique for the precise characterization of crystal defects.

**Acknowledgements:** Many thanks are due to the referees B. Grobéty and J. Wu for their very fruitful comments on the original manuscript.

## References

Bourret, A., Hinze, E., Hochheimer, H.D. (1986): Twin structure in coesite studied by high-resolution electron-microscopy. *Phys. Chem. Minerals*, **13**, 206-212.

Chao, E.C.T., Shoemaker, E.M., Madsen, B.M. (1960): First natural occurrence of coesite. *Science*, **132**, 220-222.

Coes, L. (1953): A new dense crystalline silica. *Science*, **118**, 131-132.

Cordier, P., Morniroli, J.P., Cherns, D. (1995): Characterization of crystal defects in quartz by large-angle convergent-beam electron diffraction. *Phil. Mag.*, **72**, 1421-1430.

Chopin, C. (1984): Coesite and pure pyrope in high-grade blueschists of the Western Alps – a first record and some consequences. *Contrib. Mineral. Petrol.*, **86**, 107-118.

Levien, L. & Prewitt, C.T. (1981): High-pressure crystal-structure and compressibility of coesite. *Am. Mineral.*, **66**, 324-333.

Morniroli, J.P. & Gaillot, F. (2000): Trace analysis from LACBED patterns. *Ultramicroscopy*, **83**, 227-243.

Morniroli, J.P. (2004): Large-angle convergent-beam electron diffraction. Applications to crystal defects. CRC Press.

Naka, S. (1975): Penetration twins in synthetic coesite. *Am. Mineral.*, **60**, 726-727.

Ramsdell, S. (1955): The crystallography of 'coesite'. *Am. Mineral.*, **40**, 975-982.

Schertl, H.-P., Medenbach, O., Neuser, R.D. (2005): UHP-metamorphic rocks from Dora-Maira, western Alps: cathodoluminescence of silica and twinning of coesite. *Russian Geology and Geophysics*, **46**, 1345-1351.

Sclar, C.B., Carisson, L.C., Schwartz, M.C. (1962): Optical crystallography of coesite. *Am. Mineral.*, **47**, 1292-1302.

Smyth, J.R. & Hatton, C.J.A. (1977): Coesite-sanidine grospydite from the Roberts Victor kimberlite. *Earth Planet. Sci. Lett.*, **34**, 284-290.

Stöffler, D. & Langenhorst, F. (1994): Shock metamorphism of quartz in nature and experiment. 1. Basic observation and theory. *Meteoritics*, **29**, 155-181.

Tanaka, M., Terauchi, M., Tsuda, K. (1994): Convergent Beam Electron Diffraction Vol. III, JEOL Ltd, Tokyo.

*Received 4 July 2007*
*Modified version received 24 October 2007*
*Accepted 5 November 2007*

*American Mineralogist, Volume 94, pages 684–692, 2009*

# Application of precession electron diffraction to the characterization of (021) twinning in pseudo-hexagonal coesite

**Damien Jacob,[1,*] Patrick Cordier,[1] Jean-Paul Morniroli,[2] and Hans-Peter Schertl[3]**

[1]Laboratoire de Structure et Propriétés de l'Etat Solide, UMR CNRS 8008, Université des Sciences et Technologies de Lille, Bât. C6, 59655 Villeneuve d'Ascq Cedex, France
[2]Laboratoire de Métallurgie Physique et Génie des Matériaux, UMR CNRS 8517, Université des Sciences et Technologies de Lille and Ecole Nationale Supérieure de Chimie de Lille, Bât. C6, 59655 Villeneuve d'Ascq Cedex, France
[3]Institut für Geologie, Mineralogie und Geophysik, Ruhr-Universität Bochum, D-44780 Bochum, Germany

## Abstract

Precession electron diffraction is used to characterize a (021) twin observed in coesite. Due to the quasi-hexagonal dimensions of coesite (monoclinic space group $C12/c1$ with $\beta = 120.34°$), indexing of conventional spot patterns is ambiguous and the twin law determination is impossible. With precession, spot intensities enable the absolute indexing of the patterns. The method we used is based on the analysis of the departure from hexagonal symmetry. This ensures that all possible pseudo-equivalent monoclinic orientations are taken into account for the indexing. The orientation relationships between adjacent parts of the twin are then characterized. The twin is described as a mirror along (021), which is consistent with original descriptions of twinning in synthetic coesite and a previous characterization performed using large-angle convergent-beam electron diffraction (LACBED).

**Keywords:** Coesite, twin, TEM, precession electron diffraction

## Introduction

In a previous study (Jacob et al. 2008), we reported a (021) twin characterization in coesite using large-angle convergent-beam electron diffraction (LACBED). This technique was used to overcome the difficulties encountered with the interpretation of conventional electron diffraction patterns of coesite. Indeed, the monoclinic lattice of coesite exhibits a small symmetry departure from an "ideal" hexagonal lattice. As a result, many [*uvw*] zone-axis electron diffraction patterns look similar and cannot be unambiguously identified using conventional selected-area electron diffraction (SAED) or microdiffraction techniques. Therefore, the (021) twin (Sclar et al. 1962; Schertl et al. 2005) cannot be unequivocally characterized.

Recent developments in electron diffraction call for a reappraisal of the possibilities offered by spot patterns. Among them is the Vincent-Midgley (Vincent and Midgley 1994) precession electron diffraction (PED) technique, which recently became available on transmission electron microscopes due to hardware implementations. Given the possibility of measuring the integrated intensity of the diffracted beams, this technique was originally developed for electron crystallography applications (Gjønnes 1997; Berg et al. 1998; Oleynikov et al. 2007; Sinkler et al. 2007). It has been used for space group identification (Morniroli et al. 2007, 2008), structure determination (Own et al. 2006; Kverneland et al. 2006; Weirich et al. 2006; Boulahya et al. 2007; Dorset et al. 2007; Dudka et al. 2007, 2008; Gemmi and Nicolopoulos 2007), measurement of Debye-Waller factors (Midgley et al. 1998) and chemical bonding characterization (Avilov et al. 2007; Ciston et al. 2008). In the present study, we use the intensity data provided by PED to propose an original characterization of a crystal defect. The method described in this paper is also suited to the general case of pseudo-merohedral twins occurring in crystals suffering from small symmetry departure, e.g., on $LaGaO_3$ perovskite (Ji et al. in prep).

* E-mail: Damien.Jacob@univ-lille1.fr

## Experimental methods

### The sample

Coesite is a high-pressure polymorph of silica stable in the pressure range 2.5–9 GPa, which exhibits monoclinic symmetry with space group $C12/c1$. Cell parameters are $a = 0.71356$, $b = 1.23692$, and $c = 0.71736$ nm, $\beta = 120.34°$ (Levien and Prewitt 1981). The twinned coesite investigated in this study comes from a fine-grained pyrope quartzite rock collected at Parigi, Dora-Maira Massif, Western Alps, Italy (Chopin 1984; Schertl et al. 1991). Coesite grains were selected based on optical examination of 30 μm thick sections of the sample (an optical micrograph is presented in Fig. 1 of Jacob et al. 2008). Specimens were then drilled out and glued to a 3 mm diameter copper TEM grid and ion-milled to electron transparency at 5 kV with an incident beam angle of 15°. Finally, the samples were coated with a thin carbon layer to promote electron conduction.

### Precession electron diffraction in the TEM

Applying the PED technique, the incident beam is scanned at a constant precession angle (ranging from 1 to 3°) around the optical axis, in combination with an opposite and synchronized descan of the transmitted and diffracted beams below the specimen (Vincent and Midgley 1994). During the precession movement, the reciprocal lattice nodes are thus swept through the Ewald sphere and integrated intensities over a large range of deviation parameter *s* around the Bragg orientation are collected. PED has the following main advantages: (1) the zone axis patterns are very symmetrical, even if the specimen zone axis is not exactly located along the optical axis; (2) the incident beam is never directed along the zone axis so that dynamical interactions are strongly reduced; (3) with large precession angles, a "two-beam" behavior is observed, which limits the multiple diffraction paths and allows the identification of the kinematical forbidden reflections; and (4) very small differences of intensity are visible.

TEM observations were carried out on a Philips CM30 microscope operated at 300 kV and equipped with a "Spinning Star" precession module from the Nanomegas Company. The sample is sensitive to electron irradiation, and the diffraction patterns were obtained with a low-dose parallel electron beam, using a 5

0003-004X/09/0506–684$05.00/DOI: 10.2138/am.2009.3059 

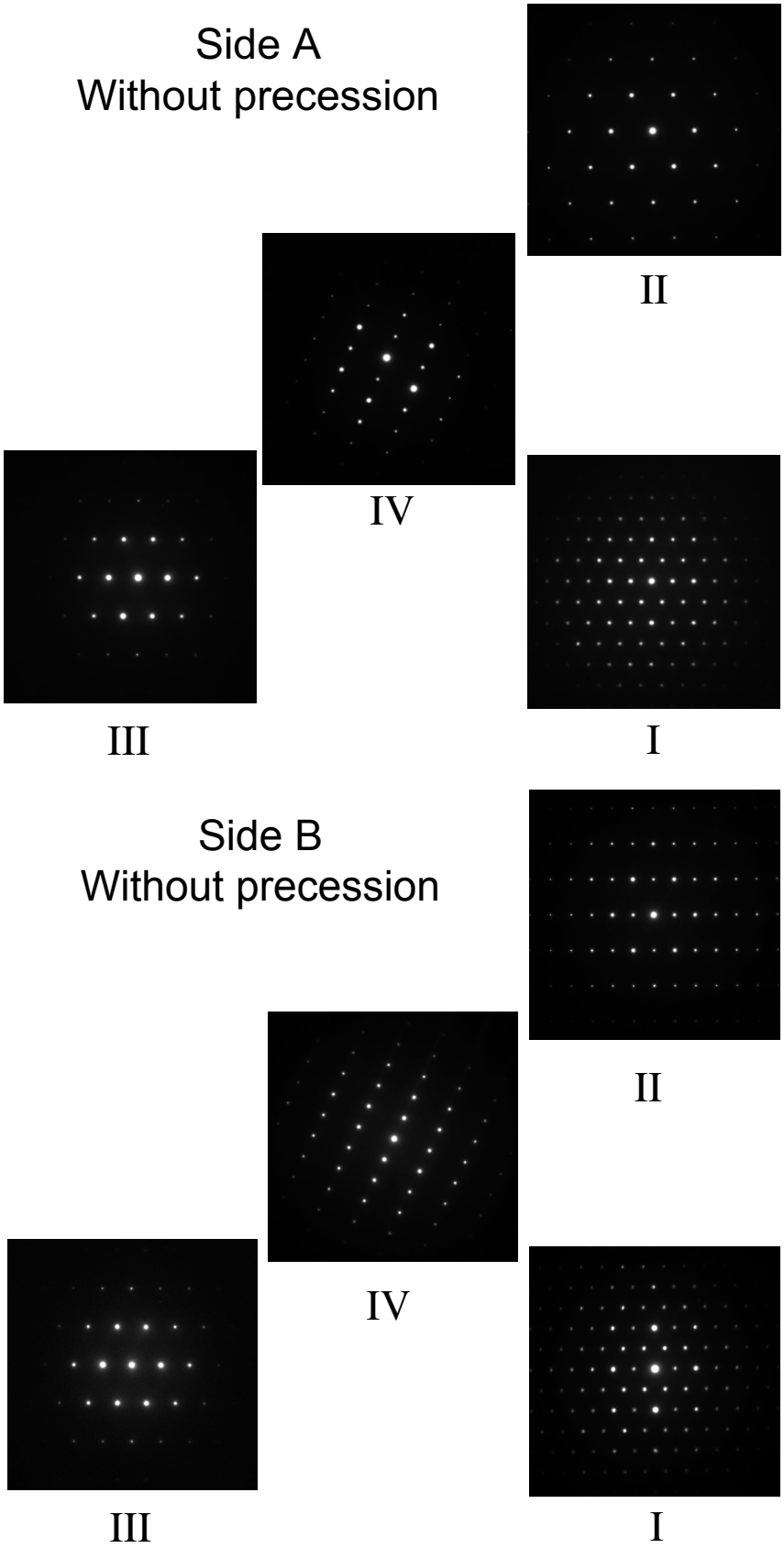


◀**FIGURE 1.** Experimental patterns taken without precession on A and B sides of the twin for four different specimen orientations. Orientation I is taken as the reference orientation, and the patterns are disposed to keep their mutual orientation.

μm selected-area aperture. Simulated kinematical and dynamical precession patterns were calculated using the "Electron Diffraction" (J.P. Morniroli) and "Jems" (P. Stadelmann, Electron Microscopy Software, java version CIME, EPFL, Switzerland) software, respectively.

## EXPERIMENTAL RESULTS

To characterize the studied twin, couples of PED patterns were obtained from each of the two sides A and B of the twin for four different specimen orientations named I, II, III, and IV, the orientation I being considered as the reference (null tilt angles). Kikuchi patterns were used to tilt the specimen from one orientation to another. To simplify the interpretations, highly symmetrical patterns were selected. On Figure 1, the patterns obtained with conventional SAED (i.e., without precession) are placed to keep their mutual orientations. The patterns from A and B sides look different for the orientation II only, which is clearly not sufficient to identify the twin. Orientation I, for instance, can be indexed as <110>, <101>, or <001>. To overcome this difficulty, the same experimental patterns have been recorded using precession. The results are shown Figure 2. The intensities are now strongly modified between patterns from both sides and this enables the absolute indexation of the patterns, as described in the following section.

## INTERPRETATION

### Introduction of a hexagonal setting

While monoclinic in symmetry, the crystal is pseudo-hexagonal with a ~ c and β ~ 120°. As a matter of fact, the *C* monoclinic lattice of coesite can be considered as a superlattice of an "ideal" smaller hexagonal that we will take as a reference (Fig. 3). The following relations connect the lattice axes in the two settings:

$$a_m = 2b_h$$
$$b_m = 2c_h$$
$$c_m = 2a_h$$

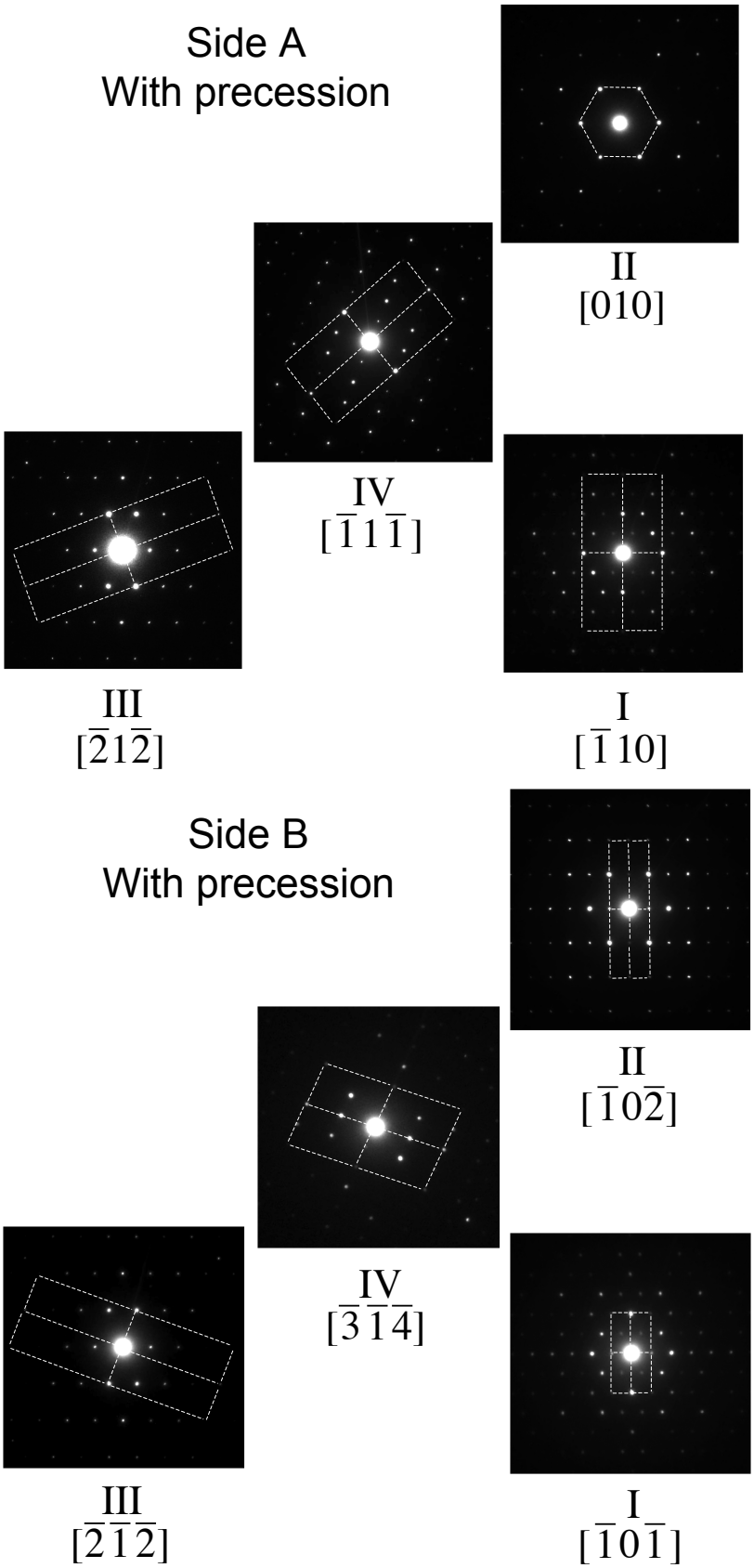


◀**FIGURE 2.** Same experiment as in Figure 1, with precession. Dashed lines lattice corresponds to the ideal hexagonal zone axis pattern (see text).

Throughout this text, the subscript "*h*" and "*m*" refer to the "ideal" hexagonal and "real" monoclinic lattices, respectively. The transformation matrix between both lattices (hexagonal to monoclinic) is thus written as:

$$M = \begin{pmatrix} 0 & 2 & 0 \\ 0 & 0 & 2 \\ 2 & 0 & 0 \end{pmatrix}$$

The transformation of directions from the hexagonal to the monoclinic setting is then obtained by application of the transposed and inverse matrix of M:

$$\begin{bmatrix} u \\ v \\ w \end{bmatrix}_m = M' \begin{bmatrix} u \\ v \\ w \end{bmatrix}_h$$

with

$$M' = (M^{-1})^t = \begin{pmatrix} 0 & 1/2 & 0 \\ 0 & 0 & 1/2 \\ 1/2 & 0 & 0 \end{pmatrix}$$

In Table 1 are listed the results of the hexagonal to monoclinic conversion of the zone axis orientations used in this study.

Due to the small symmetry departure between the real monoclinic and the ideal hexagonal lattices, many non-equivalent zone axis electron diffraction patterns look similar in conventional electron diffraction experiments. To quantify this aspect, let us consider a $<uvtw>_h$ zone axis form of the "ideal" hexagonal coesite. In the hexagonal crystal, the equivalent directions (having the same parameter $P_{[uvtw]}$ but different orientations) belonging to a $<uvtw>_h$ zone-axis form are obtained by changing the sign of *w*. In addition, the *u*, *v*, and *t* indices can also be interchanged and their sign changed if the condition $t = -(u + v)$ is maintained (see Table 1). In the general case, observed when $u \neq v \neq 0$ and $w \neq 0$, 24 equivalent directions are obtained as seen in Table 1 for the $<52\bar{7}3>_h$ zone axis form, which is the most general orientation encountered in this study. The 24 zone axes deriving from this form give

only two non-superimposable and mirror related diffraction patterns as shown on Figure 4a (top). By analogy with the ordered and disordered structures, the reflections present on these patterns are called fundamental reflections. With the "real" monoclinic coesite, the situation becomes more complex since these 24 $<52\bar{7}3>_h$ equivalent hexagonal directions are transformed into the six non-equivalent $<31\bar{1}>_m$, $<411>_m$, $<11\bar{3}>_m$, $<413>_m$, $<114>_m$, and $<314>_m$ zone axis forms (Table 1). These forms are obtained by application of [M′] to the 24 $<52\bar{7}3>_h$ directions written in the 3-indices notation. In the monoclinic system described with the unique axis *b*, the equivalent directions belonging to a $<uvw>_m$ zone axis form are obtained by either changing the sign of *v* or the sign of both the *u* and *w* indices. In the general case, observed when $u \neq v \neq w \neq 0$, four equivalent directions are obtained: $[uvw]_m$, $[\bar{u}v\bar{w}]_m$, $[u\bar{v}w]_m$, and $[\bar{u}\,\bar{v}\,\bar{w}]_m$. Thus, each of the previous monoclinic forms contains 4 equivalent directions, also giving two mirror related diffraction patterns. As a result, two sets of six different and mirror related diffraction patterns are obtained (Figs. 4b, 4c, and 4d). They differ from the corresponding hexagonal $<52\bar{7}3>_h$ patterns by (1) some very slight distortions, meaning that the positions of the reflections on the patterns are slightly shifted with respect to the positions they would occupy on the corresponding "ideal" hexagonal patterns; and (2) the presence, in addition to the fundamental reflections, of extra reflections typical of the symmetry departures. These extra reflections are located at three different positions. (1) The first position is in the middle of the large edges of the parallelograms drawn with respect to the fundamental reflections for the $<31\bar{1}>_m$ and $<411>_m$ zone axis patterns (Fig. 4b). Note that the intensity of the extra reflections is typical in each of these four patterns. (2) The second position is in the middle of the small edges of the parallelograms drawn with respect to the fundamental reflections for the $<11\bar{3}>_m$ and $<413>_m$ zone axis patterns (Fig. 4c). The intensity of the extra reflections is also typical in each of these four patterns. (3) The third position is in the middle of both sides of the parallelograms as well as in the centers of the parallelograms for the two $<114>_m$ and $<314>_m$ zone axis patterns (Fig 4d). Again, the intensity of the extra reflections is also typical of the zone axis.

It should be noted that between the ideal hexagonal and the real monoclinic structures, reflection intensities are strongly modified so that the so-called fundamental reflections may not be the most intense.

We see here that the merit of this analysis based on the "ideal" hexagonal lattice is to make sure that no pseudo-equivalent orientation is left over during the indexing. This analysis can be extended to any other zone axes. Some examples are given in Table 1 and Figures 5a to 5e for the other orientations experimentally encountered in this study: $<11\bar{2}3>_h$, $<11\bar{2}0>_h$, $<0001>_h$, $<10\bar{1}0>_h$, and $<22\bar{4}3>_h$.

**Table 1.** Conversion from the hexagonal to the monoclinic forms for the various orientations of the sample encountered in this study

| Hexagonal forms $<utvw>_h$ | Hexagonal directions $[uvtw]_h$ | Hexagonal directions $[uvw]_h$ | Monoclinic directions $[UVW]_m$ | Monoclinic forms $<uvw>_m$ |
|---|---|---|---|---|
| $<52\bar{7}3>$ | $[5\bar{7}23]$ $[5\bar{7}2\bar{3}]$ | $[1\bar{3}1]$ $[1\bar{3}\,\bar{1}]$ | $[\bar{3}11]$ $[\bar{3}\,\bar{1}\,\bar{1}]$ | $<31\bar{1}>$ |
| | $[\bar{5}72\bar{3}]$ $[\bar{5}72\,\bar{3}]$ | $[\bar{1}31]$ $[\bar{1}3\bar{1}]$ | $[31\bar{1}]$ $[3\bar{1}\,\bar{1}]$ | |
| | $[\bar{2}75\,\bar{3}]$ $[\bar{2}75\bar{3}]$ | $[14\bar{1}]$ $[14\bar{1}]$ | $[4\bar{1}1]$ $[4\bar{1}1]$ | $<411>$ |
| | $[\bar{2}7\bar{5}\bar{3}]$ $[\bar{2}7\bar{5}3]$ | $[\bar{1}\,\bar{4}\,\bar{1}]$ $[\bar{1}\,\bar{4}1]$ | $[\bar{4}\,\bar{1}\,\bar{1}]$ $[\bar{4}1\bar{1}]$ | |
| | $[\bar{7}5\,\bar{2}3]$ $[\bar{7}5\bar{2}3]$ | $[3\bar{1}1]$ $[\bar{3}11]$ | $[\bar{1}13]$ $[1\bar{1}\bar{3}]$ | $<11\bar{3}>$ |
| | $[\bar{7}52\bar{3}]$ $[\bar{7}52\,\bar{3}]$ | $[\bar{3}1\bar{1}]$ $[3\bar{1}\,\bar{1}]$ | $[1\bar{1}\,\bar{3}]$ $[\bar{1}\,\bar{1}3]$ | |
| | $[2\bar{5}73]$ $[2\bar{5}7\,\bar{3}]$ | $[341]$ $[34\bar{1}]$ | $[413]$ $[4\bar{1}3]$ | $<413>$ |
| | $[\bar{2}\,\bar{5}73]$ $[\bar{2}\,\bar{5}7\bar{3}]$ | $[\bar{3}\,\bar{4}1]$ $[\bar{3}\,\bar{4}\,\bar{1}]$ | $[\bar{4}1\bar{3}]$ $[\bar{4}\,\bar{1}\,\bar{3}]$ | |
| | $[\bar{5}\,\bar{2}7\bar{3}]$ $[\bar{5}2\bar{7}3]$ | $[\bar{4}\,\bar{3}\,\bar{1}]$ $[\bar{4}\,\bar{3}1]$ | $[\bar{3}\,\bar{1}\,\bar{4}]$ $[\bar{3}1\bar{4}]$ | $<314>$ |
| | $[52\bar{7}\,\bar{3}]$ $[52\bar{7}3]$ | $[43\bar{1}]$ $[431]$ | $[3\bar{1}4]$ $[31\bar{4}]$ | |
| | $[\bar{7}2\,\bar{5}3]$ $[\bar{7}2\,\bar{5}\,\bar{3}]$ | $[41\bar{1}]$ $[41\bar{1}]$ | $[11\bar{4}]$ $[1\bar{1}\bar{4}]$ | $<114>$ |
| | $[\bar{7}253]$ $[\bar{7}25\bar{3}]$ | $[\bar{4}\,\bar{1}1]$ $[\bar{4}\,\bar{1}\,\bar{1}]$ | $[\bar{1}\,\bar{1}4]$ $[\bar{1}\,\bar{1}\,\bar{4}]$ | |
| $<11\bar{2}3>$ | $[1\bar{2}13]$ $[1\bar{2}\bar{1}\,\bar{3}]$ | $[0\bar{1}1]$ $[01\bar{1}]$ | $[\bar{1}10]$ $[1\bar{1}0]$ | $<110>$ |
| | $[\bar{1}2\bar{1}3]$ $[\bar{1}2\bar{1}\bar{3}]$ | $[011]$ $[0\bar{1}\,\bar{1}]$ | $[110]$ $[\bar{1}\,\bar{1}0]$ | |
| | $[2\bar{1}\,\bar{1}3]$ $[2\bar{1}\,\bar{1}3]$ | $[101]$ $[10\bar{1}]$ | $[01\bar{1}]$ $[0\bar{1}1]$ | $<011>$ |
| | $[\bar{2}113]$ $[\bar{2}113]$ | $[\bar{1}01]$ $[\bar{1}0\bar{1}]$ | $[01\bar{1}]$ $[0\bar{1}\,\bar{1}]$ | |
| | $[11\bar{2}\,\bar{3}]$ $[11\bar{2}3]$ | $[11\bar{1}]$ $[111]$ | $[\bar{1}11]$ $[111]$ | $<111>$ |
| | $[\bar{1}\,\bar{1}23]$ $[\bar{1}\,\bar{1}\,\bar{1}23]$ | $[\bar{1}\,\bar{1}\,\bar{1}]$ $[\bar{1}\,\bar{1}1]$ | $[\bar{1}\,\bar{1}\,\bar{1}]$ $[\bar{1}11]$ | |
| $<11\bar{2}0>$ | $[1\bar{1}20]$ | $[110]$ | $[10\bar{1}]$ | $<101>$ |
| | $[\bar{1}\,\bar{1}20]$ | $[\bar{1}\,\bar{1}0]$ | $[\bar{1}0\bar{1}]$ | |
| | $[2\bar{1}\,\bar{1}0]$ | $[100]$ | $[00\bar{1}]$ | $<001>$ |
| | $[\bar{2}110]$ | $[\bar{1}00]$ | $[00\bar{1}]$ | |
| | $[\bar{1}2\bar{1}0]$ | $[0\bar{1}0]$ | $[\bar{1}00]$ | $<100>$ |
| | $[1\bar{2}10]$ | $[010]$ | $[100]$ | |
| $<0001>$ | $[0001]$ | $[00\bar{1}]$ | $[010]$ | $<010>$ |
| | $[000\bar{1}]$ | $[00\bar{1}]$ | $[0\bar{1}0]$ | |
| $<10\bar{1}0>$ | $[01\bar{1}0]$ | $[120]$ | $[201]$ | $<201>$ |
| | $[0\bar{1}10]$ | $[\bar{1}\,\bar{2}0]$ | $[\bar{2}0\bar{1}]$ | |
| | $[1\bar{1}00]$ | $[1\bar{1}0]$ | $[\bar{1}01]$ | $<10\bar{1}>$ |
| | $[\bar{1}100]$ | $[\bar{1}10]$ | $[10\bar{1}]$ | |
| | $[10\bar{1}0]$ | $[210]$ | $[102]$ | $<102>$ |
| | $[\bar{1}010]$ | $[\bar{2}\,\bar{1}0]$ | $[\bar{1}0\bar{2}]$ | |
| $<22\bar{4}3>$ | $[22\bar{4}\,\bar{3}]$ $[22\bar{4}3]$ | $[22\bar{1}]$ $[221]$ | $[2\bar{1}2]$ $[212]$ | $<212>$ |
| | $[\bar{2}\,\bar{2}4\bar{3}]$ $[\bar{2}\,\bar{2}43]$ | $[\bar{2}\,\bar{2}\,\bar{1}]$ $[\bar{2}\,\bar{2}1]$ | $[\bar{2}\,\bar{1}\,\bar{2}]$ $[\bar{2}1\bar{2}]$ | |
| | $[4\bar{2}\,\bar{2}3]$ $[4\bar{2}\,\bar{2}\,\bar{3}]$ | $[201]$ $[20\bar{1}]$ | $[012]$ $[0\bar{1}2]$ | $<012>$ |
| | $[\bar{4}223]$ $[\bar{4}22\bar{3}]$ | $[\bar{2}01]$ $[\bar{2}0\bar{1}]$ | $[01\bar{2}]$ $[0\bar{1}\,\bar{2}]$ | |
| | $[\bar{2}4\bar{2}3]$ $[\bar{2}4\bar{2}\,\bar{3}]$ | $[021]$ $[02\bar{1}]$ | $[\bar{2}10]$ $[\bar{2}\bar{1}0]$ | $<210>$ |
| | $[\bar{2}4\bar{2}3]$ $[\bar{2}4\bar{2}\bar{3}]$ | $[0\bar{2}1]$ $[0\bar{2}\,\bar{1}]$ | $[\bar{2}10]$ $[\bar{2}\,\bar{1}0]$ | |

*Notes:* Hexagonal directions are given in four [*uvtw*] [with $t = -(u + v)$] and 3 [*UVW*] indices using the convention: $U = u - t$, $V = v - t$, $W = w$. Conversion from hexagonal to monoclinic directions is made by application of the matrix M′ to the three indices hexagonal directions.

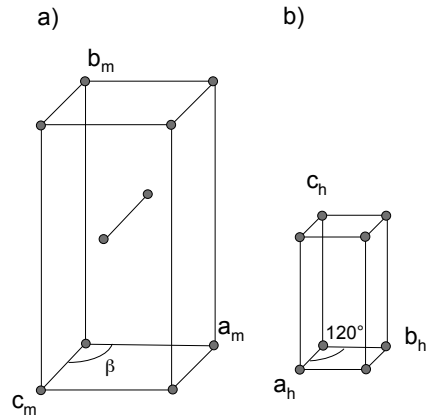


**Figure 3.** (**a**) *C* monoclinic lattice of coesite. (**b**) Hexagonal lattice. The monoclinic lattice can be considered as a superlattice of the hexagonal one.

## Pattern indexation method

The poor angular accuracy of SAED or microdiffraction does not allow the detection of the very slight pattern distortions. In addition, to these techniques, the intensities of the diffracted beams are highly affected by dynamical effects (multiple diffraction), and/or by thickness variations and crystal misorientations in the diffracted area, so that only the so-called "net" symmetry can be trusted and taken into account. This symmetry is based on the positions of the reflections on the pattern while the "ideal" symmetry takes into account both their position and intensity

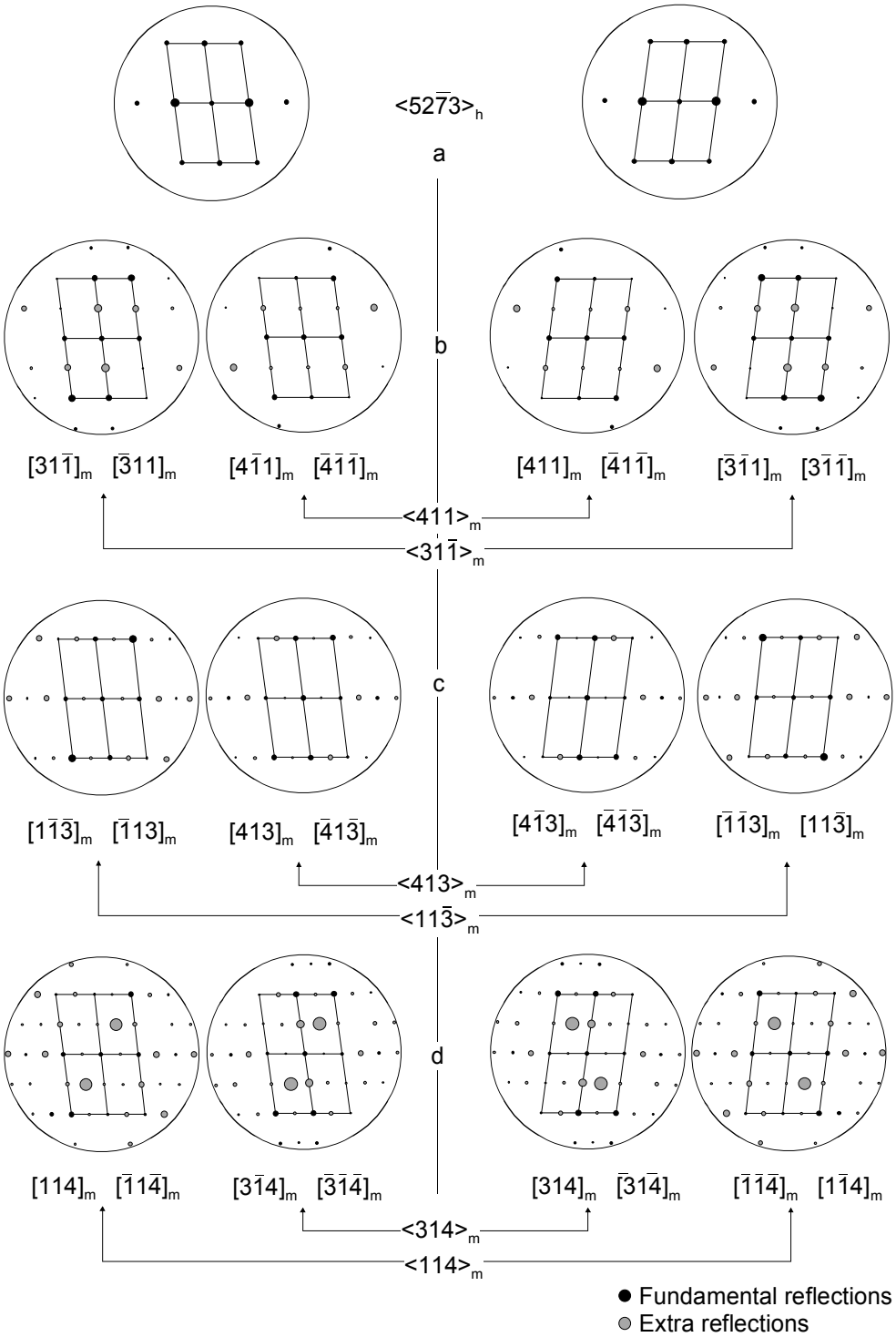


**FIGURE 4.** Relations between the diffraction patterns of equivalent zone axis forms in the hexagonal and monoclinic lattices for the general case (kinematical simulations). (**a**) Two possible patterns obtained for the $<52\bar{7}3>_h$ zone axis form of the hexagonal lattice. The patterns are mirror related. The reflections appearing in black on this patterns are called fundamental. (**b**, **c**, **d**) Patterns obtained for the corresponding six non-equivalent zone axis forms in the monoclinic lattice. Each form contains four equivalent directions and gives two mirror related patterns. Extra reflections appear in light gray on these patterns. In **b**, the extra reflections are located in the middle of the large edges of the parallelogram drawn by the fundamental reflections. In **c**, they appear in the middle of the small edges, and in **d**, they appear in the middle of both sides as well as in the center of the parallelograms.

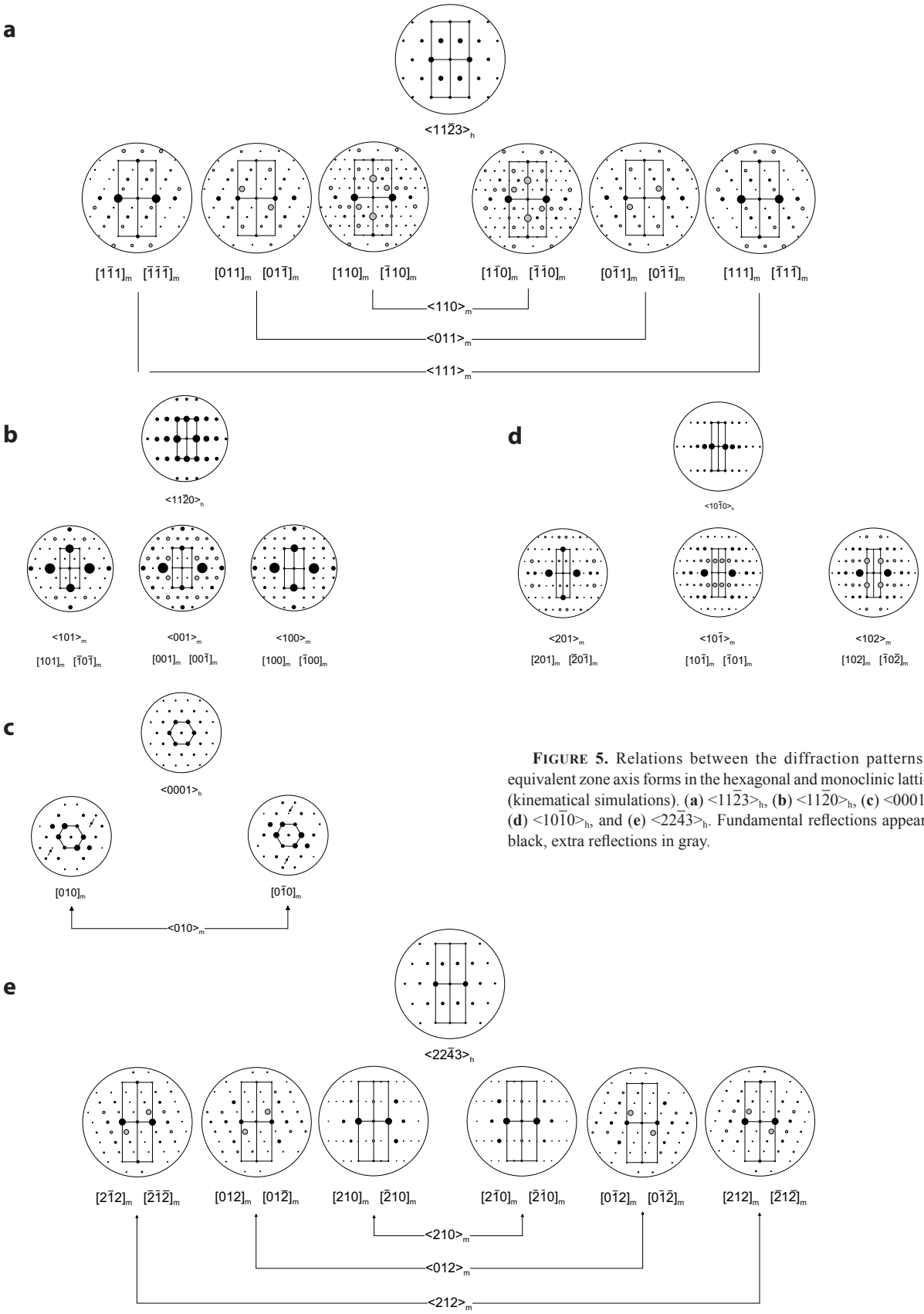


**FIGURE 5.** Relations between the diffraction patterns of equivalent zone axis forms in the hexagonal and monoclinic lattices (kinematical simulations). (**a**) $<11\bar{2}3>_h$, (**b**) $<11\bar{2}0>_h$, (**c**) $<0001>_h$, (**d**) $<10\bar{1}0>_h$, and (**e**) $<22\bar{4}3>_h$. Fundamental reflections appear in black, extra reflections in gray.

(Morniroli and Steeds 1992). This means that, for the example illustrated on Figure 4, a zone axis pattern cannot be unequivocally identified among the two $<31\bar{1}>_m$ and $<411>_m$, the two $<11\bar{3}>_m$ and $<413>_m$, or the two $<114>_m$ and $<314>_m$ zone axis patterns. This is no longer the case with electron precession since the ideal symmetry can be identified. Thus, the observation of the intensity of these typical extra reflections is the basis of the zone axis identification used in the present paper to characterize the coesite twin. The practical method we used involves three steps. (1) The patterns are indexed with respect to the "ideal" hexagonal coesite to identify the hexagonal $<uvtw>_h$ zone axis form. This can be done using automated indexing software. (2) The corresponding monoclinic zone axis forms are deduced by means of the transformation matrix and their diffraction patterns are calculated. Finally, (3) the actual experimental $[uvw]_m$ zone axis is deduced by comparison with the simulated patterns by taking into account both the position and the intensity of the extra reflections.

### Actual pattern indexations

Each precession pattern of Figure 2 is interpreted by means of the procedure described in the previous section. A $[uvw]_m$ zone axis is considered as unequivocally identified if the three following conditions are fulfilled: (1) the position of the extra spots is in agreement with the corresponding $[uvw]$ theoretical patterns; (2) the intensity of the extra spots is in agreement with the corresponding $[uvw]$ theoretical patterns; and (3) the experimental tilt angles between two crystal orientations is in agreement with the calculated angles between the corresponding zone axes.

The results fulfilling these three conditions are summarized in Table 2. Let us begin with the first orientation (reference, null tilt angles). $I_A$ can be identified from Figure 5a as the $<11\bar{2}3>_h$ form of the hexagonal lattice. From the three possible monoclinic forms (Table 2; line 3), only one is compatible with the extra spot positions: $<110>_m$. Examination of the intensity leads to select $[110]$ and $[\bar{1}10]$ among the four possible orientations (Table 2; lines 4 and 5). Since at this stage we are dealing with the reference orientation, the latter is arbitrarily chosen. The same work is performed on side B: from Figure 5b, $I_B$ is identified as $<11\bar{2}0>_h$. Among the six possible orientations associated with the three deduced monoclinic forms (Table 2; line 3), only four are kept from the observation of the inner spots within the rectangle: $[101]_m$, $[\bar{1}0\bar{1}]_m$, $[001]_m$, and $[00\bar{1}]_m$, corresponding to the two orientation forms $<101>_m$ and $<001>_m$. A closer examination of the intensity leads us to select $[101]_m$ and $[\bar{1}0\bar{1}]_m$. The latter is arbitrarily chosen.

Let us now examine the case of the second orientation. The pattern from side A exhibits a hexagon, as in Figure 5c, which corresponds to the unique $<010>_m$ form. Side B is identified from comparison with Figure 5d, i.e., the $<10\bar{1}0>_h$ form in the hexagonal lattice corresponding to three possible orientations forms in the monoclinic lattice (Table 2; line 3). A closer examination of the extra spot positions allows us to eliminate $<201>_m$ and $<10\bar{1}>_m$. Two possibilities are then left for $II_B$: $[\bar{1}0\bar{2}]_m$ and $[102]_m$ The final choices are made by taking into account the experimental tilt angles from the reference orientation. As a result, $II_B$ corresponds to $[\bar{1}0\bar{2}]_m$ and $II_A$ to $[010]_m$.

Orientation III is interesting, since it leads to a unique hexagonal orientation for both sides A and B of the twin: $<22\bar{4}3>_h$, giving three possible monoclinic forms (Table 2; line 3). The choice is made from the detailed investigation of the spot positions and intensities (Table 2; line 5). As previously, comparison with the experimental tilt angles leads to unique solutions: $[\bar{2}1\bar{2}]_m$ for $III_A$ and $[\bar{2}\,\bar{1}\,\bar{2}]_m$ for $III_B$.

Finally, the same work is done on the fourth orientation, leading to unique indexing on both sides of the twin: $[\bar{1}1\bar{1}]_m$ for A and $[\bar{3}1\bar{4}]_m$ for B. The latter orientation corresponds to the most general case described in Figure 4.

**TABLE 2.** Indexing of the four orientations of the specimen for the A and B sides of the twin

| | | Orientation I | | Orientation II | | Orientation III | | Orientation IV | |
|---|---|---|---|---|---|---|---|---|---|
| | | Area A | Area B | Area A | Area B | Area A | Area B | Area A | Area B |
| 1 | $<uvtw>_h$ identified from the fundamental reflections | $<11\bar{2}3>_h$ | $<11\bar{2}0>_h$ | $<0001>_h$ | $<10\bar{1}0>_h$ | $<22\bar{4}3>_h$ | $<22\bar{4}3>_h$ | $<11\bar{2}3>_h$ | $<52\bar{7}3>_h$ |
| 2 | Theoretical kinematical patterns | Figure 5a | Figure 5b | Figure 5c | Figure 5d | Figure 5e | Figure 5e | Figure 5a | Figure 4 |
| 3 | Possible $<uvw>_m$ | $<110>_m$<br>$<011>_m$<br>$<111>_m$ | $<101>_m$<br>$<001>_m$<br>$<100>_m$ | $<010>_m$ | $<201>_m$<br>$<10\bar{1}>_m$<br>$<102>_m$ | $<210>_m$<br>$<012>_m$<br>$<212>_m$ | $<210>_m$<br>$<012>_m$<br>$<212>_m$ | $<110>_m$<br>$<011>_m$<br>$<111>_m$ | $<411>_m$<br>$<31\bar{1}>_m$<br>$<413>_m$<br>$<11\bar{3}>_m$<br>$<314>_m$<br>$<114>_m$ |
| 4 | $[uvw]_m$ compatible with the position | $[110]_m$<br>$[\bar{1}10]_m$<br>$[1\bar{1}0]_m$<br>$[\bar{1}\,\bar{1}0]_m$ | $[101]_m$<br>$[\bar{1}0\bar{1}]_m$<br>$[001]_m$<br>$[00\bar{1}]_m$ | $[010]_m$<br>$[0\bar{1}0]_m$ | $[\bar{1}0\bar{2}]_m$<br>$[102]_m$ | $[\bar{2}1\bar{2}]_m$<br>$[212]_m$<br>$[0\bar{1}2]_m$<br>$[0\bar{1}\,\bar{2}]_m$ | $[2\bar{1}2]_m$<br>$[\bar{2}\,\bar{1}\,\bar{2}]_m$<br>$[012]_m$<br>$[01\bar{2}]_m$ | $[111]_m$<br>$[\bar{1}1\bar{1}]_m$<br>$[0\bar{1}1]_m$<br>$[1\bar{1}\,\bar{1}]_m$ | $[114]_m$<br>$[\bar{1}1\bar{4}]_m$<br>$[\bar{3}1\bar{4}]_m$<br>$[\bar{3}\,\bar{1}\,\bar{4}]_m$ |
| 5 | $[uvw]_m$ compatibility with the intensity and calculated angle with respect to the reference | $[110]_m$<br><br>$[\bar{1}10]_m$ | $[101]_m$<br><br>$[\bar{1}0\bar{1}]_m$ | $[010]_m$<br>29.98°<br>$[0\bar{1}0]_m$<br>150.02° | $[\bar{1}0\bar{2}]_m$<br>30.08°<br>$[102]_m$<br>149.92° | $[\bar{2}1\bar{2}]_m$<br>41.04°<br>$[212]_m$<br>67.54° | $[\bar{2}\,\bar{1}\,\bar{2}]_m$<br>40.98°<br>$[2\bar{1}2]_m$<br>139.01° | $[\bar{1}1\bar{1}]_m$<br>29.10°<br>$[111]_m$<br>51.11° | $[\bar{3}\,\bar{1}\,\bar{4}]_m$<br>29.01°<br>$[3\bar{1}4]_m$<br>150.98° |
| 6 | Experimental tilt angle | Ref. 0° | Ref. 0° | ~30° | ~30° | ~40° | ~40° | ~30° | ~30° |
| 7 | $[uvw]$ compatible with the tilt angle | $[\bar{1}10]_m$<br>selected | $[\bar{1}0\bar{1}]_m$<br>selected | $[010]_m$ | $[\bar{1}0\bar{2}]_m$ | $[\bar{2}1\bar{2}]_m$ | $[\bar{2}\,\bar{1}\,\bar{2}]_m$ | $[\bar{1}1\bar{1}]_m$ | $[\bar{3}\,\bar{1}\,\bar{4}]_m$ |

It should be noted that without precession, only the net symmetry can be trusted, leading to many ambiguous results (see the fourth line of Table 2), as pointed out in the experimental results section (Fig. 1).

Finally, the validity of the interpretations given in Table 2 is fully confirmed by comparison of experimental patterns with dynamical simulations (Fig. 6). The features marked with arrows on experimental and simulated patterns are in excellent agreement.

**Twin-law determination**

The previous indexing leads to the determination of the following four pairs of parallel directions in A and B variants:

$$[\bar{1}10]_A \,//\, [\bar{1}0\bar{1}]_B \quad (1)$$

$$[010]_A \,//\, [\bar{1}0\bar{2}]_B \quad (2)$$

$$[\bar{2}1\bar{2}]_A \,//\, [\bar{2}\,\bar{1}\,\bar{2}]_B \quad (3)$$

$$[\bar{1}\,1\,\bar{1}]_A \,//\, [\bar{3}\,\bar{1}\,\bar{4}]_B \quad (4)$$

For the third orientation, the twin plane is parallel to the optical axis of the microscope so that it can be directly identified on the diffraction pattern by the **g** vector normal to the trace of the plane. The twin plane is uniquely identified as:

$$(021)_A \,//\, (02\bar{1})_B \quad (5)$$

The deduction of the twin law is made classically using stereographic projections of poles $[uvw]_m$ as presented in Jacob

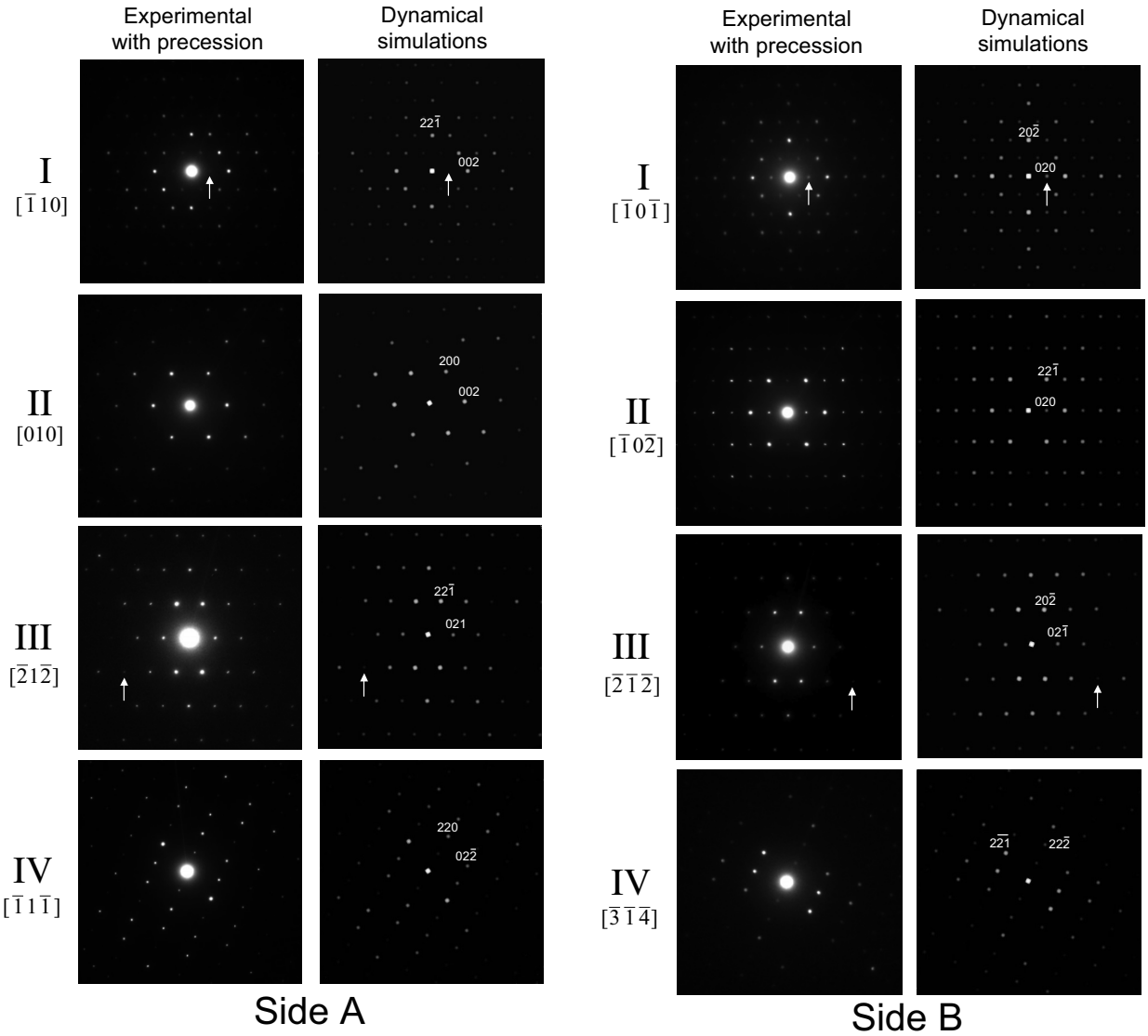


**FIGURE 6.** Comparison of experimental precession patterns with dynamical simulations for A and B sides of the twin for the same orientations as on Figure 4. For the first orientation, the arrow indicates the position of the kinematically forbidden 001 reflection on side A, whereas it corresponds to the allowed 020 reflection on side B. On the third orientation, the arrow locates a spot of weak intensity that enables the distinction between the [$\bar{2}$1$\bar{2}$] orientation for A and the [$\bar{2}$ $\bar{1}$ $\bar{2}$] orientation for B.

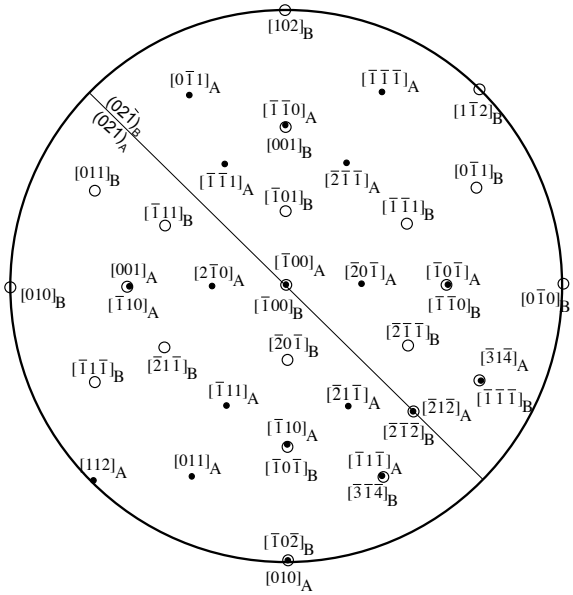


**FIGURE 7.** Superimposed [$\bar{1}$00] stereographic projections for A and B sides of the twin. Poles from A and B are drawn, respectively, in filled and empty circles. B is rotated of –89.94° with respect to A so as to put into coincidence the traces of $(021)_A$ and $(02\bar{1})_B$ planes.

et al. (2008): the stereographic projections whose central poles correspond to orientation III for area A and B (twin plane edge-on) are drawn and superimposed so that the poles for the three other orientations are in quasi coincidence (Fig. 6 in Jacob et al. 2008). This allows identifying the common [$\bar{1}$00] direction. The superimposed stereographic projections of direction poles along the [$\bar{1}$00] axis for A and B variants can then be plotted so as to place $(021)_A$ and $(02\bar{1})_B$ in coincidence (Fig. 7), which clearly shows the mirror along this plane between both variants. This result is fully consistent with that obtained in LACBED.

## Concluding remarks

In a previous work (Jacob et al. 2008), the LACBED method was used to characterize the twin-law. In LACBED, the very large number of diffraction lines present in a single pattern also allows its absolute indexing. Nevertheless, for the interpretation of the results, a large number of patterns have to be collected from both twin individuals, which makes the use of this method somewhat tedious. Furthermore, LACBED being a defocused method, the distortion of the sample can lead to inaccurate measurements of the angles between the zone axes. Compared to this method, PED appears as very simple and fast, since the interpretation of a spot pattern is much easier than interpretation of a line pattern. This is the great advantage of PED.

## Acknowledgment

Many thanks are due to G. Auchterlonie for re-reading of the manuscript.

## References cited

Avilov, A., Kuligin, K., Nicolopoulos, S., Nickolskiy, M., Boulahya, K., Portillo, J., Lepeshov, G., Sobolev, B., Collette, J.P., Martin, N., Robins, A.C., and Fischione, P. (2007) Precession technique and electron diffractometry as new tools for crystal structure analysis and chemical bonding determination. Ultramicroscopy, 107, 431–444.

Berg, B.S., Hansen, V., Midgley, P.A., and Gjønnes, J. (1998) Measurement of three-dimensional intensity data in electron diffraction by the precession technique. Ultramicroscopy, 74, 147–157.

Boulahya, K., Ruiz-González, L., Parras, M., González-Calbet, J.M., Nickolsky, M.S., and Nicolopoulos, S. (2007) Ab initio determination of heavy oxide perovskite related structures from precession electron diffraction data. Ultramicroscopy, 107, 445–452.

Chopin, C. (1984) Coesite and pure pyrope in high-grade blueschists of the Western Alps—a first record and some consequences. Contributions to Mineralogy and Petrology, 86, 107–118.

Ciston, J., Deng, B., Marks, L.D., Own, C.S., and Sinkler, W. (2008) A quantitative analysis of the cone-angle dependence in precession electron diffraction. Ultramicroscopy, 108, 514–522.

Dorset, D.L., Gilmore, C.J., Jorda, J.L., and Nicolopoulos, S. (2007) Direct electron crystallographic determination of zeolite zonal structures. Ultramicroscopy, 107, 462–473.

Dudka, A.P., Avilov, A.S., and Nicolopoulos, S. (2007) Crystal structure refinement using Bloch-wave method for precession electron diffraction. Ultramicroscopy, 107, 474–482.

Dudka, A.P., Avilov, A.A., and Lepeshov, G.G. (2008) Crystal structure refinement from electron diffraction data. Crystallography Reports, 53, 530–536.

Gemmi, M. and Nicolopoulos, S. (2007) Structure solution with three-dimensional sets of precessed electron diffraction intensities. Ultramicroscopy, 107, 483–494.

Gjønnes, K. (1997) On the integration of electron diffraction intensities in the Vincent-Midgley precession technique. Ultramicroscopy, 69, 1–11.

Jacob, D., Cordier, P., Morniroli, J.P., and Schertl, H.-P. (2008) Large-angle convergent-beam electron diffraction (LACBED) characterization of (021) twinning in natural coesite. European Journal of Mineralogy, 20, 119–124.

Kverneland, A., Hansen, V., Vincent, R., Gjønnes, K., and Gjønnes, J. (2006) Structure analysis of embedded nano-sized particles by precession electron diffraction. η'-precipitate in an Al-Zn-Mg alloy as example. Ultramicroscopy, 106, 492–502.

Levien, L. and Prewitt, C.T. (1981) High-pressure crystal-structure and compressibility of coesite. American Mineralogist, 66, 324–333.

Midgley, P.A., Sleight, M.E., Saunders, M., and Vincent, R. (1998) Measurement of Debye-Waller factors by electron precession. Ultramicroscopy, 75, 61–67.

Morniroli, J.P. and Steeds, J.W. (1992) Microdiffraction as a tool for crystal structure identification and determination. Ultramicroscopy, 45, 219–239.

Morniroli, J.P., Redjamia, A., and Nicolopoulos, S. (2007) Contribution of electron precession to the identification of the space group from microdiffraction patterns. Ultramicroscopy, 107, 514–522.

Morniroli, J.P., Houdellier, F., Roucau, C., Puiggali, J., Gesti, S., and Redjaïmia, A. (2008) LACDIF, a new electron diffraction technique obtained with the LACBED configuration and a Cs corrector: Comparison with electron precession. Ultramicroscopy, 108, 100–115.

Oleynikov, P., Hovmoller, S., and Zou, X.D. (2007) Precession electron diffraction: Observed and calculated intensities. Ultramicroscopy, 107, 523–533.

Own, C.S., Sinkler, W., and Marks, L.D. (2006) Rapid structure determination of a metal oxide from pseudo-kinematical electron diffraction data. Ultramicroscopy, 106, 114–122.

Schertl, H.-P., Schreyer, W., and Chopin, C. (1991) The pyrope-coesite rocks and their country rocks at Parigi, Dora Maira Massif, Western Alps: Detailed Petrography, Mineral Chemistry, and *PT*-Path. Contributions to Mineralogy and Petrology, 108, 1–21.

Schertl, H.-P., Medenbach, O., and Neuser, R.D. (2005) UHP-metamorphic rocks from Dora-Maira, Western Alps: cathodoluminescence of silica and twinning of coesite. Russian Geology and Geophysics, 46, 1345–1351.

Sclar, C.B., Carisson, L.C., and Schwartz, M.C. (1962) Optical crystallography of coesite. American Mineralogist, 47, 1292–1302.

Sinkler, W., Own, C.S., and Marks, L.D. (2007) Application of a 2-beam model for improving the structure factors from precession electron diffraction intensities. Ultramicroscopy, 107, 543–550.

Vincent, R. and Midgley, P.A. (1994) Double conical beam-rocking system for measurement of integrated electron diffraction intensities. Ultramicroscopy, 53, 271–282.

Weirich, T.E., Portillo, J., Cox, G., Hibst, H., and Nicolopoulos, S. (2006) Ab initio determination of the framework structure of the heavy-metal oxide $Cs_xNb_{2.54}W_{2.46}O_{14}$ from 100 kV precession electron diffraction data. Ultramicroscopy, 106, 164–175.

Manuscript received July 25, 2008
Manuscript accepted December 29, 2008
Manuscript handled by Joshua Feinberg

ARTICLE IN PRESS

Ultramicroscopy ∎ (∎∎∎∎) ∎∎∎–∎∎∎

Contents lists available at ScienceDirect

Ultramicroscopy

journal homepage: www.elsevier.com/locate/ultramic

# A precession electron diffraction study of α, β phases and Dauphiné twin in quartz

D. Jacob*, P. Cordier

*Unité Matériaux et Transformations, UMR 8207 CNRS-Université Lille 1, Univ Lille Nord de France, F-59655 Villeneuve d'Ascq, France*

ARTICLE INFO

*Article history:*
Received 20 January 2010
Received in revised form
2 April 2010
Accepted 20 April 2010

*Keywords:*
Transmission electron microscopy
Precession electron diffraction (PED)
Symmetry
Quartz
Dauphiné twin

ABSTRACT

Precession electron diffraction is used to distinguish between the hexagonal $\beta$ high-temperature and the trigonal $\alpha$ low-temperature phases of $SiO_2$ quartz. The structures just differ by a kink of the $SiO_4$ tetrahedra arranged along spiraling chains, which induces a loss of the two-fold axis and subsequent twinning in the low-temperature phase. Conventional selected-area electron diffraction (SAED) does not enable the phases distinction since only the intensity of reflections is different. It becomes possible with precession that reduces the dynamical interactions between reflections and makes their intensity very sensitive to small variations of the electron structure factors. Distinction between the twinned individuals in the low-temperature phase is then easily made and the twin law is characterized using stereographic projections. The actual symmetry of precessed zone axis patterns is also examined in detail. Using dynamical intensity simulations, it is shown that under certain thickness conditions, the diffraction class symmetry can be observed on selected area patterns that are to be used in the case of beam sensitive materials such as quartz.

© 2010 Elsevier B.V. All rights reserved.

## 1. Introduction

Thanks to recent developments and hardware implementations, the precession electron diffraction (PED) technique [1] has called for a reappraisal of the possibilities offered by spot patterns. Given the ability of measuring the integrated intensity of the diffracted beams, the technique was originally developed for electron crystallography [2–5]. It has been used for space group identification [6,7], structure determination [8–15], Debye–Waller factors measurement [16] and chemical bonding characterization [17,18]. The studies take advantage of the high sensitivity of PED data to the electron structure factors. Nevertheless, the real nature of precessed intensities is still to be understood and ultimate works are aimed at describing their behavior – kinematical or dynamical like – as a function of the precession angle and sample thickness [19–21]. It turns out that even if the dynamical oscillations of diffracted intensities with respect to the sample thickness are suppressed when precession is on, the intensities are in general far from being kinematical. Thus, a full dynamical treatment is generally required for the data analysis.

Whatever their real nature is, the attested sensitivity of PED to small variations of the electron structure factors is of great use for microstructural characterizations. In previous works, it has been shown that the technique was efficient for the characterization of pseudo-merohedral twinning occurring in crystals with lattices exhibiting a small departure from a more symmetrical one [22,23]. For this kind of applications, kinematical calculations of the reflection intensities are generally sufficient and the analysis is very fast and robust. In this work, we show that the method can be applied to merohedral twinning [23]. It occurs in crystals exhibiting symmetry elements for the lattice point group that do not belong to the crystal point group. In that case, the lattices of the twinned individuals are strictly superimposed and only the reflection intensities relate the symmetry operations between the individuals. The studied case concerns $SiO_2$ quartz, which is hexagonal ($\beta$) at high temperature and trigonal ($\alpha$) at low temperature ($T_c = 573$ °C). The symmetry lowering between $\beta$ and $\alpha$ phases induces twins in the low-temperature individuals with exactly coincident lattices. Diffraction patterns from both individuals are then discernable by the reflection intensities only, which is generally prevented in conventional selected area electron diffraction (SAED) due to the reflection intensities averaging induced by dynamical interactions. In addition, the case is interesting since quartz being beam sensitive, conventional methods for space group and point group determination using a convergent probe that would enable to distinguish between the twinned individuals are routinely prevented. Thus, the aim of the present work is also to quantitatively analyze intensities obtained in precession SAED in order to qualify the actual symmetry of a PED pattern with respect to the highest symmetry observable on a diffraction pattern using a convergent probe.

* Corresponding author.
*E-mail address:* damien.jacob@univ-lille1.fr (D. Jacob).

0304-3991/$ - see front matter © 2010 Elsevier B.V. All rights reserved.
doi:10.1016/j.ultramic.2010.04.010

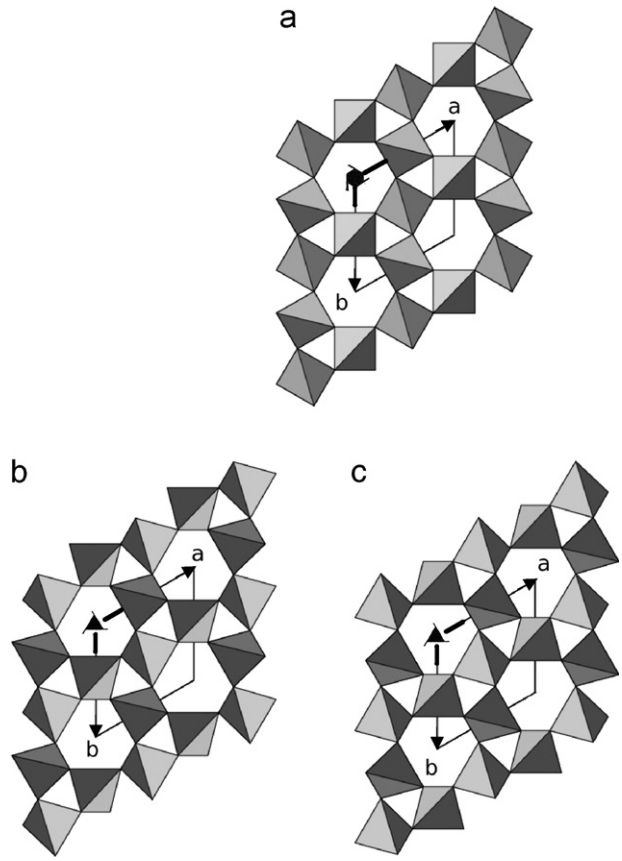


**Fig. 1.** (a) High temperature $\beta$ quartz viewed along the $c$ direction. (b) and (c) Low temperature $\alpha$ quartz twinned individuals. The two individuals are related by a 180° rotation around $c$ (after Heaney and Veblen [28]).

**Table 1**
Equivalence relationships in $\beta$ and $\alpha$ phases for a general form of reflections *hkil*. In $\alpha$, *hkil* and *hkiī* are not belonging to the same form.

| $\beta$ hexagonal Laue class 6/mmm. General multiplicity: 24 | $\alpha$ trigonal (hexagonal lattice) Laue class $\bar{3}$m1. General multiplicity: 12 | |
|---|---|---|
| $\pm(h\,k\,i\,l,\ h\,k\,i\,\bar{l},\ i\,h\,k\,l,\ i\,h\,k\,\bar{l},\ k\,i\,h\,l,\ k\,i\,h\,\bar{l},\ h\,i\,k\,l,\ h\,i\,k\,\bar{l},\ k\,h\,i\,l,\ k\,h\,i\,\bar{l},\ i\,k\,h\,l,\ i\,k\,h\,\bar{l})$ | $\pm(h\,k\,i\,l,\ i\,h\,k\,l,\ k\,i\,h\,l,\ h\,k\,i\,\bar{l},\ k\,h\,i\,\bar{l},\ i\,k\,h\,\bar{l})$ | $(h\,k\,i\,\bar{l},\ i\,h\,k\,\bar{l},\ k\,i\,h\,\bar{l},\ h\,i\,k\,l,\ k\,h\,i\,l,\ i\,k\,h\,l)$ |

## 2. Structures of $\alpha$, $\beta$ phases and Dauphiné twin description

The high temperature $\beta$ phase of quartz is hexagonal ($a$=0.49965 nm, $c$=0.54570 nm at 848 K [24]). The structure is made of coupled chains of corner-sharing $SiO_4$ tetrahedra spiraling around the sixfold screw axis parallel to the $c$-direction (Fig. 1a). Coupled spirals are connected together via the tetrahedra corners. Depending on the sense of rotation of the spirals around the screw axis, the space group is $P6_222$ (right-handed) or $P6_422$ (left-handed). In these arrangements, the twofold axis contained within the sixfold screw axes symmetrically relates the spirals. When the quartz is cooled down to 573 °C, the tetrahedral chains kink by a first-order displacive transformation [25,26] and are no longer related by a twofold rotation around $c$. The structure then becomes trigonal $\alpha$ (threefold screw axis along $c$, with $a$=0.49137 nm, $c$=0.54047 nm at 298 K [24]), with space group $P3_221$ (left-handed) or $P3_121$

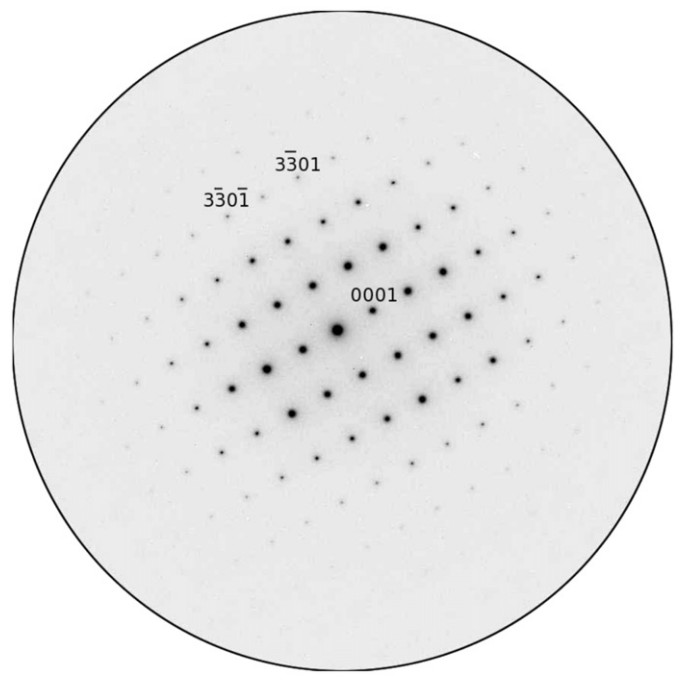


**Fig. 2.** Example of conventional SAED pattern taken along a $\langle 1\,1\,\bar{2}\,0\rangle$ zone axis in either the $\beta$ or $\alpha$ phase. No distinction is made between $\beta$ and $\alpha$ nor between $\alpha$ individuals.

**Table 2**
Structure factor amplitude and phase, extinction length of selected reflections in $\alpha$ as calculated with JEMS. *hkil* and *hkiī* reflections (lines (1) and (2)) are non-equivalent and have very different structure factors and extinction lenghts. *hkil* and $\bar{h}\bar{k}i\bar{l}$ reflections (lines (2) and (3), (4) and (5) or (7) and (8)) are equivalent with slightly different electron structure factors and extinction lengths, as well as *hkil* and circular permutations of $-h,\ -k,\ -i$ or $-h,\ -i,\ -k$ (lines (4) and (6), (7) and (9), (7) and (10)). *hkil* reflections and those related by a simple circular permutation of $\pm h,\ k,\ i$ or $\pm h,\ i,\ k$ are equivalent with equal structure factors and extinction lengths (line (7) and (11)). This last rule prevails on the previous one (lines (12) and (13)).

| | *hkil* | g ($nm^{-1}$) | Amplitude (V) | Phase (deg.) | Extinction length (nm) |
|---|---|---|---|---|---|
| (1) | $\bar{3}30\bar{1}$ | 7.2896 | 3.36081 | 1.15451 | 227.3295 |
| (2) | $\bar{3}301$ | 7.2896 | 0.70385 | 0.12859 | 1085.4682 |
| (3) | $3\bar{3}0\bar{1}$ | 7.2896 | 0.70385 | 0.12815 | 1085.4680 |
| (4) | $\bar{2}4\bar{2}0$ | 8.1417 | 1.9335 | −25.57244 | 395.1400 |
| (5) | $2\bar{4}20$ | 8.1417 | 1.9522 | 28.38005 | 391.3574 |
| (6) | $22\bar{4}0$ | 8.1417 | 1.9522 | 28.38005 | 391.3574 |
| (7) | $\bar{3}4\bar{1}0$ | 8.4741 | 2.27089 | −60.15069 | 336.4335 |
| (8) | $3\bar{4}10$ | 8.4741 | 2.2756 | 62.61367 | 335.7380 |
| (9) | $13\bar{4}0$ | 8.4741 | 2.2756 | 62.61367 | 335.7380 |
| (10) | $31\bar{4}0$ | 8.4741 | 2.2756 | 62.61367 | 335.7380 |
| (11) | $\bar{1}4\bar{3}0$ | 8.4741 | 2.27089 | −60.15069 | 336.4335 |
| (12) | $1\bar{1}00$ | 2.3503 | 3.5195 | 0.4566 | 217.0837 |
| (13) | $\bar{1}100$ | 2.3503 | 3.5195 | 0.4566 | 217.0837 |

Please cite this article as: D. Jacob, P. Cordier, Ultramicroscopy (2010), doi:10.1016/j.ultramic.2010.04.010

(right-handed). Whereas the chirality of the high-temperature phase is retained at low temperature, the symmetry lowering between $\beta$ and $\alpha$ induces twins, called Dauphiné twins, separating $\alpha_1$ and $\alpha_2$ individuals rotated by a 180° angle around $c$ (Fig. 1b and c) [27,28]. This rotation rebuilds the lost twofold axis for the twinned edifice. Between the $\alpha_1$ and $\alpha_2$ individuals, the lattice is the same but the atomic positions are modified: the twin is merohedral.

## 3. Electron diffraction and phase identification

Half of the equivalent reflections belonging to a general form *hkil* (i.e. whose reflecting planes are all related by the point group symmetry) in the hexagonal $\beta$ phase become non-equivalent in the trigonal $\alpha$ phase with reflections of the *hkil* form not belonging to the $hki\bar{l}$ form (see Table 1 for general equivalence relationships in $\alpha$ and $\beta$ phases as found in crystallography tables). These forms have the same spacing because of the same geometrical relation to the underlaying lattice but being unconnected by symmetry, their intensities of reflections are different. Differences in amplitude of electron structure factors of such $\beta$-equivalent reflections are generally large in the $\alpha$ phase (see, for instance, structure factors phase and amplitude of selected reflections listed in Table 2, as calculated with "JEMS" [29]). These differences have been originally used for dark-field imaging of Dauphiné twins related individuals, using, for example the $\bar{3}301$

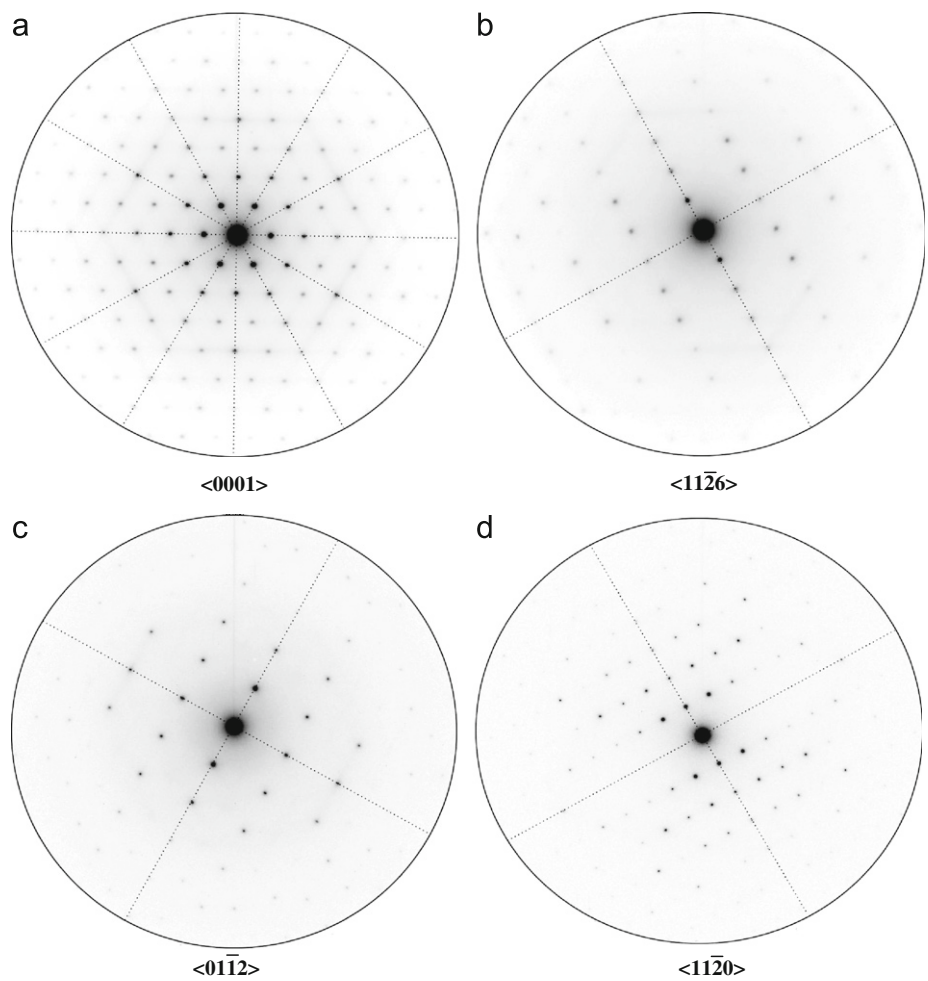


**Fig. 3.** Experimental PED patterns taken in $\beta$ ($T$~600 °C) along (a) ⟨0 0 0 1⟩, (b) ⟨1 1 $\bar{2}$ 6⟩, (c) ⟨0 1 $\bar{1}$ 2⟩ and (d) ⟨1 1 $\bar{2}$ 0⟩ orientations.

**Table 3**
Net and ideal ZAP symmetry for $\beta$ and $\alpha$ phases.

| | $\beta$ $P6_222$ point group: 622 Laue class 6/mm | | | $\alpha$ $P3_221$ point group: 32 Laue class $\bar{3}$m1 | | |
|---|---|---|---|---|---|---|
| | Diffraction class[a] | Net ZOLZ symmetry[b] | Ideal ZOLZ symmetry[b] | Diffraction class[a] | Net ZOLZ symmetry[b] | Ideal ZOLZ symmetry[b] |
| [0 0 0 1] | $6m_Rm_R$ | (6mm) | (6mm) | $3m_R$ | (6mm) | (3m) |
| ⟨1 1 $\bar{2}$ 6⟩ | $m_R$ | (2mm) | (m) | 1 | (2mm) | (1) |
| ⟨1 1 0 2⟩ | $m_R$ | (2mm) | (m) | $m_R$ | (2mm) | (m) |
| ⟨1 1 $\bar{2}$ 0⟩ | $2m_Rm_R$ | (2mm) | (2mm) | 2 | (2mm) | (2) |

[a] After Buxton et al. [33] and Tanaka et al. [34].
[b] After Morniroli and Steeds [39].

Please cite this article as: D. Jacob, P. Cordier, Ultramicroscopy (2010), doi:10.1016/j.ultramic.2010.04.010

and $3\bar{3}0\bar{1}$ reflections superimposed on parallel $\langle 1\,1\,\bar{2}\,0\rangle$ zone axis patterns (ZAP) originating from both individuals [30–32]. Nevertheless, resulting intensity differences of such non-equivalent reflections are generally not visible in a diffraction spot pattern obtained by conventional selected-area electron diffraction (SAED), due to multiple scattering (Fig. 2). Distinction of conventional spot patterns taken along parallel zone axes in $\alpha$ and $\beta$ phases, as well as in $\alpha$ twinned individuals, is then impossible. Furthermore, reflections belonging to the same form may have some slight differences in electron structure factors due to the symmetry elements of the point groups. In the $\alpha$ phase, this is the case for instance of $hkil$ and $\bar{h}\bar{k}\bar{i}\bar{l}$ reflections (and circular permutations of $\bar{h}$, $\bar{k}$, $\bar{i}$ or $\bar{h}$, $\bar{i}$, $\bar{k}$) except when they are also related by a circular permutation of $h$, $k$, $i$ or $h$, $i$, $k$ (see Table 2). To observe those weak intensity variations, convergent-beam electron diffraction (CBED) should be normally used. In this mode, intensities are displayed as a function of the orientation of the incident beam, varying within the convergence angle of the probe. Small amplitude and phase differences of reflections are then emphasized by dynamical interactions, and the so-called diffraction class symmetry is revealed [33,34]. This is the highest symmetry available on a CBED diffraction pattern taken from a thin foil. There are 31 diffraction classes and they are directly related to the 32 point groups symmetry. CBED patterns are thus of great use for crystal point and space group determination. Nevertheless, with this technique the small electron probe is focused on the sample and it generally cannot be applied on beam sensitive materials such as quartz, which rapidly becomes amorphous at ambient temperature when submitted to electron irradiation. A solution is to use the large-angle convergent-beam (LACBED) technique [35,36], in which the probe is defocused with respect to the sample position in the microscope. In this mode, numerous weak "quasi-kinematic" Bragg lines (deficiency lines), i.e. for which intensities are directly related to the square of the structure factors, are observed in the pattern and can be used to make the distinction between $\alpha$ individuals [37]. Distinction between $\alpha$ and $\beta$ phases can also be easily made. Nevertheless, the LACBED technique, whenever very sensitive to diffracted intensities and efficient for defect characterization, suffers from limiting disadvantages. As the probe is defocused, the observed area is generally large (a few microns) leading to a poor spatial resolution. Furthermore, the illuminated area may suffer from thickness variations and disorientation due to thinning of the sample to electron transparency. The patterns are then distorted, and this can severely limit the symmetry examination and phase identification. On the contrary, in SAED mode, the selected area

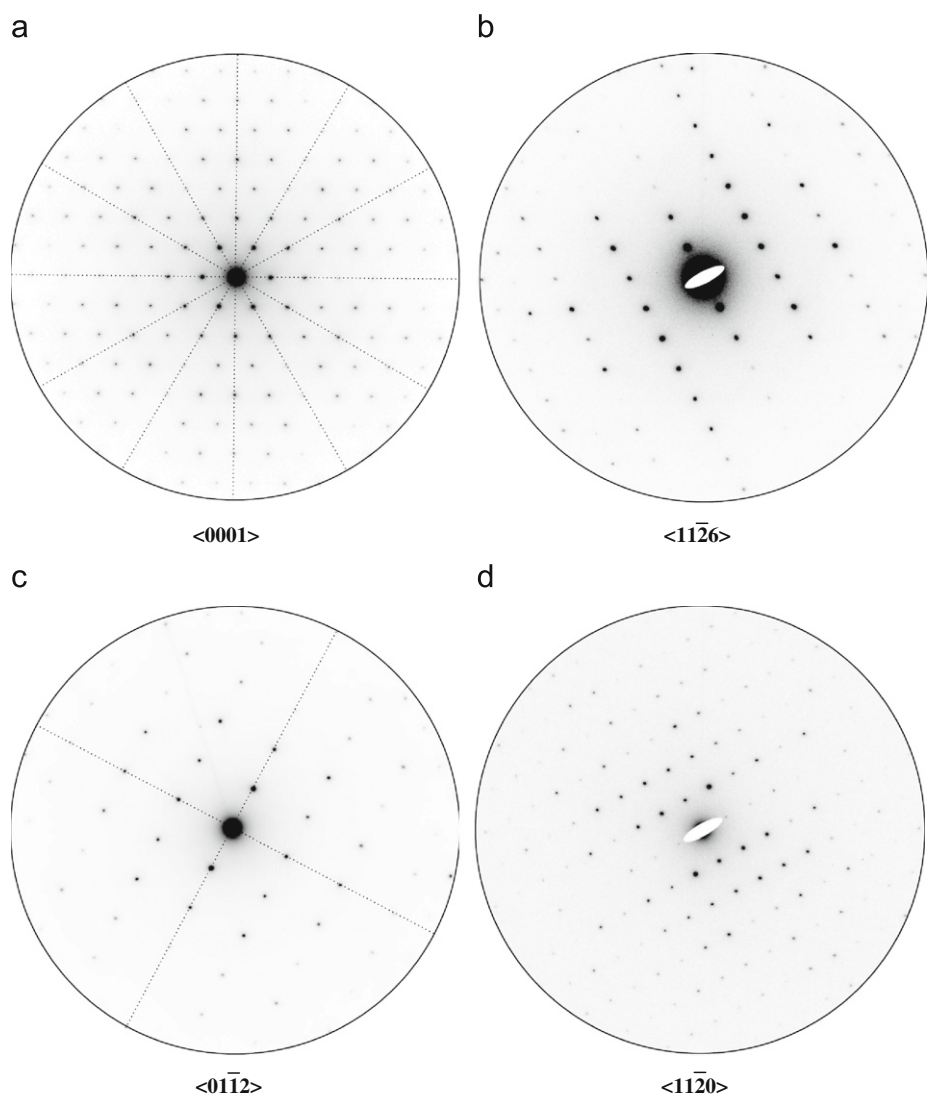


**Fig. 4.** Experimental PED patterns taken in individual $\alpha_1$ along (a) $\langle 0\,0\,0\,1\rangle$, (b) $\langle 1\,1\,\bar{2}\,6\rangle$, (c) $\langle 0\,1\,\bar{1}\,2\rangle$ and (d) $\langle 1\,1\,\bar{2}\,0\rangle$ orientations.

Please cite this article as: D. Jacob, P. Cordier, Ultramicroscopy (2010), doi:10.1016/j.ultramic.2010.04.010

can be quite small (about 500 nm). Furthermore, SAED is of low dose when a large parallel beam is used to illuminate the sample. Combined with precession, which reveals small differences in intensity related to the structure factors, the technique appears as a very good compromise for symmetry determination, phase identification and, more generally, structural characterization of a wide variety of materials, including beam sensitive minerals [22]. In this work, we take full advantage of the sensitivity of precession electron diffraction (PED) to reflection intensities to show that a distinction between the $\beta$, $\alpha$ phases and twinned individuals is readily possible in electron diffraction spot patterns. Another point that we will address concerns the relation between the symmetry of a PED patterns with respect to the highest zone axis symmetry, i.e. the diffraction class symmetry observed on CBED patterns, in the case of phases exhibiting small departure from the highest symmetry.

## 4. Experimental methods

Two specimens of synthetic $SiO_2$ quartz were cut along $\langle 0\,0\,0\,1 \rangle$ and $\langle 1\,1\,\bar{2}\,0 \rangle$ directions. The samples were mechanically thinned to about 60 μm, drilled out, glued to a 3 mm diameter copper TEM grid and ion-milled to electron transparency at 5 kV with an incident beam angle of 15°. Finally, the samples were coated with a thin carbon layer to promote electron conduction. TEM examinations were carried out in a Philips CM30 microscope operated at 300 kV. A Gatan heating holder was used to heat the specimens in-situ above the $\alpha$–$\beta$ transition (573 °C). The microscope is equipped with a Gatan 1 k × 1 k CCD camera and a Spinning Star precession module from Nanomegas. The maximum precession semi-angle is about 3°. Quartz being sensitive to electron irradiation, the diffraction patterns were generally obtained with a low-dose parallel electron incident beam, using a 5 μm selected-area aperture. Convergent-beam electron diffraction patterns were taken at high temperature (above 400 °C for the $\alpha$ phase) to slow down the amorphization of the sample exposed to the focused electron beam. Kinematical and dynamical patterns were calculated using the JEMS software from Stadelmann [29]. Dynamical multi-beam calculations of precessed patterns were carried out using the Bloch wave formalism with about 50 beams and using the Weickenmeier–Kohl atomic factors with phonon absorption. The space groups were chosen to be $P3_221$ for $\alpha$ and $P6_222$ for $\beta$. The actual chirality of the sample is not required for our analysis. In case the samples were of the opposite chirality, this would just change the absolute indexation of reflections [38].

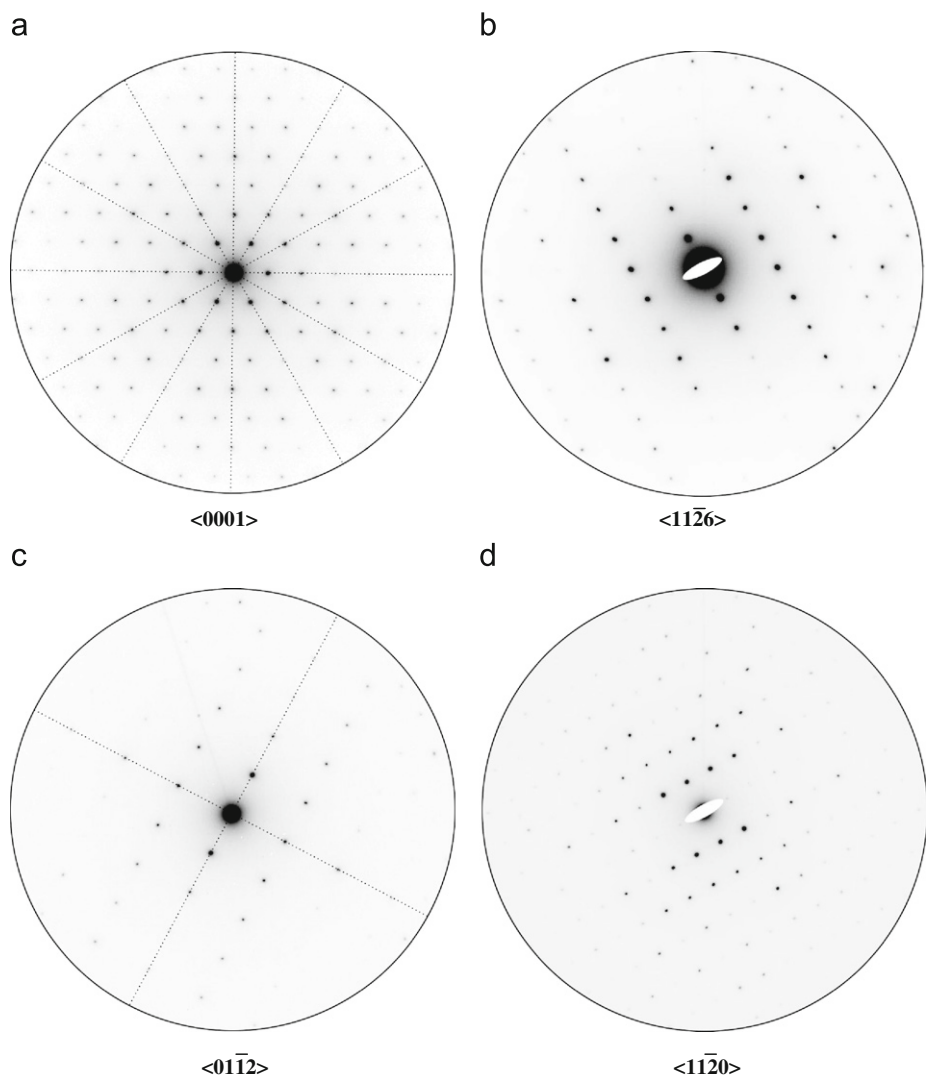


**Fig. 5.** Experimental PED patterns taken in individual $\alpha_2$ along (a) $\langle 0\,0\,0\,1 \rangle$, (b) $\langle 1\,1\,\bar{2}\,6 \rangle$, (c) $\langle 0\,1\,\bar{1}\,2 \rangle$ and (d) $\langle 1\,1\,\bar{2}\,0 \rangle$ orientations.

Please cite this article as: D. Jacob, P. Cordier, Ultramicroscopy (2010), doi:10.1016/j.ultramic.2010.04.010

ARTICLE IN PRESS



## 5. PED experimental results

### 5.1. PED patterns for the high-temperature $\beta$ phase

Four zone axis patterns (ZAP) have been recorded in the quartz samples far above the $\alpha/\beta$ transition temperature (Fig. 3a–d): $\langle 0\,0\,0\,1\rangle$, $\langle 1\,1\,\bar{2}\,6\rangle$, $\langle 0\,1\,\bar{1}\,2\rangle$ and $\langle 1\,1\,\bar{2}\,0\rangle$. Indexing is easily achieved based on the geometry and symmetry of the patterns. The $\langle 0\,0\,0\,1\rangle$ zone axis "net" symmetry is (6mm) ("net" means considering spot positions only, not intensities; parenthesis indicate that the symmetry concerns the zero-order Laue zone only [39]). The symmetry of $\langle 1\,1\,\bar{2}\,6\rangle$, $\langle 0\,1\,\bar{1}\,2\rangle$ and $\langle 1\,1\,\bar{2}\,0\rangle$ is (2mm), which is consistent with the hexagonal $\beta$ phase, as seen in Table 3. If we now refer to the point group symmetry, spots intensity distribution has to be considered, i.e. the "ideal" symmetry of the patterns has to be analyzed (Table 3). In the $\beta$ phase (point group 622), the $\langle 0\,0\,0\,1\rangle$ ZOLZ symmetry should be ($\underline{6mm}$) (underlined means "ideal"), $\langle 1\,1\,\bar{2}\,6\rangle$ and $\langle 0\,1\,\bar{1}\,2\rangle$ should be ($\underline{m}$) and $\langle 1\,1\,\bar{2}\,0\rangle$ should be ($\underline{2mm}$). These theoretical results correspond to experimental ones for $\langle 0\,0\,0\,1\rangle$ (Fig. 3a, ideal symmetry: ($\underline{6mm}$)) and $\langle 1\,1\,\bar{2}\,0\rangle$ (Fig. 3d, ideal symmetry: ($\underline{2mm}$)), but not for $\langle 1\,1\,\bar{2}\,6\rangle$ (Fig. 3b) nor $\langle 0\,1\,\bar{1}\,2\rangle$ (Fig. 3d), which also appear as ($\underline{2mm}$). Obviously the point group symmetry, which can be revealed with CBED experiments (or microdiffraction, obtained with a small convergence angle), is not fully restored with spot PED patterns obtained with a parallel beam. In this case, HOLZ reflections, which are missing on experimental patterns, are required for the point group determination. This could be achieved, thanks to a slight off-axis tilt of the beam or the specimen to see the HOLZ reflections. This is nevertheless out of the scope of the present work.

### 5.2. PED patterns for the low temperature individuals

After cooling to ambient temperature, some twins separating $\alpha_1$ and $\alpha_2$ individuals appeared. The ZAPs taken in the same orientation as for the $\beta$ phase have been recorded from both sides of a twin plane (Figs. 4 and 5). The [0 0 0 1] ZAPs (Figs. 4a and 5a) appear as (6mm) and ($\underline{6mm}$) concerning, respectively, the net and ideal symmetry. The expected ($\underline{3m}$) symmetry (loss of a mirror with respect to the $\beta$ 622 point group; see Table 3) associated with the point group 32 of the $\alpha$ phase is not observed at a first glance. This point will be analyzed more quantitatively in the last section of this paper. Furthermore, in this orientation no distinction can be made between the two individuals. On the contrary, some clear differences in spot intensities appear for the other ZAPs taken from both individuals. As for the $\beta$ phase, the patterns are (2mm) concerning the spot positions (ZOLZ only), but $\langle 1\,1\,\bar{2}\,6\rangle$ and $\langle 1\,1\,\bar{2}\,0\rangle$ are ($\underline{2}$) (Figs. 4b and d, and 5b and d)

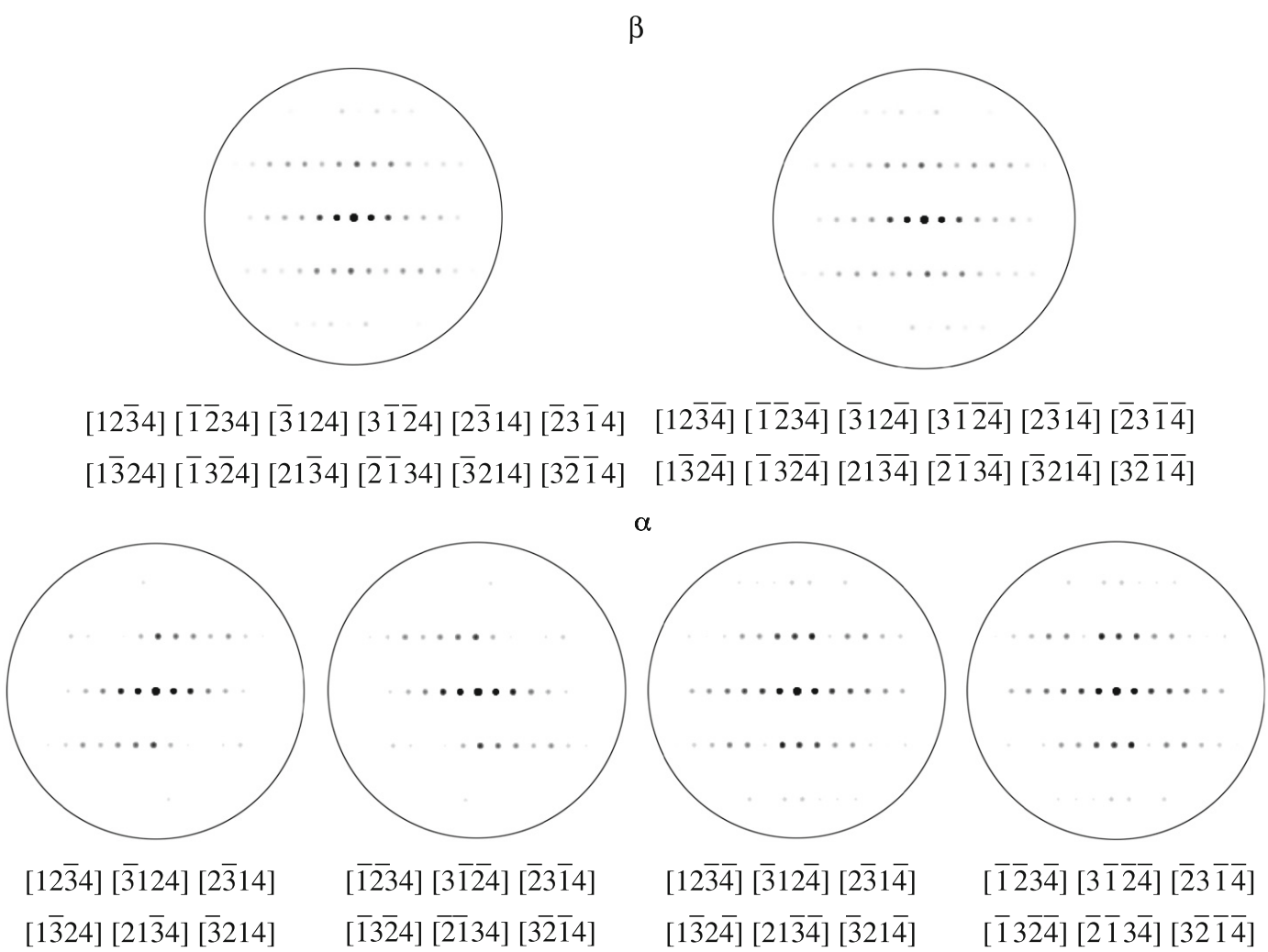


**Fig. 6.** Kinematically simulated patterns for a general $\langle 1\,2\,\bar{3}\,4\rangle$ zone axis in $\beta$ and $\alpha$.

Please cite this article as: D. Jacob, P. Cordier, Ultramicroscopy (2010), doi:10.1016/j.ultramic.2010.04.010

whereas $\langle 0\,1\,\bar{1}\,2\rangle$ is (2mm) (Figs. 4c and 5c) concerning the ideal symmetry. Even if this is not fully consistent with the ZAPs symmetry expected from the $\alpha$ phase point group – that should be (1) and (m) for $\langle 1\,1\,\bar{2}\,6\rangle$ and $\langle 0\,1\,\bar{1}\,2\rangle$, respectively (Table 3) – the distinction can be easily made between the two individuals. In particular, $\langle 1\,1\,\bar{2}\,6\rangle$ and $\langle 1\,1\,\bar{2}\,0\rangle$ patterns taken from both sides of the twin appear as mirror-like, whereas $\langle 0\,1\,\bar{1}\,2\rangle$ patterns, which contain two internal mirrors, show distinguishable spot intensity distributions.

## 6. Absolute indexing of the patterns and twin law determination

In the hexagonal phase, for the general case $u \neq v \neq 0$ and $w \neq 0$, 24 equivalent directions belonging to the $\langle u\,v\,t\,w\rangle$ form are obtained. The 24 zone axes deriving from this form give only two non-superimposable and mirror related diffraction patterns (see kinematical simulated patterns in Fig. 6 for the general $\langle 1\,2\,\bar{3}\,4\rangle$ form). In the trigonal phase, this form splits in two different forms $\langle u\,v\,t\,w\rangle$ and $\langle u\,v\,t\,\bar{w}\rangle$ containing 12 equivalent directions (Table 1). Each of this form also gives two mirror related patterns (Fig. 6). Between the hexagonal and trigonal phases, as well as between orientations belonging to the two previous forms in the trigonal phase, the geometry of the patterns is the same but the spot intensity distribution is different.

In the case of the 12 equivalent directions belonging to the $\langle u\,u\,2\,\bar{u}\,w\rangle$ form (such as $\langle 1\,1\,\bar{2}\,6\rangle$), the patterns are (2mm)/(2mm) in the hexagonal phase and there is a unique kind of pattern (Fig. 7). In the trigonal phase, the $\langle u\,u\,2\,\bar{u}\,w\rangle$ orientations are still equivalent. Nevertheless, the patterns being in this case (2mm)/(2), two kinds of mirror-related patterns are obtained. This enables to distinguish between $\langle u\,u\,2\,\bar{u}\,w\rangle$ and $\langle \bar{u}\,\bar{u}\,2\,\bar{u}\,\bar{w}\rangle$ orientations in the trigonal phase. The same applies for the 6 equivalent orientations belonging to the $\langle u\,u\,2\,\bar{u}\,0\rangle$ form (such as $\langle 1\,1\,\bar{2}\,0\rangle$; see Fig. 8) in the hexagonal and trigonal phases.

In both phases, the ZAPs belonging to the $\langle 0\,u\,\bar{u}\,w\rangle$ form such as $\langle 0\,1\,\bar{1}\,2\rangle$ are (2mm)/(2mm) (Fig. 9). For the hexagonal phase, a single kind of pattern is obtained for the 12 equivalent orientations. The form splits in two $\langle 0\,u\,\bar{u}\,w\rangle$ and $\langle 0\,u\,\bar{u}\,\bar{w}\rangle$ forms in the trigonal phase containing 6 equivalent directions. Two kinds of patterns are then obtained, exhibiting the same geometry with different spot intensities' distribution.

Finally, for the $\langle 0\,0\,0\,1\rangle$ form, there is a unique kind of pattern in both $\beta$ and $\alpha$ phases (Fig. 10). Between the two phase patterns, the geometry is the same but the intensity distribution is different.

The coherent indexing of the four $\beta$ patterns (Fig. 3) only relies on an arbitrary choice, which can be made for two patterns: the

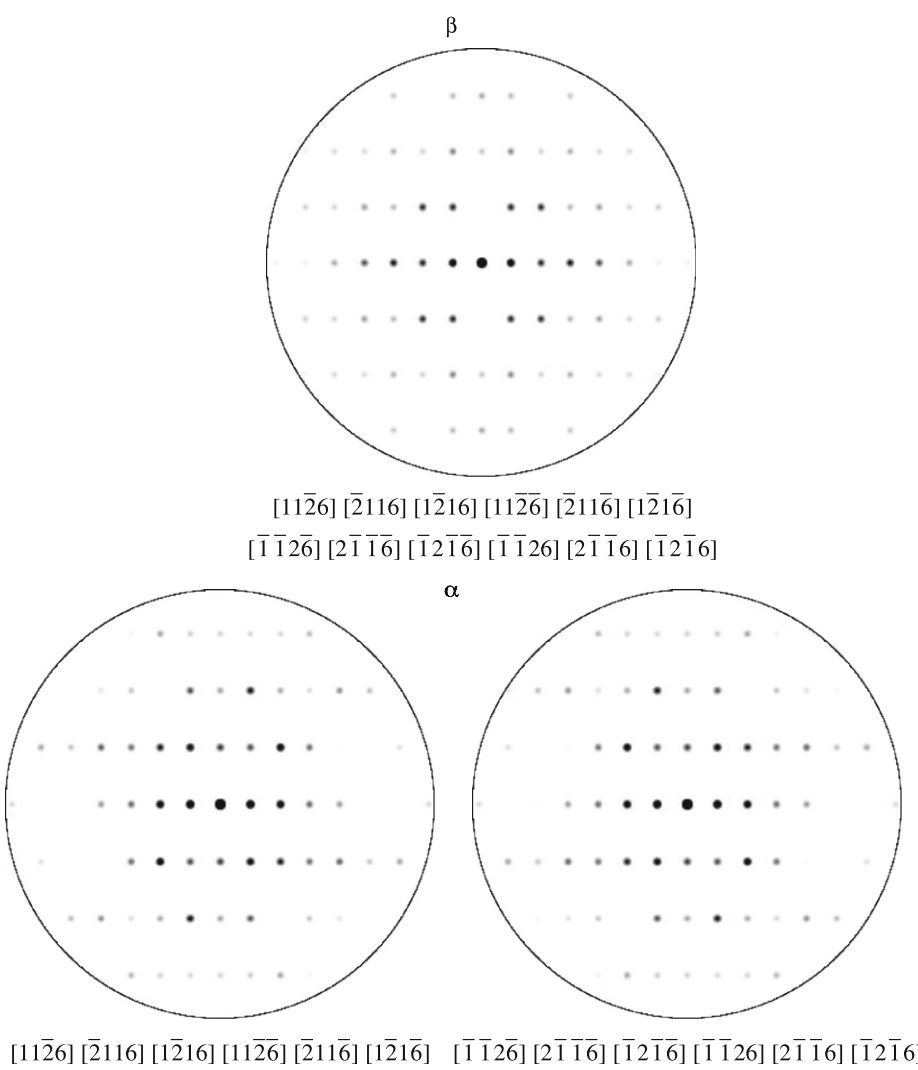


**Fig. 7.** Kinematically simulated patterns for a $\langle 1\,1\,\bar{2}\,6\rangle$ zone axis in $\beta$ (a) and $\alpha$ (b and c).

Please cite this article as: D. Jacob, P. Cordier, Ultramicroscopy (2010), doi:10.1016/j.ultramic.2010.04.010

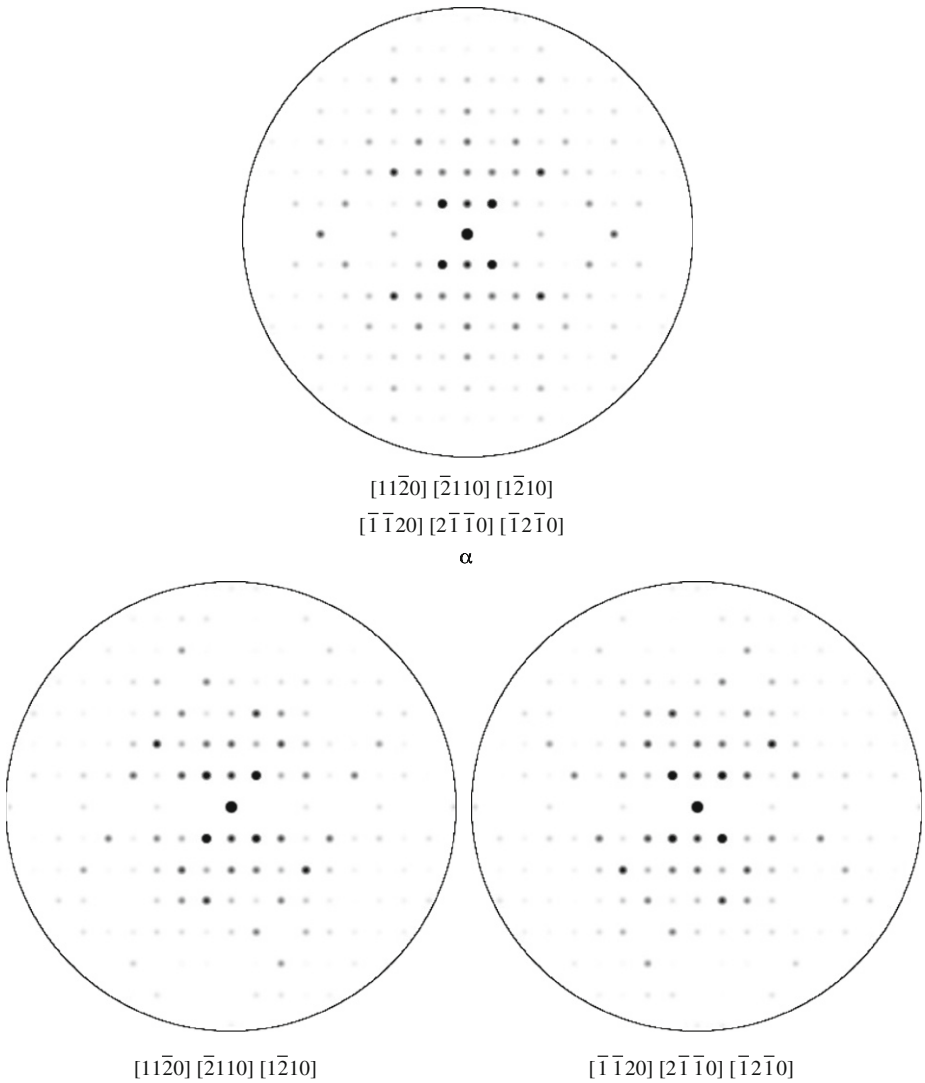


**Fig. 8.** Kinematically simulated patterns for a $\langle 0\,1\,\bar{1}\,2 \rangle$ zone axis in $\beta$ (a) and $\alpha$ (b and c).

first pattern is chosen to be [0 0 0 1] and the second one [1 1 $\bar{2}$ 6]. Then, taking into account the experimental tilt angle between the orientations, the third pattern corresponds to [0 1 $\bar{1}$ 2] (about 20° from [1 1 $\bar{2}$ 6]) and the fourth one to [1 1 $\bar{2}$ 0] (90° from [0 0 0 1], see the stereographic projection in Fig. 11). In the $\alpha$ phase (Figs. 4 and 5), the absolute patterns indexing from each individual have to be made, thanks to comparison with simulations, taking into account the spot intensities. Obviously, the match between experimental and kinematically simulated patterns is not fully satisfactory due to dynamical effects in the experimental patterns, but it is sufficient to properly index the patterns. For instance, the experimental patterns of Figs. 4b and 5b best correspond to $\langle 1\,1\,\bar{2}\,6 \rangle$ and $\langle \bar{1}\,\bar{1}\,2\,\bar{6} \rangle$ types (Fig. 7). If the direction is chosen to be [1 1 $\bar{2}$ 6] for the first individual $\alpha_1$, then it can either be [$\bar{1}$ $\bar{1}$ 2 6], [2 $\bar{1}$ $\bar{1}$ 6] or [$\bar{1}$ 2 $\bar{1}$ 6] for the second one $\alpha_2$. We choose first [$\bar{1}$ $\bar{1}$ 2 6]. Then, the patterns are coherently indexed in $\alpha_1$ and $\alpha_2$ taking into account the experimental tilt angles between the zone axes. Comparison of Figs. 4 and 5 with Figs. 7–9 leads to the determination of the following four pairs of parallel directions in $\alpha_1$ and $\alpha_2$ individuals:

$$[0\,0\,0\,1]_1 \parallel [0\,0\,0\,1]_2 \quad \text{(I)}$$

$$[1\,1\,\bar{2}\,6]_1 \parallel [\bar{1}\,\bar{1}\,2\,6]_2 \quad \text{(II)}$$

$$[0\,1\,\bar{1}\,2]_1 \parallel [0\,\bar{1}\,1\,2]_2 \quad \text{(III)}$$

$$[1\,1\,\bar{2}\,0]_1 \parallel [\bar{1}\,\bar{1}\,2\,0]_2 \quad \text{(IV)}$$

The deduction of the twin law is obvious based on the stereographic projection drawn along the common [0 0 0 1] orientation (Fig. 11), which corresponds to the rotation axis between the two individuals. The rotation angle is equal to 180°, as expected for the Dauphiné twin. Having chosen [2 $\bar{1}$ $\bar{1}$ 6] or [$\bar{1}$ 2 $\bar{1}$ 6] for the second orientation in $\alpha_2$ would have result in a 60° rotation between the two individuals, which leads to the same structural results with a change of basis vector for the unit cell.

## 7. Comparison of PED and CBED patterns' symmetry

For comparison with PED data, CBED experiments have been performed at high temperature ( > 400 °C) to slow down the amorphization of the sample under the electron beam. Results are shown in Fig. 12 for the $\beta$ and $\alpha$ [0 0 0 1] ZAPs. The patterns

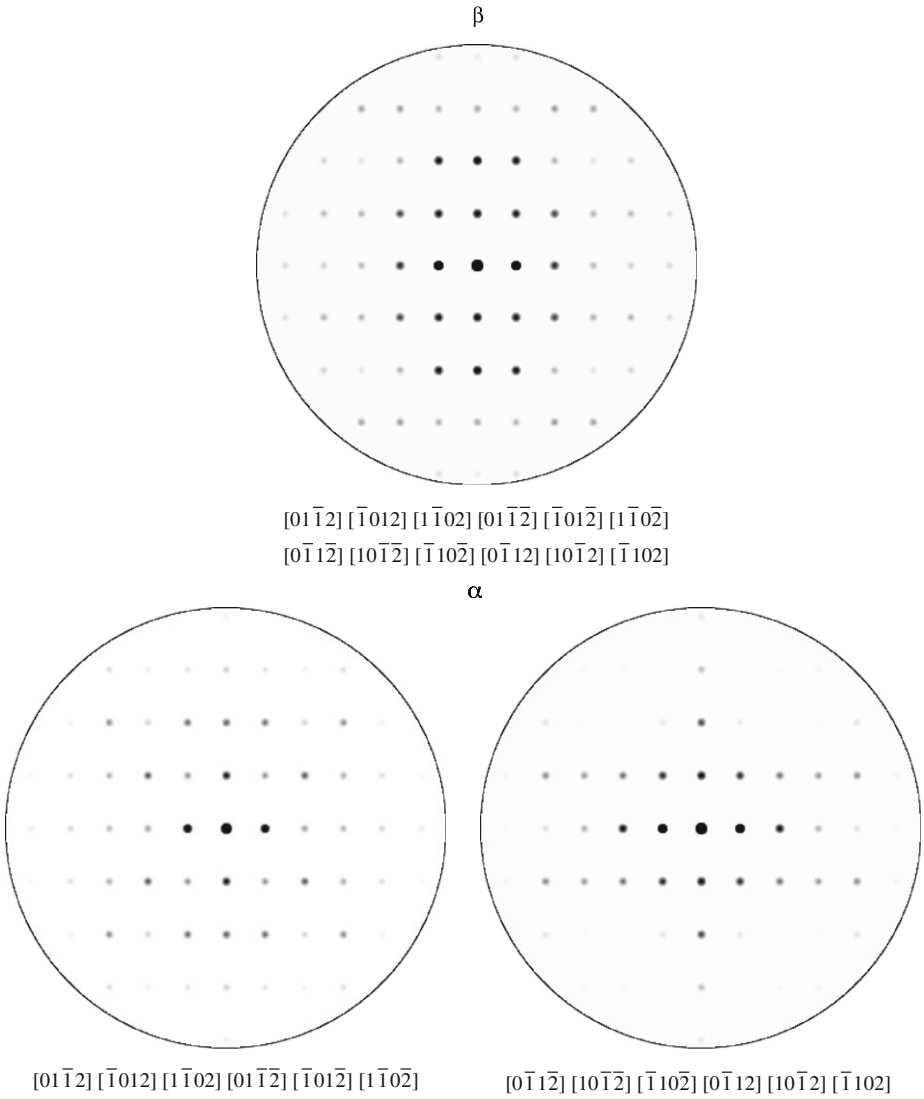


**Fig. 9.** Kinematically simulated patterns for a $\langle 1\,1\,\bar{2}\,0 \rangle$ zone axis in $\beta$ (a) and $\alpha$ (b and c).

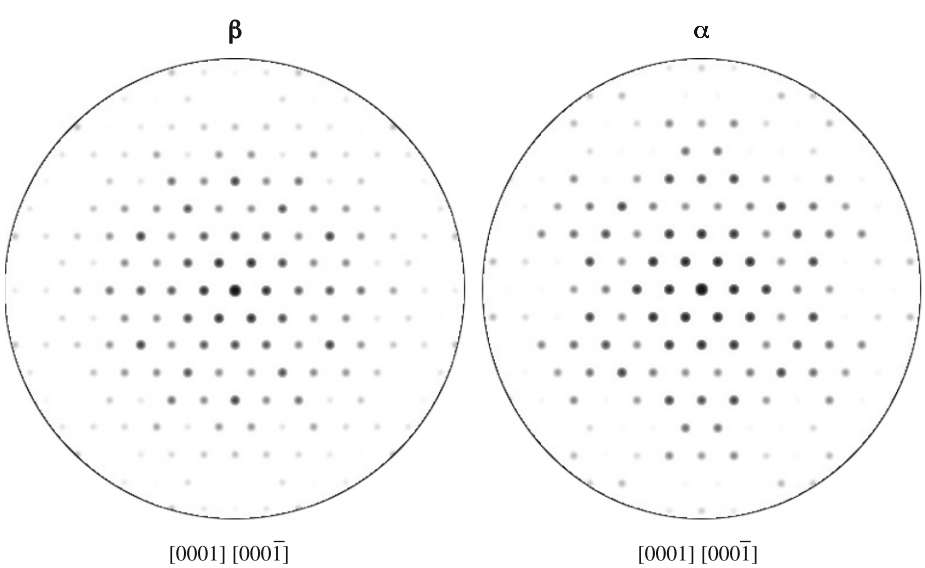


**Fig. 10.** Kinematically simulated patterns for a $\langle 0\,0\,0\,1 \rangle$ zone axis in $\beta$ (1a) and $\alpha$ (1b).

Please cite this article as: D. Jacob, P. Cordier, Ultramicroscopy (2010), doi:10.1016/j.ultramic.2010.04.010

exhibit the expected (6mm) and (3m) projected symmetries for the hexagonal 622 and trigonal 32 point groups (Table 3), respectively. In comparison, the PED [0 0 0 1] ZAP in $\alpha$ (Fig. 4a) seems to be (6mm). Nevertheless, a careful examination of intensity distribution for reflections located far away from the transmitted spot reveals the (3m) symmetry, with different intensity levels for equivalent reflections located at 30°from each other (such as $\bar{3}4\bar{1}0$ and $13\bar{4}0$, $\bar{1}4\bar{3}0$ and $31\bar{4}0$, see Fig. 13). This intensity distribution is well reproduced all over the pattern as shown on the intensity profiles of selected reflections in Fig. 13. Nevertheless, this result is very dependant of the chosen illuminated area, and most of the patterns taken in various places of the specimen only exhibit a (6mm) symmetry without intensity modulation for reflections located at 30° from each other. This behavior is well understood, thanks to dynamical simulations. They show that intensity variations of equivalent reflections such as those observed experimentally are sensitive to the actual sample thickness (Fig. 14). The intensity distribution revealing the (3m) symmetry – with $\bar{3}4\bar{1}0$ and $13\bar{4}0$, $\bar{1}4\bar{3}0$ and $31\bar{4}0$, having different intensity levels with $\bar{2}4\bar{2}0$ and $22\bar{4}0$, respectively – is only found for thickness values around 65 nm, which must then approximately correspond to the sample thickness for the pattern of Fig. 13. For higher thicknesses, the two sets of reflections tend to have the same intensity levels. Of course, this kind of comparison between simulated and experimental data has to remain semi-quantitative since, quartz being beam sensitive, our experimental results correspond to SAED patterns. In this mode, intensities are averaged over the illuminated area, which can be as large as a few hundreds of nanometers and is not perfectly flat contrarily to the ideal crystal considered for simulations.

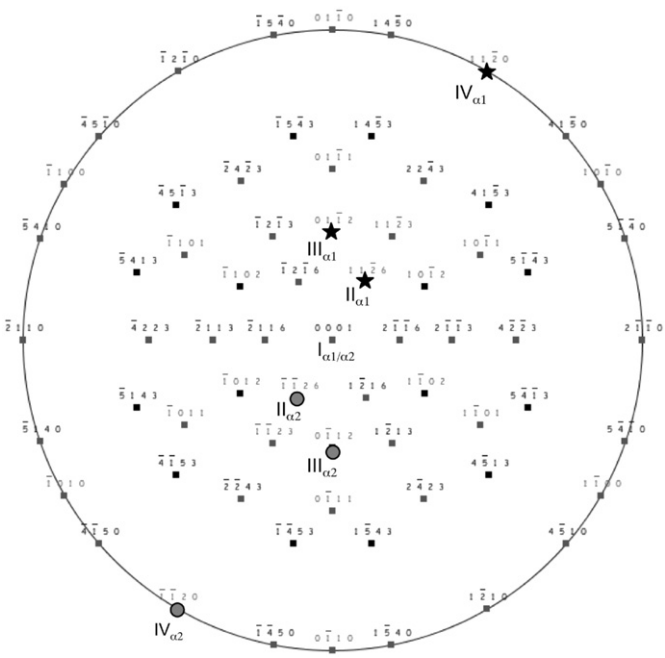


**Fig. 11.** [0 0 0 1] stereographic projection in $\alpha$. Poles from individual $\alpha_1$ and $\alpha_2$ are labelled with stars and circles, respectively. A 180° rotation along [0 0 0 1] put the zone axes of both individuals in coincidence.

## 8. Conclusion

PED has been successively used for the distinction of $\beta$ and $\alpha$ phases of quartz, which only differ by a small kink of the $SiO_4$ tetrahedra inducing a symmetry lowering from an hexagonal to a trigonal space group. This distinction cannot be achieved using conventional SAED patterns, due to the dynamical averaging of the intensity. Examination of the intensity distribution in the $\alpha$ patterns also enabled the characterization of the merohedral twinning induced by the $\beta$–$\alpha$ transition, the so-called Dauphiné twin, as it has been previously done in the case of the pseudo-merohedral twinning in $SiO_2$ coesite [22]. On these beam sensitive materials, observations can be made in low-dose SAED and some simple kinematical simulations are needed for the interpretation.

As far as the symmetry of the PED patterns is concerned, we showed that a careful examination of intensity distribution in the $\alpha$ phase enables to retrieve the diffraction class symmetry

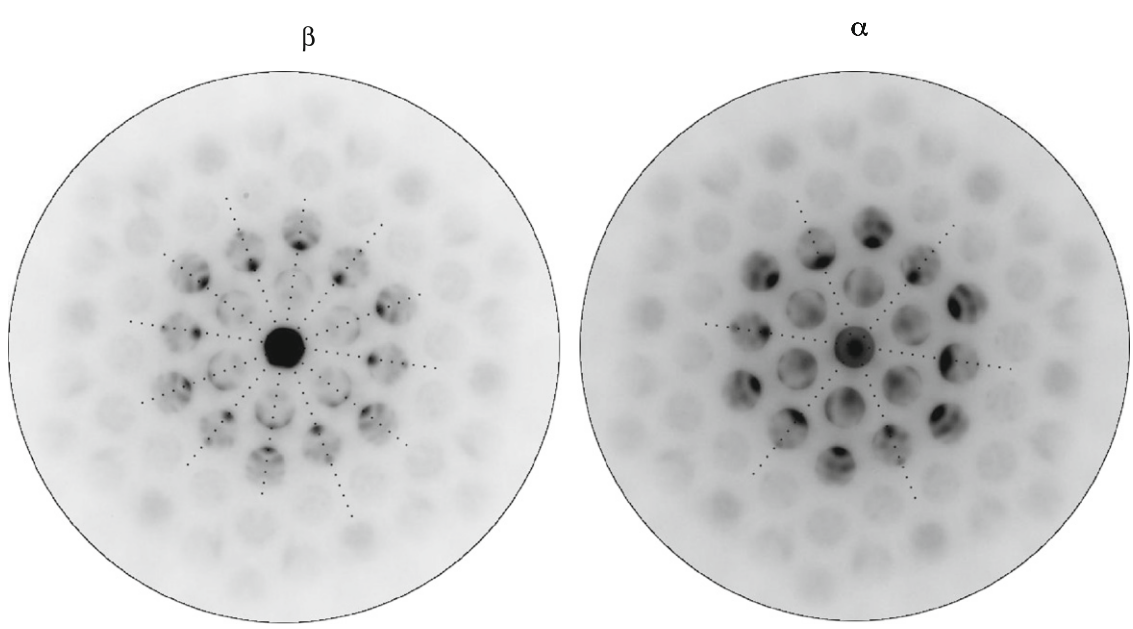


**Fig. 12.** CBED [0 0 0 1] patterns in $\beta$ and $\alpha$ phases.

Please cite this article as: D. Jacob, P. Cordier, Ultramicroscopy (2010), doi:10.1016/j.ultramic.2010.04.010

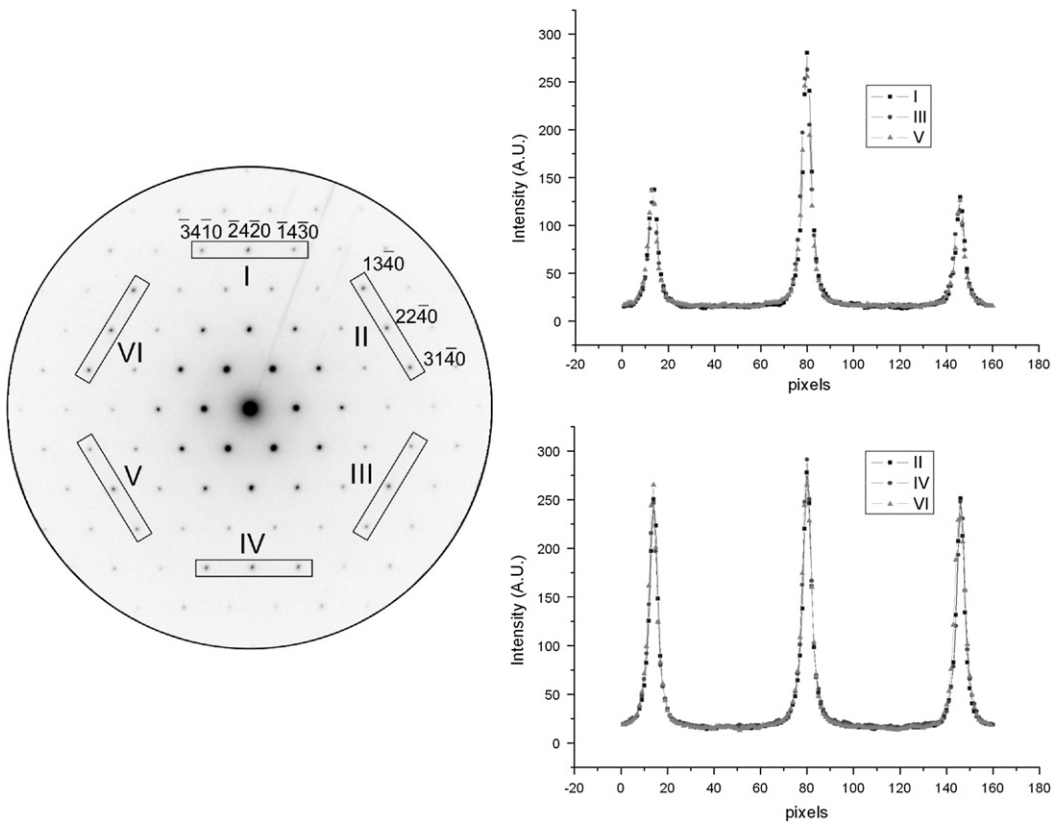


**Fig. 13.** PED [0 0 0 1] pattern in α phase and intensity profiles of reflections belonging to the $\langle 1\,3\,\bar{4}\,0 \rangle$ and $\langle \bar{2}\,4\,\bar{2}\,0 \rangle$ forms.

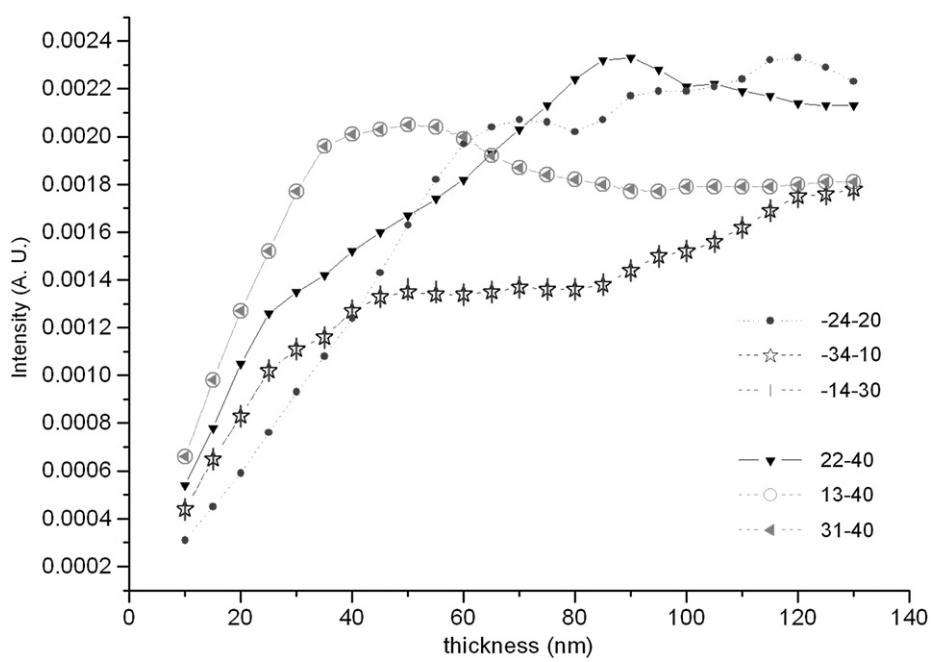


**Fig. 14.** Dynamical simulations of intensities of reflections belonging to the $\langle 1\,3\,\bar{4}\,0 \rangle$ and $\langle \bar{2}\,4\,\bar{2}\,0 \rangle$ forms as a function of the sample thickness. Precession semi-angle is 3°, corresponding to the experimental value.

connected to the point group, as it is currently done in CBED. Nevertheless, this result strongly depends on the thickness of the sample and is not systematically achievable using a finite size aperture for SAED experiments. When possible, CBED should be preferred for the point group determination.

## Acknowledgments

Many thanks are due to J.P. Morniroli for fruitful discussions and re-reading the manuscript. We are also very grateful to Priscille Cuvillier for valuable help in data interpretation. The TEM

ARTICLE IN PRESS



national facility in Lille is supported by the CNRS (INSU) and the Conseil Régional du Nord – Pas de Calais, France.

## References

[1] R. Vincent, P.A. Midgley, Ultramicroscopy 53 (1994) 271–282.
[2] K. Gjönnes, Ultramicroscopy 69 (1997) 1–11.
[3] B.S. Berg, V. Hansen, P.A. Midgley, J. Gjönnes, Ultramicroscopy 74 (1998) 147–157.
[4] P. Oleynikov, S. Hovmôller, X.D. Zou, Ultramicroscopy 107 (2007) 523–533.
[5] W. Sinkler, C.S. Own, L.D. Marks, Ultramicroscopy 107 (2007) 543–550.
[6] J.P. Morniroli, A. Redjaïmia, S. Nicolopoulos, Ultramicroscopy 107 (2007) 514–522.
[7] J.P. Morniroli, F. Houdellier, C. Roucau, J. Puiggali, S. Gestia, A. Redjaïmia, Ultramicroscopy 108 (2008) 100–115.
[8] C.S. Own, W. Sinkler, L.D. Marks, Ultramicroscopy 106 (2006) 114–122.
[9] A. Kverneland, V. Hansen, R. Vincent, K. Gjönnes, J. Gjönnes, Ultramicroscopy 106 (2006) 492–502.
[10] T.E. Weirich, J. Portillo, G. Cox, H. Hibst, S. Nicolopoulos, Ultramicroscopy 106 (2006) 164–175.
[11] K. Boulahya, L. Ruiz-Gonzalez, M. Parras, J.M. Gonzalez-Calbet, M.S. Nickolsky, S. Nicolopoulos, Ultramicroscopy 107 (2007) 445–452.
[12] D.L. Dorset, C.J. Gilmore, J.L. Jorda, S. Nicolopoulos, Ultramicroscopy 107 (2007) 462–473.
[13] A. Dudka, A. Avilov, G. Lepeshov, Crystallography Reports 53 (2008) 530–536.
[14] A.P. Dudka, A.S. Avilov, S. Nicolopoulos, Ultramicroscopy 107 (2007) 474–482.
[15] M. Gemmi, S. Nicolopoulos, Ultramicroscopy 107 (2007) 483–494.
[16] P.A. Midgley, M.E. Sleight, M. Saunders, R. Vincent, Ultramicroscopy 75 (1998) 61–67.
[17] A. Avilov, K. Kuligin, S. Nicolopoulos, M. Nickolskiy, K. Boulahya, J. Portillo, G. Lepeshov, B. Sobolev, J.P. Collette, N. Martin, A.C. Robins, P. Fischione, Ultramicroscopy 107 (2007) 431–444.
[18] J. Ciston, B. Deng, L.D. Marks, C.S. Own, W. Sinkler, Ultramicroscopy 108 (2008) 514–522.
[19] T.A. White, A.S. Eggeman, P.A. Midgley, Ultramicroscopy 110 (2010) 763–770.
[20] A.S. Eggeman, T.A. White, P.A. Midgley, Ultramicroscopy 110 (2010) 771–777.
[21] C.S. Own, L.D. Marks, W. Sinkler, Acta Crystallographica: Section A 62 (2006) 434–443.
[22] D. Jacob, P. Cordier, J.P. Morniroli, H.P. Schertl, American Mineralogist 94 (2009) 684–692.
[23] G. Ji, J.P. Morniroli, G.J. Auchterlonie, J. Drennan, D. Jacob, Ultramicroscopy 109 (2009) 1282–1294.
[24] K. Kihara, European Journal of Mineralogy 2 (1990) 63–77.
[25] G. Dolino, Phase Transitions 21 (1990) 59–72.
[26] M.H. Muser, K. Binder, Physics and Chemistry of Minerals 28 (2001) 746–755.
[27] C. Frondel, American Mineralogist 30 (1945) 447–460.
[28] P.J. Heaney, D.R. Veblen, American Mineralogist 76 (1991) 1018–1032.
[29] P. Stadelmann, JEMS, Electron Microscopy Software, java Version, CIME-EPFL, CH 1015 Lausanne, 2004.
[30] A.C. McLaren, P.P. Phakey, Physica Status Solidi 31 (1969) 723–737.
[31] J.J. Comer, Journal of Crystal Growth 15 (1972) 179–187.
[32] G. Van Tendeloo, J. Van Landuyt, S. Amelinckx, Physica Status Solidi A—Applied Research 33 (1976) 723–735.
[33] B.F. Buxton, J.A. Eades, J.W. Steeds, G.M. Rackham, Philosophical Transactions of the Royal Society of London Series A—Mathematical Physical and Engineering Sciences 281 (1976) 171–194.
[34] M. Tanaka, R. Saito, H. Sekii, Acta Crystallographica A 39 (1983) 357–368.
[35] M. Tanaka, K. Ueno, Y. Harada, Journal of Electron Microscopy 29 (1980) 408–412.
[36] D. Jacob, P. Cordier, J.P. Morniroli, H.-P. Schertl, European Journal of Mineralogy 20 (2008) 119–124.
[37] P. Cordier, J.P. Morniroli, D. Cherns, Philosophical Magazine A 72 (1995) 1421–1430.
[38] P. Goodman, T.W. Secomb, Acta Crystallographica A 33 (1977) 126–133.
[39] J.P. Morniroli, J.W. Steeds, Ultramicroscopy 45 (1992) 219–239.

Please cite this article as: D. Jacob, P. Cordier, Ultramicroscopy (2010), doi:10.1016/j.ultramic.2010.04.010

# Microstructures des échantillons cométaires de la mission Stardust

*Meteoritics & Planetary Science* 44, Nr 10, 1475–1488 (2009)
Abstract available online at http://meteoritics.org

# Pyroxenes microstructure in comet 81P/Wild 2 terminal Stardust particles

Damien JACOB[1*], Julien STODOLNA[1], Hugues LEROUX[1], Falko LANGENHORST[2], and F. HOUDELLIER[3]

[1]Laboratoire de Structure et Propriétés de l'Etat Solide, Université des Sciences et Technologies de Lille and CNRS, UMR 8008, F-59655 Villeneuve d'Ascq, France
[2]Bayerisches Geoinstitut, Universität Bayreuth, D-95440 Bayreuth, Germany
[3]CEMES/CNRS, 29 rue Jeanne Marvig, 31055 Toulouse, France
[*]Corresponding author. E-mail: damien.jacob@univ-lille1.fr

*(Received 24 March 2009; revision accepted 25 June 2009)*

**Abstract**–We report the examination by transmission electron microscopy (TEM) of four Stardust terminal particles extracted from two neighboring tracks (32 an 69). The particles are made of well-preserved crystalline grains dominated by low-Ca pyroxene ranging from nearly pure enstatite to pigeonite. Some olivine grains are also found, in chemical equilibrium with the surrounding pyroxenes. Various microstructures are observed, as a function of the composition of the grains. They include (100)-twinned pigeonite, clino/ortho domains in enstatite and exsolution in a Ca-rich grain. The microstructures are mostly consistent with a formation by cooling from high-temperature phases, which could be associated to igneous processes. Some dislocations in glide configuration are also present, probably attesting for small intensity shocks. Possible effects of the rapid heating/cooling stage and thermal shock associated to the collect are discussed. It appears that most of the microstructural features reported here are plausibly pristine.

## INTRODUCTION

The first examinations of captured dust particles from comet Wild 2 have been carried out in laboratories since the NASA Stardust capsule successfully returned the samples to Earth in January 2006 (Brownlee et al. 2006). Preliminary examination period revealed that the Wild 2 particles have been more or less severely thermally modified by the capture process due to hypervelocity impact at 6.1 km $s^{-1}$ into silica aerogel capture media (Zolensky et al. 2006). The shape of tracks and the presence of individual components dispersed along the track indicates that Wild 2 dust have been alternatively loose aggregates (Hörz et al. 2006; Zolensky et al. 2006) or large mineral grains that have fragmented along the tracks (Burchell et al. 2008). In all cases, the larger components have penetrated more deeply into the aerogel and are found as terminal particles. These terminal particles are usually coarse-grained crystalline material (over 1 micrometer) and are found relatively well preserved from thermal capture modification. They include CAI-like particles (Simon et al. 2006) and chondrule-like objects (Nakamura et al. 2008), which suggests that some Wild 2 material is comparable to already known chondritic meteorites from the asteroid belt (Ishii et al. 2008). These observations support also the view of particle formation in the inner region of solar nebula followed by a large-scale radial mixing of matter in the protoplanetary disk before accretion in the comet.

Terminal particles are dominated by coarse-grained silicate grains (olivine and pyroxene) with a wide compositional variation (Zolensky et al. 2008a). In this context, fine-scale analysis of pyroxene-bearing particles is of peculiar interest to estimate formation conditions because pyroxenes are good indicators of thermal and deformational events. "Two pyroxene" thermometry is a useful tool for constraining the equilibration temperature of igneous and metamorphic rocks. This method is based on the distribution of Ca, Fe, and Mg between orthopyroxene and clinopyroxene over the 700–1500 °C range of temperatures (e.g., Ross and Huebner 1979; Lindsley 1983; Lindsley and Andersen 1983; Davidson and Lindsley 1985). Mg, Ca, and Fe cations ordering is also used as geospeedometer (e.g., Zema et al. 2003). Pyroxenes easily incorporate minor elements such as Na, Al, Ti, Cr, and Mn, and their partitioning in the crystallographic sites is a sign of the conditions of phase formation. This also applies to rare earth elements (REE), which frequently display zoning because of their slow diffusion rate (e.g., Papike et al. 2005; Papike 1996). Unlike olivine, pyroxene grains frequently record complex exsolution textures during cooling, and this can be used to decipher the igneous history (e.g., McCalister and Nord 1981;


© The Meteoritical Society, 2009. Printed in USA.

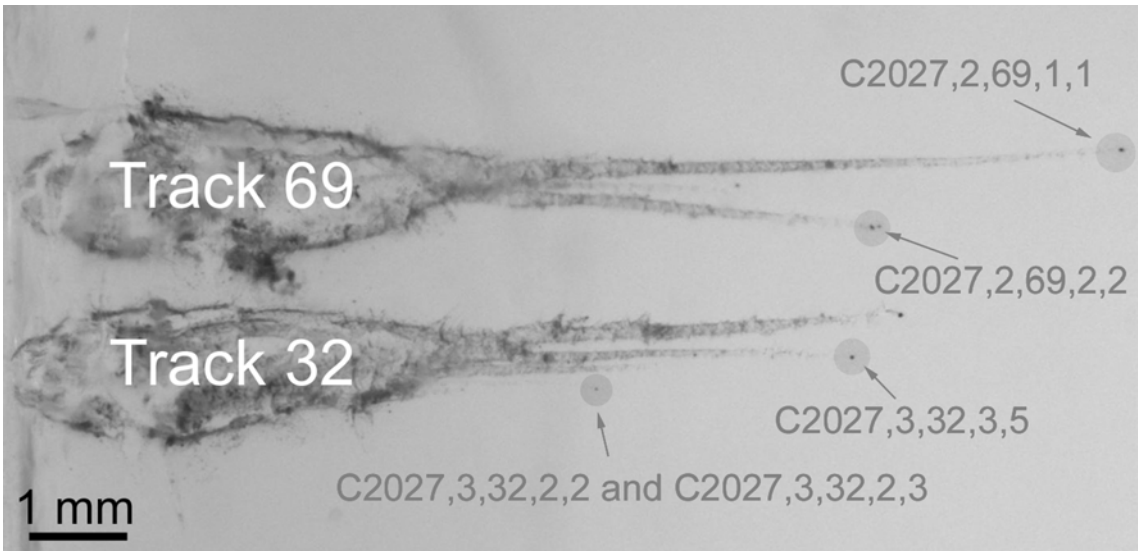


Fig. 1. Optical micrograph of tracks 32 and 69. (Image courtesy of NASA)

Leroux et al. 2004). Finally, pyroxenes are also known to display a wide variety of crystal defects, like, for instance, those occurring during shock deformation (e.g., Leroux et al. 1994; Langenhorst et al. 1995; Leroux 2001).

In this paper, we present data on the composition and microstructure of four pyroxene-rich terminal particles from Wild 2 studied by analytical transmission electron microscopy (ATEM).

## SAMPLES AND ANALYTICAL PROCEDURE

The five Wild 2 samples analyzed in this study originate from four terminal particles of the neighboring tracks 32 and 69 from cell 27 (Fig. 1). They are TEM ultramicrotomed slices with the following labels: C2027,2,69,1,1: track 69, grain 1 (allocated to Univ. Lille), C2027,2,69,2,2: track 69, grain 2 (allocated to Univ. Lille), C2027,3,32,2,3: track 32, grain 2 (allocated to Univ. Lille), C2027,3,32,2,2: track 32, grain 2 (allocated to BGI Bayreuth), C2027,3,32,3,5: track 32, grain 3 (allocated to BGI Bayreuth).

The corresponding cometary grains were extracted from aerogel at NASA Johnson Space Center (JSC) Stardust curatorial facility. Details about extraction and manipulation can be found in Zolensky et al. (2008b). The extracted particles were embedded in EMBED-812 epoxy for serial sectioning using ultramicrotome equipped with a diamond knife. Each sample consisted of several TEM slices placed on a supporting carbon thin film stretched on a copper grid.

TEM results are acquired using a Phillips CM20 (Schottky field emitter operated at 200 kV, BGI, Bayreuth), a Philips CM30 ($LaB_6$ filament operated at 300 kV, Univ. Lille) and a FEI Tecnai G2-20 twin ($LaB_6$ filament operated at 200 kV, Univ. Lille). Chemical compositions are measured using energy dispersive X-ray spectroscopy (EDS) with Thermo-Noran and EDAX Si-detectors (CM30 and Tecnai, respectively), and a Thermo-Noran Ge-detector (CM20). Analyses are recorded using a probe size ranging from 5 to 15 nm, either with a fixed probe for spot analyses or with a scanning probe for more spatially extended analyses and elemental distribution. Detailed description of analysis procedure and data reduction is given in Leroux et al. (2008a).

The microstructure of the samples is studied by conventional bright-field and dark-field imaging. For defect imaging, weak-beam conditions are used. High-resolution images are taken for fringe spacing measurements and planar defects characterization. Some high-resolution images have been obtained on the SACTEM-Toulouse (spherical aberration corrected TEM), a Tecnai F20 (FEI) equipped with a FEG source operated at 200 kV and an objective lens spherical aberration corrector (CEOS company). Among numerous advantages, the aberration correction enables the acquisition of good quality high-resolution images even for thick areas of the sample. Crystallographic data are obtained by selected-area electron diffraction (SAED). The CM30 (Univ. Lille) microscope is equipped with a Spinning Star precession module from the Nanomegas Company. Applying precession, the incident beam is scanned at a constant angle around the optic axis, in combination with a similar de-scan of the beam below the specimen (Vincent and Midgley 1994). The reflections are thus swept successively through the Ewald sphere and integrated intensities over a large range of deviation parameter are collected. Resulting diffraction patterns are thus always symmetric in intensity, even if the sample is not precisely oriented. Furthermore, dynamical interactions are strongly reduced, which limits the occurrence of double diffraction spots and makes the intensities more related to the structure factor. These points are of great use for the phase identification of small and imbricate crystallites as is the case in this study.

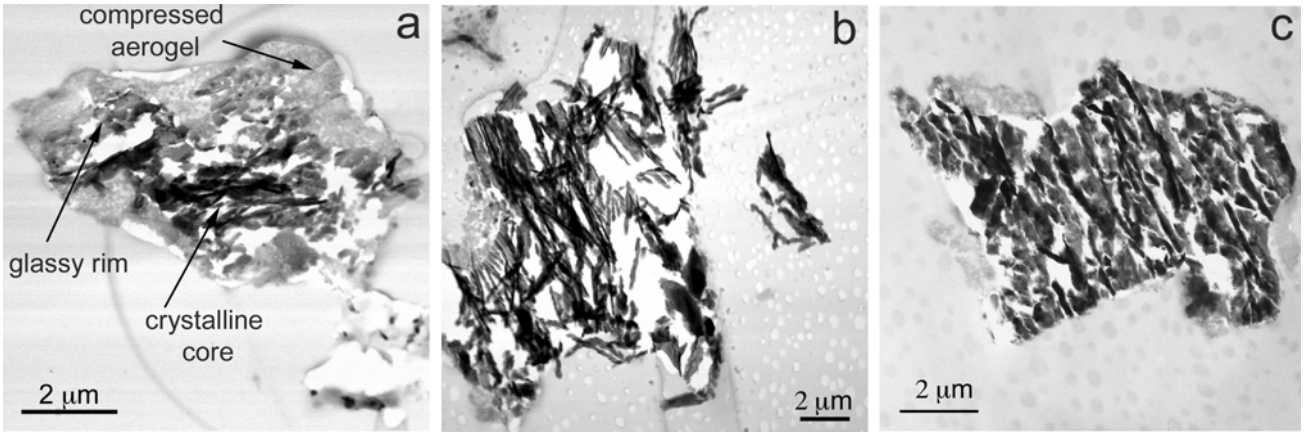


Fig. 2. Bright-field STEM images of samples a) C2027,2,69,1,1, b) C2027,2,69,2,2, and c) C2027,3,32,2,3. The sections are composed by a crystalline core surrounded by a dense silica-rich glass containing Fe-Ni-S phases and vesicles. Compressed aerogel is also present at the margin.

## RESULTS

### General Description and Compositions

The samples exhibit the same general aspect. They are made of a central area composed of crystalline shards partially overlapping due to the sample preparation. General views of the samples are shown in Fig. 2 for C2027,2,69,1,1, C2027,2,69,2,2, and C2027,3,32,2,3, showing various extent of damage relative to the preparation. A more or less broad rim of dense $SiO_2$-rich amorphous material surrounds the crystalline cores. Compressed aerogel is also frequently present at the margin. In sample C2027,2,69,1,1 (Fig. 2a), the glassy rim is much broader than in the other samples. This glassy material is silica-rich, with variable concentration of other elements. It contains Fe-Ni-S nanophases and large vesicles. Representative compositions are given in Table 1 for C2027,2,69,1,1. The characteristics of the glassy rim are quite comparable to those of the thermally modified particles which originate from melting and mixing of cometary material and aerogel (Leroux et al. 2008a).

The studied particles are dominated by low-Ca pyroxenes. C2027,2,69,1,1 is constituted of pigeonite with minor olivine, while the other samples are Mg-rich orthopyroxene, i.e., orthoenstatite. In C2027,2,69,1,1 and C2027,2,69,2,2 minor Ca-rich pyroxene is also found. Representative compositions are summarized in Table 2. In the following sections, we describe the microstructure of the two types of samples: pigeonite (C2027,2,69,1,1) and orthoenstatite (C2027,2,69,2,2, C2027,3,32,2,2/3 and C2027,3,32,3,5).

### Pigeonite (C2027,2,69,1,1)

#### *(100) Twinning*

The dominant microstructure consists of a high density of lamellae parallel to the (100) planes (Figs. 3a, 3b). The (100) lamellae are roughly aligned from one shard to another, suggesting a common monocrystalline parent grain prior to the TEM preparation. Lamella widths range from 5 to 50 nm. These lamellae correspond to twinned domains as shown by the SAED pattern on Fig. 3c, which consists of the superposition of two monoclinic $P2_1/c$ phases, related by a mirror plane along (100). Distinction between the two monoclinic space groups of the pigeonite, namely the "high temperature" $C2/c$ and the "low temperature" $P2_1/c$, is made using the presence of $h$-odd $h00$ reflections. In the $C2/c$ space group, those reflections are kinematically forbidden ($h + k$ odd) and cannot appear by double diffraction, whereas they are visible in the $P2_1/c$ space group.

#### *Inclusions: Olivine and Chromite*

Small olivine grains, typically 200 nm in size, are also found as inclusions in the pigeonite host (Fig. 4a). Their composition ranges from $Fo_{76}$ to $Fo_{83}$ (Table 1). The Mg/(Mg + Fe) ratio close to that of the pigeonite host suggests a chemical equilibrium between the two phases. A second population of inclusions is occasionally present in the (100) habit planes of the pigeonite host (Fig. 4b). These inclusions are typically 20–30 nm in size, which is too small to be individually analyzed by EDS without including the pigeonite host. Nevertheless, spot analyses on the inclusions display strong Cr and Fe enrichments. Subtraction of the spectra from those recorded in the adjacent matrix strongly suggests that the inclusions are chromite ($FeCr_2O_4$). High-resolution images taken on the SACTEM-Toulouse clearly reveals the crystallographic orientation relationship of the {111} planes of the precipitates (spinel structure, space group F$d$-3$m$) with the (100) planes of the pigeonite host (Fig. 4c). The Fourier transform diagram corresponds to a face-centered cubic structure oriented along a <110> zone axis. The {111} interplanar spacing is about 0.48 nm, which is compatible with the expected $FeCr_20_4$ cell parameter (a = 0.830–0.838 nm).

Table 1. Representative EDS composition (at%) for sample C2027,2,69,1,1. The silica-rich glass compositions are from about $300 \times 300$ nm$^2$ wide areas. They are highly variables from place to place. For the pyroxene compositions, we have found a quasi-systematic $SiO_2$ excess, from 5 to 10 mol %. This excess probably originates from the adjacent silica glass that embedded the grains during the collect. In order to best report the cation distribution in the pyroxene structure, we subtracted this $SiO_2$ excess according to the ideal pyroxene structural formulae $(M,Al)_2(Si,Al)_2O_6$, with M are divalent cations and Al being for reason of charge compensation distributed between the tetrahedral and octahedral sites. For data reduction we used the following formulae: (Si + ½ Al) = (sum of the other cation + ½ Al). Once the excess of $SiO_2$ subtracted, the compositions were then renormalized to 100%. The same problem occurred for the olivine compositions. Since the tetrahedral sites in olivine is occupying only by Si, with a general structural formulae $M_2SiO_4$, we used the equation 2M = Si.

| O | Si | Mg | Fe | Ni | S | Al | Ca | Cr | Mn |
|---|---|---|---|---|---|---|---|---|---|
| Silica-rich glassy areas | | | | | | | | | |
| 62.3 | 27.1 | 6.0 | 1.4 | 0.1 | 1.5 | 0.8 | 0.3 | 0.1 | 0.3 |
| 63.3 | 28.4 | 4.5 | 1.8 | 0.1 | 1.0 | 0.5 | 0.3 | 0.1 | 0.1 |
| 62.2 | 26.9 | 5.4 | 2.8 | 0.1 | 1.3 | 0.5 | 0.4 | 0.2 | 0.1 |
| Pigeonite | | | | | | | | | |
| 60.1 | 19.6 | 13.8 | 4.2 | nd | nd | 0.9 | 0.7 | 0.6 | 0.2 |
| 60.0 | 19.7 | 14.2 | 4.0 | nd | nd | 0.7 | 0.9 | 0.3 | 0.2 |
| 60.1 | 19.6 | 14.2 | 4.2 | nd | nd | 0.8 | 0.8 | 0.1 | 0.2 |
| 60.2 | 19.5 | 14.4 | 3.6 | nd | nd | 1.0 | 0.4 | 0.6 | 0.2 |
| 60.2 | 19.6 | 13.8 | 3.9 | nd | nd | 0.8 | 0.8 | 0.6 | 0.3 |
| High-Ca pyroxene | | | | | | | | | |
| 60.1 | 19.4 | 8.6 | 3.0 | nd | nd | 1.2 | 7.2 | 0.3 | 0.3 |
| Olivine | | | | | | | | | |
| 55.7 | 13.9 | 23.0 | 7.0 | nd | 0.1 | nd | nd | 0.1 | 0.2 |
| 50.8 | 12.7 | 28.9 | 6.1 | nd | 0.2 | | nd | nd | 0.4 |
| 57.2 | 14.3 | 22.6 | 5.6 | nd | nd | 0.1 | 0.0 | 0.0 | 0.1 |
| 57.2 | 14.3 | 23.3 | 3.7 | nd | 0.0 | 0.4 | 0.0 | 0.0 | 0.3 |

Table 2. Summary of the representative compositions (at%) for the four studied grains.

| | | |
|---|---|---|
| C2027,2,69,1,1 | Pigeonite (Pi) $P2_1/c$ with minor olivine (Ol) and diopside (Di) | Pi: $En_{72-78}Wo_{2-6}Fs_{17-24}$ Ol: $Fo_{76-83}$ Di: $En_{45}Wo_{39}Fs_{16}$ |
| C2027,2,69,2,2 | Orthopyroxene (Opx) with minor diopside | Opx: $En_{94-97}Wo_{1-4}Fs_{1-5}$ Di: $En_{76}Wo_{21}Fs_3$ |
| C2027,3,32,2,3 | Orthopyroxene | $En_{91-95}Wo_{2-4}Fs_{3-6}$ |
| C2027,3,32,3,5 | Orthopyroxene | $En_{94-95}Wo_{2-3}Fs_{2-4}$ |

*Dislocations*

Dislocations lying in the (100) planes are found in pigeonite (Fig. 5a). They are visible with the diffraction vector $\boldsymbol{g} = \mathbf{002}$ and are out of contrast with $\boldsymbol{g} = \mathbf{310}$, which suggests a Burgers vector $\boldsymbol{c}$ and a screw character. Dislocations are also present in olivine (Fig. 5b). Observations with several diffraction vectors are compatible with dislocations having a Burgers vector $\boldsymbol{c}$.

*Damaged Areas*

Locally, the pyroxene grains exhibit lamellar microstructures that appear damaged compared with those of the surrounding shards (Fig. 6a). The lamellar laths are roughly parallel to (100) planes, but are misoriented by a few degrees with respect to one another. Nevertheless, diffraction patterns of these areas indicate a common mean orientation with the surrounding undamaged twinned grains (Fig. 6b). Composition analysis of these areas does not reveal any differences from the surrounding pyroxene grains.

Note that such damaged areas are not found in this sample only but are present in all observed samples. There occurrence may be due to the sample preparation by ultramicrotomy.

**Enstatite (C2027,2,69,2,2, C2027,3,32,2,2/3 and C2027,3,32,3,5)**

The four other samples are constituted of enstatite. A bright-field image of an enstatite grain in C2027,2,69,2,2 with the SAED pattern corresponding to the classical orthorhombic *Pbca* space group is reproduced on Fig. 7. In all the samples, the microstructure is characterized by the presence of (100) planar defects. Lattice fringe images (Fig. 8) reveal that they consist in the insertion of

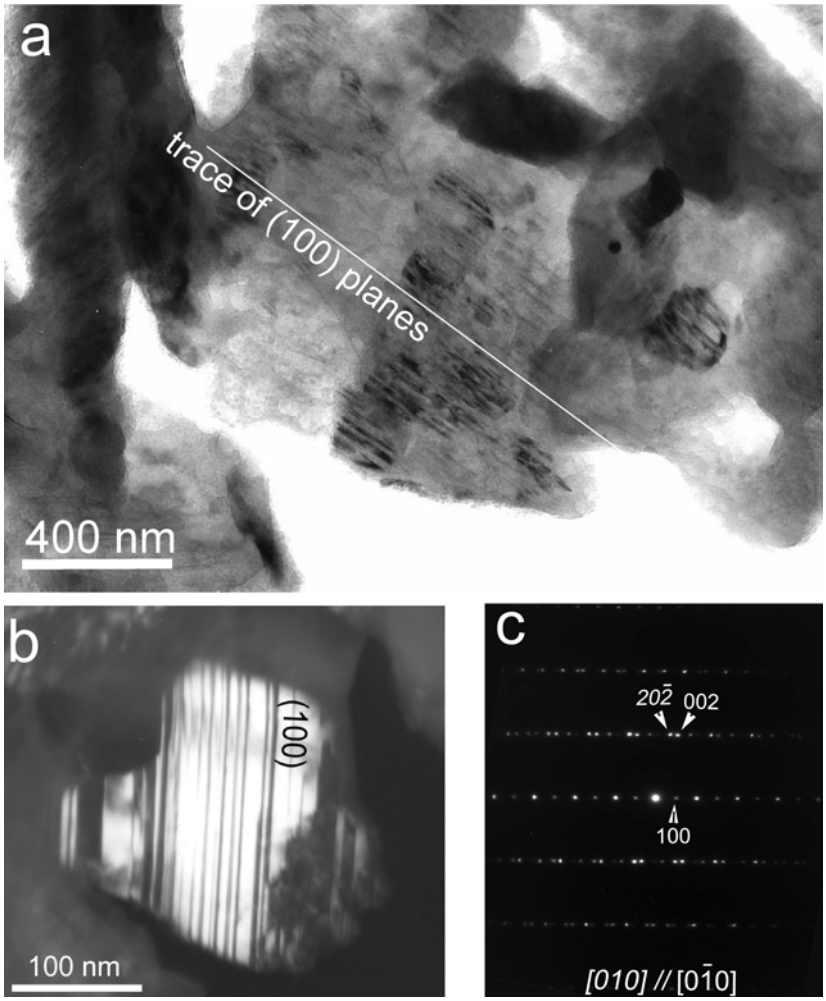


Fig. 3. Crystalline core of sample C2027,2,69,1,1. a) General view. The pyroxene grains exhibit a lamellar microstructure associated with twinning along (100). b) Dark-field image of a pigeonite grain with (100) planes oriented edge-on. Twinned domains exhibit strong contrast variations. c) Associated precession diffraction pattern corresponding to the superimposition of [010] and [0$\bar{1}$0] zone-axes of the $P2_1/c$ space group related by a mirror along (100) plane.

clinoenstatite lamellae (CLEN, space group $P2_1/c$, fringe spacing along (100) ~ 9 Å) in orthoenstatite (OEN, space group *Pbca*, fringe spacing ~18 Å). The basic structural unit of both structures are corner-sharing $SiO_4$ tetrahedra forming chains along the *c*-axis (Papike and Cameron 1976). CLEN consists of two alternating chains whereas OEN is made of four alternating chains. Thus, when (100) planes are oriented edge-on, the OEN lamellae exhibit a fringe spacing which is twice that of the CLEN. Among the observed samples, a distinction can be made as a function of their CLEN/OEN ratio.

### *CLEN-Poor Samples: C2027,2,69,2,2 and C2027,3,32, 2,2/3*

In those samples, the ratio of CLEN in OEN is about 20% (Fig. 8). The CLEN phase generally appears as isolated double (100) lamellae, more rarely as stacks of even numbers of lamellae (between 4 and 14). The lamellae usually transect the entire shards, but some of them stop in the OEN and are terminated by partial dislocations. These dislocations are invisible in dark-field images taken with $\boldsymbol{g}$ = **400** and visible with $\boldsymbol{g}$ = **002**, indicating a Burgers vector parallel to [001]. Some rare subgrain boundaries are found with lamellae stopping on them (Fig. 9), indicating that the lamellae postdate the subgrain boundaries.

### *CLEN-Rich Sample: C2027,3,32,3,5*

In this sample, the ratio of CEN lamellae is much higher, about 50% (Fig. 10). As a consequence, strong streaks parallel to the $a^*$ direction appear on the SAED patterns. Lattice fringe images reveal in this case that the CEN domains are constituted of even or odd numbers of lamellae (Fig. 11). Some twinning is also observed between adjacent clinoenstatite domains. Similar observations have been recently reported on the same particle by Schmitz and Brenker (2008).

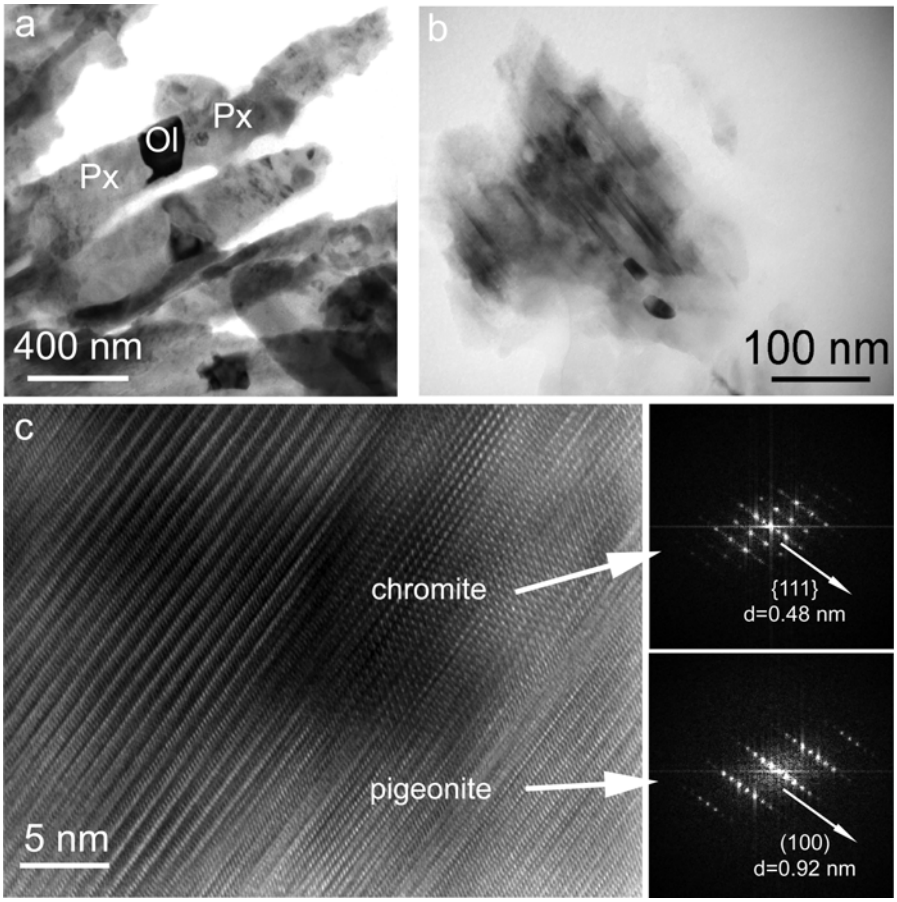


Fig. 4. Sample C2027,2,69,1,1. a) Olivine inclusions imbricate in pigeonite. b) Chromite inclusions in a twinned pigeonite host grain. c) High-resolution image of the chromite inclusion together with the Fourier transform diagrams of the chromite and pigeonite areas.

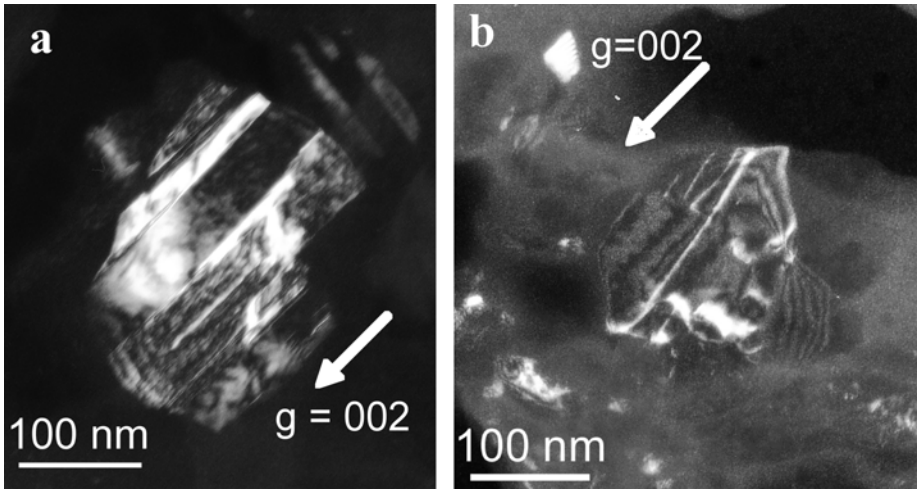


Fig. 5. Dark-field images of dislocations in sample C2027,2,69,1,1. a) In a pigeonite grain. b) In an olivine grain.

*Dislocations*

Free dislocations lying in the (100) planes of the orthoenstatite crystallites are observed in C2027,2,69,2,2, and C2027,3,32,2,2/3. They are elongated along the [100] direction and show small segments perpendicular to it (Fig. 12a). The long segments are visible with the diffraction vector $\boldsymbol{g}$ = **310** and invisible with $\boldsymbol{g}$ = **202**, which is compatible with $\boldsymbol{b}$ screw dislocations. Some other short segments visible with **202** are compatible with $\boldsymbol{c}$ Burgers vectors.

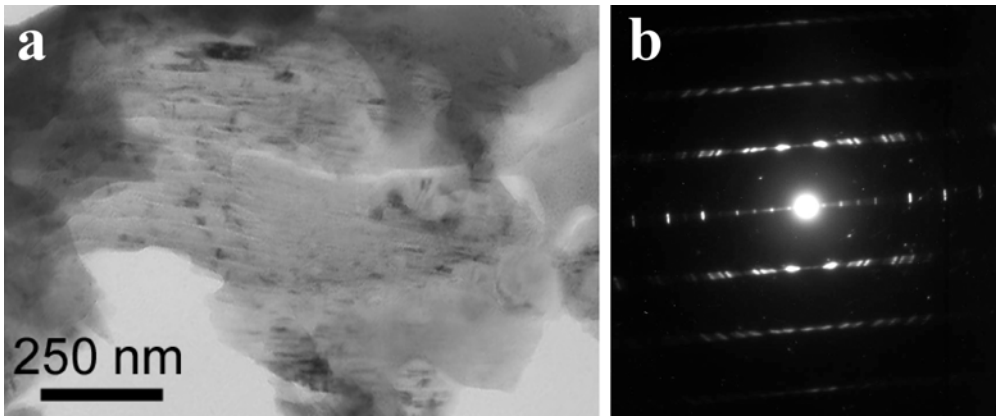


Fig. 6. Sample C2027,2,69,1,1. a) Bright-field image of a damaged pigeonite grain. b) Associated diffraction pattern along a [010] zone-axis. The mean orientation of the grain is the same as the surrounding twinned pigeonite grain.

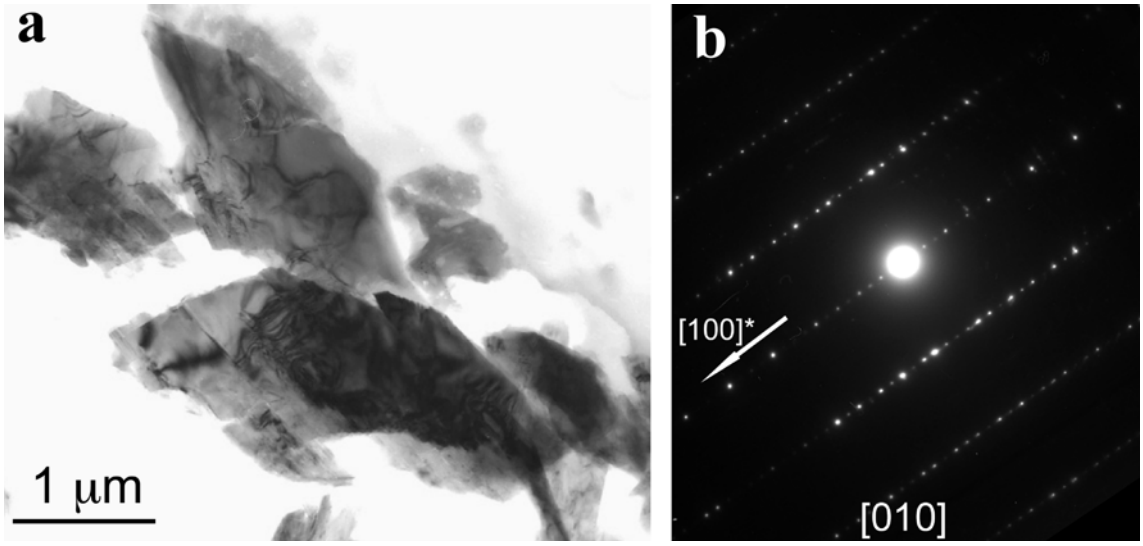


Fig. 7. Sample C2027,2,69,2,2. a) Bright-field image of an orthoenstatite grain. b) Corresponding SAED pattern along the [010] zone-axis (space group *Pbca*).

*Exsolved Ca-Rich Grain in C2027,2,69,2,2*

The Ca-rich grain found in C2027,2,69,2,2 exhibits a diopside-pigeonite exsolution microstructure on (001), with an average wavelength of 25 nm. A detailed description of this grain is given in Leroux et al. (2008b), and the main conclusions of this paper will be taken up in the discussion section. Dislocations are also present in this grain (Fig.12b). Dislocation lines cross the (001) lamellae but are also locally curved along (001) planes. This interaction indicates that the dislocation formation postdates the exsolution phenomena. As in the CPX grain (C2027,2,69,1,1), the diffraction-imaging experiments with various diffraction vectors suggest a ***c*** Burgers vector.

## DISCUSSION

The four terminal particles studied in this work are coarse-grained pyroxenes that have survived the high-velocity capture in the collector. They appear relatively undamaged in comparison to the thermally modified grains frequently found in samples extracted from the wall tracks (Zolensky et al. 2006; Leroux et al. 2008a). They are single crystal particles several micrometers in diameter with a homogeneous microstructure. In the following discussion, we examine the possible origins of their main features: twinned pigeonite (C2027,2,69,1,1), CLEN lamellae in OEN (C2027,2,69,2,2, C2027,3,32,2,2/3 and C2027,3,32,3,5), and dislocations. The possible influence of the capture heating is also addressed.

### Twinned Pigeonite

Pigeonite in sample C2027,2,69,1,1 contains a high density of (100) twins. Twinning in clinopyroxene can be obtained by two mechanisms: (1) quenching from the protopyroxene stability field and (2) plastic deformation

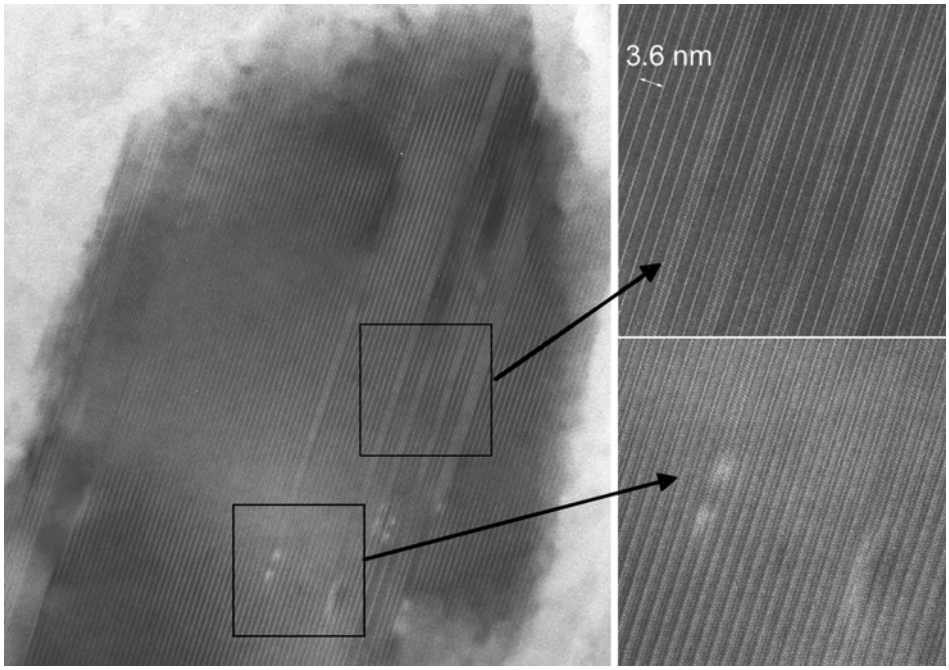


Fig. 8. Sample C2027,2,69,2,2. Lattice fringe image of an orthoenstatite grain. The 18 Å fringe spacing is associated with orthopyroxene whereas the 9 Å spacing corresponds to clinopyroxene. The CLEN phase generally appears as isolated double (100) lamellae, more rarely as stacks of even numbers of lamellae (between 4 and 14). When the clinopyroxene lamellae stop within the orthoenstatite matrix, some strain contrast associated to the stacking fault is observed.

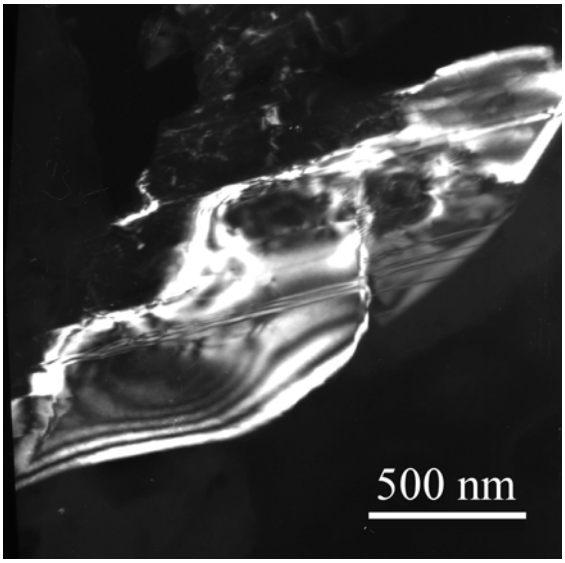


Fig. 9. Sample C2027,2,69,2,2. Dark-field image of (100) lamellae stopping on a grain boundary.

under high deviatoric stress (e.g., by shock deformation). For Ca-poor pyroxenes such as those observed in this sample, a high-temperature protopyroxene stability field extends for compositions ranging from pure enstatite to about $En_{80}Fs_{20}$ (Huebner 1980). Rapid cooling of protopyroxene (mechanism 1) leads to the formation of clinopyroxene with fine (100) polysynthetic twins, as observed experimentally (Shimobayashi and Kitamura 1991) or in natural objects such as chondrules (Kitamura et al. 1983). In the case of plastic deformation (mechanism 2), the (100) twins occur as thin lamellae in the host, bordered by partial dislocations (Kirby and Christie 1977; Leroux et al. 1994). In our sample, the large fraction of twin domains (approximately 50%) and the absence of partial dislocations in the twin boundaries are not in agreement with a plastic deformation process. Thus, the twinned pigeonite microstructure of sample C2027,2,69,1,1 likely originates from cooling from the high temperature protopyroxene phase. Exsolution of chromite could have then occurred on further cooling.

## CLEN Lamellae in Orthoenstatite

The dominant microstructure of the enstatite samples is the alternation of CLEN and OEN lamellae along the (100) planes. In C2027,2,69,2,2 and C2027,3,32,2,2/3 the CLEN/OEN ratio is about 20%, whereas it is about 50% in C2027,3,32,3,5. Furthermore, in the two first samples, CLEN domains are made of even numbers of lamellae, whereas in the latter, they are made of even or odd numbers, with occurrence of twinning. These differences must be related to different thermal histories. Indeed, following the review of Buseck et al. (1980), various possible mechanisms can be invoked to account for the observed mixed microstructures: (1) inversion from the high-temperature protoenstatite (PEN) stability field, (2) transformation from OEN by application of

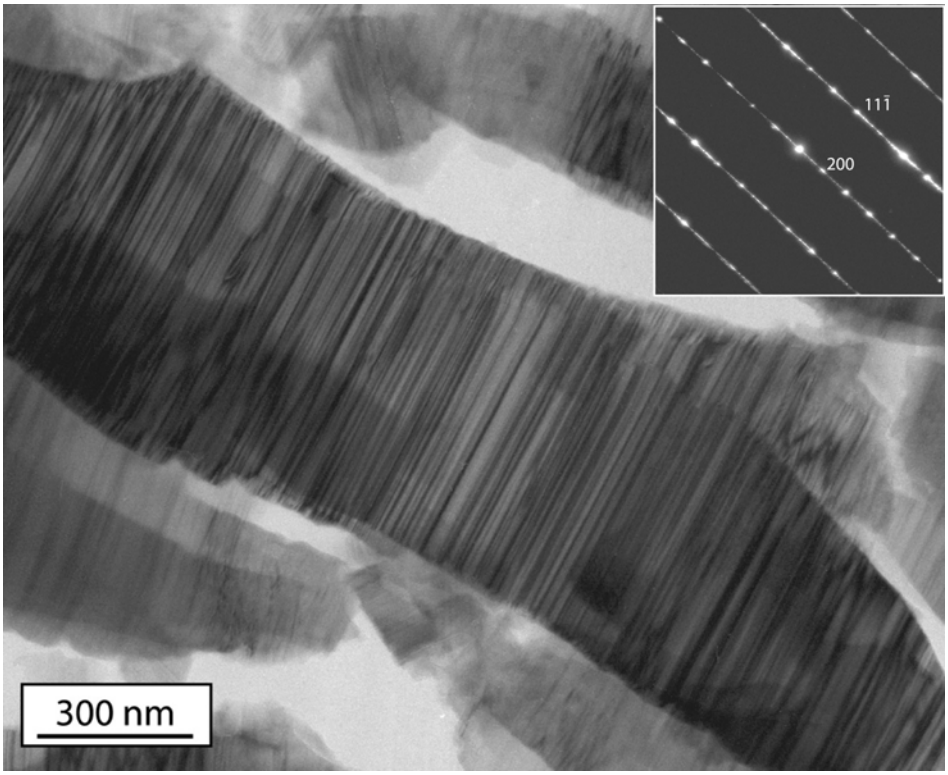


Fig. 10. Bright-field image of sample C2027,3,32,3,5 and the associated SAED pattern in the [011] zone axis orientation. Strong striking associated with stacking disorder is observed in the $a^*$ direction.

homogeneous shear or shock, (3) static transformation from OEN. For the distinction between these various mechanisms, the widths and twinning of the CLEN lamellae are used. Direct inversion from the high-temperature PEN (mechanism 1) should lead to the formation of multiple 9 Å wide CLEN domains, with abundant twins and stacking disorder. CLEN domains that are produced from OEN (mechanisms 2 and 3) should be visible as multiples of 18 Å lattice repeats, since a single OEN lamella gives rise to a pair of CLEN lamellae. For mechanism 2, abundant twinning should be present only if the transformation is due to strong shock. If the transformation is shear-induced, no twinning is expected since the shear should result in most of the CLEN having a common orientation. For mechanism 3, the CLEN domains could exhibit the two twins orientation in approximately equal proportions. Following this classification, mechanism 1—cooling from the high temperature PEN—should be at the origin of the microstructure of sample C2027,3,32,3,5, whereas mechanisms 2 or 3—shear-induced or static transformation from OEN—could be responsible for the microstructure of samples C2027,2,69,2,2 and C2027,3,32,2,2/3. We consider here that the absence of twinning in the studied area of these two samples may be not representative of the entire samples, and thus that the distinction between either a shear-induced or a static transformation from OEN is not straightforward. There are abundant evidences that external stress favors the formation of clinopyroxene from orthopyroxene. The transformation is then martensitic in nature, with slip occurring on (100) planes. The transformation can also result from the passage through the crystal of partial dislocations with Burgers vector parallel to [001] (Coe and Kirby 1975; McLaren and Etheridge 1976). In our samples, the CEN lamellae often stop inside the OEN matrix, which suggests the formation via dislocation glide. Finally, in shocked OEN the CEN lamellae are abundant (e.g., Ashworth and Barber 1975; Ashworth 1985; Langenhorst et al. 1995; Leroux 2001), with pervasive twinning along (100). This is not the case for samples C2027,2,69,2,2 and C2027,3,32,2,2/3, for which this scenario can be excluded. In conclusion, the mixed CEN/OEN microstructures of the three enstatite samples are probably related to two types of mechanisms: cooling from the high temperature PEN phase for C2027,3,2,3,5 and direct inversion from OEN—either static or shear-induced—for samples C2027,2,69,2,2 and C2027,3,32,2,2/3.

**Exsolved Diopside (C2027,2,69,2,2)**

In C2027,2,69,2,2, a diopside grain has been found with an exsolution microstructure made of the alternating Ca-rich and Ca-poor lamellae parallel to (001) planes. In a previous paper (Leroux et al. 2008b), we have attributed the occurrence of this exsolved Ca-rich grain among a Ca-poor OEN to an igneous process, i.e., crystallization from a FeO-poor melt, pyroxene-like in composition, followed by a subsolidus

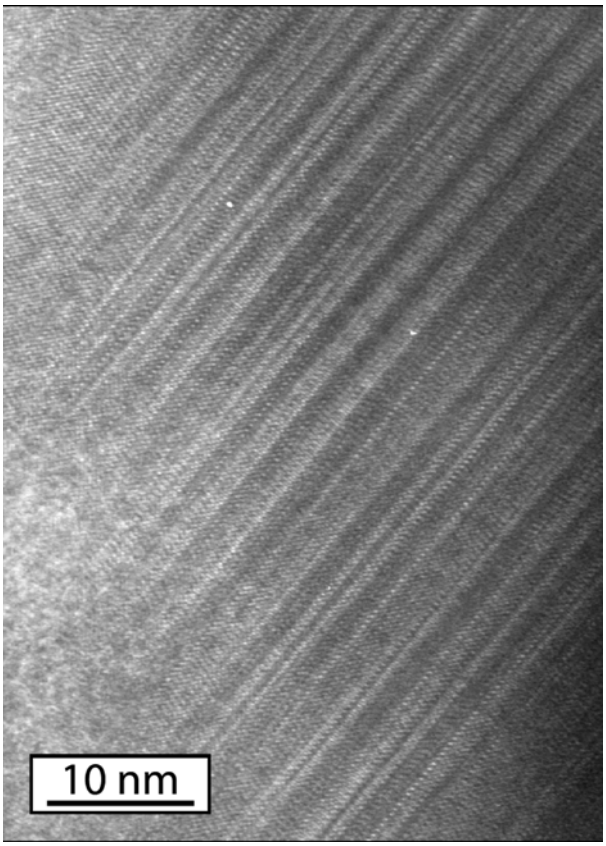


Fig. 11. Lattice fringe image of sample C2027,3,32,3,5.

exsolution process. Using the wavelength of the lamellae (25 nm) and a time-temperature transformation (TTT) diagram constructed with isothermal growths (Weinbruch and Müller 1995), the cooling rate has been estimated to 10–100 °C/h, within the temperature interval 1350–1200 °C. This cooling rate is very close to that of chondrule-like materials (Weinbruch and Müller 1995).

**Dislocations: Evidence for Shock Deformation?**

Dislocations have been found in all the samples. Free dislocations in olivine and pyroxene are generally clear indicators of shock deformation. The Stardust OEN grains (C2027,2,69,2,2, C2027,3,32,2,2/3) contain free dislocations in (100) with Burgers vectors [001] and [010] in edge orientation. These configurations correspond to the most active slip systems as observed in experimentally or naturally deformed orthopyroxene (Kohlstedt and Vander Sande 1973; McLaren and Etheridge 1976; Van Duysen et al. 1985; Nazé et al. 1987). In olivine grains found in C2027,2,69,1,1 dislocations have a Burgers vector [001] with screw orientation. This configuration is strongly dominant in shock-deformed olivine (e.g., Leroux [2001], and reference therein). The density of dislocations in olivine is increasing with the peak pressure but the olivine grains in C2027,2,69,1,1 are small and the poor statistical occurrence preclude any speculation on the shock intensity. In clinopyroxene, i.e., pigeonite from C2027,2,69,1,1, the dislocations are screw [001] in (100). This configuration is once again the easiest activated glide system of clinopyroxene under shock deformation conditions (e.g., Leroux et al. 1994; Langenhorst et al. 1995). Partial [001] dislocations do not seem to be present in the twin walls of pigeonite as it might be the case for a shock deformation origin. In summary the dislocation microstructure observed in these samples is likely due to a shock event of small intensity. The occurrence of dislocations in glide configuration has already been reported in an olivine grain of Stardust samples (Tomeoka et al. 2008), and is also attributed to a shock origin. In Stardust samples, the peak pressure associated with the capture deceleration period into aerogel (Trigo-Rodríguez et al. 2008) could have reached a mean maximum value of 300 MPa, which is about one order of magnitude smaller than the Hugoniot elastic limit of pyroxene and olivine. Application of this peak pressure during the very brief period of capture (1 μs) is not expected to induce some dislocations motion, suggesting that the dislocations microstructure was established prior to the capture. Nevertheless, stress concentration within the particle is possible, leading to higher local stress values. Furthermore, heating of the collected grains is attested by the occurrence of the melt rim around the samples. The rapid heating and cooling of the particles during the collect could have induced a thermal shock, associated with high thermal gradient acting on an anisotropic elastic media such as pyroxene. This may also have contributed to the dislocations motion during capture.

**Heating Effect**

The interpretation of the microstructure of Stardust material is rendered complex because of the possible high-temperature regime that may have occurred during the capture deceleration. The capture of particles in aerogel has been demonstrated to induce local melting due to the hypervelocity impact at 6.1 km $s^{-1}$ in the silica aerogel collectors (Zolensky et al. 2006; Leroux et al. 2008a; Roskosz et al. 2008). The melted material has been quenched as a glass mixed with silica coming from melted silica aerogel. This easily recognized microstructure is not observed in our samples, except at the periphery of the particles. Thus, if the studied pyroxene grains have been prevented from melting, they may have undergone a short excursion at high temperature. If the temperature exceeded 1000 °C the enstatite grains could have entered into the high temperature PEN stability field. The transformation from CEN to PEN (and reverse) is very fast (Smyth 1974), martinsitic in nature, whereas the transformation from ortho- to proto-pyroxene, which requires a coordinated motion of alternating pairs of octahedral layers, is very sluggish (Smyth

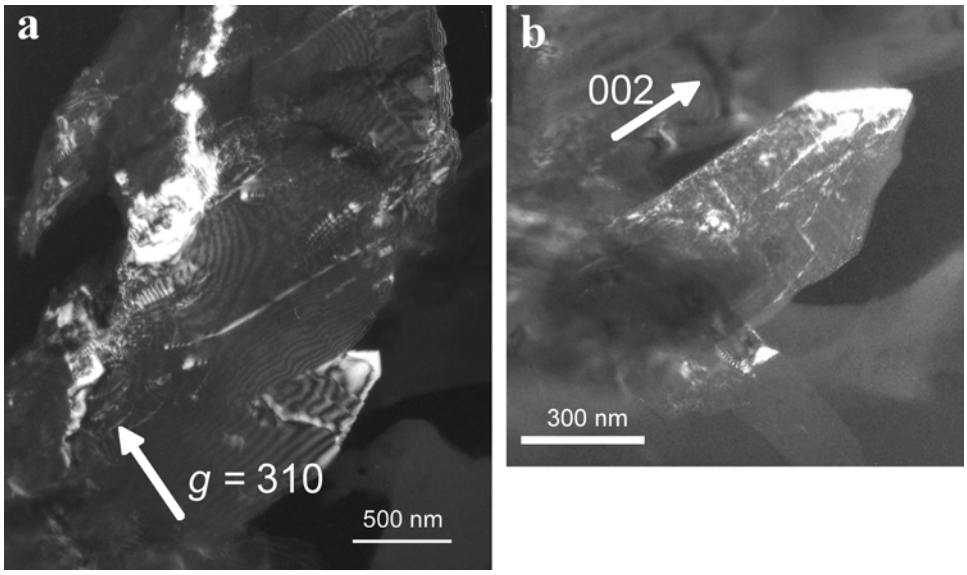


Fig. 12. Dark-field images of dislocations in sample C2027,2,69,2,2. a) In an orthoenstatite grain. b) In the exsolved diopside grain.

1974). If the grain was originally CEN rich, as C2027,3,32,3,5, some modifications of the microstructure may have then occurred. It is also the case of sample C2027,2,69,1,1 (Fe-rich clinopyroxene), but in that case the required temperature to reach the PEN domain is around 1400 °C. Nevertheless, in this sample, the presence of chromite exsolution on the twin boundaries, which requires time at high temperature, favors the twins formation before the capture process. For the OEN- rich samples such as C2027,2,69,2,2 and C2027,3,32,2,2/3, even if the PEN domain was reached, some time would have been needed to induce the sluggish transformation of OEN, much more than that of the high temperature period deduced from the observation of melted material in Stardust samples (Roskosz et al. 2008). Concerning the exsolved diopside grain in C2027,2,69,2,2, the cooling rate of 10–100 °C (Leroux et al. 2008b) appears much lower than the one deduced from the thermal regime associated to the capture (Roskosz et al. 2008), showing that the formation of an exsolution microstructure in pyroxene during the capture is unrealistic. In conclusion, we are likely to argue that the entire microstructures reported here are pristine, i.e., associated to natural pre-capture events.

Nevertheless, some possible small modifications of the pristine microstructures are possible. Indeed, as previously noticed concerning dislocations motion, even if 1000 °C was not reached, high thermal gradients are likely in the Stardust samples due to rapid heating and cooling. Thermal shear stresses must then have been produced. In these conditions the formation of clino-lamellae in orthoenstatite, as that observed in samples C2027,2,69,2,2, C2027,3,32,2,2/3, and C2027,3,32,3,5 is likely since this deformation process is starting at relatively low shear stress >70 MPa (Coe and Kirby 1975).

## CONCLUSIONS

We have reported the detailed microstructure of four terminal particles coming from two neighboring tracks (69 and 32, cell 27) of Stardust collector. The two terminal particles from track 69 strongly differ. Particle 1 consists of twinned pigeonite: $En_{75}Wo_4$ $Fs_{21}$ with minor olivine $Fo_{76–83}$. The twinned microstructure is not usual in pigeonite and is probably related to its specific FeO content and a corresponding protoenstatite—pigeonite transition at relatively high temperature (typically around 1400 °C). Particle 2 is an almost pure enstatite single crystal (average $En_{95}Wo_2Fs_3$). The CEN lamellae distribution is compatible with an OEN to CEN transition, likely assisted by a shear stress because of the presence of dislocations terminating CEN lamellae. The microstructure does not show evidence for a signature of a PEN-OEN transition, suggesting a moderate or low cooling after the crystal formation (supposing it formed at high temperature). Observation in this particle of an exsolved diopside grain is fully consistent with an igneous formation process, with a cooling rate similar to that of chondrule-like materials. Igneous textures or potential chondrule-bearing minerals have been identified in other Wild 2 particles (Zolensky et al. 2006; Joswiak et al. 2007; Nakamura et al. 2008), showing that chondrule-like objects are found not only in meteorites but also in bodies assembled at large distances from the inner region of the solar system. This important finding, together with the discovery of calcium-aluminium-rich inclusions (CAIs) (Simon et al. 2008), supports the model of radial transport in the protoplanetary disk into the region of comet formation (Brownlee et al. 2006; Zolensky et al. 2006).

In track 32, both studied terminal particles (grain 2 and 3) are OEN with very close compositions (respectively $En_{97–98}$

$Wo_{0-1}Fs_{1-2}$ and $En_{94-95}Wo_{2-3}Fs_{2-4}$). However they strongly differ by their CEN/OEN ratio. Grain 3 probably acquired its high density of CEN lamellae during cooling from the PEN high-temperature phase field. It is not excluded that the grain experienced a high temperature regime during capture within the protoenstatite stability field. In contrast, grain 2 is rather compatible with a transition from OEN to CEN assisted by glide of partial dislocation in (100).

The pyroxene terminal grains in track 32 and 69 clearly demonstrate that the corresponding Wild 2 dusts were made by several coarse-grained silicates having different and probably unrelated origins. Differences are evidenced both by grain compositions and defect microstructures. These observations are important to constrain the comet grain model. The Wild 2 dust is likely a mixture between micro-sized silicates and very fine-grained material. The terminal particles likely correspond to the more resistant phases, i.e., the coarse-grained silicates. Some material is also present all along the track cavities but is found unfortunately largely melted. In this case the composition is frequently close to CI (Leroux et al. 2008a; Stephan et al. 2008) and the deduced original grain size is more than one order smaller than the terminal particles. All these observations lead to conclude that dust particles which impacted the aerogel capture medium were weakly bound aggregates constituted by one or several large silicate grains together with a very fine grained matrix.

The defect microstructure in pyroxene is comparable to those already reported in chondritic meteorites. Twinned pigeonite was observed in chondrules (Kitamura et al. 1983), as well as the exsolved diopside with comparable lamellae wavelength (Weinbruch and Müller 1995). Clinopyroxene lamellae microstructure in orthopyroxene is a very frequent defect microstructure in meteorites. Following Ishii et al. (2008), we conclude that terminal particles closely resemble to chondritic meteorite minerals.

The presence of free dislocations as well as the partial dislocations in OEN are clear indicators for shock deformation. The relatively low density of dislocations suggests nevertheless a moderate shock. The deformation features may probably have formed prior to the high-velocity capture into aerogel because the peak pressure due to the capture is probably lower than 0.3 GPa, i.e., well below the Hugoniot elastic limit of silicates (Trigo-Rodríguez et al. 2008). Nevertheless the exceptional physical conditions of the capture include a possible intense thermal pulse. A thermal shock as possible cause for the observed microstructures cannot be ruled out. We expect that the in coming comparison at the microscopic scale of pre- and post-capture microstructures of experimentally shocked materials will help clarify this point.

*Acknowledgments*—The authors thank the Stardust curator M. Zolensky and Keiko Messenger for the preparation of the ultramicrotomed TEM samples and helpful information about the preparation process. We also thank J. F. Dhenin for his careful maintenance of the TEMs. The CNES (Centre National des Etudes Spatiales), the CNRS, the CEA-METSA network, and the INSU electron microscopy facility are acknowledged for financial support. One of us (F. L.) is grateful for the financial support by the Leibniz programme of the Deutsche Forschungsgemeinschaft (DFG LA830/14-1).

*Editorial Handling*—Dr. Anthony Jones

## REFERENCES

Ashworth J. R. and Barber D. J. 1975. Electron petrography of shock effects in a gas-rich enstatite achondrite. *Contributions to Mineralogy and Petrology* 49:149–162.

Ashworth J. R. 1985. Transmission electron microscopy of L-group chondrites, 1. Natural shock effects. *Earth and Planetary Science letters* 73:17–32.

Brownlee D., Tsou P., Aléon J., Alexander C. M. O'D., Araki T., Bajt S., Baratta G. A., Bastien R., Bland P., Bleuet P., Borg J., Bradley J. P., Brearley A., Brenker F., Brennan S., Bridges J. C., Browning N. D., Brucato J. R., Bullock E., Burchell M. J., Busemann H., Butterworth A., Chaussidon M., Cheuvront A., Chi M., Cintala M. J., Clark B. C., Clemett S. J., Cody G., Colangeli L., Cooper G., Cordier P., Daghlian C., Dai Z., D'Hendecourt L., Djouadi Z., Dominguez G., Duxbury T., Dworkin J. P., Ebel D. S., Economou T. E., Fakra S., Fairey S. A. J., Fallon S., Ferrini G., Ferroir T., Fleckenstein H., Floss C., Flynn G., Franchi I. A., Fries M., Gainsforth Z., Gallien J.-P., Genge M., Gilles M. K., Gillet Ph., Gilmour J., Glavin D. P., Gounelle M., Grady M. M., Graham G. A., Grant P. G., Green S. F., Grossemy F., Grossman L., Grossman J. N., Guan Y., Hagiya K., Harvey R., Heck P., Herzog G. F., Hoppe P., Hörz F., Huth J., Hutcheon I. D., Ignatyev K., Ishii H., Ito M., Jacob D., Jacobsen C., Jacobsen S., Jones S., Joswiak D., Jurewicz A., Kearsley A. T., Keller L. P., Khodja H., Kilcoyne A. L. D., Kissel J., Krot A., Langenhorst F., Lanzirotti A., Le L., Leshin L. A., Leitner J., Lemelle L., Leroux H., Liu M.-C., Luening K., Lyon I., MacPherson G., Marcus M. A., Marhas K., Marty B., Matrajt G., McKeegan K., Meibom A., Mennella V., Messenger K., Messenger S., Mikouchi T., Mostefaoui S., Nakamura T., Nakano T., Newville M., Nittler L. R., Ohnishi I., Ohsumi K., Okudaira K., Papanastassiou D. A., Palma R., Palumbo M. E., Pepin R. O., Perkins D., Perronnet M., Pianetta P., Rao W., Rietmeijer F. J. M., Robert F., Rost D., Rotundi A., Ryan R., Sandford S. A., Schwandt C. S., See T. H., Schlutter D., Sheffield-Parker J., Simionovici A., Simon S., Sitnitsky I., Snead C. J., Spencer M. K., Stadermann F. J., Steele A., Stephan T., Stroud R., Susini J., Sutton S. R., Suzuki Y., Taheri M., Taylor S., Teslich N., Tomeoka K., Tomioka N., Toppani A., Trigo-Rodríguez J. M., Troadec D., Tsuchiyama A., Tuzzolino A. J., Tyliszczak T., Uesugi K., Velbel M., Vellenga J., Vicenzi E., Vincze L., Warren J., Weber I., Weisberg M., Westphal A. J., Wirick S., Wooden D., Wopenka B., Wozniakiewicz P., Wright I., Yabuta H., Yano H., Young E. D., Zare R. N., Zega T., Ziegler K., Zimmermann L., Zinner E., and Zolensky M. 2006. Comet 81P/Wild 2 under a microscope. *Science* 314:1711–1716.

Burchell M. J., Fairey S. A. J., Wozniakiewicz P., Brownlee D. E., Hörz F., Kearsley A. T., See T. H., Tsou P., Westphal A., Green S. F., Trigo-Rodríguez J. M., and Dominguez G. 2008. Characteristics of cometary dust tracks in Stardust aerogel and

laboratory calibrations. *Meteoritics & Planetary Science* 43:23–40.

Buseck P. R., Nord G. L., and Veblen D. R. 1980. Subsolidus phenomena in pyroxenes. In *Pyroxenes*, edited by Prewitt C. T. Reviews in Mineralogy, vol. 7. Washington, D.C.: Mineralogical Society of America. pp. 117–211.

Coe R. S. and Kirby S. H. 1975. The orthoenstatite to clinoenstatite transformation by shearing and reversion by annealing: Mechanism and potential applications. *Contributions to Mineralogy and Petrology* 52:29–55.

Davidson P. M. and Lindsley D. H. 1985. Thermodynamic analysis of quadrilateral pyroxenes. Part II: Model calibration from experiments and applications to geothermometry. *Contributions to Mineralogy and Petrology* 91:390–404.

Hörz F., Bastien R., Borg J., Bradley J. P., Bridges J. C., Brownlee D. E., Burchell M. J., Chi M., Cintala M. J., Dai Z. R., Djouadi Z., Dominguez G., Economou T. E., Fairey S. A. J., Floss C., Franchi I. A., Graham G. A., Green S. F., Heck P., Hoppe P., Huth J., Ishii H., Kearsley A. T., Kissel J., Leitner J., Leroux H., Marhas K., Messenger K., Schwandt C. S., See T. H., Snead C., Stadermann F. J. I., Stephan T., Stroud R., Teslich N., Trigo-Rodríguez J. M., Tuzzolino A. J., Troadec D., Tsou P., Warren J., Westphal A., Wozniakiewicz P., Wright I., and Zinner E. 2006. Impact features on Stardust: Implications for comet 81P/Wild 2 dust. *Science* 314:1716–1719.

Huebner J. S. 1980. Pyroxene phase at low pressure. In *Pyroxenes*, edited by Prewitt C. T. Reviews in Mineralogy, vol. 7. Washington, D.C.: Mineralogical Society of America. pp. 213–288.

Ishii H. A., Bradley J. P., Dai Z. R., Chi M., Kearsley A. T., Burchell M. J., Browning N. D., and Molster F. 2008. Comparison of comet 81P/Wild 2 dust with interplanetary dust from comets. *Science* 319:447–450.

Joswiak D. J., Matrajt G., Brownlee D. E., Westphal A. J., and Snead C. J. 2007. A roedderite-bearing terminal particle from Stardust track 56: Comparison with rare peralkaline chondrules in ordinary chondrites (abstract #2142). 38th Lunar and Planetary Science Conference. CD-ROM.

Kirby S. H. and Christie J. M. 1977. Mechanical twinning in diopside $Ca(Mg,Fe)Si_2O_6$: Structural mechanisms and associated crystal defects. *Physics and Chemistry of Minerals* 1:137–163.

Kitamura M., Yasuda M., Watanabe S., and Morimoto N. 1983. *Earth and Planetary Science Letters* 63:189–201.

Kohlstedt D. L. and Vander Sande J. B. 1973. Transmission electron microscopy investigation of the defect microstructure of four natural orthopyroxenes. *Contributions to Mineralogy and Petrology* 42:169–180.

Langenhorst F., Joreau P., and Doukhan J. C. 1995. Thermal and shock metamorphism of the Tenham chondrite: A TEM examination. *Geochimica et Cosmochimica Acta* 59:1835–1945.

Leroux H., Doukhan J. C., and Langenhorst F. 1994. Microstructural defects in experimentally shocked diopside: A TEM characterization. *Physics and Chemistry of Minerals* 20:521–530.

Leroux H. 2001. Microstructural shock signatures of major minerals in meteorites. *European Journal of Mineralogy* 13:253–272.

Leroux H., Devouard B., Cordier P., and Guyot F. 2004. Pyroxene microstructure in the Northwest Africa 856 Martian meteorite. *Meteoritics & Planetary Science* 39:711–722.

Leroux H., Rietmeijer F. J. M., Velbel M. A., Brearley A. J., Jacob D., Langenhorst F, Bridges J. C., Zega T. J., Stroud R. M., Cordier P., Harvey R. P., Lee M., Gounelle M., and Zolensky M. 2008a. A TEM study of thermally modified comet 81P/Wild 2 dust particles by interactions with the aerogel matrix during the Stardust capture process. *Meteoritics & Planetary Science* 43:97–120.

Leroux H., Jacob D., Stodolna J., Nakamura-Messenger K., and Zolensky M. 2008b. Igneous Ca-rich pyroxene in 81P/Wild 2 comet. *American Mineralogist* 93:1933–1936.

Lindsley D. H. 1983. Pyroxene Thermometry. *American Mineralogist* 68:477–493.

Lindsley D. H. and Andersen D. J. 1983. A two-pyroxene thermometer. *Journal of Geophysical Research* 88:A887–A906.

McCallister R. H. and Nord G. L. 1981. Subcalcic diopsides from kimberlites: Chemistry, exsolution microstructures, and thermal history. *Contribution to Mineralogy and Petrology* 78:118–125.

McLaren A. C. and Etheridge M. A. 1976. A transmission electron microscope study of naturally deformed orthopyroxene. *Contributions to Mineralogy and Petrology* 57:163–177.

Nakamura T., Noguchi T., Tsuchiyama A., Ushikubo T., Kita N. T., Valley J. W., Zolensky M. E., Kakazu Y., Sakamoto K., Mashio E., Uesugi K., and Nakano T. 2008. Chondrule-like objects recovered from short-period comet 81P/Wild 2. *Science* 321: 1664–1667.

Nazé L., Doukhan N., Doukhan J. C., and Latrous K. 1987. A TEM study of lattice defects in naturally and experimentally deformed orthopyroxenes. *Bulletin de Minéralogie* 110:497–512.

Papike J. J. and Cameron M. 1976. Crystal Chemistry of Silicate Minerals of Geophysical Interest. *Review of Geophysics* 14:37–80.

Papike J. J. 1996. Pyroxene as a recorder of cumulate formational processes in asteroids, Moon, Mars, Earth: Reading the record with the ion microprobe. *American Mineralogist* 81:525–544.

Papike J. J., Karnet J. M., and Shearer C. K. 2005. Comparative planetary mineralogy: Valence state partitioning of Cr, Fe, Ti, and V among crystallographic sites in olivine, pyroxene, and spinel from planetary basalts. *American Mineralogist* 90:277–290.

Roskosz M., Leroux H., and Watson H. C. 2008. Thermal history, partial preservation and sampling bias recorded by Stardust cometary grains during their capture. *Earth and Planetary Science Letters* 273:195–202.

Ross M. and Huebner J. S. 1979. Temperature-composition relationships between naturally occurring augite, pigeonite, and orthopyroxene at one bar pressure. *American Mineralogist* 64: 1133–1155.

Schmitz S. and Brenker F. 2008. Microstructural indications for protoenstatite precursor of cometary $MgSiO_3$ pyroxene: A further high temperature component of comet Wild 2. *The Astrophysical Journal* 681:L105–L108.

Shimobayashi N. and Kitamura M. 1991. Phase transition in Ca-poor clinopyroxenes. *Physics and Chemistry of Minerals* 18:153–160.

Simon S. B., Joswiak D. J., Ishii H. A., Bradley J. P., Chi M., Grossman L., Aléon J., Brownlee E., Fallon S., Hutcheon I. D., Matrajt G., and McKeegan K. D. 2008. A refractory inclusion returned by Stardust from comet 81P/Wild 2. *Meteoritics & Planetary Science* 43:1861–1877.

Smyth J. R. 1974. Experimental study of the polymorphism of enstatite. *American Mineralogist* 59:345–352.

Stephan T., Rost D., Vicenzi E. P., Bullock E. S., MacPherson G. J.,Westphal A. J., Snead C. J., Flynn G. J., Sandford S. A., and Zolensky M. 2008. TOF-SIMS analysis of cometary matter in Stardust aerogel tracks. *Meteoritics & Planetary Science* 43:233–246.

Tomeoka K., Tomioka N., and Ohnishi I. 2008. Silicate minerals and Si-O glass in comet Wild 2 samples: Transmission electron microscopy. *Meteoritics & Planetary Science* 43:273–284.

Trigo-Rodríguez J. P., Dominguez G., Burchell M. J., Hörz F., and Llorca J. 2008. Bulbous tracks arising from hypervelocity capture in aerogel. *Meteoritics & Planetary Science* 43:75–86.

Van Duysen J. C., Doukhan N., and Doukhan J. C. 1985. Transmission electron microscope study of dislocations in

orthopyroxene $(Mg,Fe)_2Si_2O_6$. *Physics and Chemistry of Minerals* 12:39–44.

Vincent R. and Midgley P. A. 1994. Double conical beam-rocking system for measurement of integrated electron diffraction intensities. *Ultramicroscopy* 53:271–282.

Weinbruch S. and Müller W. F. 1995. Constraints on the cooling rates of chondrules from the microstructure of clinopyroxene and plagioclase. *Geochimica et Cosmochimica Acta* 59:3221–3230.

Zema M., Tarantino S., Domeneghetti M. C., and Tazzoli V. 2003. Ca in orthopyroxene: Structural variations and kinetics of the disordering process. *European Journal of Mineralogy* 15:373–380.

Zolensky M. E., Zega T. J., Yano H., Wirick S., Westphal A. J., Weisberg M. K., Weber I., Warren J. L., Velbel M. A., Tsuchiyama A., Tsou P., Toppani A., Tomioka N., Tomeoka K., Teslich N., Taheri M., Susini J., Stroud R., Stephan T., Stadermann F. J., Snead C. J., Simon S. B., Simionovici A., See T. H., Robert F., Rietmeijer F. J. M., Rao W., Perronnet M. C., Papanastassiou D. A., Okudaira K., Ohsumi K., Ohnishi I., Nakamura-Messenger K., Nakamura T., Mostefaoui S., Mikouchi T., Meibom A., Matrajt G., Marcus M. A., Leroux H., Lemelle L., Le L., Lanzirotti A., Langenhorst F., Krot A. N., Keller L. P., Kearsley A. T., Joswiak D., Jacob D., Ishii H., Harvey R., Hagiya K., Grossman L., Grossman J. N., Graham G. A., Gounelle M., Gillet Ph., Genge M. J., Flynn G., Ferroir T., Fallon S., Ebel D. S., Dai Z. R., Cordier P., Clark B., Chi M., Butterworth A. L., Brownlee D. E., Bridges J. C., Brennan S., Brearley A., Bradley J. P., Bleuet P., Bland P. A., and Bastien R. 2006. Mineralogy and petrology of comet 81P/Wild 2 nucleus samples. *Science* 314:1735–1739.

Zolensky M., Nakamura-Messenger K., Rietmeijer F., Leroux H., Mikouchi T., Ohsumi K., Simon S., Grossman L., Stephan T., Weisberg M., Velbel M., Zega T., Stroud R., Tomeoka K., Ohnishi I., Tomioka N., Nakamura T., Matrajt G., Joswiak D. Brownlee D., Langenhorst F., Krot A., Kearsley A., Ishii H., Graham G., Dai Z. R., Chi M., Bradley J., Hagiya K., Gounelle M., and Bridges J. 2008a. Comparing Wild 2 particles to chondrites and IDPs. *Meteoritics & Planetary Science* 43:261–272.

Zolensky M., Nakamura-Messenger K., Fletcher L., and See T. 2008b. Curation, spacecraft recovery and preliminary examination for the Stardust mission: A perspective from the curatorial facility. *Meteoritics & Planetary Science* 43:5–21.

*American Mineralogist, Volume 93, pages 1933–1936, 2008*

LETTER

# Igneous Ca-rich pyroxene in comet 81P/Wild 2

HUGUES LEROUX,[1,*] DAMIEN JACOB,[1] JULIEN STODOLNA,[1] KEIKO NAKAMURA-MESSENGER,[2] AND MICHAEL E. ZOLENSKY[2]

[1]Laboratoire de Structure et Propriétés de l'Etat Solide, Université des Sciences et Technologies de Lille and CNRS, UMR 8008, F-59655 Villeneuve d'Ascq, France
[2]Astromaterials Research and Exploration Science, NASA Johnson Space Center, Houston, Texas 77058, U.S.A.

## ABSTRACT

The Stardust spacecraft successfully returned dust from comet 81P/Wild 2 to Earth in January 2006. Preliminary examination of the samples showed abundant crystalline silicates comparable to those found in chondritic meteorites presumably formed in the asteroid belt. Here, we report results of a transmission electron microscopy (TEM) study of a pyroxene-bearing terminal particle, which contains lamellar intergrowths of pigeonite and diopside on the (001) plane. This microstructure is typical for an igneous process and formation by exsolution during cooling. Width and wavelength of the lamellae indicate a cooling rate within the range 10–100 °C/h, in close agreement with those of chondrules or lava from an asteroidal igneous rock. This observation shows that some Stardust material experienced periods of igneous processing similar to material found in the inner early solar system. This implies that igneous materials were common materials in a large region of the protoplanetary disk and were not restricted to the asteroid belt. Their presence in comet Wild 2 also supports the favored view of large radial mixing from the inner to the outer regions before the comet's accretion.

**Keywords:** Comet dust, electron microscopy, pyroxene, Stardust, phase transformation

## INTRODUCTION

Samples returned from the Stardust mission show an unexpectedly high abundance of crystalline materials (Brownlee et al. 2006; Zolensky et al. 2006). Dust from comet Wild 2 therefore differs from anhydrous chondritic interplanetary dust particles (Ishii et al. 2008) that contain abundant amorphous materials, and from interstellar silicates, believed to be dominated by amorphous phases (Kemper et al. 2004). In this context, it is important to identify the process responsible for crystallization of the Stardust materials. Suggested crystallization mechanisms include thermal annealing of amorphous interstellar precursors, direct condensation in hot regions of the solar nebula, or crystallization from a melt during an igneous event such as those that result in chondrule formation or volcanic activity at a planetoid surface. Signatures of crystal formation are recorded in morphology, composition, and microstructure of crystals. Thus, their detailed study can provide better constraints for active processes that occurred in the early solar nebula and refine the understanding of the petrogenetic continuum between asteroids and comets.

Along with the high-temperature minerals, pyroxenes are of special interest because they are useful indicators for thermal and deformational events. In this paper, we use analytical transmission electron microscopy (ATEM) to study the microstructure of a Ca-rich pyroxene in one Wild 2 particle to provide information about its thermal history and the possible origin of the parent Stardust particle.

* E-mail: hugues.leroux@univ-lille1.fr

## SAMPLE AND ANALYTICAL PROCEDURE

The studied Wild 2 sample is a terminal particle (grain 2) from track 69, labeled C2027,2,69,2,2 (Fig. 1). The sample, about 5 μm in diameter, was removed from aerogel, embedded in epoxy and sliced into ~70 nm thick sections with an ultramicrotome at the Johnson Space Center (NASA) (Zolensky et al. 2008). Sections were then transferred to amorphous C-supported Cu TEM grids. The ATEM study was performed using a Philips CM30 ($LaB_6$ filament) operating at 300 kV and a Tecnai G2-20 twin ($LaB_6$ filament) operating at 200 kV. Specimens were mounted on a Be low-background double-tilt holder. Microstructural analysis was carried out using conventional bright and dark field imaging. Chemical compositions were measured using energy dispersive X-ray spectroscopy (EDS) with a Thermo Noran Si-detector (CM30) and an EDAX Si(Li)-detector (Tecnai), both having ultrathin windows. For quantitative analyses, calculations of element concentrations and atomic ratios were carried out using calibrated *k*-factors and thin film matrix correction procedures. The absorption correction procedure was based on the principle of electroneutrality (Van Cappellen and Doukhan 1994). The *k*-factors for O and Mg were determined using quartz and forsterite standards by the parameter-less method of Van Cappellen (1990).

## RESULTS

The sample in this study does not demonstrate significant thermal alteration caused by the capture process, in contrast to several other Wild 2 particles (Zolensky et al. 2006; Leroux et al. 2008). Only a minor amount of melted material is found at the periphery in contact with compressed aerogel. The sample is dominated by orthopyroxene (enstatite) and minor Ca-rich clinopyroxene, both Fe-poor. Orthopyroxene contains a low density of crystal defects. A few dislocations and planar defects along the (100) plane are observed. The main feature of the diopside grain is an exsolution microstructure, consisting of continuous coherent (001) lamellae, ~7 nm in thickness, with wavelengths from 20 to 30 nm (Fig. 2a). The small thickness

of the lamellae precluded the measurement of their individual compositions and only the average composition of the grain was obtained. Measured average compositions are $En_{95.8}Wo_{1.7}Fs_{2.5}$ for enstatite and $En_{71.4}Wo_{25.7}Fs_{2.9}$ for the Ca-rich component (see Table 1 for details). Selected area electron diffraction patterns (Figs. 2b–2c) confirm two distinct contributions, diopside with space group $C2/c$ and pigeonite with space group $P2_1/c$. These two phases are distinguishable by their different monoclinic lattice angles and a slight difference in their lattice parameters in the 100* and 001* directions. Misfit dislocations are not present at the lamellae/host interface.

## Discussion

The composition and the exsolution microstructure of the Ca-rich Wild 2 grain are hardly compatible with a formation by condensation or annealing from an amorphous precursor. While exceedingly rapid vapor condensation or rapid decompression (from impact) can result in immiscible glasses (Zolensky and Koeberl 1991), it is difficult to conceive of a situation leading from this to a pyroxene exsolution texture, or vapor condensation scenario that would lead directly to such an exsolution structure (G. Lofgren, personal communication). The microstructure

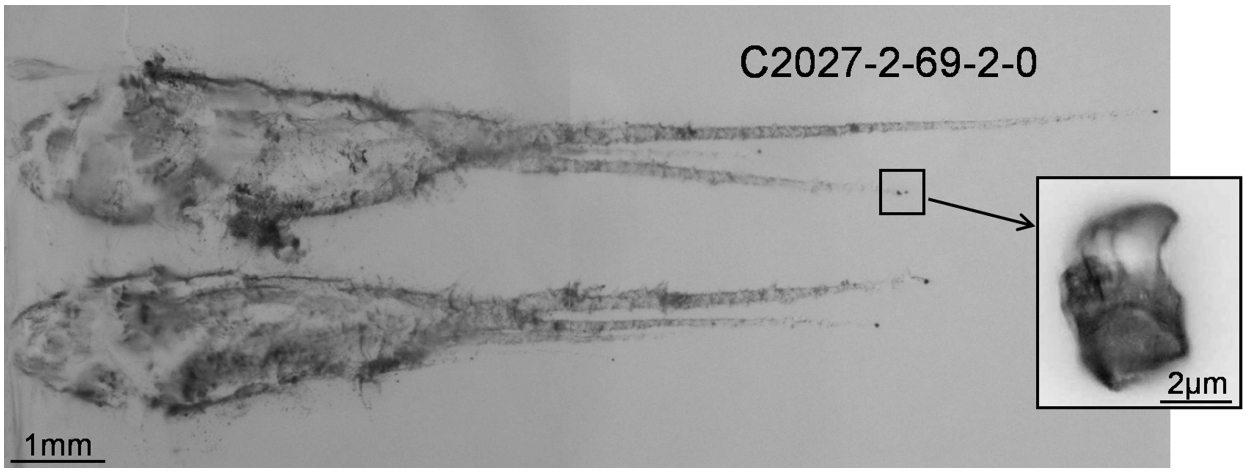


**Figure 1.** Optical micrograph of tracks 32 and 69. Impacting comet dust particles created tracks with various morphologies. Both of these tracks have a bulbous entry region (left side) and are terminated by several carrot-like sub-tracks (right side). The studied grain comes from one of the track termini of track 69. The grain particle has been extracted and prepared for TEM by ultramicrotomy at NASA-JSC.

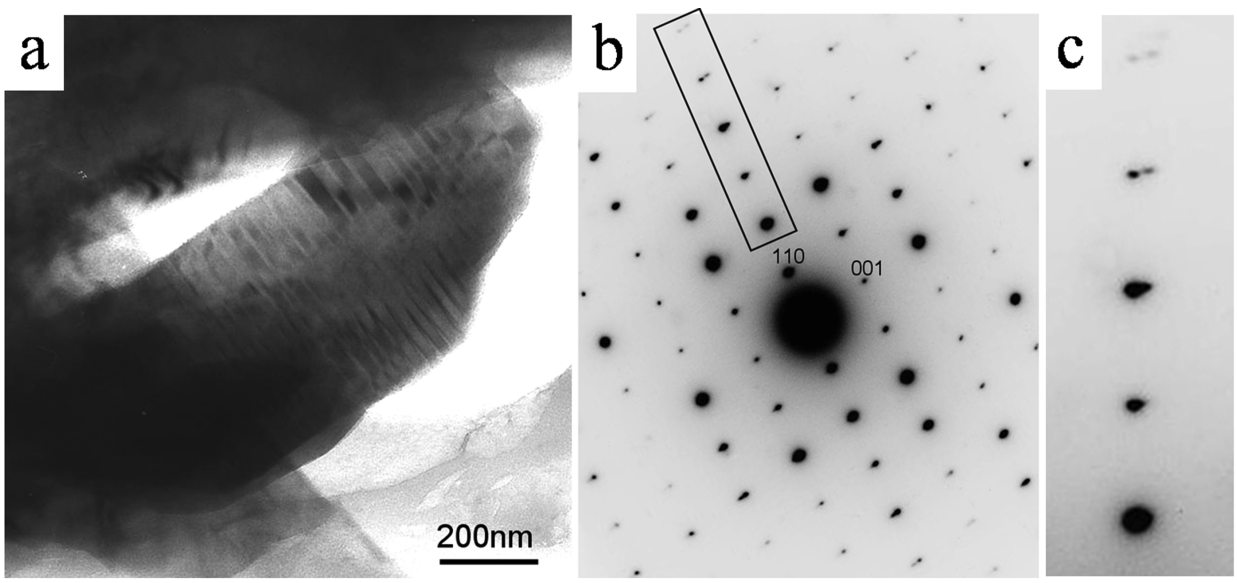


**Figure 2.** (**a**) TEM bright field image of the Ca-rich grain showing exsolution lamellae in (001). (**b**) SAED pattern, zone axis [$\bar{1}$10]. The spots show splitting along the [110]* direction, as better seen on the enlargement on **c**. This splitting is due to an alternation of Ca-rich and Ca-poor clinopyroxene corresponding to a $\Delta\beta$ of about 3° in the [100]* direction.

**TABLE 1.** EDS composition for the pyroxene particle from track 69 (normalized to 60 at% oxygen)

| O | Si | Mg | Ca | Al | Ti | Cr | Mn | Fe |
|---|---|---|---|---|---|---|---|---|
| | | | | **Enstatite** | | | | |
| 60.0 | 19.6 | 19.0 | 0.33 | 0.28 | 0.01 | 0.27 | 0.10 | 0.50 |
| – | (0.1) | (0.1) | (0.04) | (0.04) | (0.01) | (0.02) | (0.03) | (0.04) |
| | | | | **Diopside** | | | | |
| 60.00 | 18.6 | 13.6 | 4.9 | 1.4 | 0.16 | 0.40 | 0.24 | 0.56 |
| – | (0.1) | (0.6) | (0.5) | (0.3) | (0.02) | (0.03) | (0.03) | (0.09) |

*Note:* Estimated standard deviations are given in parentheses.

is fully consistent with crystallization from a FeO-poor melt, pyroxene-like in composition. According to the $Mg_2Si_2O_6$-$CaMgSi_2O_6$ binary phase diagram (Fig. 3[1], see also Carlson 1988), the primary crystallization leads to the formation of orthoenstatite and diopside. The bulk composition of the diopside grain includes approximately 32 mol% of $CaSiO_3$, indicating a temperature of crystallization of 1400 °C. During subsequent cooling, the solubility of enstatite decreases rapidly in Ca-rich compositions while it only slightly increases in the Mg-rich end-member. The primary diopside crystals thus enter a two-phase field, namely pigeonite + diopside. During subsequent cooling, pigeonite is exsolved in the form of coherent lamellae in the (001) plane in a diopside matrix that becomes enriched in Ca. This formation mechanism has been explained as a spinodal-decomposition-like process or coherent nucleation and growth, followed by coarsening (e.g., McCallister and Yund 1977; Grove 1982; Jantzen 1984). In contrast, the adjacent enstatite grains, because of the relatively constant Ca solubility within the range of temperature 1200–1400 °C, do not present an exsolution microstructure on cooling.

Exsolution formation and coarsening in pyroxene is controlled by diffusion, which is a time and temperature-dependent process. The widths of exsolution lamellae can be used to estimate the cooling rate of terrestrial and extraterrestrial rocks (e.g., Champness and Lorimer 1971; Takeda et al. 1975; Lally et al. 1975; Grove 1982; Schwartz and McCallum 2005; Weinbruch and Müller 1995; Weinbruch et al. 2001; Watanabe et al. 1985; McCallister and Nord 1981; Leroux et al. 2004). The development of (001) lamellae first requires an incubation period for the spinodal process or coherent nucleation to be completed, followed by the coarsening process. Lamellae coarsening have been calibrated with isothermal annealing or continuous cooling experiments (Grove 1982; Weinbruch et al. 2001), including experiments at compositions close to those found in this Wild 2 sample (McCallister 1978; Weinbruch et al. 2003, 2006). Coarsening in isothermal growth experiments is described by an empirical equation $\lambda^n(t) - \lambda_0^n = k\,(t - t_0)$, where k and n are empirical constants, $\lambda_0$ the average initial wavelength at $t_0$, $\lambda(t)$ is the wavelength at time $t$. The exponent factor n is close to 3, indicating a volume diffusion controlled process (Weinbruch et al. 2003). For continuous cooling, the cooling rate can be estimated with a time-temperature transformation (TTT) diagram constructed with isothermal growths (Fig. 4[1], see also Weinbruch et al. 1995). The average wavelength observed in the Wild 2 sample is 25 nm. When plotted in the TTT diagram, this value yields a cooling rate in the range 10–100 °C/h, within the temperature interval 1350–1200 °C. At lower temperature, the diffusion is too slow to account for coarsening. The main coarsening process occurred at $T > 1200$ °C.

The diopside-enstatite phase assemblage, the composition and the exsolution microstructure of the Ca-rich component show that the studied Wild 2 particle experienced an igneous (melting) episode. Before discussing an indigenous origin, it is necessary to know if the capture of the particle in silica aerogel could be responsible for this igneous microstructure. The capture of particles in aerogel has been demonstrated to induce local melting due to the hypervelocity impact at 6.2 km/s in the silica aerogel collectors (Zolensky et al. 2006; Leroux et al. 2008). The melted material has been quenched as a glass mixed with silica glass coming from melted silica aerogel. This easily recognized microstructure is not observed in our sample, except at the periphery of the grain. The cooling rate we deduced in the present study appears to be much lower than the one deduced from the thermal regime associated to the capture (Roskosz et al. 2008), showing that the formation of an exsolution microstructure in pyroxene during the capture is unrealistic. The igneous microstructure is thus indigenous to this particular Wild 2 material itself.

Several causes can be invoked for melt formation in the solar system. They include chondrule formation, volcanic activity at asteroid or planetoid surfaces, and impact melting. Exsolution microstructure in impact melt rocks has never been observed, probably because most material experienced rapid cooling after shock heating. Exsolution in pyroxene occurs frequently in igneous rocks originated from lava of differentiated asteroids or planets with associated cooling rates usually lower that the one we extracted from the Wild 2 Ca-rich particle (e.g., Takeda et al. 1975; Leroux et al. 2004; Schwartz and McCallum 2005). If the Wild 2 particle originated from such an igneous environment, it might be located at the upper part of the lava flow. Exsolution lamellae in Ca-rich pyroxene were also found in an almost Fe-free clinopyroxene in granular olivine-pyroxene chondrules from the Allende CV3 chondrite for which the wavelength of the exsolution lamellae is within the range 25–33 nm (Weinbruch and Müller 1995). This microstructure (and the associated cooling rate) is quite comparable to the one of the studied Ca-rich pyroxene grain and suggests that the studied Wild 2 particle could originate from a fragmented chondrule. Igneous textures or potential chondrule-bearing minerals have been identified in other Wild 2 particles (Zolensky et al. 2006; Joswiak et al. 2007; Nakamura et al. 2008) and suggest that chondrule-like objects are found not only in meteorites but also in bodies assembled at large distances from the inner region of the solar system.

A significant fraction of dust is crystalline in the circumstellar disks of Herbig Ae/Be and T Tauri stars (Waelkens et al. 1996; Van Boekel et al. 2004) and in cometary trails (Crovisier et al.

[1] Deposit item AM-08-058, Figures 3 and 4 (binary phase diagram and a time-temperature transformation diagram). Deposit items are available two ways: For a paper copy contact the Business Office of the Mineralogical Society of America (see inside front cover of recent issue) for price information. For an electronic copy visit the MSA web site at http://www.minsocam.org, go to the American Mineralogist Contents, find the table of contents for the specific volume/issue wanted, and then click on the deposit link there.

1997; Wooden 2002). The Stardust sample return of comet Wild 2 provides the unique opportunity to study extraterrestrial material coming from a location other than the asteroid belt, and thus to discuss the ubiquitous occurrence of crystalline silicates in the protoplanetary disk. Diopside-pigeonite exsolution microstructure in a Wild 2 particle demonstrates that igneous material is present, with comparable characteristics to the chondrules from primitive meteorites (Weinbruch and Müller 1995). The occurrence of igneous signatures in comet Wild 2, together with the discovery of calcium-aluminum inclusions (CAIs) (Brownlee et al. 2008), suggest that minerals formed in the inner region of the solar nebula were redistributed by a radial transport mechanism in the protoplanetary disk into the region of comet formation (Brownlee et al. 2006; Zolensky et al. 2006). Alternatively, it could indicate that igneous episodes were not restricted to the inner region and could have occurred at various distances in the protoplanetary disk, including beyond Jupiter. The recent report of a collisionally fragmented large Kuiper Belt object (Brown et al. 2007) demonstrates that fragments of geologically evolved outer solar system bodies were available for incorporation into later-formed comet nuclei.

## Acknowledgments

The authors thank Jean-François Dhenin for his assistance with the microscopes, M. Roskosz and S. Merkel for constructive discussions. We are thankful for support from CNES (Centre National des Etudes Spatiales) and from the electron microscope facility by European FEDER and region Nord-Pas-de-Calais. M. Zolensky was supported by NASA's Stardust Data Analysis Program. The paper has benefited from extremely helpful and constructive reviews by H.A. Ishii and an anonymous reviewer.

## References cited

Brown, M.E., Barkume, K.M., Ragozzine, D., and Schaller, E.L. (2007) A collisional family of icy objects in the Kuiper belt. Nature, 446, 294–296.

Brownlee, D. and others (2006) Comet 81P/Wild 2 under a microscope. Science, 314, 1711–1716.

Brownlee, D.E., Joswiak, D.J., Matrajt, G., Bradley, J.P., and Ebel, D.S. (2008) Ultra-refractory attogram inclusions in comet dust—First condensates? Proceedings of the 39th Lunar and Planetary Science Conference, p. 1978. Lunar and Planetary Institute, Houston, Texas.

Carlson, W.D. (1988) Subsolidus phase equilibria on the forsterite-saturated join $Mg_2Si_2O_6$-$CaMgSi_2O_6$ at atmospheric pressure. American Mineralogist, 73, 232–241.

Champness, P.E. and Lorimer, G.W. (1971) An electron microscopic study of a lunar pyroxene. Contributions to Mineralogy and Petrology, 33, 171–183.

Crovisier, J., Leech, K., Bockelée-Morvan, D., Brooke, T.Y., Hanner, M.S., Altieri, B., Keller, H.U., and Lellouch, E. (1997) The spectrum of Comet Hale-Bopp (C/1995 01) observed with the Infrared Space Observatory at 2.9 AU from the Sun. Science, 275, 1904–1907.

Grove, T.L. (1982) Use of exsolution lamellae in lunar clinopyroxenes as cooling rate speedometers: An experimental calibration. American Mineralogist, 67, 251–268.

Ishii, H.A., Bradley, J.P., Dai, Z.R., Chi, M., Kearsley, A.T., Burchell, M.J., Browning, N.D., and Molster, F. (2008) Comparison of Comet 81P/Wild 2 dust with interplanetary dust from comets. Science, 319, 447–450.

Jantzen, C.M. (1984) On spinodal decomposition in Fe-free pyroxenes. American Mineralogist, 69, 277–282.

Joswiak, D.J., Matrajt, G., Brownlee, D.E., Westphal, A.J., and Snead, C.J. (2007) A Roedderite-Bearing Terminal Particle from Stardust Track 56: Comparison with Rare Peralkaline Chondrules in Ordinary Chondrites. Proceedings of the 38th Lunar and Planetary Science Conference, p. 2142. Lunar and Planetary Institute, Houston, Texas.

Kemper, F., Vriend, W.J., and Tielens, A.G.G.M. (2004) The absence of crystalline silicates in the diffuse interstellar medium. The Astrophysical Journal, 609, 826–837.

Lally, J.S., Heuer, A.H., Nord Jr., G.L., and Christie, J.M. (1975) Subsolidus reactions in lunar pyroxenes: An electron petrographic study. Contributions to Mineralogy and Petrology, 51, 263–281.

Leroux, H., Devouard, B., Cordier, P., and Guyot, F. (2004) Pyroxene microstructure in the North West Africa 856 Martian meteorite. Meteoritics and Planetary Science, 39, 711–722.

Leroux, H., Rietmeijer, F.J.M., Velbel, M.A., Brearley, A.J., Jacob, D., Langenhorst, F, Bridges, J.C., Zega, T.J., Stroud, R.M., Cordier, P., Harvey, R.P., Lee, M., Gounelle, M., and Zolensky, M. (2008) TEM study of thermally modified Comet 81P/Wild 2 dust particles by interactions with the aerogel matrix during the Stardust capture process. Meteoritics and Planetary Science, 43, 97–120.

McCallister, R.H. (1978) The coarsening kinetics associated with exsolution in an iron-free clinopyroxene. Contributions to Mineralogy and Petrology, 65, 327–331.

McCallister, R.H. and Nord Jr., G.L. (1981) Subcalcic diopsides from kimberlites: Chemistry, exsolution microstructures, and thermal history. Contributions to Mineralogy and Petrology, 78, 118–125.

McCallister, R.H. and Yund, R.A. (1977) Coherent exsolution in Fe-free pyroxenes. American Mineralogist, 62, 721–726.

Nakamura, T., Noguchi, T., Tsuchiyama, A., Ushikubo, T., Kita, N.T., Valley, J.W., Zolensky, M.E., Kakazu, Y., Sakamoto, K., Mashio, E., Uesugi, K., and Nakano, T. (2008) Chondrule-like objects recovered from short-period comet 81P/Wild 2. Science, 321, 1664–1667.

Roskosz, M., Leroux, H., and Watson, H.C. (2008) Thermal history, partial preservation and sampling bias recorded by Stardust cometary grains during their capture. Earth and Planetary Science Letters, 273, 195–202.

Schwartz, J.M. and McCallum, I.S. (2005) Comparative study of equilibrated and unequilibrated eucrites: Subsolidus thermal histories of Haraiya and Pasamonte. American Mineralogist, 90, 1871–1886.

Takeda, H., Miyamoto, M., Ishii, T., and Lofgren, G.E. (1975) Relative cooling rates of mare basalts at the Apollo 12 and 15 sites as estimated from pyroxene exsolution data. Proceedings of the 6th Lunar Science Conference, p. 987–996, Houston, Texas.

Van Boekel, R. and others (2004) The building blocks of planets within the "terrestrial" region of protoplanetary disks. Nature, 432, 479–482.

Van Cappellen, E. (1990) The parameterless correction method in X-ray microanalysis. Microscopy Microanalysis Microstructures, 1, 1–22.

Van Cappellen, E. and Doukhan, J.C. (1994) Quantitative transmission X-ray microanalysis of ionic compounds. Ultramicroscopy, 53, 343–349.

Waelkens, C. and others (1996) SWS observations of young main-sequence stars with dusty circumstellar disks. Astronomy and Astrophysics, 315, L245–L248.

Watanabe, S., Kitamura, M., and Morimoto, N. (1985) A transmission electron microscope study of pyroxene chondrules in equilibrated L-group chondrites. Earth and Planetary Science Letters, 72, 87–98.

Weinbruch, S. and Müller, W.F. (1995) Constraints on the cooling rates of chondrules from the microstructure of clinopyroxene and plagioclase. Geochimica et Cosmochimica Acta, 59, 3221–3230.

Weinbruch, S., Müller, W.F., and Hewins, R.H. (2001) A transmission electron microscope study of exsolution and coarsening in iron-bearing clinopyroxene from synthetic analogues of chondrules. Meteoritics and Planetary Science, 36, 1237–1248.

Weinbruch, S., Styrsa, V., and Müller, W.F. (2003) Exsolution and coarsening in iron-free clinopyroxene during isothermal annealing. Geochimica et Cosmochimica Acta, 67, 5071–5082.

Weinbruch, S., Styrsa, V., and Dirsch, T. (2006) The size distribution of exsolution lamellae in iron-free clinopyroxene. American Mineralogist, 91, 551–559.

Wooden, D.H. (2002) Comet grains: Their IR emission and their relation to ISM grains. Earth, Moon, and Planets, 89, 247–287.

Zolensky, M. and Koeberl, C. (1991) Why are blue zhamanshinites blue?: Liquid immiscibility in an impact melt. Geochimica et Cosmochimica Acta, 55, 1483–1486.

Zolensky, M.E. and others (2006) Mineralogy and petrology of comet 81P/Wild 2 nucleus samples. Science, 314, 1735–1739.

Zolensky, M., Nakamura-Messenger, K., Fletcher, L., and See, T. (2008) Curation, spacecraft recovery and preliminary examination for the Stardust Mission: A perspective from the Curatorial Facility. Meteoritics and Planetary Science, 43, 5–21.

Manuscript received June 27, 2008
Manuscript accepted September 4, 2008
Manuscript handled by Bryan Chakoumakos

Author's personal copy

Available online at www.sciencedirect.com
ScienceDirect
Geochimica et Cosmochimica Acta 73 (2009) 767–777
Geochimica et Cosmochimica Acta
www.elsevier.com/locate/gca

# Oxidation state of iron and extensive redistribution of sulfur in thermally modified Stardust particles

Hugues Leroux *, Mathieu Roskosz, Damien Jacob

*Laboratoire de Structure et Propriétés de l'Etat Solide, Université des Sciences et Technologies de Lille and CNRS, UMR 8008, F-59655 Villeneuve d'Ascq, France*

Received 4 June 2008; accepted in revised form 21 September 2008; available online 3 January 2009

**Abstract**

Two representative thermally modified Stardust samples were investigated by analytical transmission electron microscopy in order to decipher their iron oxidation state after the strong thermal episode due to the capture in aerogel. Their dominant microstructure consists of evenly distributed rounded Fe–Ni–S nano-droplets within a silica-rich glassy matrix. The mineralogy and associated redox state of iron is assessed using a Fe–Mg–S ternary diagram on which ferromagnesian silicates, sulfides and metal can be represented and potentially compared with any other extraterrestrial material. In this diagram, all the data (bulk and local analysis of silicates, sulfide + metal) scatter along a mixing line between the Mg corner and the average composition of the iron-sulfide. There is an obvious genetic relationship between the different phases observed in such samples, further supported by the very low concentration of iron in the glassy matrix. Silicate glasses contain a significant concentration of dissolved sulfur probably present as MgS complexes. This chemical signature is typical of highly reduced environments. These secondary microstructures were established during the high temperature stage of the capture. A significant part of the Fe-droplets formed in situ by reduction at high temperature of ferromagnesian silicates (olivine and pyroxenes) during the impact. At this stage, the indigenous sulfides destabilized and sulfur readily volatilized as $S_2$, diffused into molten materials and condensed later onto the Fe-precipitates that formed in the silicate melt. This scenario is supported by the structure of Fe–Ni–S beads with a metal core and a sulfide rim. It will be difficult to derive reliable information on the redox state of 81P/Wild 2 particles based on bulk analyses of whole tracks because particles found along the walls of tracks suffered strong reduction reactions, contrary to terminal particles that may have preserved their pristine redox state. The capture effect must be taken into account for comparison of Wild 2 particles with other chondritic material.
© 2008 Elsevier Ltd. All rights reserved.

## 1. INTRODUCTION

In January 2006 the Stardust mission brought to Earth samples from comet 81P/Wild 2 (Brownlee et al., 2006). The collection was performed at an encounter speed of ~6.1 km/s into silica aerogel, an underdense (0.01–0.05 g/cm$^3$) capture medium. The hypervelocity impacts created deceleration tracks in the aerogel (Hörz et al., 2006). Using synchrotron-based X-ray microprobes (SXRM), Flynn et al. (2006) showed that a major fraction of the comet material is unevenly distributed along most tracks, suggesting that cometary materials mechanically disaggregated during the impact into aerogel (Zolensky et al., 2006; Hörz et al., 2006). This distribution suggests the impact of loosely bonded aggregates of relatively large minerals (over 1 μm) and fine grains (Zolensky et al., 2006). The large particles are crystalline and, so far, were found mainly at the ends of tracks. In contrast, the walls contain abundant fine, submicron scale material. A number of Stardust samples, in particular those extracted from track walls, show evidences for strong thermally induced modifications in addition to strong intermixing with melted aerogel (Zolensky et al., 2006; Leroux et al., 2008; Rietmeijer et al., 2008). This situation significantly complicates the analyses and the understanding of these samples.

* Corresponding author.
*E-mail address:* Hugues.Leroux@univ-lille1.fr (H. Leroux).

0016-7037/$ - see front matter © 2008 Elsevier Ltd. All rights reserved.
doi:10.1016/j.gca.2008.09.037

Author's personal copy



An important question regarding the Wild 2 materials is the oxidation state of iron. Urey and Craig (1953) showed that the oxidation state of Fe differs among meteorite groups and consequently could be used as a proxy to classify extraterrestrial material. First attempts to this effect with Stardust material were recently provided by Westphal et al. (2008) and Ogliore et al. (2008) by X-ray absorption near edge structure (XANES) of iron using synchrotron microprobe. Track 124 revealed a high diversity of Fe-bearing minerals indicating a complex cometary particle (Ogliore et al., 2008). With analyses of several tracks, Westphal et al. (2008) showed metal- and sulfide-rich materials, inconsistent with any meteorite group. They also emphasized the role of the capture effect on the oxidation state of iron. During hypervelocity capture iron would tend to become reduced due to the presence of residual carbon in aerogel. Since large numbers of grains suffered from thermal alteration during capture (Zolensky et al., 2006; Leroux et al., 2008) it appears essential to understand the evolution of the iron oxidation states during the high temperature period of the hypervelocity impact.

The typical microstructure of thermally altered particles consists of dense silica-rich glassy matrix containing widespread beads of nanoscale Fe–Ni–S phases. This microstructure gives clear evidence for melting of the cometary dust and mixing with molten aerogel. On the other hand, mixing was spatially limited and heterogeneous as shown by the presence of "dust-rich" submicron patches dispersed in formerly molten aerogel (Leroux et al., 2008). In addition, chemical reactions were documented in the high temperature melt phase as demonstrated by the presence of iron-silicides in some samples (Rietmeijer et al., 2008). Hence it appears that the cometary grains have lost their original microstructures during thermal modification yet their composition seems to be preserved beside an obvious contribution of $SiO_2$ from the aerogel. Once a correction applied for $SiO_2$, Leroux et al. (2008) showed that numbers of these samples are close to a CI composition (including sulfur) and that they likely originated from small aggregated material similar to materials found in interplanetary dust particles (IDPs), in contrast to the conclusion drawn by Ishii et al. (2008) who recently stated that Wild 2 grains resemble meteoritic material from the asteroid belt.

Continuing the efforts of Leroux et al. (2008) to decipher the complexity of the thermally modified grains, and using analytical transmission electron microscopy, we studied the mineralogy, petrology and associated oxidation state of iron in two representative thermally altered Stardust samples. For this purpose we propose a new petrological groundwork based on a Fe–Mg–S ternary representation. In this way, some major distinguishing features of chondritic materials are plotted in terms of composition and with strong indications of their mineralogical nature (sulfides, metals and silicates), but without artefacts caused by the contribution of aerogel to the bulk chemical composition of materials. This approach, complementary to XANES studies undertaken with synchrotron X-ray microbeam, is particularly useful to understand iron and sulfur speciation in the thermally modified Stardust samples.

## 2. ANALYTICAL PROCEDURES, STUDIED SAMPLES

Stardust grains were removed from aerogel at the NASA Johnson Space Center (JSC) with micromanipulators, embedded in EMBED-812 epoxy and sliced into 70 nm thick sections with an ultramicrotome equipped with a diamond knife. Sections were deposited onto C-coated transmission-electron-microscope (TEM) copper grids. The detailed procedures were given by [Zolensky et al. (2006) – supporting online material]. The results presented in this paper come from track 35, grains 51 and 52, allocations C2054,0,35,51,3 and C2054,0,35,52,3. Track 35 is 1.17 cm in length with a large bulbous cavity at the entrance side and a long carrot-like track emerging from the bulbous region. The two grains studied here were extracted at the place where the bulbous cavity closes up and the slender track emerges.

The samples were studied at the university of Lille using a Philips CM30 ($LaB_6$ filament, working at 300 keV) and a Tecnai G2-20 twin ($LaB_6$ filament, 200 kV). The microscopes are equipped with Energy Dispersive X-ray Spectroscopy (EDS) with Thermo-Noran and EDAX Si-detectors (CM30 and Tecnai, respectively). Grain microstructures were studied using bright and dark field imaging in conventional TEM mode and with annular-bright and dark field detectors in scanning (STEM) mode. Compositions were studied by EDS with probe sizes ranging from 5 to 10 nm in the STEM configuration. For quantitative analyses, calculations of element concentrations and atomic ratios were carried out using calibrated *k*-factors and thin film matrix correction procedures. The *k*-factors for the major elements were determined using standard specimens according to the parameter-less method of Van Cappellen (1990). For silicates, the absorption correction procedure based on the principle of electroneutrality was applied (Van Cappellen and Doukhan, 1994). Elemental distributions were obtained by EDS X-ray intensity maps, using spectral imaging wherein each pixel of a spectrum image contains a full EDS spectrum (see Leroux et al., 2008 for details).

## 3. RESULTS

Thermally modified grains have two main characteristics. First, they contain a high density of small and rounded Fe–Ni–S phases and vesicles within a glassy matrix (Fig. 1a). Sizes of the Fe–Ni–S droplets extend from a few nm to a hundred nm. A number of them consist of a Fe,Ni metal core and a Fe-sulfide rim (Fig. 1b). A more extensive description can be found in Leroux et al. (2008). Second, there is the contribution of the molten aerogel to the composition of the glassy matrix as illustrated by the anomalously high $SiO_2$ concentration (typically 90–95 mol.%; Table 1). In the most extreme case, some areas are pure $SiO_2$ and correspond to compressed aerogel or quenched glass containing numerous vesicles, but no Fe–Ni–S droplets. Beside $SiO_2$, other major elements are Mg, Fe and S and to a lesser extent Al, Ca, Cr, Mn and Ni. Their distributions are highly variable from place to place

Author's personal copy



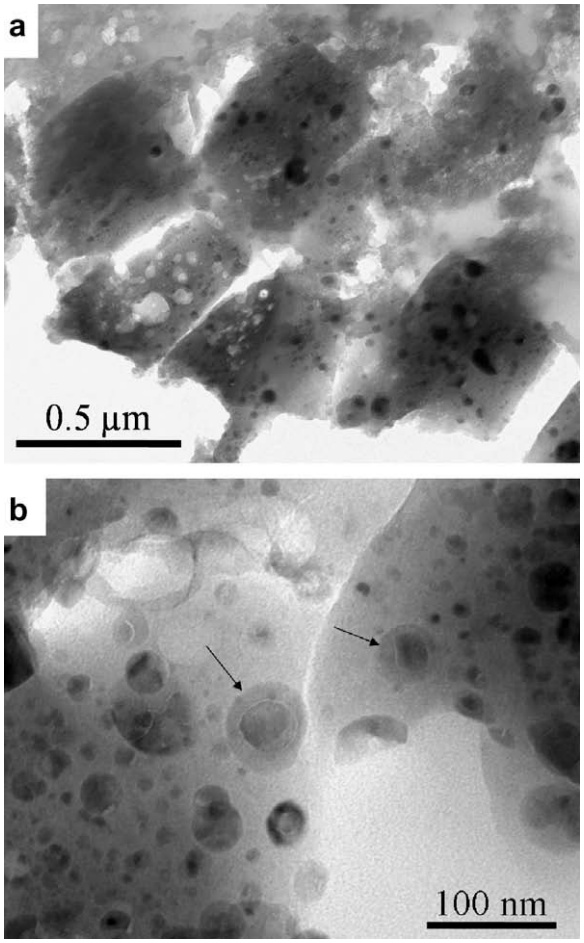


Fig. 1. Bright field images from C2054,0,35,52,3. (a) Typical microstructure of thermally modified samples consisting of a silica-rich glassy matrix embedding Fe–Ni–S nanophases which appear as dark dots on the micrograph. Note the presence of a large number of small rounded vesicles which appear brighter within the glassy matrix. (b) A number of the Fe-Ni-S phases consist of a Fe,Ni metal core covered by a Fe-sulfide rim (two of them are arrowed).

Table 1
Representative EDS compositions (at.%) for samples C2054, 0,35,51,3 and C2054,0,35,52,3. For each sample the scanned surface was 500 × 500 nm, randomly selected. nd, not detected.

| O | Si | Mg | Fe | Ni | S | Al | Ca | Cr | Mn |
|---|---|---|---|---|---|---|---|---|---|
| *C2054,0,35,51,3* | | | | | | | | | |
| 62.3 | 27.0 | 6.8 | 1.7 | 0.07 | 1.3 | 0.44 | 0.21 | 0.05 | 0.05 |
| 62.8 | 28.8 | 4.0 | 1.9 | 0.10 | 1.6 | 0.33 | 0.18 | 0.06 | 0.05 |
| 62.5 | 28.3 | 3.9 | 2.5 | 0.16 | 1.7 | 0.53 | 0.15 | 0.06 | 0.06 |
| 64.4 | 30.6 | 2.5 | 1.1 | 0.04 | 1.0 | 0.25 | 0.10 | 0.03 | nd |
| *C2054,0,35,52,3* | | | | | | | | | |
| 62.4 | 28.8 | 3.0 | 3.0 | 0.17 | 2.1 | 0.34 | 0.11 | 0.04 | 0.08 |
| 61.7 | 25.2 | 9.8 | 1.6 | 0.07 | 0.9 | 0.42 | 0.15 | 0.04 | 0.05 |
| 61.2 | 28.5 | 2.8 | 3.6 | 0.22 | 3.1 | 0.31 | 0.09 | 0.09 | 0.04 |
| 65.1 | 31.7 | 1.6 | 0.9 | 0.07 | 0.7 | nd | nd | nd | nd |

as illustrated by the EDS X-ray intensity distribution maps (Fig. 2). As in Leroux et al. (2008), we will refer to the areas enriched in Mg, Fe, S, and occasionally in Ca and Al as "dust-rich patches". Representative compositions of the two studied samples are given in Table 1.

Interestingly, Fe and S are dominantly found in the Fe–Ni–S nanophases, the distribution of which correlates frequently with the distribution of Mg in the glassy matrix (Fig. 3). In other words, regions containing a high density of Fe–Ni–S nanophases without Mg are rare. The positive correlations between Fe–Mg and Fe–S distribution are observed for a large number of measurements (Fig. 4a, b and c, d, respectively). The best correlation lines are found for S/Fe close to 0.75. This ratio is significantly lower than the S/Fe ratio for pyrrhotite (=1.14). This is a general feature since the average measured bulk S/Fe ratios in the Fe–Ni–S nanophases extend from 0.65 to 0.82, depending on the studied area but never attain the pyrrhotite or troilite values.

A major challenge with these thermally modified samples is to find a way of representing the bulk and local compositions without taking into account the contribution of molten aerogel. Because these samples are clearly composite in nature, no simple phase diagram can account for the complex assemblage of metal, sulfide and silicates described above. In addition, the strong contribution of the aerogel (pure $SiO_2$) makes difficult the representation of the composition of silicates and more generally of oxides. It precludes Fe–Mg–Si ternary representations successfully used for fine-grained matrix of primitive meteorite or IDPs. For this reason we propose to represent data in the Fe–Mg–S ternary diagram (Fig. 5). In this way, the distinction between the most common of the three classes of material is straightforward. Consequently, Fe–Ni metal, Fe-sulfides and Fe–Mg-silicates can be presented on a single diagram and genetic links between these materials can be deciphered (Fig. 5).

Bulk compositions of the two thermally modified particles are presented in this ternary diagram (Fig. 6). Both are found to be close to the CI composition, within a deviation from CI less than 20%, in close agreement with Leroux et al. (2008). For these bulk analyses of TEM slices, the analyzed surface is typically one to several tens of $\mu m^2$, for a thickness of ~80 nm. It is then interesting to establish how the composition changes in the diagram as the analyzed volume is decreased. These sub-areas were selected randomly over the sample (of course, the zones found to be pure aerogel were discarded). On Fig. 7, we report the average composition compared to a set of data collected on different sub-areas: $400 \times 400\ nm^2$ (Fig. 7a), $200 \times 200\ nm^2$ (Fig. 7b) and $30 \times 30\ nm^2$ (Fig. 7c). When the analyzed volume decreases, data scatter around the average bulk composition, along a mixing line from approximately the pure Mg end-member to an average composition along the Fe–S join. The scatter along this line increases when the analyzed surface decreases. The extreme case is shown in the last diagram (Fig. 7d), where analyses were carried out on Mg-rich areas of the glassy matrix, between the Fe–Ni–S inclusions. It is remarkable that these areas have a very low Fe concentration (Fe/Mg ratio <0.02) while S is still present in a significant relative proportion. The atomic ratio S/Mg ranges from 0.02 and 0.08,

Author's personal copy



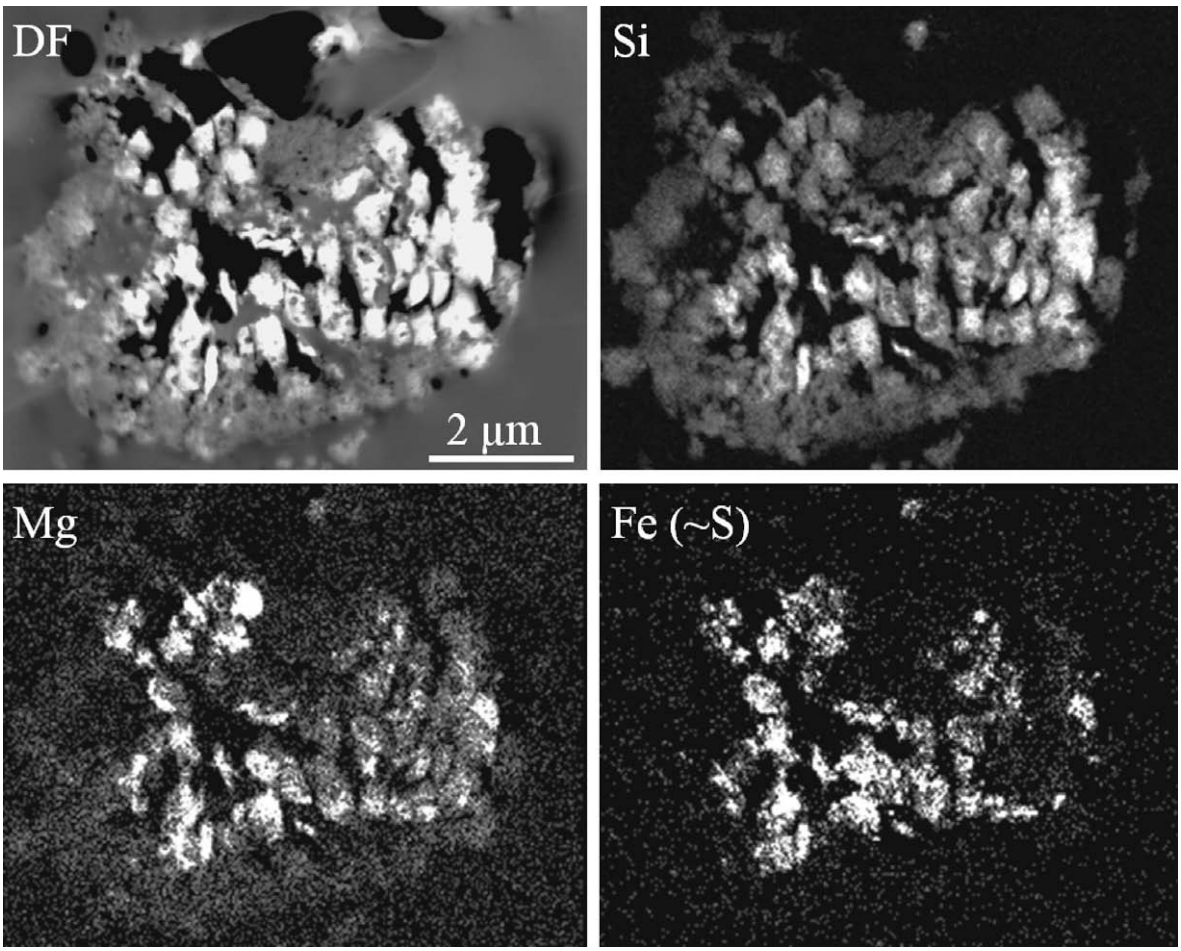


Fig. 2. Dark field (DF) STEM image and X-ray intensity maps for Si, Mg and Fe for an entire TEM slice in C2054,0,35,52,3. The distribution of S is very close to the one of Fe. Note that the distributions of Mg and Fe are heterogeneous and poorly correlated to the one of Si.

depending of the studied particle or areas in a given particle, while the S/Fe ratio is well above unity (Fig. 7d). The two studied samples, and sub-areas in a given sample, display similar trends although it was not possible to measure for each of them an accurate composition of the Mg-rich areas between the Fe–Ni–S phases. Representative Mg-rich compositions are given in Table 2. The average composition of the Fe–Ni–S phases was also measured in this sub-area. They display a S/Fe below unity (typically S/Fe ranges between 0.7 and 0.8).

## 4. DISCUSSION

### 4.1. A secondary origin for Fe–Ni–S droplets by reduction during the high temperature stage of the collection

#### *4.1.1. A positive correlation between Fe and Mg*

Among the major elements, iron is particularly important because it gives strong constraints on the redox state of extraterrestrial materials. Iron may be present as metal, sulfide, and oxides (FeO in silicates and $Fe_2O_3$ in simple oxides). As detailed above, one of the common features of Stardust thermally modified samples is the ubiquitous presence of Fe–Ni–S nano-droplets. The key question is thus to know if this microstructure might be characteristic of the Wild 2 metal and sulfide components or if these phases were produced during the high temperature stage of the capture. In this respect, the positive correlation between Mg and Fe (Fig. 5a) suggests that Fe is generally associated with Mg-rich areas. In other words, iron is frequently associated with the "dust-rich patches", which are the relicts of silicate minerals (Leroux et al., 2008). Initially, these minerals were likely pyroxene or olivine but glasses with embedded metal and sulfides (GEMS), a major component of chondritic porous IDPs (Bradley, 1994), cannot be excluded. The variability of the Mg–Fe correlation is high, showing that sulfide components are also a source of Fe–Ni–S nanophases, together with the ferromagnesian silicates.

#### *4.1.2. Reduction reaction in impact melts*

The Fe–Mg–S ternary diagrams are helpful to understand the chemical state of the thermally modified grains. Multi-scale analyses clearly show that data scatter along a mixing line between the Mg corner and the average composition of the Fe–Ni–S nanophases (Fig. 7a–d). This trend implies that the samples extracted from the deceleration track are constituted of two dominant components, the

Author's personal copy



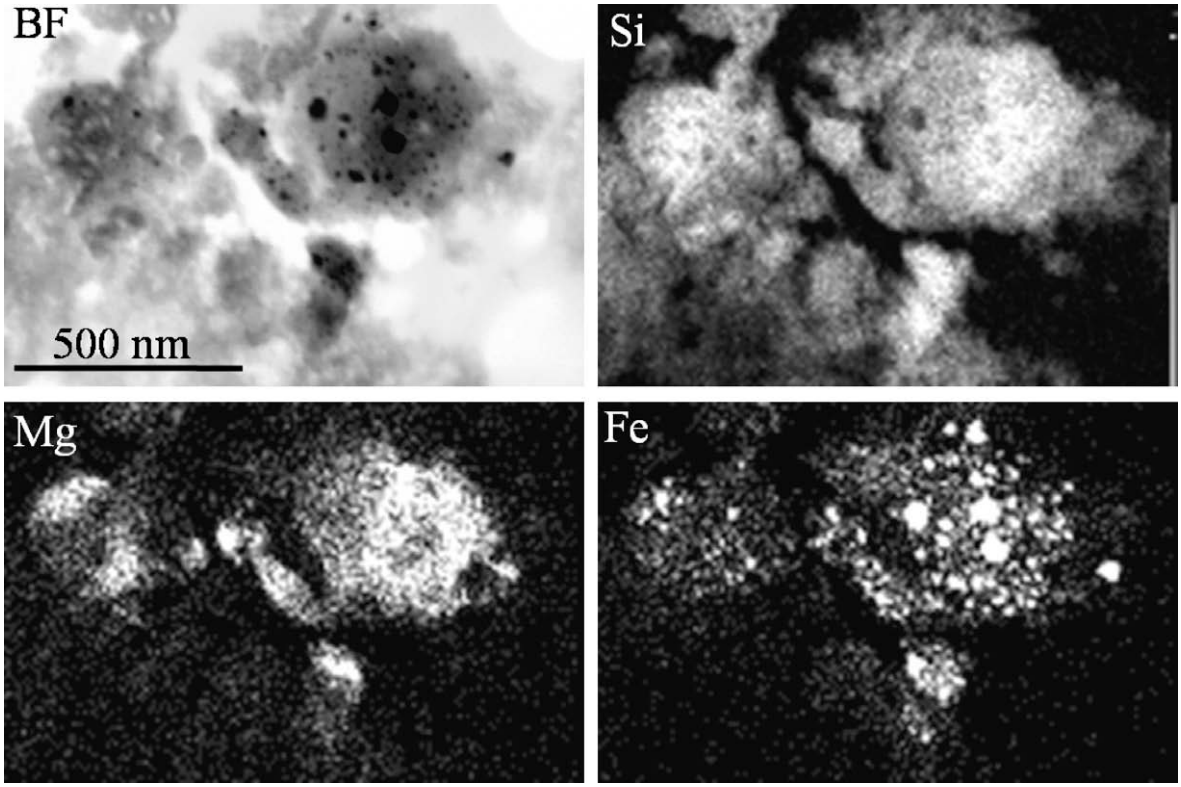


Fig. 3. Bright field (BF) STEM image and X-ray intensity maps for Si, Mg and Fe in C2054,0,35,52,3. The variation of contrast in the Si map is due to variation of sample thickness. The distribution of the Fe–Ni–S droplets generally correlates well with the distribution of Mg.

glassy matrix and Fe–Ni–S nanophases, integrated in various proportions in the selected areas for analyses. More importantly, the scattering indicates first that the S/Fe ratio is relatively constant within the selected sub-areas and thus Fe–Ni–S nanophases have strikingly comparable compositions. The data also show that the glassy matrix is strongly depleted in iron oxide as confirmed by spot analysis performed between the Fe–Ni–S nanophases for which almost no iron is detected (Fig. 7d). Because the glassy matrix contains the other elements at ~CI values (Mg, Ca, Al, Cr, Mn for the majors), it could imply that the silicate fraction of the impacting Wild 2 particles was highly reduced and/or depleted in iron. However, such an interpretation is doubtful because all materials from IDPs, micrometeorites or fine-grained matrix from primitive chondrites exhibit a wide range of Fe/Mg ratios in their silicate fraction. Finally this interpretation would not be consistent with the fact that surviving silicate minerals analyzed from the Stardust aerogel collector have a significant FeO content (Zolensky et al., 2006, 2008). The only alternative explanation that can account both for the FeO depletion in the matrix and for the remarkable homogeneity of Fe–Ni–S nanophases is that a reduction reaction occurred during the high temperature stage of the capture into aerogel.

#### *4.1.3. Origin of the heat, of the reducing agent and putative reaction*

Wild 2 dust was captured into aerogel at a relative velocity of 6.1 km/s. During the impact, a fraction of the incident kinetic energy contributed to mechanical compression of aerogel and the breaking up of poorly cohesive dusts along the tracks. Another fraction of the incident energy was converted into heat due to the strong deceleration in less than a microsecond of the hypervelocity impact. Consequently, aerogel was heated by the shock wave that develops in front of the moving particle. In terms of impact physics, such a configuration is very comparable to the implantation of particles into hot, locally melted, aerogel (Anderson and Arhens, 1994), which in turn induces melting of a fraction of incident particles (Zolensky et al., 2006). This configuration is particularly favorable to induce high temperature chemistry. Furthermore, if the implantation of the particles was achieved in less than one microsecond, the time scale of the high temperature stage was much longer and measured to be close to the millisecond (Roskosz et al., 2008). In these conditions, extensive modification of pristine material took place, in particular for fine-grained materials. Turning now to the nature of the reducing agent, it cannot be determined unambiguously but (i) any atmosphere becomes more reducing as temperature increases, (ii) carbonaceous components are present in all primitive materials and (iii) carbon was also detected in freshly manufactured aerogel as a by-product of the gel synthesis (Spencer and Zare, 2007). When carbon or carbon monoxide is present together with iron oxides at high temperature, a reduction reaction occurs. Assuming that carbon is present in the Wild 2 particles impacting the aerogel or as an internal source in aerogel, we propose the following reaction:

Author's personal copy



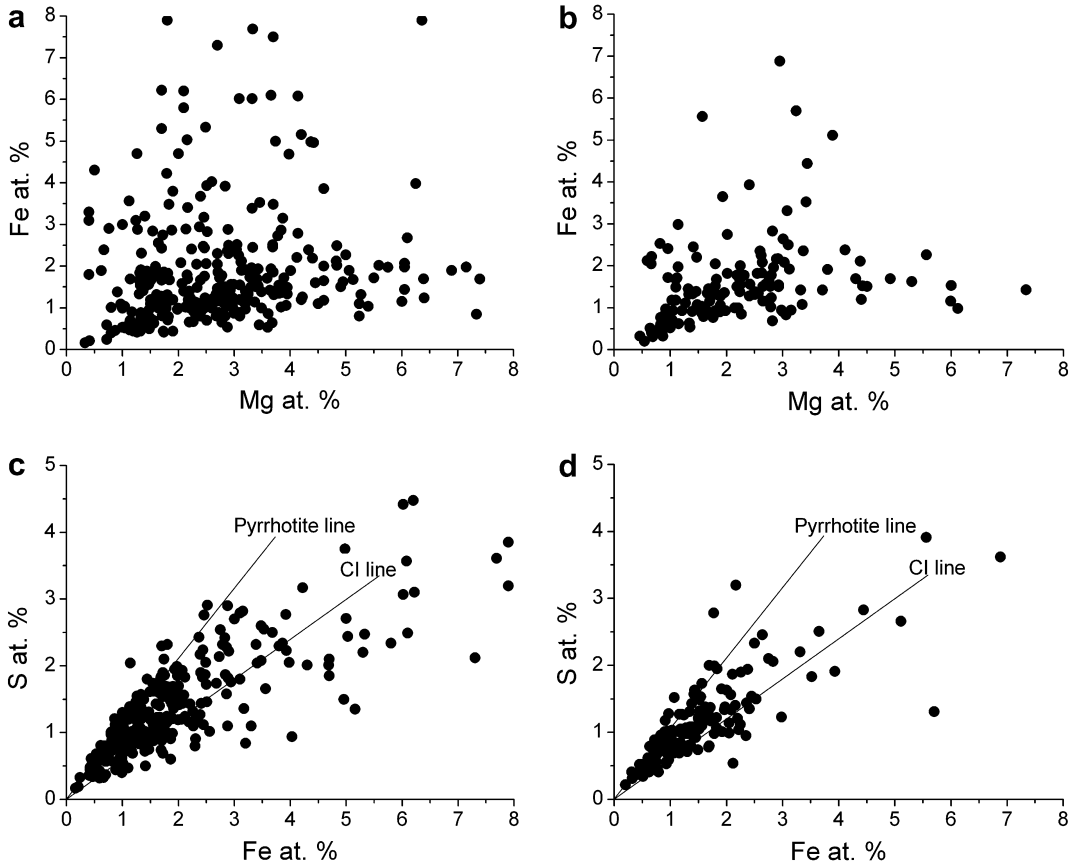


Fig. 4. Fe–Mg–S relationship in C2054,0,35,51,3. Data are given in atom%. (a–b) Correlation between Mg and Fe for relatively large analyzed areas, 100 nm and 200 nm square windows (300 and 143 measurements, respectively). The general correlation tendency is positive, suggesting that Mg and Fe are related despite the fact that Fe is found in the Fe–Ni–S nanophases. (c–d) Abundances of S vs Fe showing that S is clearly correlated with Fe, 100 nm and 200 nm square areas, respectively.

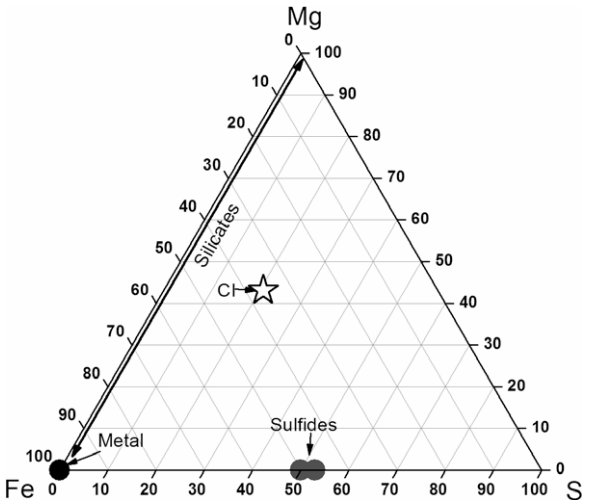


Fig. 5. Fe–Mg–S ternary diagram (atom%) with position of major components expected in Wild 2 (ferromagnesian silicates, iron-sulfides and metal). This representation is useful because many particles display evidence of silica admixture from aerogel. The CI composition is indicated by a star (from Anders and Ebihara, 1982).

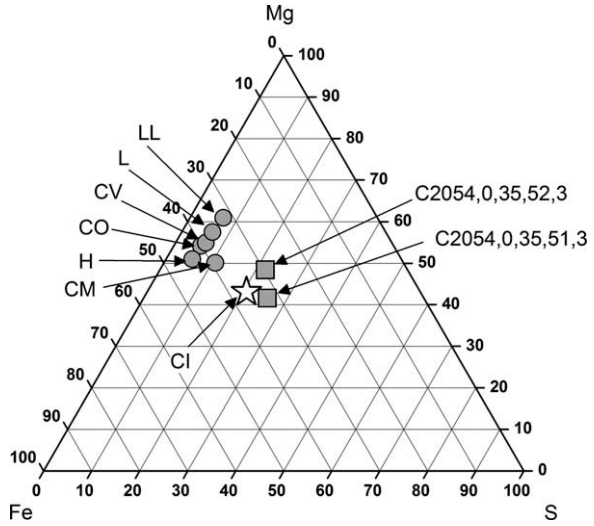


Fig. 6. Composition of the two samples (C2054,0,35,51,3, C2054,0,35,52,3) in the ternary Fe–Mg–S diagram (atom%). These compositions are deduced from bulk analysis of microtomed slices. Note that they are close to the composition of CI, within a deviation less than 20%. CI composition is from Anders and Ebihara (1982). Composition of CM, CO, CV, H, L and LL chondrites are shown for comparison (Wasson and Kallemeyn, 1988).

Author's personal copy



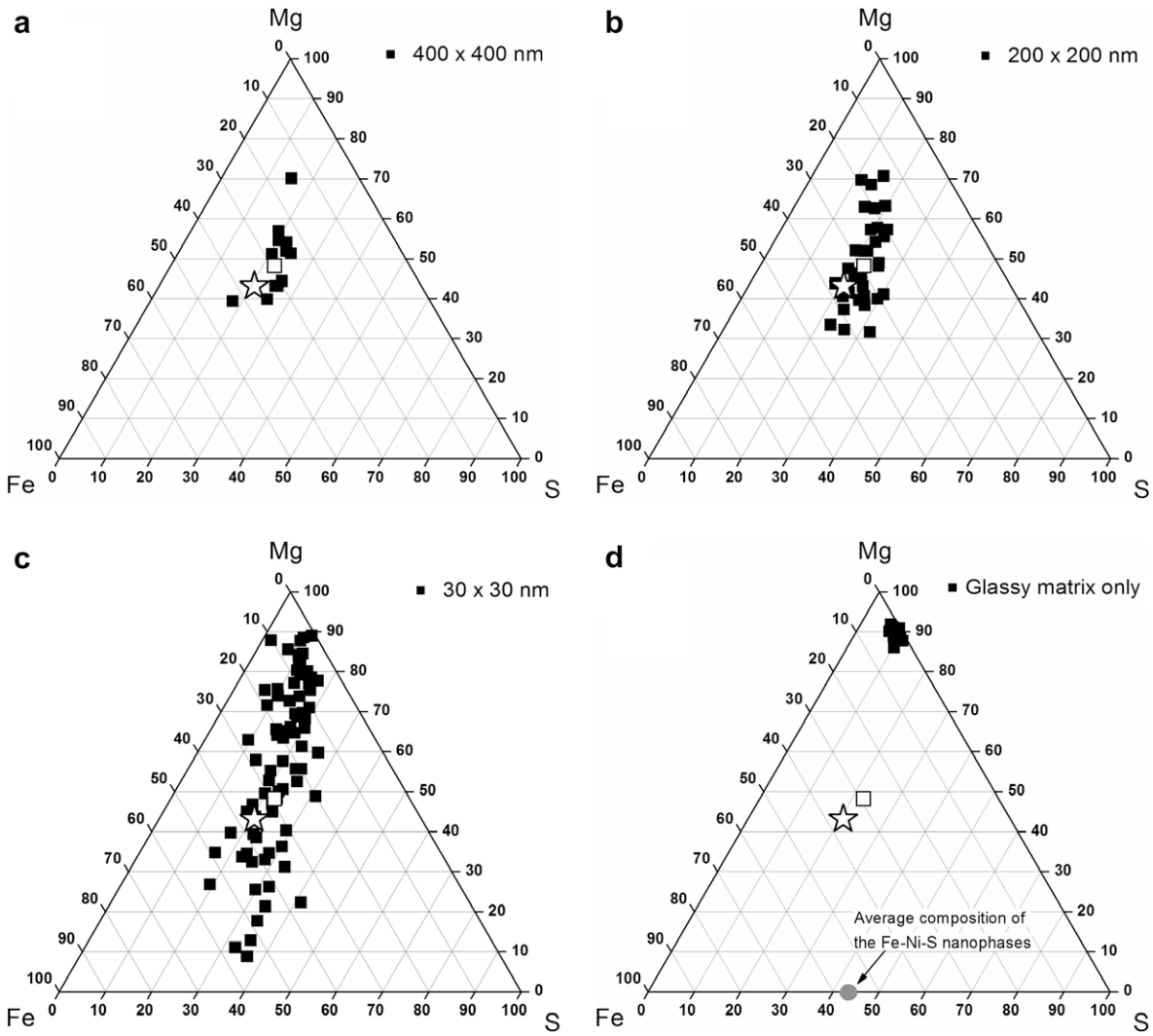


Fig. 7. Compositions for C2054,0,35,51,3 in ternary Fe–Mg–S diagrams. (a) Composition of areas 400 × 400 nm$^2$; the average composition of the studied areas (2.2 × 1.5 μm$^2$ in size) is also indicated by an open square. (b) Areas 200 × 200 nm$^2$. (c) Areas 30 × 30 nm$^2$. When the analyzed areas are decreased in size the data are found to align along a line which approximately joins the Mg pole and the Fe–S baseline. (d) Average composition of the Fe–Ni–S nanophases (S/Fe = 0.75, average on 27 measurements) and composition of the glassy matrix, in Mg-rich areas, taken between the Fe–Ni–S nanophases. The CI composition is indicated by a star.

$$FeO_{(silicate)} + C = Fe_{(metal)} + CO_{(gas)} \quad (1)$$

A similar reaction was proposed recently to explain the origin of the metal beads in dusty olivine in chondrules (Leroux et al., 2003) or proposed as an alternative model to explain the microstructure of GEMS in IDPs (Davoisne et al., 2006). According to the Gibbs free energy change for the reduction–oxidation reactions concerning carbon and iron, this reaction occurs for $T > 700$ °C. The temperature reached in the thermally modified samples is clearly higher since the initial cometary material and aerogel were found to be quenched from a melt. A natural conclusion is therefore that the Fe-rich nanophases distributed in the glassy matrix are predominantly secondary products, resulting from a reduction process of FeO-bearing silicates at high temperature. This correlation is not exclusive because a few areas with a high density of Fe–Ni–S nanophases are found occasionally without obvious correlations with Mg concentrations. In the latter configuration, the nanophases may originate from the melting and the thermal decomposition of iron-sulfides, as demonstrated experimentally by Ishii et al. (2008), or from the reduction of FeO-rich (MgO-poor) silicates or oxides.

### 4.2. Volatilization, diffusion and re-condensation of sulfur during the impact: moderate oxidation upon quenching of metal droplets

Using synchrotron-based X-ray microprobes (SXRM), Flynn et al. (2006) reported that sulfur is depleted on both tracks and craters when compared to chondritic CI. This depletion suggests that S evaporated during the high temperature regime of the hypervelocity impact into aerogel. The present study does not find evidence for comparable sulfur depletions despite the fact that the two samples

Author's personal copy



Table 2
Representative EDS compositions (at.%) for Mg-rich areas between the Fe–Ni–S nanophases in C2054,0,35,51,3 and C2054,0,35,52,3. They correspond to low count analysis causing difficulties for the determination of the concentrations of minor elements. Note that the S concentration is always well above the Fe concentration showing the presence of S in the silicate glass. nd, not detected.

| O | Si | Mg | Fe | S | Al | Ca |
|---|---|---|---|---|---|---|
| *C2054,0,35,51,3* | | | | | | |
| 61.3 | 24.0 | 13.1 | 0.03 | 1.2 | 0.1 | 0.2 |
| 64.0 | 28.8 | 6.3 | 0.1 | 0.8 | 0.1 | 0.1 |
| 63.2 | 27.4 | 8.5 | 0.2 | 0.7 | 0.1 | 0.1 |
| 62.7 | 26.5 | 9.1 | 0.1 | 1.2 | nd | 0.2 |
| *C2054,0,35,52,3* | | | | | | |
| 61.1 | 22.7 | 15.3 | 0.2 | 0.4 | nd | 0.2 |
| 61.0 | 21.8 | 15.7 | 0.05 | 0.5 | nd | 0.1 |
| 60.4 | 21.4 | 17.6 | nd | 0.5 | nd | nd |
| 62.5 | 25.5 | 11.1 | 0.3 | 0.5 | 0.1 | 0.1 |

studied are strongly thermally modified. These new results thus confirm previous data obtained by TEM-EDS (Leroux et al., 2008). The observed core-rim texture is not yet seen in metal and sulfide components of chondritic meteorite or IDPs (Zolensky and Thomas, 1995; Rietmeijer, 1998; Dai and Bradley, 2001). Several schemes have been proposed to explain the formation mechanism of the Fe–Ni–S nanophases, all implying formation during the high temperature stage of the capture. These include reduction of initial iron-sulfide (Ishii et al., 2008), compositions inherited from deep metastable eutectic compounds (Rietmeijer et al., 2008; Rietmeijer, 2008) or from more conventional fractional crystallization (Leroux et al., 2008) in the Fe–S system at high cooling rate.

The positive correlation between Mg and Fe concentrations and the presence of S in the glassy matrix lead us to propose an alternative model to explain the core-mantle texture of the Fe–Ni–S nanophases in the Stardust samples. Large S contents in silicate glasses are very unusual in terrestrial and extraterrestrial materials. We suggest that sulfur was redistributed by a process which implies the melting of the Wild 2 particle, sulfur volatilization followed by dissolution in silicate melts, and finally S condensation on metal cores, the latter formed originated partly from reduction of ferromagnesian silicates. Based on available data on the sulfur behavior under very reducing conditions, we propose the following mechanism for the formation and the core-shell texture of metal/sulfide nanophases (Fig. 8).

(1) During the impact, melting of pristine sulfide occurred. Indeed, the melting point is ~1200 °C for pyrrhotite (at one bar), while the melting point of any silicate present in Stardust samples is between 1300 and 1900 °C. If we consider that just after the initial shock wave, the total pressure in the track was much lower than one bar, we can easily expect a significant volatilization of sulfur following the equation:

$$2\mathrm{FeS}\,(\mathrm{liq}) = 2\mathrm{Fe}\,(\mathrm{liq}) + \mathrm{S}_2\,(\mathrm{g}) \tag{2}$$

(2) Due to the fast diffusion of gas species through metal and silicate melts, an extensive redistribution of sulfur occurred during the millisecond period of heating (Roskosz et al., 2008). This redistribution is attested by the S/Fe ratio, which is found fairly constant whatever the analyzed area. The high sulfur content of silica-rich glassy matrix between the Fe–Ni–S nano-droplets is up to one order of magnitude larger than concentrations found in natural environments, with the notable exception of Aubrite basalt vitrophyres (Fogel, 2005). Such a high solubility is generally interpreted as the consequence of formation of MgS complexes under very reducing conditions (Fogel, 2005; Moretti and Ottonello, 2005) according to the following the reaction:

$$1/2\,\mathrm{S}_{2(\mathrm{gas})} + \mathrm{O}^{2-}_{(\mathrm{silicate\ melt})} = 1/2\,\mathrm{O}_{2(\mathrm{gas})} + \mathrm{S}^{2-}_{(\mathrm{silicate\ melt})} \tag{3}$$

$$\text{Or } 1/2\,\mathrm{S}_{2(\mathrm{gas})} + \mathrm{MgO}_{(\mathrm{silicate\ melt})} = 1/2\,\mathrm{O}_{2(\mathrm{gas})} + \mathrm{MgS}_{(\mathrm{silicate\ melt})} \tag{4}$$

(3) The latter steps are associated with a reducing and high temperature environment. Inversely, the last step can be envisaged as an oxidation processes which corresponds to corrosion of metal droplets (which originated from iron-sulfide breakdown and from reduction of Fe–Mg-silicates) by gaseous sulfur and thus to the transfer of electrons from metal to sulfur to form sulfides. This corrosion occurs upon the cooling and the quench of samples and explains the core/shell structure (metal core and iron-sulfide rim) of Fe–Ni–S nanophases with a S/Fe ratio close to the bulk S/Fe ratio.

## 5. CONCLUSIONS

A number of Wild 2 grains were strongly modified by the collection process. Generally, the structure of the Wild 2 mineral components of such samples were fully destroyed by the flash heating upon impact with the collector but some micro-chemical signatures are still decipherable, even when strongly modified by high temperature capture effects and mixing with melted aerogel. The dominant microstructure of these thermally altered particles consists of Fe–Ni–S nano-droplets within a silica-rich glassy matrix. Because of the strong silica admixture coming from molten aerogel, the use of traditional petrology is precluded. In this paper we introduced a new petrological groundwork, based on Fe–Mg–S ternary representations, which are demonstrated to be well suited for the Wild 2 particles when mixed with aerogel. All major components (Fe–Ni metal, iron-sulfide and Mg–Fe silicates) expected from the Wild 2 comet can be plotted on the diagram. Although some intrinsic limitation may be invoked (for instance olivine and pyroxene cannot be distinguished and pure fayalite or iron oxides are superimposed with iron-metal), these ternary Fe–Mg–S diagrams will probably be useful for comparing Wild 2 materials

Author's personal copy



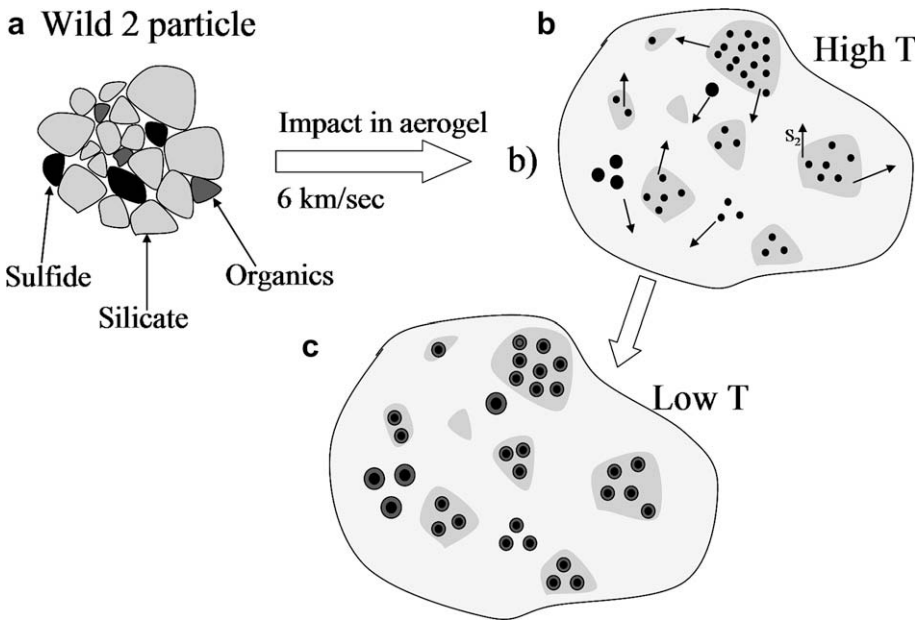


Fig. 8. Cartoon illustrating the formation of iron-sulfide nanophases in the thermally modified Stardust particles. (a) Incoming Wild 2 particle impacting the aerogel at 6 km $s^{-1}$. The particle is assumed to be an aggregate of silicates (light grey), organics (dark grey) and iron-sulfide (dark). The silicate components could include GEMS. The individual components are likely cemented by a fine-grained matrix (not represented here) made of nanometer scale minerals (silicates, sulfides, and probably organics). (b) During impact heating of the aerogel, the particle breaks down and the individual components are dispersed into melted aerogel. Silicates and sulfides are melted and mixed partially with molten silica. Sulfides undergo thermal decomposition and deliver gaseous $S_2$ (symbolized by arrows). Reduction of FeO initially present in silicates occurred due to the combustion of organics, and lead to the formation of metal droplets (black dots) in the silicate melt. (c) Upon cooling, the gaseous $S_2$ condensed onto the metal droplets leading to the observed core/shell structure of the Fe–Ni–S nanophases. The silicate melt is quenched as a glass because of its high silica content.

with other fine-grained assemblage such as those present in primitive meteorites or IDPs.

The Fe–Mg–S diagrams are also a good tool to study the oxidation state of iron in Wild 2 particles. We found that the glassy matrix of the two strongly thermally altered particles studied here are strongly depleted in FeO and enriched in dissolved S. However, these features, associated with the presence of evenly distributed metal-sulfide droplets, are secondary in origin. They formed in situ by high temperature reduction of ferromagnesian silicates in the molten state, volatilization and further condensation of sulfur during cooling. Alternatively a part of the Fe–Ni–S droplets may originate from indigenous sulfides which decomposed (Ishii et al., 2008) and/or from a reduced ultra-fine-grained matrix frequently found in IDPs. Along the same lines we cannot rule out the presence of GEMS in the Wild 2 particles.

Our study shows that the high temperature stage during deceleration tends to lower the oxidation state of iron for thermally modified particles. In the light of these results it appears difficult to derive a single and self-consistent redox value from the bulk analysis of a track, as shown by the high variability of oxidation state of iron in whole tracks (Westphal et al., 2008). Each fragment of particle found in the walls of tracks has suffered redox changes at very variable levels depending on their initial mineralogy and of the peak temperature they suffered during collection. Terminal particles appear relatively preserved and may exhibit their pristine redox state. In these conditions data collected along a track cannot be considered as representative of an average "bulk" redox state of cometary grains. Instead, the capture effect must be taken into account for comparison of Stardust particles with other chondritic material. Yet further work is required to know if some correction could be proposed to overcome this difficulty. In this respect the use of S solubility data in silicate melts could be of critical help to determine quantitatively the redox conditions prevailing during the collection.

## ACKNOWLEDGEMENTS

K. Nakamura-Messenger is gratefully acknowledged for the preparation of high quality ultramicrotomed TEM samples. We appreciated fruitful discussions with F.J.M. Rietmeijer. D. Neuville is also acknowledged for interesting discussions on the behavior of sulfur in silicate liquids. The paper has benefited from extremely helpful and constructive reviews by M. Lee, M.A. Velbel and an anonymous reviewer, as well as from the careful editorial work by the associate editor S. Russell. We thank support by Centre National d'Etudes Spatiales (CNES) and the electron microscope facility by European FEDER and region Nord-Pas-de-Calais. We also thank J.F. Dhenin for his careful maintenance of the TEMs.

## REFERENCES

Anders E. and Ebihara M. (1982) Solar-system abundances of the elements. *Geochim. Cosmochim. Acta* **46**, 2363–2380.

Author's personal copy



Anderson W. W. and Arhens T. J. (1994) Physics of spacecraft-based interplanetary dust collection by impact into low-density media. LPI Technical Report 94-05, 16–21.

Bradley J. P. (1994) Chemically anomalous, preaccretionally irradiated grains in interplanetary dust from comets. *Science* **265**, 925–929.

Brownlee D., Tsou P., Aléon J., Alexander C. M. O'D., Araki T., Bajt S., Baratta G. A., Bastien R., Bland P., Bleuet P., Borg J., Bradley J. P., Brearley A., Brenker F., Brennan S., Bridges J. C., Browning N. D., Brucato J. R., Bullock E., Burchell M. J., Busemann H., Butterworth A., Chaussidon M., Cheuvront A., Chi M., Cintala M. J., Clark B. C., Clemett S. J., Cody G., Colangeli L., Cooper G., Cordier P., Daghlian C., Dai Z., d'Hendecourt L., Djouadi Z., Dominguez G., Duxbury T., Dworkin J. P., Ebel D. S., Economou T. E., Fakra S., Fairey S. A. J., Fallon S., Ferrini G., Ferroir T., Fleckenstein H., Floss C., Flynn G., Franchi I. A., Fries M., Gainsforth Z., Gallien J.-P., Genge M., Gilles M. K., Gillet P. h., Gilmour J., Glavin D. P., Gounelle M., Grady M. M., Graham G. A., Grant P. G., Green S. F., Grossemy F., Grossman L., Grossman J. N., Guan Y., Hagiya K., Harvey R., Heck P., Herzog G. F., Hoppe P., Hörz F., Huth J., Hutcheon I. D., Ignatyev K., Ishii H., Ito M., Jacob D., Jacobsen C., Jacobsen S., Jones S., Joswiak D., Jurewicz A., Kearsley A. T., Keller L. P., Khodja H., Kilcoyne A. L. D., Kissel J., Krot A., Langenhorst F., Lanzirotti A., Le L., Leshin L. A., Leitner J., Lemelle L., Leroux H., Liu M.-C., Luening K., Lyon I., MacPherson G., Marcus M. A., Marhas K., Marty B., Matrajt G., McKeegan K., Meibom A., Mennella V., Messenger K., Messenger S., Mikouchi T., Mostefaoui S., Nakamura T., Nakano T., Newville M., Nittler L. R., Ohnishi I., Ohsumi K., Okudaira K., Papanastassiou D. A., Palma R., Palumbo M. E., Pepin R. O., Perkins D., Perronnet M., Pianetta P., Rao W., Rietmeijer F. J. M., Robert F., Rost D., Rotundi A., Ryan R., Sandford S. A., Schwandt C. S., See T. H., Schlutter D., Sheffield-Parker J., Simionovici A., Simon S., Sitnitsky I., Snead C. J., Spencer M. K., Stadermann F. J., Steele A., Stephan T., Stroud R., Susini J., Sutton S. R., Suzuki Y., Taheri M., Taylor S., Teslich N., Tomeoka K., Tomioka N., Toppani A., Trigo-Rodríguez J. M., Troadec D., Tsuchiyama A., Tuzzolino A. J., Tyliszczak T., Uesugi K., Velbel M., Vellenga J., Vicenzi E., Vincze L., Warren J., Weber I., Weisberg M., Westphal A. J., Wirick S., Wooden D., Wopenka B., Wozniakiewicz P., Wright I., Yabuta H., Yano H., Young E. D., Zare R. N., Zega T., Ziegler K., Zimmermann L., Zinner E. and Zolensky M. (2006) Comet 81P/Wild 2 under a microscope. *Science* **314**, 1711–1716.

Dai Z. R. and Bradley J. P. (2001) Iron-nickel sulfides in anhydrous interplanetary dust particles. *Geochim. Cosmochim. Acta* **65**, 3601–3612.

Davoisne C., Djouadi Z., Leroux H., d'Hendecourt L., Jones A. and Deboffle D. (2006) The origin of GEMS in IDPs as deduced from microstructural evolution of amorphous silicates with annealing. *Astron. Astrophys.* **448**, L1–L4.

Flynn G. J., Bleuet P., Borg J., Bradley J. P., Brenker F. E., Brennan S., Bridges J., Brownlee D. E., Bullock E. S., Burghammer M., Clark B. C., Dai Z. R., Daghlian C. P., Djouadi Z., Fakra S., Ferroir T., Floss C., Franchi I. A., Gainsforth Z., Gallien J.-P., Gillet Ph., Grant P. G., Graham G. A., Green S. F., Grossemy F., Heck P. R., Herzog G. F., Hoppe P., Hörz F., Huth J., Ignatyev K., Ishii H. A., Janssens K., Joswiak D., Kearsley A. T., Khodja H., Lanzirotti A., Leitner J., Lemelle L., Leroux H., Luening K., MacPherson G. J., Marhas K. K., Marcus M. A., Matrajt G., Nakamura T., Nakamura-Messenger K., Nakano T., Newville M., Papanastassiou D. A., Pianetta P., Rao W., Riekel C., Rietmeijer F. J. M., Rost D., Schwandt C. S., See T. H., Sheffield-Parker J., Simionovici T., Sitnitsky I., Snead C. J., Stadermann F. J., Stephan T., Stroud R. M., Susini J., Suzuki Y., Sutton S. R., Taylor S., Teslich N., Troadec D., Tsou P., Tsuchiyama A., Uesugi K., Vekemans B., Vicenzi E. P., Vincze L., Westphal A. J., Wozniakiewicz P., Zinner E. and Zolensky M. E. (2006) Elemental compositions of comet 81P/Wild 2 samples collected by Stardust. *Science* **314**, 1731–1735.

Fogel R. A. (2005) Aubrite basalt vitrophyres: the missing basaltic component and high-sulfur silicate melts. *Geochim. Cosmochim. Acta* **69**, 1633–1648.

Hörz F., Bastien R., Borg J., Bradley J. P., Bridges J. C., Brownlee D. E., Burchell M. J., Chi M., Cintala M. J., Dai Z. R., Djouadi Z., Dominguez G., Economou T. E., Fairey S. A. J., Floss C., Franchi I. A., Graham G. A., Green S. F., Heck P., Hoppe P., Huth J., Ishii H., Kearsley A. T., Kissel J., Leitner J., Leroux H., Marhas K., Messenger K., Schwandt C. S., See T. H., Snead C., Stadermann F. J., Stephan T., Stroud R., Teslich N., Trigo-Rodríguez J. M., Tuzzolino A. J., Troadec D., Tsou P., Warren J., Westphal A., Wozniakiewicz P., Wright I. and Zinner E. (2006) Impact features on Stardust: implications for Comet 81P/Wild 2 dust. *Science* **314**, 1716–1719.

Ishii H. A., Bradley J. P., Dai Z. R., Chi M., Kearsley A. T., Burchell M. J., Browning N. D. and Molster F. (2008) Comparison of comet 81P/Wild 2 dust with interplanetary dust from comets. *Science* **319**, 447–450.

Leroux H., Libourel G., Lemelle L. and Guyot F. (2003) Experimental study and TEM characterization of dusty olivines in chondrites: evidence for formation by in situ reduction. *Meteorit. Planet. Sci.* **38**, 81–94.

Leroux H., Rietmeijer F. J. M., Velbel M. A., Brearley A. J., Jacob D., Langenhorst F., Bridges J. C., Zega T. J., Stroud R. M., Cordier P., Harvey R. P., Lee M., Gounelle M. and Zolensky M. E. (2008) A TEM study of thermally modified Comet 81P/Wild 2 dust particles by interactions with the aerogel matrix during the Stardust capture process. *Meteorit. Planet. Sci.* **43**, 97–120.

Moretti R. and Ottonello G. (2005) Solubility and speciation of sulfur in silicate melts: the Conjugated Toop-Samis-Flood-Grjotheim (CTSFG) model. *Geochim. Cosmochim. Acta* **69**, 801–823.

Ogliore R. C., Butterworth A. L., Fakra S., Frank D. R., Gainsforth Z., Marcus M. A., Westphal A. J. (2008) Chemical analysis of a large Stardust track associated with a presolar grain. *Lunar Planet. Sci. XXXIX*. Lunar Planet. Inst., Houston. #2363 (abstr.).

Rietmeijer F. J. M. (1998) Interplanetary dust particles. In *Planetary Materials, Reviews in Mineralogy*, vol. 36 (ed. J. J. Papike). The Mineralogical Society of America, Washington, DC, pp. 2-1–2-95.

Rietmeijer F. J. M. (2008) Time, temperatures and pressure indicated by metastable iron-sulfide nano-phases in melted Stardust aerogel. *Lunar Planet. Sci. XXXIX*. Lunar Planet. Inst., Houston. #1188 (abstr.).

Rietmeijer F. J. M., Nakamura T., Tsuchiyama A., Uesugi K., Nakano T. and Leroux H. (2008) Origin and formation of iron-silicide phases in the aerogel of the Stardust mission. *Meteorit. Planet. Sci.* **43**, 121–134.

Roskosz M., Leroux H. and Watson H. C. (2008) Thermal history, partial preservation and sampling bias recorded by Stardust cometary grains during their capture. *Earth Planet. Sci. Lett.* **273**, 195–202.

Spencer M. K. and Zare R. N. (2007) Comment on "Organics Captured from Comet 81P/Wild 2 by the Stardust Spacecraft" by Sandford et al. (2006 – Science 314, p. 1720). Science 317, p. 1680.

Urey H. C. and Craig H. (1953) The composition of the stone meteorites and the origin of the meteorites. *Geochim. Cosmochim. Acta* **4**, 36–82.

Author's personal copy



Van Cappellen E. (1990) The parameterless correction method in X-ray microanalysis. *Microsc. Microanal. Microstruct.* **1**, 1–22.

Van Cappellen E. and Doukhan J. C. (1994) Quantitative transmission X-ray microanalysis of ionic compounds. *Ultramicroscopy* **53**, 343–349.

Wasson J. T. and Kallemeyn G. W. (1988) Composition of chondrites. *Phil. Trans. Roy. Soc.* **A325**, 535–544.

Westphal A. J., Brownlee D. E., Butterworth A. L., Fakra S., Gainsforth Z., Joswiak D., Marcus M. A., Snead C. J. and Ogliore R. C. (2008) Oxidation state of iron in the Jupiter family comet Wild 2. *Lunar Planet. Sci. XXXIX*. Lunar Planet. Inst., Houston. #2133 (abstr.).

Zolensky M. E. and Thomas K. L. (1995) Iron and iron-nickel sulfides in chondritic interplanetary dust particles. *Geochim. Cosmochim. Acta* **59**, 4707–4712.

Zolensky M. E., Zega T. J., Yano H., Wirick S., Westphal A. J., Weisberg M. K., Weber I., Warren J. L., Velbel M. A., Tsuchiyama A., Tsou P., Toppani A., Tomioka N., Tomeoka K., Teslich N., Taheri M., Susini J., Stroud R., Stephan T., Stadermann F. J., Snead C. J., Simon S. B., Simionovici A., See T. H., Robert F., Rietmeijer F. J. M., Rao W., Perronnet M. C., Papanastassiou D. A., Okudaira K., Ohsumi K., Ohnishi I., Nakamura-Messenger T., Nakamura T., Mostefaoui S., Mikouchi T., Meibom A., Matrajt G., Marcus M. A., Leroux H., Lemelle L., Le L., Lanzirotti A., Langenhorst F., Krot A. N., Keller L. P., Kearsley A. T., Joswiak D., Jacob D., Ishii H., Harvey R., Hagiya K., Grossman L., Grossman J. N., Graham G. A., Gounelle M., Gillet Ph., Genge M. J., Flynn G., Ferroir T., Fallon S., Ebel D. S., Dai Z. R., Cordier P., Clark B., Chi M., Butterworth A. L., Brownlee D. E., Bridges J. C., Brennan S., Brearley A., Bradley J. P., Bleuet P., Bland P. A. and Bastien R. (2006) Mineralogy and petrology of comet 81P/Wild 2 nucleus samples. *Science* **314**, 1735–1739.

Zolensky M., Nakamura-Messenger K., Rietmeijer F., Leroux H., Mikouchi T., Ohsumi K., Simon S., Grossman L., Stephan T., Weisberg M., Velbel M., Zega T., Stroud R., Tomeoka K., Ohnishi I., Tomioka N., Nakamura T., Matrajt G., Joswiak D., Brownlee D., Langenhorst F., Krot A., Kearsley A., Ishii H., Graham G., Dai Z. R., Chi M., Bradley J., Hagiya K., Gounelle M. and Bridges J. (2008) Comparing Wild 2 particles to chondrites and IDPs. *Meteorit. Planet. Sci.* **43**, 261–272.

*Associate editor:* Sara S. Russell

**References and Notes**

1. P. Tsou *et al.*, *J. Geophys. Res.* **109**, E12S01 (2004).
2. A. J. Westphal *et al.*, *Meteorit. Planet. Sci.* **39**, 1375 (2004).
3. G. J. Flynn, F. Hörz, S. Bajt, S. R. Sutton, *Lunar. Planet. Sci.* **XXVII**, 369 (1996).
4. See the supporting material on *Science* Online.
5. K. Lodders, *Astrophys. J.* **591**, 1220 (2003).
6. E. Anders, N. Grevese, *Geochim. Cosmochim. Acta* **53**, 197 (1989).
7. M. E. Zolensky *et al.*, *Science* **314**, 1735 (2006).
8. S. A. Sandford *et al.*, *Science* **314**, 1720 (2006).
9. A. T. Kearsley *et al.*, *Meteorit. Planet. Sci.*, in press.
10. A. T. Kearsley, M. J. Burchell, F. Hörz, M. J. Cole, C. S. Schwandt, *Meteorit. Planet. Sci.* **41**, 167 (2006).
11. F. Hörz *et al.*, *Science* **314**, 1716 (2006).
12. D. E. Brownlee, in *Properties and Interactions of Interplanetary Dust*, Proceedings of the Eighty-fifth Colloquium, Marseille, France, 9–12 July 1984 (Reidel, Dordrecht, Netherlands, 1985), pp. 143–147.
13. G. J. Flynn, S. R. Sutton, in *Proceedings of the 20th Lunar and Planetary Science Conference* (Lunar and Planetary Institute, Houston, TX, 1990), pp. 335–342.
14. J. Kissel, in *Advances in Mass Spectroscopy 1985, Proceedings of the 10th International Mass Spectrometry Conference*, Swansea, UK, 9–13 September 1985 (Wiley and Sons, Hoboken, NJ, 1986), pp. 175–184.
15. E. K. Jessberger, *Space Sci. Rev.* **90**, 91 (1999).
16. L. S. Schramm, D. E. Brownlee, M. M. Wheelock, *Meteoritics* **24**, 99 (1989).
17. G. J. Flynn *et al.*, in *Physics, Chemistry, and Dynamics of Interplanetary Dust*, B. Å. S. Gustafson, M. S. Hanner, Eds. (Astronomical Society of the Pacific, San Francisco, 1996), pp. 291–294.
18. D. E. Brownlee *et al.*, *Lunar. Planet. Sci.* **XXIV**, 205 (1993).


19. Four synchrotrons used in this effort are national user facilities supported in part by the U.S. Department of Energy, Office of Science, Office of Basic Energy Sciences, under contract numbers (with managing institutions in parentheses) DE-AC02-05CH11231 (Advanced Light Source, University of California), DE-AC02-06CH11357 (Advanced Photon Source, University of Chicago Argonne, LLC), DE-AC02-98CH10886 (National Synchrotron Light Source, Brookhaven Science Associates), and DE-AC03-765F00515 (Stanford Synchrotron Radiation Laboratory, Stanford University). Experiments were performed at the BL47XU in the SPring-8 with the approval of the Japan Synchrotron Radiation Research Institute. The European Synchrotron Radiation Facility provided synchrotron radiation facilities. Stardust was the fourth flight project of NASA's Discovery Program.


**Supporting Online Material**
www.sciencemag.org/cgi/content/full/314/5806/1731/DC1
SOM Text
Figs. S1 to S11
Tables S1 to S4
References


10 October 2006; accepted 20 November 2006
10.1126/science.1136141


REPORT

# Mineralogy and Petrology of Comet 81P/Wild 2 Nucleus Samples


**Michael E. Zolensky,[1]* Thomas J. Zega,[2] Hajime Yano,[3] Sue Wirick,[4] Andrew J. Westphal,[5] Mike K. Weisberg,[6] Iris Weber,[7] Jack L. Warren,[8] Michael A. Velbel,[9] Akira Tsuchiyama,[10] Peter Tsou,[11] Alice Toppani,[12,13] Naotaka Tomioka,[14] Kazushige Tomeoka,[14] Nick Teslich,[12] Mitra Taheri,[2] Jean Susini,[15] Rhonda Stroud,[2] Thomas Stephan,[7] Frank J. Stadermann,[16] Christopher J. Snead,[5] Steven B. Simon,[17] Alexandre Simionovici,[18] Thomas H. See,[19] François Robert,[20] Frans J. M. Rietmeijer,[21] William Rao,[22] Murielle C. Perronnet,[1] Dimitri A. Papanastassiou,[23] Kyoko Okudaira,[3] Kazumasa Ohsumi,[24] Ichiro Ohnishi,[14] Keiko Nakamura-Messenger,[8] Tomoki Nakamura,[25] Smail Mostefaoui,[20] Takashi Mikouchi,[26] Anders Meibom,[20] Graciela Matrajt,[27] Matthew A. Marcus,[28] Hugues Leroux,[29] Laurence Lemelle,[18] Loan Le,[8] Antonio Lanzirotti,[30] Falko Langenhorst,[31] Alexander N. Krot,[32] Lindsay P. Keller,[1] Anton T. Kearsley,[33] David Joswiak,[27] Damien Jacob,[29] Hope Ishii,[12] Ralph Harvey,[34] Kenji Hagiya,[35] Lawrence Grossman,[17,36] Jeffrey N. Grossman,[37] Giles A. Graham,[12] Matthieu Gounelle,[20,33] Philippe Gillet,[18] Matthew J. Genge,[38] George Flynn,[39] Tristan Ferroir,[18] Stewart Fallon,[12] Denton S. Ebel,[40] Zu Rong Dai,[12] Patrick Cordier,[29] Benton Clark,[41] Miaofang Chi,[12] Anna L. Butterworth,[5] Donald E. Brownlee,[27] John C. Bridges,[42] Sean Brennan,[43] Adrian Brearley,[21] John P. Bradley,[12] Pierre Bleuet,[15] Phil A. Bland,[33,38] Ron Bastien[8]**



The bulk of the comet 81P/Wild 2 (hereafter Wild 2) samples returned to Earth by the Stardust spacecraft appear to be weakly constructed mixtures of nanometer-scale grains, with occasional much larger (over 1 micrometer) ferromagnesian silicates, Fe-Ni sulfides, Fe-Ni metal, and accessory phases. The very wide range of olivine and low-Ca pyroxene compositions in comet Wild 2 requires a wide range of formation conditions, probably reflecting very different formation locations in the protoplanetary disk. The restricted compositional ranges of Fe-Ni sulfides, the wide range for silicates, and the absence of hydrous phases indicate that comet Wild 2 experienced little or no aqueous alteration. Less abundant Wild 2 materials include a refractory particle, whose presence appears to require radial transport in the early protoplanetary disk.


The nature of cometary solids is of fundamental importance to our understanding of the early solar nebula and protoplanetary history. Until now, we have had to study comets from afar using spectroscopy or settle for analyses of interplanetary dust particles (IDPs) of uncertain provenance. We report here mineralogical and petrographic analyses of particles derived directly from comet 81P/Wild 2.

All of the Wild 2 particles we have thus far examined have been modified in various ways by the capture process, in which cometary particles punched into the silica aerogel capture media, making various types of tracks and disaggregating into grains distributed along the tracks. All particles that may have been loose aggregates ("traveling sand piles") disaggregated into individual components, with the larger, denser components penetrating more deeply into the aerogel, making thin tracks with terminal grains (fig. S1). Individual grains experienced heating effects that produced results ranging from excellent grain preservation to melting (Fig. 1); such behavior was expected (*1–3*). What is remarkable is the extreme variability of these modifications and the fact that unmodified and severely modified materials can be found within 1 μm of each other, requiring tremendous local temperature gradients. Fortunately, we have an internal gauge of impact collection heating. Fe-Ni sulfides are ubiquitous in the Wild 2 samples and are very sensitive indicators of heating, and accurate chemical analyses can reveal which have lost S and which have not (and are therefore stoichiometric) (Fig. 2). Our surveys show that crystalline grains are found along the entire lengths of tracks, not just at track termini (fig. S1).

There appears to be very limited contamination from the spacecraft in the aerogel. Potential problems with secondary impacts (cometary grains striking the spacecraft, ricocheting, and splashing onto the aerogel) failed to materialize (*4*).

We have harvested samples from 52 tracks and have obtained a substantial understanding of the mineralogy of 26 of these. These tracks were chosen at random from those of average length. Analyses have also been performed on impact residues in seven aluminum foil craters >50 μm in diameter and on over 200 craters <5 μm in diameter (*5*). Crystalline materials are abundant in comet Wild 2 and many are coarse-grained relative to the submicrometer scales characteristic of many anhydrous IDPs and interstellar dust populations (*6*). Of the best-studied 26 tracks, 8 are dominated by olivine [$(Mg,Fe)_2SiO_4$] grains (tracks 1, 22, 26, 43, 57, 68, 71, and 77); 7 by low-Ca pyroxene [$(Mg,Fe)SiO_3$] (tracks 17, 20, 24, 27, 32, 41, and 69); 3 by a fairly equal amount of olivine and pyroxene (tracks 5, 10, and 35); and the remaining 8 by other minerals, mainly Fe-Ni sulfides. One of the latter tracks contains predominantly refractory minerals, one contains Na-silicate minerals, and five (tracks 36, 38, 42, 52, and 59) are dominated by ~5-μm-sized sulfide grains. These results suggest that crystalline materials are abundant in Wild 2.

In the seven large craters in aluminum foil that we examined, one contains only remnants of stoichiometric olivine, three are dominated by Mg-

silicates and sulfide, and two contain a mixture of mafic silicates and Na- and Ca-rich silicates. The last complex impact feature has overlapped bowl-shaped depressions containing residues with a heterogeneous collection of stoichiometric compositions, suggesting impact by an aggregate of micrometer-scale grains of Ca-rich clinopyroxene, Mg-rich pyroxene (probably enstatite), and a mixture of Fe-Ni sulfides, as well as grains composed of finely mixed silicate and sulfide. Just over half of the residue-bearing very small craters we examined contain mixtures of silicate and sulfur-bearing residue, whereas the others are mainly monomineralic olivine, pyroxene, and Fe-Ni sulfides, with occasional preservation of crystalline material.

Olivine, one of the most abundant minerals in the solar system (*7–9*), is present in the majority of Wild 2 particles. Its observed grain sizes range from submicrometer to over 10 μm. Wild 2 olivine has an extremely wide compositional range, from $Fo_4$ to $Fo_{100}$ ["Fo" being the 100 × molar Mg/(Mg+Fe) ratio for olivine, just as "En" is the same ratio for low-Ca pyroxenes] (Fig. 3), with a pronounced frequency peak at $Fo_{99}$. Although it is possible that collection effects have biased surviving olivines to the most refractory, Mg-rich compositions, the abundance of Fe-rich olivine among the Wild 2 samples suggests that this effect has been minor. One olivine crystal in track 22 was found to display dramatic reverse chemical zoning, from the $Fo_{70}$ core to the $Fo_{92}$ rim. It is clear that these grains were not equilibrated during capture, because we would then observe a greatly reduced compositional range and a peak at a high Fe (low Fo value) concentration (*1*, *2*, *10*, *11*).

Wild 2 olivines include varieties with very elevated MnO, $Al_2O_3$, and $Cr_2O_3$ contents, up to 6.45, 0.71, and 1.46 weight %, respectively. About 25% of these Mn- and Cr-rich olivines contain <<1% FeO. Olivines with enrichments in these elements have been reported in carbonaceous chondrites, micrometeorites, and chondritic IDPs, though they are very rare (*12–16*). The compositions of the Mn- and Cr-rich olivines in the Wild 2 samples are similar to those in IDPs, carbonaceous chondrites, and unequilibrated ordinary chondrites (fig. S2). Many Wild 2 olivines contain inclusions of other phases, notably Fe-Cr-Ti oxides (including chromite), but thus far, melt inclusions have not been observed within any silicates. Olivine with low Fe and elevated Mn has been proposed to form from condensation in the protosolar nebula (*12*).

Wild 2 olivine-dominated grains are commonly polycrystalline, with some interstitial glass, which could be indigenous cometary glass. One fragment from the wall of the 1-cm-long track 35 was investigated by microtomography (*17*) and found to have a microporphyritic texture with olivine crystals (~$Fo_{80}$) set within lower-density fine-grained material, probably glass. From the manner in which the enclosing aerogel wraps around this particular grain without intruding into it, the glass appears to be indigenous. This fragment has an obvious igneous origin and resembles a microporphyritic chondrule. A terminal grain from track 26 consists of an intergrowth of fayalite ($Fo_4$) and tridymite, another texture observed in some chondrules.

Both low- and high-Ca pyroxenes are present among the Wild 2 grains, with the former being dominant. In some cases, synchrotron x-ray diffraction (SXRD) or selected-area electron diffraction

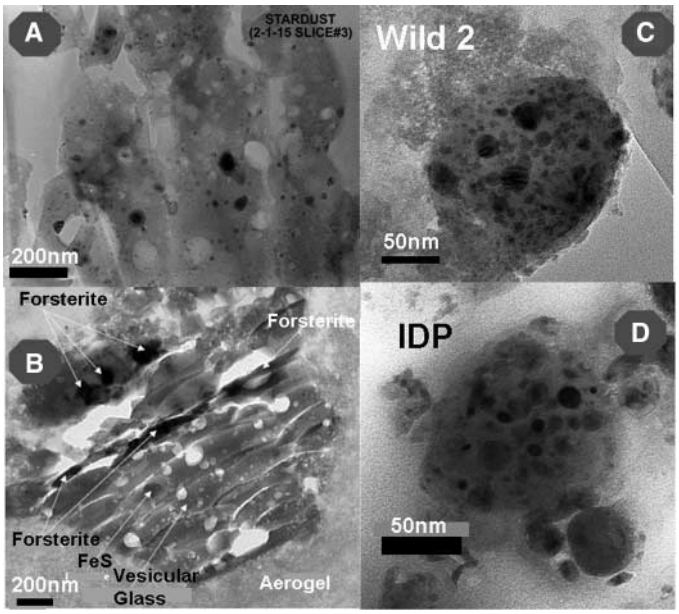


**Fig. 1.** Bright-field TEM images of Wild 2 grains. (**A**) View of the compressed and vesicular melted aerogel surrounding grains and lining track walls. Dark gray and black objects are admixed silicates, Fe-Ni metal, and Fe-Ni sulfides. (**B**) Captured Wild 2 grain composed predominantly of forsterite and Fe-sulfides, mantled by compressed-to-melted aerogel. (**C**) Glassy body from Wild 2 track 10, resembling a GEM; rounded dark inclusions are predominantly Fe-Ni metal, Fe-Ni sulfides, and ferromagnesian silicates. (**D**) GEM from an anhydrous chondritic IDP; rounded dark inclusions are predominantly Fe-Ni metal, Fe-Ni sulfides, and ferromagnesian silicates.

[1]Astromaterials Research and Exploration Science, NASA Johnson Space Center, Houston, TX 77058, USA. [2]Naval Research Laboratory, Code 6360, 4555 Overlook Avenue SW, Washington, DC 20375, USA. [3]JAXA-ISAS, 3-1-1 Yoshinodai, Sagamihara, Kanagawa 229-8510, Japan. [4]National Synchrotron Light Source, Brookhaven National Laboratory, Upton, NY 11973, USA. [5]Space Sciences Laboratory, University of California, 7 Gauss Way, Berkeley, CA 94720–7450, USA. [6]Department of Physical Sciences, Kingsborough Community College (CUNY), Brooklyn, NY 11235, USA. [7]Institut für Planetologie, Westfälische Wilhelms-Universität Münster, Wilhelm-Klemm-Strasse 10, 48149 Münster, Germany. [8]Jacobs Sverdrup, Engineering Science Contract Group, Houston, TX 77058, USA. [9]Department of Geological Sciences, 206 Natural Science Building, Michigan State University, East Lansing, MI 48824–1115, USA. [10]Department of Earth and Space Science, Osaka University, 1-1 Machikaneyama-cho, Toyonaka 560-0043, Japan. [11]Jet Propulsion Laboratory, M/S 183-501, 4800 Oak Grove Drive, Pasadena, CA 91109, USA. [12]Institute for Geophysics and Planetary Physics, Lawrence Livermore National Laboratory, Livermore, CA 94550, USA. [13]Centre de Spectrometrie Nucleaire et de Spectrometrie de Masse, Bâtiment 104, 91405 Orsay Campus, France. [14]Department of Earth and Planetary Sciences, Faculty of Science, Kobe University, Nada, Kobe 657-8501, Japan. [15]European Synchrotron Radiation Facility, Boîte Postale 220, 38043 Grenoble, France. [16]Department of Physics, Washington University, St. Louis, MO 63130, USA. [17]Department of Geophysical Sciences, The University of Chicago, 5734 South Ellis Avenue, Chicago, IL 60637, USA. [18]Laboratoire de Sciences de la Terre, Ecole Normale Superieure de Lyon, 46, Allee d'Italie, 69007 Lyon, France. [19]Engineering Science Contract/Barrios Technology, ARES/JSC, Houston, TX 77258–8447, USA. [20]Museum National d'Histoire Naturelle, Laboratoire d'Etude de la Matiere Extraterrestre, USM 0205 (LEME), Case Postale 52, 57 Rue Cuvier, 75005 Paris, France. [21]Department of Earth and Planetary Sciences, University of New Mexico, MSC 03-2040, Albuquerque, NM 87131–0001, USA. [22]Savannah River Ecology Lab, Aiken, SC 29801, USA. [23]Science Division, Jet Propulsion Laboratory, M/S 183-335, 4800 Oak Grove Drive, Pasadena, CA 91109, USA. [24]Institute of Materials Structure Science, Tsukuba-shi, Ibaraki-ken 305, Japan. [25]Department of Earth and Planetary Sciences, Faculty of Sciences, Kyushu University, Hakozaki, Fukuoka 812-8581, Japan. [26]Department of Earth and Planetary Science, University of Tokyo, Hongo, Bunkyo-ku, Tokyo 113-0033, Japan. [27]Department of Astronomy, University of Washington, Seattle, WA 98195, USA. [28]Advanced Light Source, Lawrence Berkeley National Laboratory, 1 Cyclotron Road, MS 2R2100, Berkeley, CA 94720, USA. [29]Laboratoire de Structure et Propriétés de l'Etat Solide, Bâtiment C6, Université des Sciences et Technologies de Lille, 59655 Villeneuve d'Ascq, France. [30]Consortium for Advanced Radiation Sources, The University of Chicago, Chicago, IL 60637, USA. [31]Institute of Geosciences, Friedrich-Schiller-University Jena, Burgweg 11, D-07749 Jena, Germany. [32]Hawaii Institute of Geophysics and Planetology, University of Hawaii, Honolulu, HI 96822, USA. [33]Impact and Astromaterials Research Centre, Department of Mineralogy, Natural History Museum, Cromwell Road, London, SW7 5BD, UK. [34]Department of Geology, Case Western Reserve University, Cleveland, OH 44106, USA. [35]Graduate School of Life Science, University of Hyogo, Koto 3-2-1, Kamigori, Ako-gun, Hyogo 678-1297, Japan. [36]Enrico Fermi Institute, The University of Chicago, 5640 South Ellis Avenue, Chicago, IL 60637, USA. [37]U.S. Geological Survey, 954 National Center, Reston, VA 20192, USA. [38]Impact and Astromaterials Research Centre, Department of Earth Sciences and Engineering, Imperial College of Science Technology and Medicine, Prince Consort Road, London, SW7 2AZ, UK. [39]Department of Physics, State University of New York, Plattsburgh, NY 12901, USA. [40]Department of Earth and Planetary Sciences, American Museum of Natural History, Central Park West at 79th Street, New York, NY 10024, USA. [41]Lockheed Martin Astronautics, Denver, CO 80201, USA. [42]Planetary and Space Sciences Research Institute, Open University, Milton Keynes, MK7 6AA, UK. [43]Stanford Linear Accelerator Center, Menlo Park, CA 94025, USA.

*To whom correspondence should be addressed. E-mail: michael.e.zolensky@nasa.gov

(SAED) patterns reveal low-Ca pyroxenes to be orthoenstatite, requiring slow cooling (*18*), but in the majority of cases we have only energy-dispersive x-ray analyses and are not certain whether we have ortho- or clinopyroxene. The compositional range displayed by the low-Ca pyroxene is also very extensive, from $En_{52}$ to $En_{100}$, with a significant frequency peak centered at $En_{95}$ (Fig. 3). Low-Ca pyroxene usually coexists with olivine, but the Mg/Fe ratios for coexisting phases are not always similar. Track 17 contains olivine in the range $Fo_{55–69}$, whereas associated low-Ca pyroxene is $En_{52–96}$. Flash heating during sample collection may account for this disparity, because olivine equilibrates faster than orthopyroxene under identical circumstances (*19*). Diopside occurs in several grains, usually in association with low-Ca pyroxene. A Ti-, Al-rich diopside is abundant within the calcium-, aluminum-rich inclusion (CAI)–like particle.

Sulfides are the only mineral group found in all extraterrestrial materials. Fe-Ni sulfides are also ubiquitous in the Wild 2 grains, grading from sulfides apparently melted and mixed with Fe-Ni metal, all the way to apparently unmodified FeS and pentlandite [$(Fe,Ni)_9S_8$] grains (fig. S3). Several tracks (such as track 59) have FeS- or pentlandite-dominated terminal grains. In this paper, we collectively refer to troilite (stoichiometric FeS) and pyrrhotite ($Fe_{1-x}S$) as FeS because the exact stoichiometry and structure are unknown in most instances. A plot of analyses of Wild 2 Fe-Ni sulfides (Fig. 2) shows that many have compositions close to that of FeS, with less than 2 atom % Ni. Only two pentlandite grains have been found. The complete lack of compositions in between these (intermediate solid solution compositions) suggests (but does not require) that FeS and pentlandite condensed as crystalline species [that is, did not condense as amorphous phases, which later became annealed (*20*)]. The remaining Fe-Ni sulfides (approximately half) have compositions that reflect progressive loss of S, because they trend from FeS directly toward the Fe apex. SAED patterns of these S-depleted phases show the presence of two different lattices: strong maxima for a Fe-Ni sulfide phase and a much finer pattern consistent with a metal phase, but which could be an oxide. Loss of S from Fe-Ni sulfides is almost certainly a result of capture heating and could be used to gauge the degree of capture modification of the enclosing Wild 2 grains. The two verified pentlandite crystals in only two Wild 2 tracks are intriguing because this phase is frequently an indicator of low-temperature metamorphism under oxidizing conditions and/or of aqueous alteration (*21*).

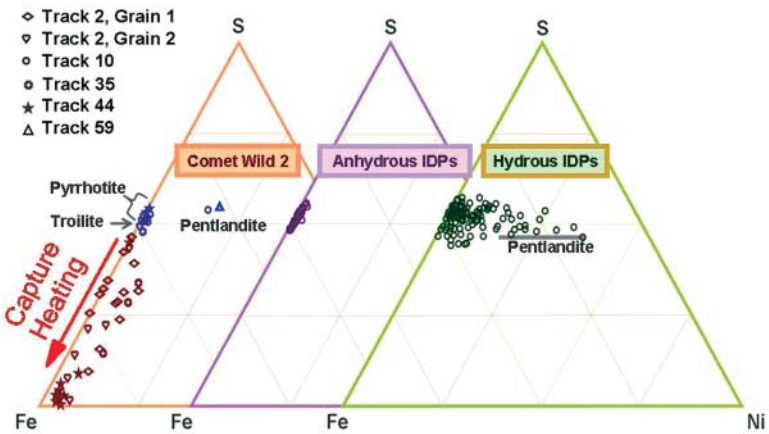


**Fig. 2.** Composition ranges of Fe-Ni sulfides from six grains from five Wild 2 particle tracks. Grains from track walls as well as track termini were analyzed. Most Wild 2 sulfides are probably a mixture of troilite and pyrrhotite, and two grains of pentlandite are present. Many sulfides plot with nonstoichiometric, low-S compositions reflecting capture heating. The corresponding composition ranges for hydrous and anhydrous chondritic IDPs (*21*) are also shown. Anhydrous chondritic IDPs contain only troilite and pyrrhotite, whereas the hydrous chondritic IDPs also have equally abundant Ni-rich sulfides, including pentlandite. With the exception of the two identified pentlandite crystals, the Wild 2 grains have the same Fe-Ni sulfide composition range as the anhydrous chondritic IDPs.

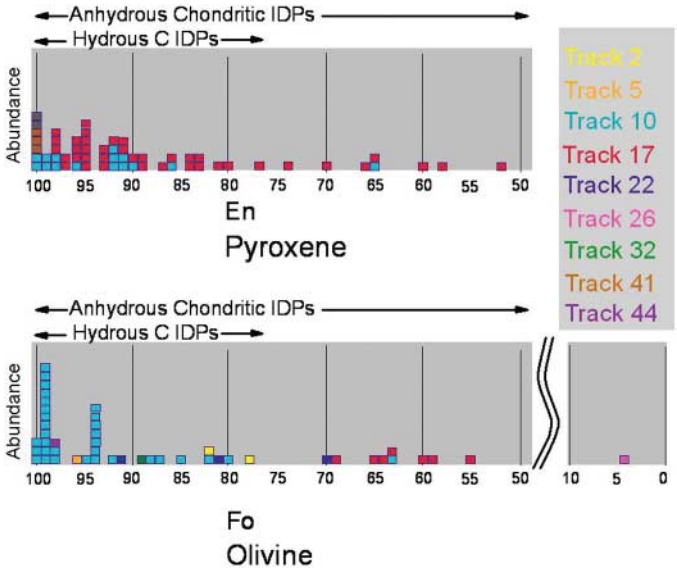


**Fig. 3.** Composition ranges of low-Ca pyroxene (En) and olivine (Fo) in grains from nine Wild 2 particles (tracks). Grains from track walls as well as track termini were analyzed, but predominantly the latter. The corresponding composition ranges for hydrous and anhydrous chondritic IDPs are also shown (*34*). The Wild 2 grains have the same olivine and low-Ca pyroxene composition ranges as the anhydrous chondritic IDPs, although the presence of mixed hydrous and anhydrous materials is compatible with these data.

A Cu-Fe sulfide, probably cubanite ($CuFe_2S_3$), is present within terminal grains in at least two tracks (tracks 22 and 26). Cubanite is occasionally encountered in extraterrestrial materials, most commonly in carbonaceous chondrites. (Fe,Zn)S was found within a terminal grain from track 22. If it can be established that this phase is in equilibrium with FeS and metal, it may be appropriate to apply the sphalerite cosmobarometer to this particular particle (*22*).

Fe-Ni metal is present as nanoscale beads in significant quantities in most tracks, partly as a product of capture heating of Fe-Ni sulfides, but the high abundance of Ni in these shows that some of this metal is intrinsic to the comet particles. In addition, tracks 38 and 43 have ~5-μm-sized Fe-Ni metal terminal grains (Ni/Fe ~ 0.03), which appear to be indigenous cometary phases.

Some Wild 2 grains contain alkali-rich mineral assemblages, including phases in tracks 3 and 16 with compositions corresponding to K-feldspar (SAED patterns suggest a feldspar-like structure, but the exact phase is not known) and what appears to be eifelite [$KNa_2(MgNa)Mg_3Si_{12}O_{30}$] (track 56). Eifelite is in the osumilite mineral group, whose members have been reported in iron meteorites, as well as enstatite and ordinary chondrites (*23*), where they formed from a combination of igneous and metasomatic processes. In addition, alkali-rich silicate material is present in some of the larger craters in aluminum foil, but it has not been well characterized.

Transmission electron microscope (TEM) observations of some tracks revealed the presence of carbonaceous phases. In the terminal grain from tracks 10, 13, 27, 41, 57, and 58, there are submicrometer-sized subgrains of poorly crystalline carbon. Some of these are attached to Fe-Ni sulfides, suggesting a genetic relationship.

No evidence of phyllosilicates or indigenous carbonate has been seen in any Wild 2 samples. Despite the fact that substantial heating and structural modification accompanied the collection of many grains in the aerogel, we would have seen characteristic compositions, grain morphologies, and lattice fringes of phyllosilicates or carbonates had they

been present (*2*, *3*, *24*). Serpentine and Ca carbonates of the same sizes as in IDPs have been successfully captured in silica aerogel even at velocities 1 km/s higher than those experienced at Wild 2, in both laboratory simulations and actual IDP collection in Earth orbit aboard the Mir space station. In instances where phyllosilicates have been dehydrated, rendered amorphous, or recrystallized during capture in silica aerogel, characteristic grain morphologies and basal lattice spacings are formed, which signal the original mineralogy (*2*, *24*). Thus, the lack of these phases among the ~50 Wild 2 grains we have so far well characterized suggests that they could not have composed more than a few percent of the more coarse-grained fraction of captured Wild 2 samples.

Along most tracks are found abundant rounded, glassy silicate bodies containing submicrometer-sized beads of silicates, Fe-Ni sulfides, and Fe-Ni metal (Fig. 1, C and D). In some respects these bodies are similar to the bits of glass with embedded metal and sulfides (GEMS) common to most anhydrous chondritic IDPs (*6*), as well as one peculiar clast in the unequilibrated carbonaceous chondrite Ningqiang (*25*). It has been proposed that GEMS are among the most primitive of solar system materials, possibly recording the radiation environment of the early Sun or of a presolar environment (*6*).

The GEMS-like bodies in the tracks often stand out texturally from the typical and dominating aerogel capture medium in terms of composition, structure, and morphology. A composition comparison with true GEMS (Table 1) shows similarities but also important differences. For example, compared to the GEMS, the glassy bodies in the tracks have low Fe as compared to Mg and S (Table 1). Additionally, there exists a textural difference between GEMS and the Stardust glassy bodies. In GEMS, the inclusions are scattered about randomly and grade from nanometer- to submicrometer-sized objects (*6*). The glassy bodies in the aerogel tracks have coarser-grained inclusions and a tendency for these to be arranged in nonrandom patterns. Also, there are sometimes no distinct boundaries between the GEMS-like objects and the embedding aerogel. In addition, some of the metal grains in the Stardust glassy bodies have S-rich rims, which are not observed in GEMS. Because <5% of GEMS have isotopic compositions very different from terrestrial values (*26*), we have not been able to determine which, if any, of the glass bodies in the aerogel collectors are cometary "GEMS" and which might be formed as a result of the melting and intermingling of fine-grained cometary matter with aerogel during the capture process.

**Table 1.** Quantitative energy-dispersive x-ray spectral analyses (atomic %) of two GEMS-like objects embedded in the aerogel of track 35 (GEMS 1 and 2) compared with actual GEMS in a chondritic IDP and CI chondrite (CI) abundances.

| Element (atom %) | GEMS-like 1 (60 nm in diameter) | GEMS-like 2 (100 nm in diameter) | | GEMs in IDPs (*6*) | | | CI (*39*, *40*) |
|---|---|---|---|---|---|---|---|
| O | 64.95 | 65.8 | 65.7 | 75.3 | 61.9 | 56.2 | 49.7 |
| Mg | 6.3 | 3.5 | 4.6 | 1.2 | 2.9 | 22.3 | 10.3 |
| Si | 26.4 | 28.4 | 26.0 | 19.1 | 16.9 | 13.3 | 11.5 |
| S | 1.75 | 1.65 | 2.7 | 1.2 | 6.1 | 3.2 | 5.7 |
| Ca | 0.1 | 0.1 | 0.15 | Nd | 0.15 | nd | 0.3 |
| Cr | trace | trace | trace | 0.2 | 0.3 | 0.1 | 0.3 |
| Mn | 0.1 | 0.1 | 0.15 | 0.1 | nd | nd | 0.2 |
| Fe | 0.3 | 0.2 | 0.5 | 2.2 | 11.1 | 4.2 | 20.0 |
| Ni | 0.1 | 0.1 | 0.2 | 0.4 | nd | 0.1 | 1.1 |
| Al | nd | nd | nd | 0.5 | 0.8 | 0.6 | 0.9 |

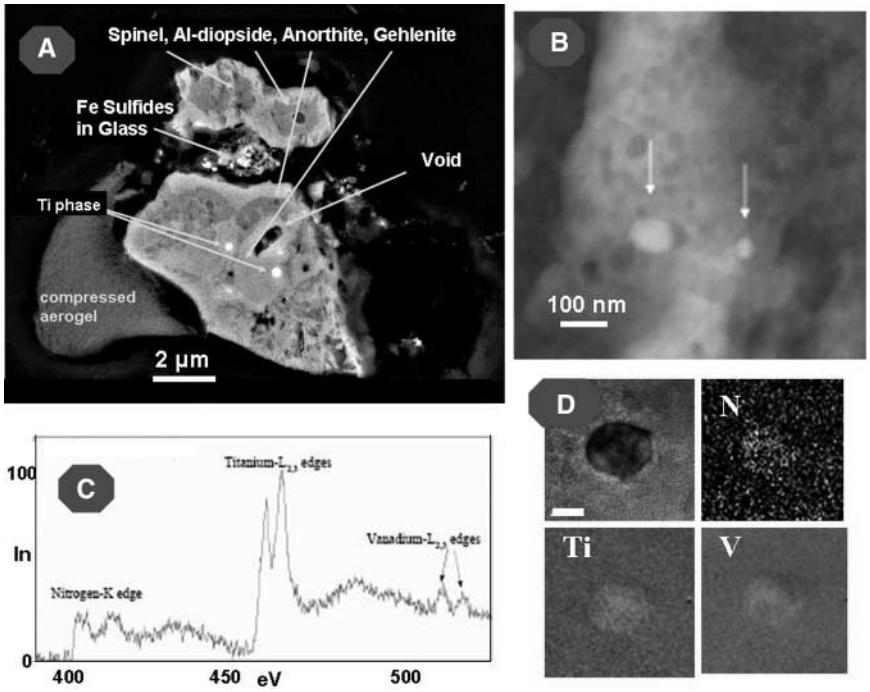


**Fig. 4.** The CAI-like grain from track 25. (**A**) Backscattered electron (BSE) image of the CAI-like grain from track 25, showing the gray shell of compressed-to-melted aerogel at lower left. (**B**) High-angle annular dark-field TEM image of two osbornite grains (arrows) within spinel. (**C**) EELS spectrum of an osbornite grain showing peaks for N, Ti, and V; scales represent intensity (In) and energy (in electron volts). (**D**) EELS element maps of an orbornite grain: BSE, N, Ti, and V. Scale bar, 40 nm.

One Wild 2 sample (track 25) has received special attention (Fig. 4) because it consists of very refractory minerals, including anorthite; a Ca-, Al-, Ti-rich clinopyroxene; gehlenite; spinel; corundum; FeS; V-bearing osbornite [(Ti,V)N]; and a phase that is probably perovskite. The osbornite occurs as sub–100-nm-sized grains within spinel, and its identification was carefully established by a combination of electron energy-loss spectroscopy (EELS) and SAED work; it may be associated with titanium oxide. The largest terminal grain from track 25 is $^{16}$O-rich (*27*).

Track 25 yielded a terminal particle and at least four major subparticles, which have been characterized. These particles exhibit some similarities to and differences from the CAIs found in carbonaceous chondrites; in particular, they have mineralogies similar to CAIs in CV3 and CM2 chondrites (*5*) (CV3 and CM2 are among the most abundant types of carbonaceous chondrites), an important finding because the inclusions are known to be among the most primitive solar system objects (based on their mineralogy, reduced oxidation state, enrichments in refractory trace elements, isotopes, etc.).

The minerals within the Wild 2 CAI-like particle, especially the osbornite, require rather high temperatures for formation, possibly higher than 2000 K, depending on oxygen fugacity (*28*). According to equilibrium thermodynamic calculations, osbornite + spinel + Ca-rich clinopyroxene is a stable condensate assemblage in systems that are otherwise solar in composition only if their atomic C/O ratio lies between ~0.79 and ~0.97, which is well above the solar value of 0.5. The presence of a CAI-like particle in comet Wild 2 appears to require large-scale radial transport in the protoplanetary disk (*29*, *30*). Although the anorthite in this particle is too small for a meaningful search for evidence of $^{26}$Al, this may prove possible in some refractory Wild 2 grains.

The recovered Wild 2 samples are mixtures of crystalline and amorphous materials. Analytical

electron microscopy (AEM) analysis of grains from the upper, often bulb-shaped, portions of tracks shows that they typically have widely varying compositions, sometimes similar to chondrites for most elements except Si, even in severely heated and melted regions (Table 1) (*31*). The crystalline grains observed among the upper portions of individual tracks are almost always submicrometer in grain size. These observations suggest that the materials captured in the upper portions of the tracks are, in general, much finer-grained than the material at the end of the slender, so-called stylus tracks that almost always project from the bulb-like upper tracks (fig. S1). AEM of very small craters on the aluminum foil also reveals crystalline olivine, pyroxene, and sulfides derived from separate submicrometer components within micrometer-sized particles. Synchrotron x-ray fluorescence (SXRF) analyses (*31*) suggest that 65 to 90% of the collected grains' mass is found in the upper portions of tracks, and only 10 to 35% is represented by the track termini grains. Our emerging model of the structure of the captured grains is that many were predominantly very fine-grained (submicrometer-sized) loosely bound aggregates with a bulk chondritic composition, most also containing much larger individual crystals (most commonly) of olivine, pyroxene, and Fe-Ni sulfides. Out of the ~70 tracks we have carefully photo-documented, only 2 appear to have no visible terminal grains, which indicates that practically all collected cometary particles contained some of these larger grains, which therefore probably served to nucleate the cometary particles. This view is supported by some of the larger crater morphologies observed on the Stardust Al foils, which have a multilobe appearance rather than being simple hemispherical craters (fig. S5) and can contain diverse subgrain compositions. This physical structure is consistent with several chondritic materials, most notably chondritic IDPs (*13*). In general, the captured Wild 2 grains are much finer-grained than the bulk of meteoritic matrix materials or IDPs.

Considering first the ferromagnesian mineral–dominated Wild 2 grains, the olivine and pyroxene crystals have the same range of Mg, Fe, Mn, and Cr compositions as those in anhydrous chondritic IDPs [with the exception of a single $Fo_4$ terminal grain (Fig. 3)] and are very similar to those in type 2 and some type 3 carbonaceous chondrites. The lack of hydrous phases among the Wild 2 samples precludes a common origin with type 1 or 2 chondrites. The type 3 carbonaceous chondrites (including primitive chondrites Acfer 094 and ALHA 77307) (*32*, *33*) and hydrous chondritic IDPs generally have narrower or somewhat equilibrated olivine and pyroxene compositional ranges (*34*). However, with the exception of the two pentlandite grains encountered in our examination, the Fe-Ni sulfide compositions of the Wild 2 grains are similar only to the anhydrous chondritic IDPs. Hydrous IDPs and all chondrites contain large amounts of pentlandite and low-Ni pentlandite (*21*). In addition, the absence of any identified aqueous alteration products in the Wild 2 grains (no phyllosilicates or indigenous carbonates, etc.) eliminates the hydrous chondritic materials from direct comparison.

No nuclear tracks (which are linear defects made by penetrating solar flare particles from the Sun) have yet been observed among Wild 2 samples. It is possible that the majority of these, if ever present, were annealed during capture, although some were observed in crater residue on the Long Duration Exposure Facility and in lunar silicate grains shot into aerogel (*35*).

In summary, the bulk of the Wild 2 samples appear to be weakly constructed mixtures of nanometer-scale grains with occasional much larger (>1 μm) ferromagnesian silicates, Fe-Ni sulfides, and Fe-Ni metal. The restricted compositional ranges of the sulfides and very wide range for silicates suggest that Wild 2 experienced little or no aqueous alteration. Of known extraterrestrial materials, the anhydrous chondritic IDPs and anhydrous micrometeorites are most similar to the Wild 2 grains, and in fact a cometary origin for anhydrous IDPs has been suspected for many years (*36*), whereas models of weakly constructed comet grains have been popular for years (*37*). The similarity of Wild 2 samples to some IDPs demands reexamination of the latter with new eyes, for there are some apparent differences. For example, Fe-Cr-Ti oxides have not been reported as inclusions in IDP olivines, nor has orthoenstatite been reported (*13*). The very wide ranges of olivine and low-Ca pyroxene compositions in Wild 2 require a wide range of formation conditions, including diverse temperatures and oxygen fugacities, probably reflecting different locations in the protoplanetary disk. It is critical to determine the role of annealing in cometary grain formation, but this cannot be done with the mineralogic data in hand.

The presence of a refractory particle resembling a meteoritic CAI among the Wild 2 grains raises many new questions. IDPs are believed to contain samples of both asteroids and comets, and wholly refractory IDPs were identified two decades ago (*31*, *32*) but have received very little attention. In mineralogical terms, the Wild 2 CAI-like particle appears similar to these poorly understood IDPs and is similar (though finer-grained) in various respects to CAI from CM, CR, and CH-CB carbonaceous chondrites. The presence of CAI-like material in a comet appears to require substantial radial transport of material across the early protoplanetary disk, as does the rather wide range of olivine and pyroxene compositions discussed above.

The lack of aqueous alteration products in Wild 2 samples is in clear contrast to the mineralogy reported for comet Tempel 1, based on Spitzer Space Observatory data in support of the Deep Impact mission (*9*). This mineralogical difference could be due to differences in the geological histories of Jupiter-family comets (*38*).

### References and Notes


1. R. A. Barrett, M. E. Zolensky, R. Bernhard, *Lunar Planet. Sci.* **24**, 65 (1993).
2. F. Hörz, M. E. Zolensky, R. P. Bernhard, T. H. See, J. L. Warren, *Icarus* **147**, 559 (2000).
3. M. J. Burchell, G. Graham, A. Kearsley, *Annu. Rev. Earth Planet. Sci.* **34**, 385 (2006).
4. These issues are treated at greater length in the supporting material on *Science* Online.
5. F. Hörz *et al.*, *Science* **314**, 1716 (2006).
6. J. P. Bradley, *Science* **265**, 925 (1994).
7. E. K. Jessberger, A. Christoforidis, J. Kissel, *Nature* **332**, 691 (1988).
8. M. E. Lawler, D. E. Brownlee, S. Temple, M. M. Wheelock, *Icarus* **80**, 225 (1989).
9. C. Lisse *et al.*, *Science* **313**, 635 (2006).
10. J. Akai, *Proc. NIPR Symp. Antarct. Meteorites* **3**, 55 (1990).
11. M. E. Zolensky, W. H. Kinard, *Adv. Space Res.* **13**, 75 (1993).
12. W. Klöck, K. L. Thomas, D. S. McKay, H. Palme, *Nature* **339**, 126 (1989).
13. F. J. M. Rietmeijer, in *Planetary Materials*, J. J. Papike, Ed. (Mineralogical Society of America, Washington, DC, 1998), pp. 2-1–2-95.
14. M. Gounelle *et al.*, *Meteorit. Planet. Sci.* **37**, A55 (2002).
15. S. B. Simon, L. Grossman, *Meteorit. Planet. Sci.* **38**, 813 (2003).
16. M. K. Weisberg, H. C. Connolly, D. S. Ebel, *Meteorit. Planet. Sci.* **39**, 1741 (2004).
17. A. Tsuchiyama, *Lunar Planet. Sci. Conf.* **XXXVII**, abstract 2001 (2006).
18. W. A. Deer, R. A. Howie, J. Zussman, *Rock-Forming Minerals, Volume 2A, Single-Chain Silicates* (Longman, London, 1978).
19. J. Ganguly, V. Tazzoli, *Am. Mineral.* **79**, 930 (1994).
20. D. Vaughan, J. Craig, *Mineral Chemistry of Metal Sulfides* (Cambridge Univ. Press, Cambridge, 1978).
21. M. E. Zolensky, K. Thomas, *Geochim. Cosmochim. Acta* **59**, 4707 (1995).
22. M. N. Hutchison, S. D. Scott, *Geochim. Cosmochim. Acta* **47**, 101 (1983).
23. A. N. Krot, J. T. Wasson, *Meteoritics* **29**, 707 (1994).
24. R. A. Barrett, M. E. Zolensky, F. Hörz, D. J. Lindstrom, E. K. Gibson, *Proc. 19th Lunar Planet. Sci. Conf.* **22**, 203 (1992).
25. M. E. Zolensky *et al.*, *Meteorit. Planet. Sci.* **38**, 305 (2003).
26. S. Messenger, L. P. Keller, F. J. Stadermann, R. M. Walker, E. Zinner, *Science* **300**, 105 (2003).
27. K. D. McKeegan *et al.*, *Science* **314**, 1724 (2006).
28. D. Ebel, in *Meteorites and the Early Solar System II*, D. S. Lauretta, H. Y. McSween Jr., Eds. (Univ. of Arizona Press, Tucson, AZ, 2006), pp. 253–278.
29. F. Shu, H. Shang, A. E. Glassgold, T. Lee, *Science* **277**, 1475 (1997).
30. J. Cuzzi, S. Davis, A. Dobrovolskis, *Icarus* **166**, 385 (2003).
31. G. Flynn *et al.*, *Science* **314**, 1731 (2006).
32. A. J. Brearley, *Geochim. Cosmochim. Acta* **57**, 1521 (1993).
33. A. Greshake, *Geochim. Cosmochim. Acta* **61**, 437 (1997).
34. M. E. Zolensky, R. A. Barrett, *Meteoritics* **29**, 616 (1994).
35. P. Tsou *et al.*, *Lunar Planet. Sci. Conf.* **XXI**, 1264 (1990).
36. A. O. Nier, D. J. Shlutter, *Meteoritics* **28**, 675 (1993).
37. A. Li, M. Greenberg, *Astrophys. J.* **498**, L83 (1998).
38. D. E. Brownlee *et al.*, *Science* **314**, 1711 (2006).
39. E. Anders, M. Ebihara, *Geochim. Cosmochim. Acta* **46**, 2363 (1982).
40. In (*39*), carbon is ignored in the calculations and oxygen is calculated.


41. We thank the U.S. public for supporting the Stardust mission with valuable tax dollars and our many home institutions and funding agencies for making possible this concentrated 9-month-long analytical effort. The dedicated personnel of the Johnson Space Center Curation Facility were critical to our analytical efforts. We also thank our good friends at Lockheed Martin Space Systems for the wonderful spacecraft.


**Supporting Online Material**
www.sciencemag.org/cgi/content/full/314/5806/1735/DC1
Materials and Methods
Figs. S1 to S6
References

3 October 2006; accepted 20 November 2006
10.1126/science.1135842

# Résumé

La microscopie électronique en transmission (MET) est un outil puissant et polyvalent pour les analyses microstructurales des matériaux à l'échelle nanométrique. Sur la même zone d'observation, on peut réaliser une image de la microstructure et de ses défauts, en faire une analyse chimique et une détermination structurale en diffraction. Mon activité de recherche porte sur le développement de méthodes de caractérisation par diffraction électronique quantitative. Par « quantitative », nous entendons la mesure absolue ou relative des intensités diffractées et leur comparaison à des grandeurs simulées.

Concernant les matériaux semiconducteurs, mes recherches ont porté sur la mesure des déformations dans les nanostructures épitaxiées. Dans ces systèmes, les champs de déformation jouent un rôle prépondérant sur les propriétés de maintien (mécanique) et sur les propriétés d'usage (opto-électroniques, transport). Il est donc important de les caractériser avec précision. Nous avons développé des méthodes de mesure originales basées sur l'analyse des intensités électroniques recueillies en diffraction en faisceau convergent conventionnel et à grand angle (CBED et LACBED).

Les développements récents portent sur la caractérisation des phases cristallines et de leurs défauts structuraux dans les minéraux. Dans ces matériaux, de cristallochimie souvent complexe, l'analyse quantitative des intensités diffractées permet notamment de discerner des phases cristallographiquement proches ou de révéler les relations d'orientation existant entre des domaines voisins. Ceci est essentiel aux analyses microstructurales locales et à leur interprétation en vue de déterminer les conditions de pression et de température ayant prévalu à leur formation. Mon apport dans le domaine est essentiellement basé sur l'utilisation de la précession électronique.

Dans le domaine de la minéralogie, un autre type d'étude a été mené parallèlement aux précédentes. Il s'agit de l'analyse des échantillons cométaires provenant de la mission « Stardust » de la NASA. Pour ces études, on utilise toutes les techniques de MET disponibles pour révéler la nature et les mécanismes possibles de formation des échantillons observés: micro-analyse X, imagerie conventionnelle et haute résolution, diffraction. Ma contribution a essentiellement porté sur l'analyse de la microstructure des pyroxènes, qui sont en général des traceurs fiables pour rendre compte du passé thermique et mécanique des minéraux.

La première partie de ce mémoire concerne la présentation de ces travaux. La seconde partie détaille la description plus individuelle de mon parcours scientifique ainsi que la liste des publications, des activités d'encadrement et d'animation scientifique qui y sont associées.